Modelling Thermodynamic and Kinetic Reactions Between Ceramic Oxides and Ti-Alloy Melt

by

Joseph S Moses

A thesis submitted to the University

of Birmingham for the degree of Doctor

of Philosophy

School of Metallurgy and Materials

University of Birmingham

United Kingdom

October 2024

Acknowledgements:

First and foremost, I would like to thank Almighty God for providing me with the strength and encouragement needed to persevere through the challenging moments of completing this thesis.

I am deeply grateful to my supervisor, Dr. Nils Warnken, for his invaluable advice, continuous support and patience throughout my PhD journey. His guidance has been instrumental in shaping this work and I am truly thankful for his mentorship.

Finally, I would like to express my heartfelt gratitude to my parents, sister and friends. Their unwavering understanding and encouragement over the past few years made it possible for me to complete my studies. I could not have achieved this milestone without their love and support.

Abstract

Casting titanium alloys presents significant challenges due to the high reactivity of titanium in its molten state. This reactivity renders ceramic mould oxides highly susceptible to chemical reactions, leading to premature mould failure and contamination of the liquid metal by ceramic inclusions. Developing robust oxide systems is therefore crucial to mitigating mould degradation and ensuring the homogeneity, precision and geometric accuracy of the final cast. While numerous experimental studies have examined the behaviour of oxides in contact with liquid titanium alloys, there is limited understanding of how to select and design new oxide systems. Furthermore, modelling efforts in this field remain scarce, often constrained by the lack of reliable thermodynamic data, insufficient insight into metal-mould interactions and an over reliance on simplified binary system models. This study introduces a combined thermodynamic and kinetic framework to analyse metal-mould reactions. CALPHAD-based thermodynamic data was used to evaluate the interactions between titanium and mould oxides, providing inputs for a kinetic model based on the Frozen Gradient Approximation (FGA). The FGA was extended to incorporate multi-component and multi-phase interactions, enabling a more comprehensive analysis of oxide behaviour. The results demonstrate that all mould oxides dissolve to some extent and none studied remain completely stable in contact with the TiAl

alloy. However, several strategies were identified to minimize reaction rates and improve oxide stability. Among these, multi-phase oxide systems, such as Al_2O_3-Mullite and YAG-YAP demonstrated enhanced stability when combined, compared to their performance as individual oxides. This is attributed to the potential of multi-phase oxides with shared ions to serve as more durable mould materials. Notably, Al_2O_3-Mullite proved effective in suppressing alpha-case formation, further enhancing oxide stability in titanium casting applications. In existing literature, Y_2O_3 is widely regarded as the most stable oxide for titanium casting, with CaO typically ranked as the second most stable. However, the sequential oxide selection method employed in this study reveals additional oxides and oxide combinations with stability levels that fall between those of yttria and calcia. These include, systems such as YAM, $CaYAlO_4$ and YAM-YAP. These demonstrate significant potential as alternative mould materials, offering intermediate stability.

Contents

List of Figures

List of Tables

1 Introduction

Casting titanium alloys has a rich history marked by numerous advances, yet a significant challenge still remains—the scarcity of fully inert crucible and mould materials that can withstand the high temperatures and reactivity of titanium. To date, no mould material has been found that can completely resist the reactivity of titanium during high-temperature casting, which restricts the potential for large-scale production of titanium alloys and impacts the quality of final castings. This work aims to advance understanding of the thermo-kinetic phenomena that govern metal-mould reactions during casting and to explore the design of improved oxide systems with minimal reactivity towards titanium. Addressing these interactions involves three primary levels:

- **Thermodynamic Interactions Between Mould and Metal**: This involves determining the driving forces behind the dissolution, growth, and precipitation of reaction products.
- **Kinetic Analysis**: Once the thermodynamic driving forces are identified, the kinetic processes—such as diffusion and mass transfer rates under varying conditions—can be analysed.
- **Development of Oxide Systems**: With such information it is possible to

introduce strategies to improve stability of oxides and develop/identify more stable oxide systems

The three hierarchical levels of analysis introduces varying degrees of complexity based on factors such as number of elements, phase interactions, ceramic stoichiometry, reaction products, transport mechanisms and the dynamics of moving boundaries. Taking these aspects into consideration, this work proposes a methodology to investigate bulk metal-mould reactions within multi-component and multi-phase systems and to accurately distinguish between least stable and most stable ceramic systems. Using this approach, 25 distinct oxides or oxide combinations were analysed. The initial material selection was based on literature review, identifying certain oxides as the least reactive and most promising for further development. A second selection round then refined these choices using insights from the model, enabling targeted exploration of oxide stability and reactivity.

In this thesis, it will be demonstrated that through the use of this simple methodology in conjunction with CALPHAD (Calculation Of Phase Diagrams) data, it is possible to perform quasi-equilibrium calculations to extract kinetics of multi-component, multiple-phase systems in relatively quick manner as opposed to relying on more complex models like Phase Field. This simple model will also demonstrate that

strategies can be implemented to extend the kinetic stability of oxides in contact with liquid titanium and pave pathways for future research into novel oxide systems.

The organization of this work is as follows:

In **Chapter 2**, a comprehensive background on titanium and the casting of Ti-alloys is presented, laying the foundation for understanding the complexities of this field. The chapter continues with a detailed review of the most relevant research on Ti-mould reactions, specifically emphasising experimental findings that shed light on the interactions between titanium and various mould materials. Furthermore, the chapter explores the available thermodynamic and kinetic reaction models that are crucial for understanding metal-mould interactions. In addition, the limitations that currently restrict the advancement of oxide systems are critically analysed.

In **Chapter 3**, the thermodynamic driving force (change in free energy of reaction) for metal-mould reactions are explored using the mass action law. Although this approach has been applied for several decades, there has been very limited research and few available results specifically addressing Ti-mould reactions, particularly under non-ideal conditions. A few approximations of the mass action law have been developed in the past, these were revisited and further examined to identify their strengths

and limitations. This included modifying existing approximations and incorporating data from additional sources, such as the Miedema model and CALPHAD data. Although these approximations showed some correlation with experimental findings, they still diverged significantly from real-world behaviour, underscoring the need for a complete and accurate calculation of the thermodynamic driving force to ensure precise predictions. To achieve this, CALPHAD data was utilized to fully apply the mass action law to many of the systems. Based on this, the thermodynamic driving forces for various oxides as a function of Ti-Al composition are calculated, providing basis for kinetic analysis in the next section. Stability ranking of different oxides is established and compared with experimental ranking.

Chapter 4, focuses primarily on the kinetics of reactions between metal and the mould. The frozen gradient approximation is a well-established model used to simulate the growth of spherical particles in a supersaturated matrix. In this chapter, the model is further developed to account for multi-component, multiphase reactions by incorporating CALPHAD data-driven mass action law. By combining these approaches, the kinetics of dissolution and/or growth in Ti-mould reactions are determined. Several strategies are introduced into the model to enhance the kinetic stability of oxides in contact with liquid titanium. Additionally, the chapter explores

how variations in oxide formulation affect reaction rates, providing further insights into optimizing material performance.

Chapters 3 and 4, serve as the core sections of this study, each comprising a method, results and a discussion section.

Finally, **Chapter 5** presents the overall discussion, while **Chapter 6**, covers the conclusion and future work.

Overall Aim: This thesis addresses the thermodynamic and kinetic instability of mould materials when in contact with molten titanium during casting. The goal is to identify or improve existing oxide systems to better withstand the high reactivity of titanium. The following approach was developed to tackle this challenging issue.

1. To develop a simple model which can simulate both the thermodynamics and kinetics of metal-mould interaction.

2. Ensure the model can account for both multi-component and multi-phase interactions between the metal and the mould.

3. To use the model to identify strategies that can improve stability of mould materials and be able to identify suitable mould materials for casting Ti-alloys.

2 Literature Review

2.1 Ti and Ti-Alloys

2.1.1 Titanium Background

In 1791, a geologist named William Gregor stumbled upon an unidentified mineral while examining magnetic black sand from a local river in Cornwall, England [38]. Upon removing the magnetic iron oxide and subjecting the residue to treatment with hydrochloric acid, he discovered an impure white oxide of a previously unknown element. Within four years of its discovery, Martin Heinrich Klaproth (German chemist), independently isolated the white oxide from a Hungarian mineral known as rutile and subsequently named the element 'Titanium', drawing inspiration from the Titans of Greek mythology, powerful giants renowned for their strength [39, 1]. The Titans, despised by their father, were confined deep within the earth's crust, much like the difficult-to-extract ore [1]. In its natural state, titanium is not found in pure form due to its high reactivity, instead it is commonly present as Ti-oxide minerals. The two main titanium minerals are ilmenite ($FeTiO_3$) and rutile (TiO_2) (smaller quantities are also obtained from perovskite ($CaTiO_3$) or sphene ($CaTiSiO_5$)) [1].

The isolation of titanium as a pure metal was first achieved in 1910 by Matthew A. Hunter by reducing titanium tetrachloride ($TiCl_4$) with sodium in a high-pressure vessel [1]. However, it wasn't until 1948 that the metal was commercially produced through the Kroll process, named after its developer, William Kroll of Luxembourg [40]. Today titanium is recognized as the ninth most abundant element in the Earth's crust, comprising approximately 0.6% of the Earth's crust [41] (equivalent to about 0.57 wt% by weight). Titanium and its alloys are considered expensive materials when evaluating the cost per kilogram compared to metals like steel. The high cost is associated with the substantial energy requirements for its extraction, melting and manufacturing processes [42]. Compared to steel, the processing of titanium necessitates ten times the energy, as reported by Digital Alloys in 2019 [43]. As a consequence of this, titanium and its alloys are predominantly utilized mainly in high-performance applications [44]. In recent years, several manufacturing techniques have emerged as alternatives to the traditional Kroll process for extracting pure titanium. These include the Hunter process, Armstrong process, Fused Salt Electrolysis, Hydrogen-Assisted Magnesium Reduction Process, among others [45]. These processes represent advancements in titanium production methods, each with its own set of characteristics and advantages. Nevertheless, the Kroll process seems to be the most dominant method for extracting titanium to date, mainly due to its

long-standing use, established infrastructure and economic viability [46].

Figure 1 shows the stages in which titanium ore is turned into mill products, and figure 2 illustrates the Kroll process.

The process of extracting titanium is summarised below with reference to figure 1 and 2:

1. Titanium tetrachloride is reduced with liquid magnesium in a high-temperature reaction vessel to produce titanium and magnesium chloride, following the Kroll process (figure 2). Titanium is extracted as titanium-sponge.

2. The titanium sponge undergoes a vacuum distillation process to completely remove the by-products (magnesium chloride) formed during the Kroll process.

3. The titanium sponge or alloy is pressed into briquettes.

4. These briquettes are welded together to form electrodes.

5. The electrode is melted using the vacuum arc remelting (VAR) process to remove hydrogen and other volatiles picked up during earlier stages.

6. During the VAR process, an ingot is produced as the electrode is melted and re-melted, resulting in a high-quality titanium ingot with improved homogeneity and reduced segregation of alloy components.

7. The ingots are further processed to obtain mill products such as bars, plates, sheets, strips, wires, etc.

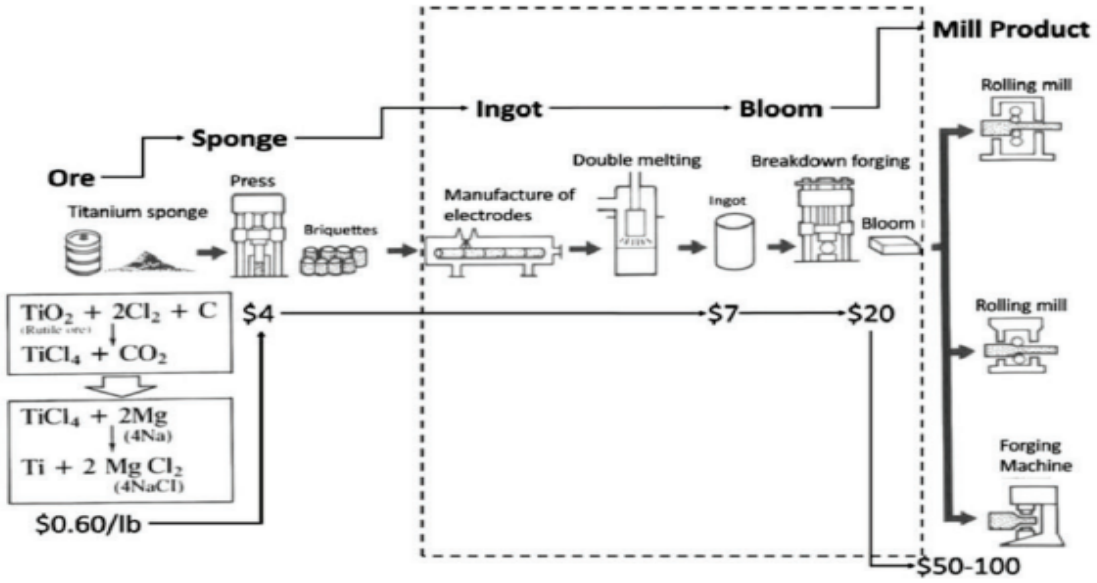

Figure 1: Summary of manufacturing pathway of titanium [47]

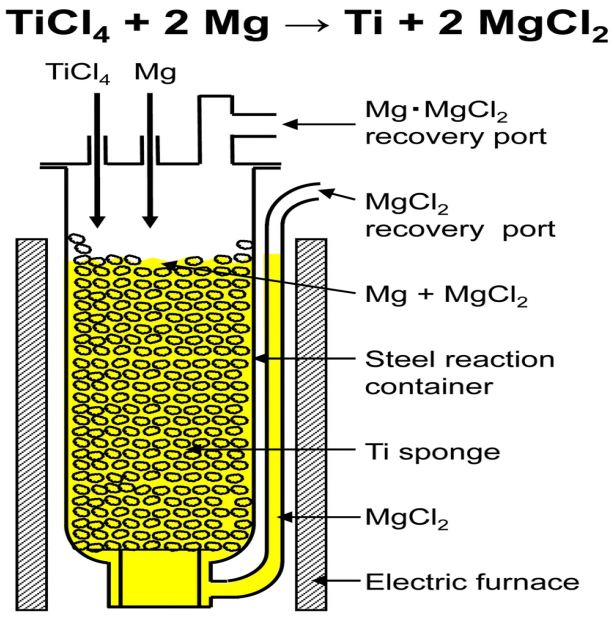

Figure 2: Ti Reduction process (Kroll Process)[48].

2.1.2 Global Titanium Market

Figure 3 illustrates the global annual production of ilmenite and rutile as reported by the US Geological Survey (USGS) since 1950 [49]. The chart indicates a substantial growth in the annual global production of titanium since 1950 with short-term fluctuations and this trend is expected to continue in tandem with the rising global population and per capita consumption in the coming decade [50].

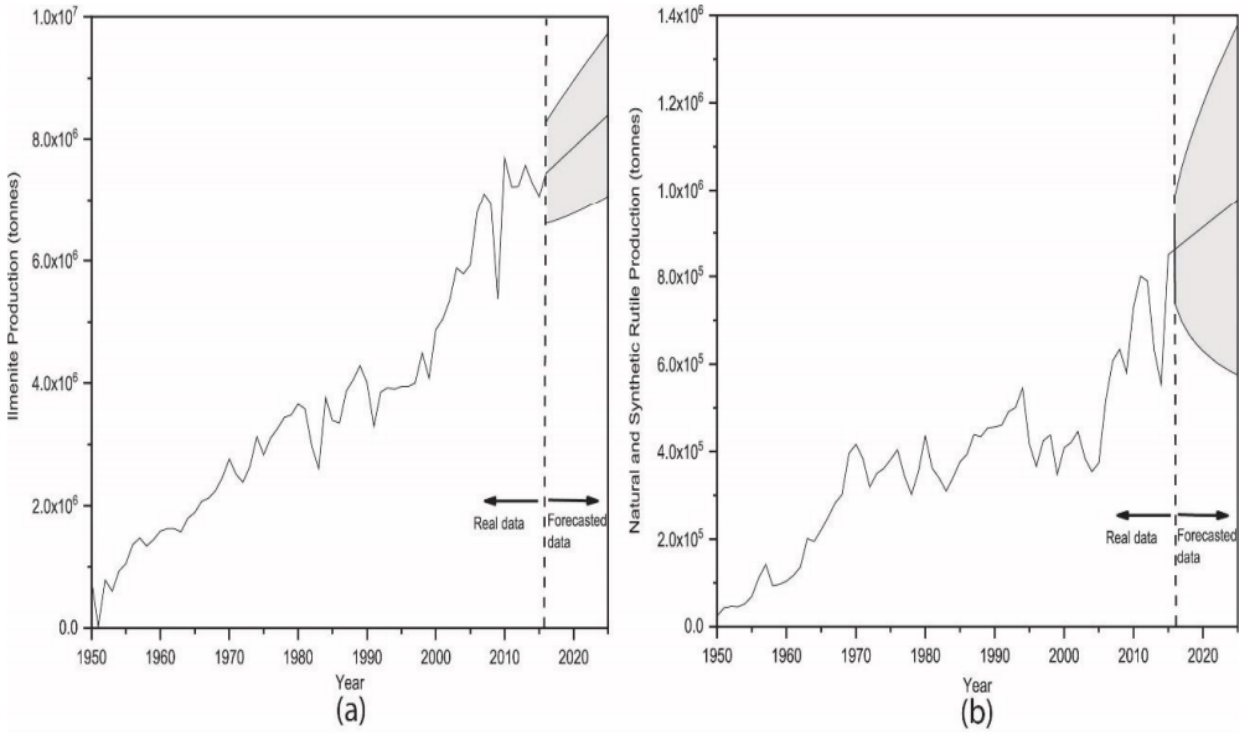

Figure 3: The global annual production of ilmenite (a) and rutile (b) from 1950 to 2015, along with forecasts until 2025, data from USGS (2021) [49]. The highlighted zone represents the 95% confidence interval of the forecast.

The short-term variations in titanium production over the years can be attributed to various factors. For instance, recent fluctuations may be linked to events such as the peak in rare earth elements during the 'Rare Earth Crisis' in 2010 [51]. Additionally, the impact of the COVID-19 pandemic has led to a decrease in demand and disrupted operations in the titanium mining and processing industries [52]. A comparison between the 2015 projections and current data from 'Statista' [53] shows that ilmenite production has closely tracked earlier forecasts, reaching approximately 9.35 million tonnes by 2024—near the upper limit of the projected range. In contrast, rutile production has grown more slowly than anticipated, remaining around 560,000 tonnes in 2023 [54], well below the forecast midpoint. This divergence indicates sustained strong demand for ilmenite, while growth in rutile production has fallen short of expectations.

As indicated in figure 3, the heightened interest in titanium during the 1950s is largely attributed to its significant advantages, particularly its high strength-to-weight ratio and exceptional corrosion resistance, which made it an ideal material for aerospace applications [55]. Figure 4 shows the evolving utilization of titanium as a percentage of materials in Boeing and Airbus aircraft, specifically focusing on its use in airframes.

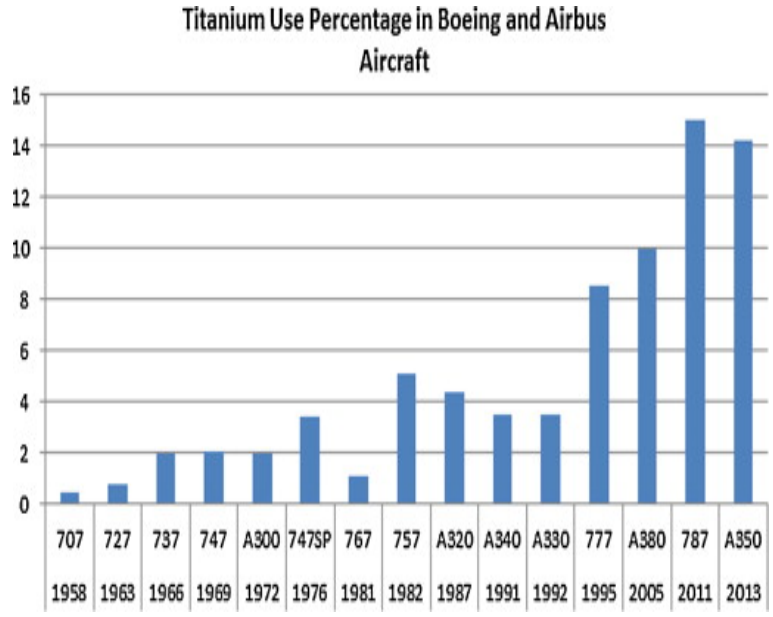

Figure 4: Use of Ti in airframes by Airbus and Boeing [56]

Starting from minimal usage in 1950, titanium has progressively increased its presence to constitute approximately 15-20% of materials used in modern aircraft frames by 2013, showcasing its pivotal role in aerospace engineering. Moreover, the utilization of titanium, particularly in the form of titanium alloys, has expanded beyond aerospace to encompass diverse industries such as automotive, biomedical, marine, military and dental [57]. As a result of its versatile utility and growing demand across industries, the global titanium market size reached USD 25.2 billion in 2022 according to 'Precedence Research' [58] and is projected to reach approximately USD 47.08 billion by 2032. This growth prediction represents a compound annual growth rate (CAGR) of 6.50% for the forecast period from 2023 to 2032,

highlighting the significance of titanium in modern manufacturing and engineering. Therefore, focused research efforts need to address the evolving challenges to meet the requirements of the future. These research endeavours should aim to enhance existing titanium manufacturing processes, develop innovative alloy compositions, improve material properties and explore novel applications. To ensure sustainability and efficiency in titanium production, advancements in recycling techniques and the reduction of environmental impact are also critical.

2.1.3 Characteristics of Titanium and Titanium-Alloys

The structural and phase characteristics of pure titanium are vital considerations in understanding its behaviour at different temperatures. Pure titanium exists in two allotropic forms: alpha-titanium (alpha-phase) and beta-titanium (beta-phase) [37]. The alpha phase possesses a hexagonal close-packed (HCP) crystal structure, while the beta phase features a body-centered cubic (BCC) crystal structure, as depicted in figure 5. At temperatures below 882°C, the alpha phase is stable, however, when the temperature surpasses 882°C, an allotropic phase transformation occurs, leading to the transition from the alpha phase to the beta phase [37]. This critical temperature is commonly referred to as the beta-transus temperature.

It is important to note that the specific beta-transus temperature is influenced by

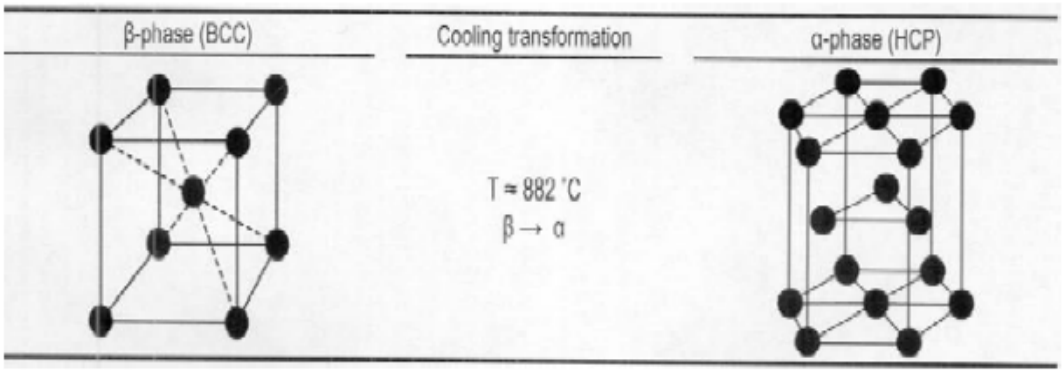

Figure 5: Crystallographic Structure and allotropic transformation of pure titanium [59][37].

the presence of alloying elements in titanium, making it a factor of alloy composition. The impact of alloying additions on the beta-transus temperature is illustrated in figure 6. Certain elements added to titanium serve as alpha-stabilizers, increasing the beta-transus temperature and stabilizing the alpha phase. Conversely, there are elements that act as beta-stabilizers, reducing the beta-transus temperature thus stabilizing the beta phase. Beta-stabilizing elements are further divided into beta-isomorphous elements, which exhibit high solubility in titanium and beta-eutectoid elements, which have limited solubility and are inclined to form intermetallic phases. Elements that do not significantly affect the beta-transus temperature are referred to as neutral elements. Furthermore, alloying elements can be classified based on the position they occupy in the crystal lattice, which may be either interstitial or substitutional. Beta-stabilizers such as O, N, and C occupy the interstitial regions within the lattice and are considered interstitials, while elements such as Al, Mo, and

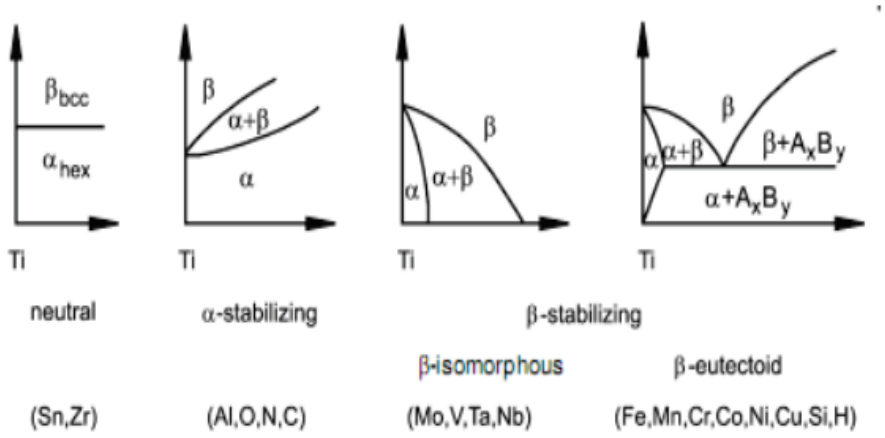

Figure 6: Effects of alloying additions on Ti phase diagram [37]

V dissolve substitutionally. In addition to influencing the beta-transus temperature, alloying elements also impart specific characteristics and properties that are highly valuable in many applications. Introducing modifications to Ti-Al alloys through the addition of alloying elements is a common strategy aimed at enhancing specific properties. Various elements, both metallic and non-metallic, have been added to Ti-Al alloys to achieve desired improvements. Figure 7 shows some examples of alloying elements and their effects on the mechanical properties of Ti-Al alloys:

Understanding the phase transformations and microstructural changes induced by these alloying elements is crucial for alloy design. However, one challenge in alloying is that while an element may improve one desired property, it may also limit or compromise another property. Therefore, careful selection and optimization of alloying elements are necessary to achieve the desired balance of properties in Ti-Al

Element	Effect
Aluminum (Al)	A reduction in aluminum content tends to increase strength but may reduce ductility.
Chromium (Cr)	Up to 2 at% enhances ductility.
Manganese (Mn)	Up to 2 at% enhances ductility.
Vanadium (V)	Up to 2 at% enhances ductility.
Niobium (Nb)	Additions of 1–2 at% are necessary for sufficient oxidation resistance.
Tungsten (W), Molybdenum (Mo), Silicon (Si), Carbon (C)	Added in levels of 0.2–2 at% to improve creep resistance.
Boron (B)	At 0.2–2 at%, acts as a grain-refining coagulant and stabilizes microstructure.

Figure 7: Effects of alloying additions on Ti phase diagram, adapted from Leyens [1]

alloys.

2.1.4 Classification and Industrial Application of Ti-Alloys

Ti-alloys are classified based on their chemical composition, primarily with regard to the concentration of alloying elements. The main categories of alloys include alpha-Ti, beta-Ti, alpha+beta-Ti, Near-alpha, meta-stable beta, and intermetallic compounds [1]. Each of these categories will be briefly discussed with information obtained from Leyens and Veiga [1], [37].

Alpha-Ti and Near-alpha-Ti: Commercially pure titanium alloys, also known as CP-Titanium, contain alpha-stabilizers such as oxygen, carbon, and aluminium.

Among these, only oxygen is intentionally alloyed to attain the necessary strength levels of CP titanium grades, while the other alpha-stabilizers are considered impurities. CP-Titanium alloys are further classified into Grades 1-7. Grades 1-4 are oxygen-containing, and the specific grade designation depends on the oxygen content present in the alloy. The presence of oxygen significantly enhances strength while simultaneously reducing ductility. These alloys offer high corrosion resistance and deformability, meeting the primary requirements of the chemical and process engineering industry. Some examples of alpha-Ti alloys and their applications in industry are provided in table 1.

Near alpha alloys are characterized by containing small amounts of beta-stabilizing elements in alpha-Ti. They were specifically engineered to operate at high temperatures ranging from 500 to 550°C, largely due to their exceptional creep behaviour and high strength. For example, Ti-6-2-4-2-S shown in table 1, the enhancement in creep behaviour is attributed to the addition of small amounts, of silicon typically up to 0.1 wt%. It is believed that Si precipitates at high temperatures onto dislocations, impeding their climb and consequently deformation. Moreover, it has been observed that the addition of high amounts of aluminium (Al) can lead to stress corrosion problems and is limited to less than 6 at%.

Alpha+Beta-Ti: Alpha+beta titanium alloys contain both alpha and beta sta-

Materials	***System and Parts***	***Type***	***Industry***
CP-Ti	Floors	Airframe Structure	Aerospace
Ti-3Al-2.5V	Hydraulic Tubing		
Ti-6-2-4-2S	Fan discs and blades	Gas Turbine Engines	
	Compressor discs		
	Compressor Blades		
CP-Ti (Grade4)	Body	Engine	Automotive
CP-Ti (Grade 2)	Exhause System	Engine	
CP-Ti	Valves and connectors	Heart	Medical
CP-Ti (Grades 1,2,3 and 4)	Dental Implants	Dental	

Table 1: Application of alpha Ti-alloys in industry [1], [37]

bilizing elements in significantly larger quantities than near alpha-alloys. These alloys exhibit a combination of high strength and ductility, distinguishing them from the previous two classes of titanium alloys [22]. Ti-6Al-4V stands out as the most popular titanium alloy, constituting to over 50 percent of all Ti-alloys. It is also the most extensively developed and tested titanium alloy, primarily due to its widespread use in the aerospace, automotive and medical industry as shown in table 2. Moreover, Ti-6Al-4V boasts exceptional processability in terms of castability, plastic workability, heat treatability, and weldability. Other alloys, such as Ti6-2-2-2-2, Ti-55-24-S, or Ti-17, have been specifically developed for elevated operating temperatures of up to about 400°C.

Materials	***System and Parts***	***Type***	***Industry***
Ti-5AI-2Sn-2Zr-4Mo-4Cr	Fans and Compressor Discs	Gas Turbine Engine	Aerospace
Ti-6Al-4V	Window Frames	Airframe Structure	
	Fan discs and blades	Gas Turbine Engines	
	Compressor discs		
	Compressor Blades		
	Suspension Springs	Frame Structures	Automotive
	Armor		
	Body		
	Outet Valves	Engines	
	Intake Valves		
	Connecting Rods		
	Hip and Knee Joints	Joints	Medical
	Dental	Dental	

Table 2: Application of alpha+beta Ti-alloys in industry [1], [37]

Materials	***System and Parts***	***Type***	***Industry***
TIMRTAL 21S	Nozzle Assembly	Gas Turbine Engines	Aerospace
Ti-10-2-3	Landing Gear	Airframe Structures	
Ti-15V-3Cr-3Sn-3Al	Springs		

Table 3: Application of beta Ti-alloys in industry [1], [37]

Beta-alloys and near beta–alloys Also known as metastable beta-alloys, can be hardened to high strength levels exceeding 1400 MPa [60]. Beta-alloys typically contain more than 15 wt% of beta-stabilizing elements. The complexity within the microstructure allows for optimized high strength and toughness, as demonstrated in the case of TIMETAL 10-2-3. TIMETAL 21S was specifically developed as an oxidation-resistant material intended for use as the matrix in long fiber-reinforced titanium alloys. However, the widespread applications of beta-alloys are constrained by their relatively high density, modest weldability, poor oxidation behaviour, and complex microstructure. Typical industrial applications for these alloys are given in table 3.

Intermetallic: Amongst the class of alpha and beta alloys, Ti-aluminides embody a special class of alloys with exceptional set of physical and mechanical properties which has gained much interest in recent times. Figure 8 depicts the Ti-Al

phase diagram, showcasing not only the large solid solution phases but also several stable intermetallic phases. These intermetallic phases form the foundation for titanium-aluminium intermetallic, which are known for their high strength at elevated temperatures. However, they also exhibit significantly lower ductility and fracture toughness compared to the conventional titanium alloys mentioned earlier.

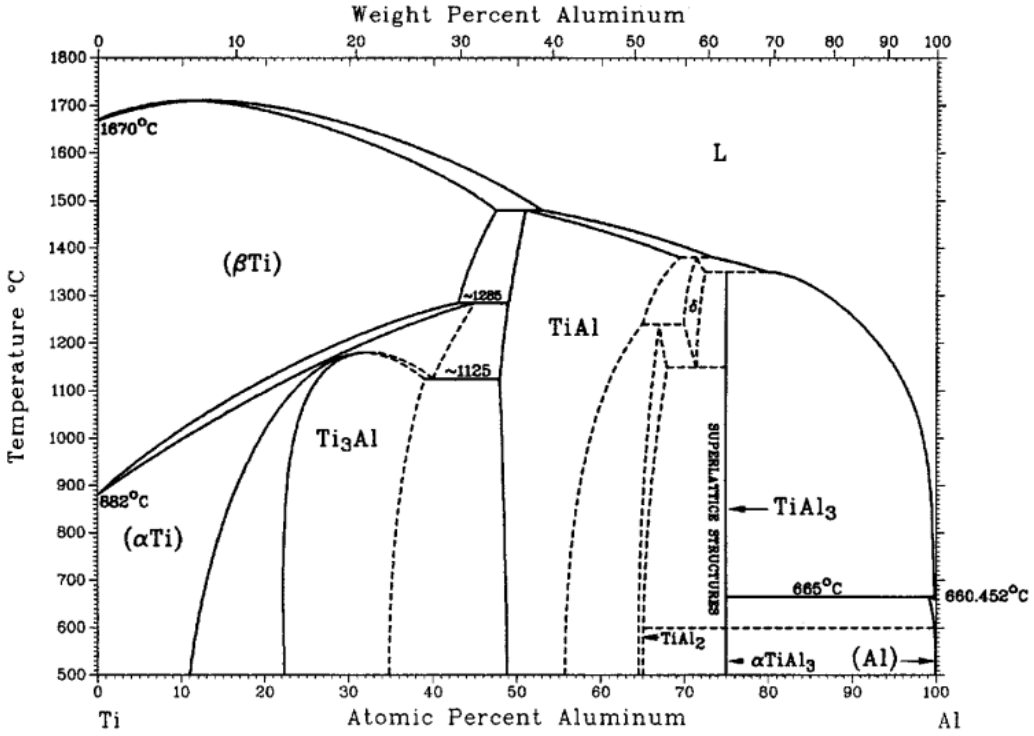

Figure 8: Typical Ti-Al phase diagram [1]

Notably, Ti3Al and TiAl are the most common aluminides of titanium. Due to the modest long-term stability of Ti3Al alloys, the primary focus of research and development on titanium aluminides is currently directed towards TiAl-based alloys. In the following section, a comprehensive analysis of TiAl alloys will be provided, as they represent a significant focus of the present study.

2.1.5 Advancements in Intermetallics

In sectors such as aerospace and aviation, the push for future-generation alloys is driven by the demand for higher service temperatures, reduced emissions, lighter weight and increased operational speeds [61]. Among the promising materials in this pursuit are titanium aluminide alloys, including gamma-$TiAl$ and Ti_3Al. These alloys are highly regarded for their potential to fulfill the design criteria of high-strength, low-density materials operating at elevated temperatures [61]. Furthermore, titanium aluminides have been recognized as a potential material for replacing traditional nickel-based superalloys in aircraft engines, helping to achieve the emission reduction goals set for 2050 [62, 63, 64, 65]. Some of the properties of gamma-TiAl, alloy have proven to be much superior to Ni-based superalloys as outlined in figure 9 and a comparison of specific strength of titanium with other alloys is given in figure 10.

Property	TiAl-base alloys	Superalloys
Density (g/cm^3)	3.7–3.9	8.3
Room temperature modulus (GPa)	160–176	206
Yield strength (MPa)	400–630	1000
Tensile strength (MPa)	450–700	1200
Ductility at room temperature (%)	1–3	15
Creep limit (°C)	1000	1090
Oxidation (°C)	900–1000	1090
Cost ($/lb)	1300[a]	20

Figure 9: Comparison of mechanical properties of gamma-TiAl and Ni-based superalloys [2], [3]

By transitioning to titanium aluminides, aircraft engines can benefit from several advantages. 1) These alloys offer superior strength-to-weight ratios compared to traditional single crystal superalloys as shown in figure 10, allowing for lighter engine components without compromising structural integrity. This reduction in weight translates to improved fuel efficiency and reduced carbon emissions during flight. 2) Titanium aluminides exhibit excellent high-temperature performance and thermal stability, making them well-suited for the demanding operating conditions within aircraft engines. 3) Their resistance to oxidation and corrosion ensures long-term reliability and durability, contributing to overall engine efficiency and service life.

Ni-based superalloys have traditionally found application in turbine blades re-

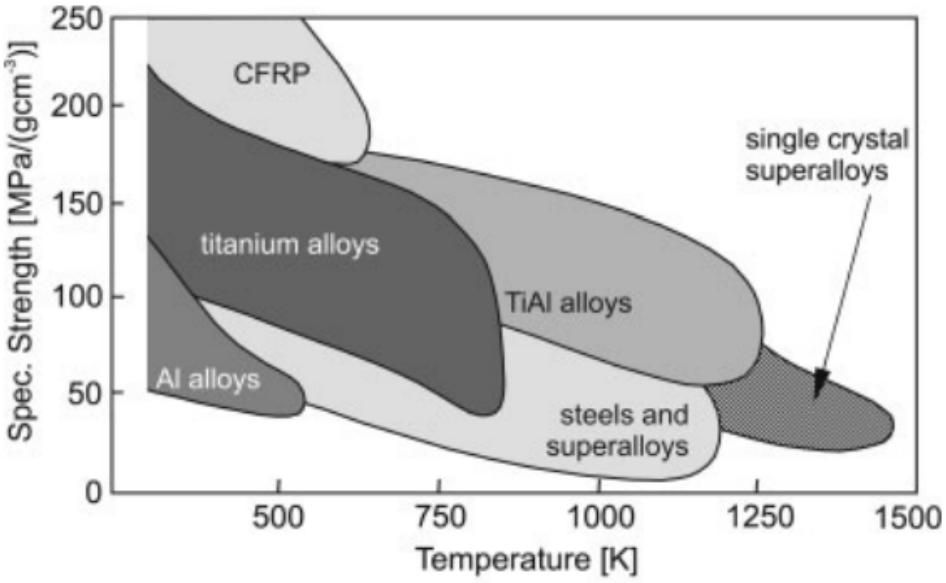

Figure 10: Relationship between specific strength versus temperature of structural materials compared with Ti-Alloys and aluminides [1]

cently, the Ti-48Al-2Cr-2Nb alloy, has been used in the low-pressure turbine blades of the GEnx engine for the Boeing 787 (patented by General Electric) [4], as shown in figure 11. The figure shows the gas turbine with an isolated single blade (right side) predicted to be operating at a maximum temperature of 700°C.

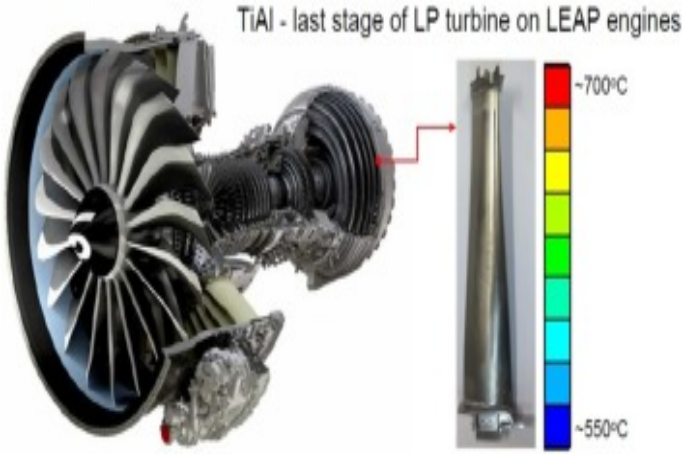

Figure 11: Low pressure turbine blades by GE using Ti-48Al-2Cr-2Nb alloy, duplex microstructure [4]

However, it is important to note that titanium aluminides are significantly more costly to produce—approximately 65 times more expensive than nickel-based superalloys [3]. Mechanical properties such as ductility at room temperature and yield strength are notably insufficient at room temperature [3]. In addition, creep and oxidation resistance of Ni-based superalloys are superior to that of TiAl alloy, which is crucial for components like turbine blades that are subjected to prolonged exposure to elevated temperatures and mechanical stresses. Due to such reasons Ni-based superalloys remain as the primary superalloy for use in turbine blades whilst, TiAl are limited to applications below 800°C (primarily low-pressure turbines, as in figure 11). Nevertheless, various methods such as alloying, microstructural control and advanced manufacturing techniques are being explored to overcome their limitations

to introduce Ti-Al alloys into high pressure turbine blades (HPTB) [64], [66].

2.1.5.1 Ti-Al Alloy Microstructure

The following texts and diagrams illustrate the various microstructures of Ti-Al alloys along with their properties.

Equiaxed Microstructure

Figure 12 shows the equiaxed microstructure formed when equal amounts of Ti and Al are mixed (Ti50Al). In this microstructure, the grains are roughly equal in size and shape, which typically leads to improved mechanical properties such as ductility and toughness. The equiaxed structure is often characterized by a uniform distribution of phases, which can enhance the material's overall performance under various loading conditions. This microstructure is used in applications demanding high strength-to-weight ratios, such as in aerospace components [6].

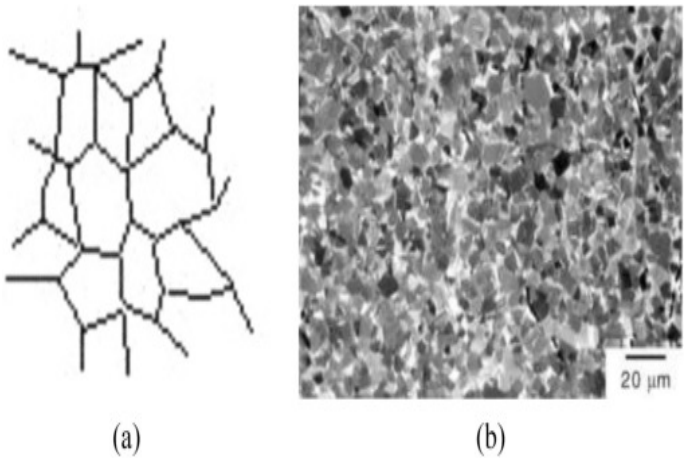

Figure 12: Gamma TiAl eqiuaxed microstructure. (a) Schematic diagram [5] (b)SEM micrographs of eqiuaxed microstructure [6]

Advantages:

High elastic modulus. Improved high-temperature properties [1].

Disadvantages:

Weak fracture toughness. Low ductility. High brittleness, making it unsuitable for structural applications [1].

Lamellar Microstructure

Structural Description:

The lamellar structure in TiAl typically consists of alternating layers of the alpha and gamma phases. The alpha phase is a titanium-rich phase with a hexagonal crystal structure, while the gamma phase is an aluminium-rich phase with a cubic

crystal structure. Figure 13 shows the lamellar microstructure where gamma and alpha plates form zebra-looking grains in the lamellar microstructure [6].

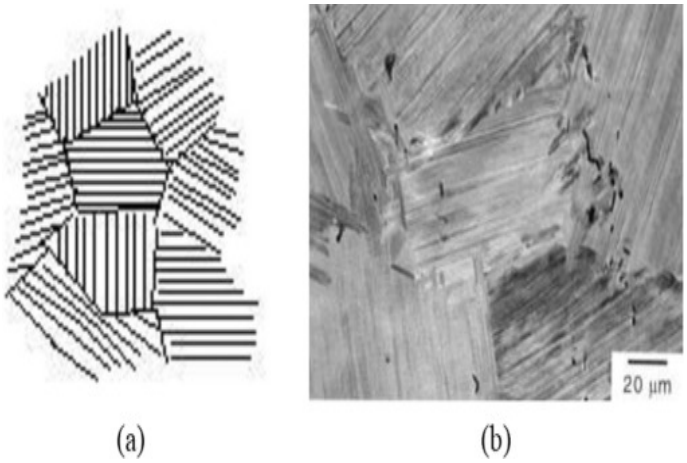

Figure 13: Gamma-TiAl Lamellar Microstructure. (a) Schematic diagram of Lamellar microstructure[5] (b)SEM micrographs of gamma-TiAl Lamellar microstructure [6]

Advantages:

Twinning and dislocations at the interface contribute to increased creep resistance, including high-temperature strength and fracture toughness. It is also more ductile than equiaxed structure due to gaps between lamellae plates.

Disadvantages:

Poor ductility at room temperatures. Improved ductility may require the addition of smaller particles (10–30 micrometers).

Duplex Microstructure

Structural Description:

Figure 14 illustrates the duplex microstructure, composed of a combination of equiaxed gamma grains and lamellar colonies, which produces a more ductile structure [6]. It contains the mechanical properties of both equiaxed and lamellar microstructures.

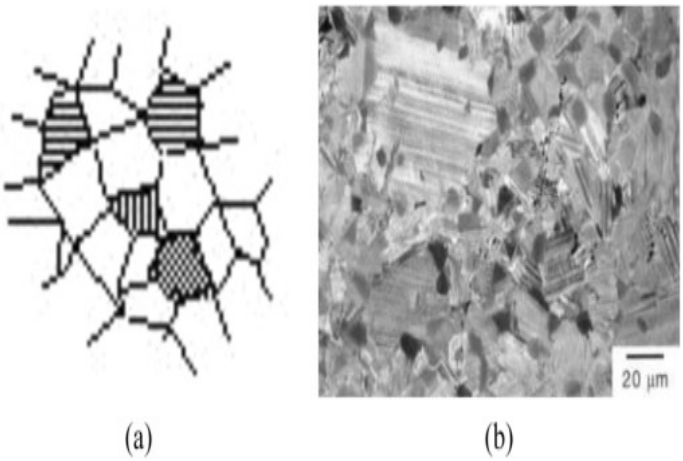

Figure 14: Gamma TiAl Duplex Microstructure. (a) Schematic diagram of duplex microstructure [5] (b)SEM micrographs of gamma-TiAl duplex microstructure [6]

Advantages:

More ductile structure. Combines the mechanical properties of both equiaxed and lamellar microstructures. Highly preferred for structural applications.

Pseudo Duplex:

Structural Description: Figure 15 shows the pseudo duplex structure. Pseudo-duplex contains a larger amount of gamma-phase compared to duplex micro-structure above as well as gamma-phase in the layered colonies [67].

The optimal mechanical properties are achieved in lamellar microstructures with

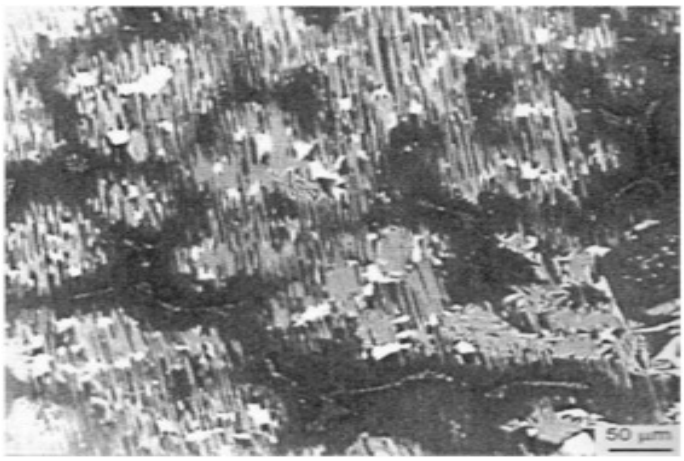

Figure 15: SEM micrographs of gamma-TiAl duplex microstructure [7]

fine lamellar spacing and small colony sizes. Consequently, alloy development is primarily focused on this microstructural type [1]. Titanium aluminides are brittle at low and room temperatures, making processing, machining, and handling challenging [1]. Fracture behaviour varies with microstructure: in duplex microstructures, inter-granular fractures and cleavage predominate, while in lamellar alloys, failure primarily occurs through interfacial delamination, trans-lamellar fractures, and decohesion of lamellar colonies [1].

2.2 Investment Casting of Ti-Alloys

2.2.1 Background to Investment Casting

Investment casting (IC) has a rich history that spans millennia. The earliest evidence of this technique dates back to around 4000 BC, with artifacts discovered in ancient Mesopotamia crafted using lost-wax casting methods. Following this, investment casting has been utilized for centuries in the creation of various items, ranging from rudimentary objects like jewellery, idols and art castings to more complex works. Figure 16 shows the estimated ages of investment castings objects plotted according to the area where they were recovered [8].

Jewellery castings have been unearthed not only in the treasures of the Pharaohs of Egypt and the Inca tombs of Central and South America but also among the ancient Etruscans and Greeks in Europe, as documented by Kotzin [68]. Idols made through investment casting have been discovered across the globe, particularly in regions like China and the Indus Valley and Harappan civilizations of India[12], [68]. Additionally, artifacts such as the Vittoria Alata Statue during the Imperial Roman Period, items from the Aztecs of pre-Columbian Mexico, and those found in Egypt's tombs of Tutankhamun, as well as artworks from Mesopotamia and Mayan Mexico, exemplify the widespread use of investment casting for producing artwork using materials such as copper, bronze and gold [12] [68]. Kotzin's review highlights the

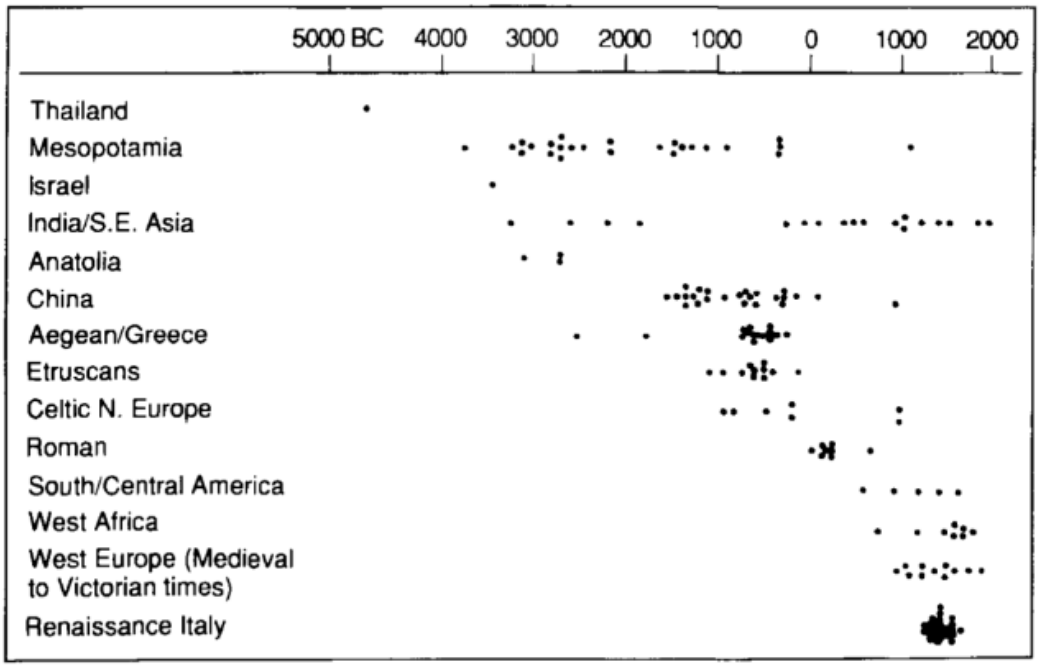

Figure 16: Estimated ages of investment castings objects found by location [8]

pivotal role played by the investment casting process in transforming and enhancing the cultures of ancient civilizations throughout history [68]. Investment casting techniques persisted throughout the middle-ages, into the Renaissance and into the industrial revolution. However, it remained primarily a craft-based process up-until the 20th century [12].

The IC process underwent significant evolution during the Second World War, mainly due to the heightened demand for precision components with intricate geometries, such as aircraft components [12]. Traditional tooling techniques proved insufficient

to meet the increased demand prompted by the war effort, necessitating the need to explore alternative manufacturing methods [69]. During this critical period, the investment casting process emerged as one of the key alternatives [12]. It became indispensable in fulfilling the urgent need for producing finished components, particularly for the machining tool industry. The process offered a viable solution for manufacturing a wide array of complex-shaped components, including parts with intricate geometries, smooth surfaces, precise dimensions and fine details, which were essential for meeting the stringent requirements of wartime production [12]. The three main aspects of precision casting are depicted in figure 17.

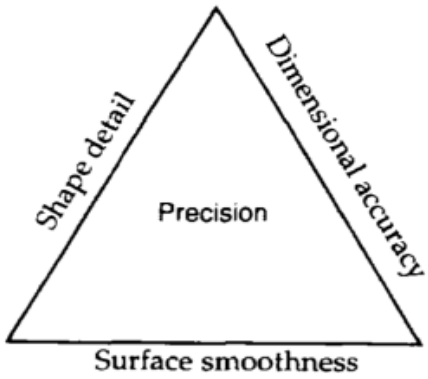

Figure 17: Aspects of precision casting [8]

The investment casting industry has grown steadily, driven by its advantages as a casting process and its applications across diverse sectors, including automotive, marine, and medical fields [12]. The investment casting process has become widely used in aerospace, especially for producing single-crystal turbine blades, transforming

a once small, specialized sector into a global industry [12], [8].

The investment casting market was valued at approximately USD 17.41 billion in 2022 and is expected to grow significantly, reaching USD 27.48 billion by 2031, with a compound annual growth rate (CAGR) of 5.2% during the forecast period from 2024 to 2031 [70, 71]. Figure 18 forecasts the market for IC by industry for 2032. The rising need for complex, high-performance parts, particularly in aerospace and automotive, is one of the key growth drivers for the investment casting market.

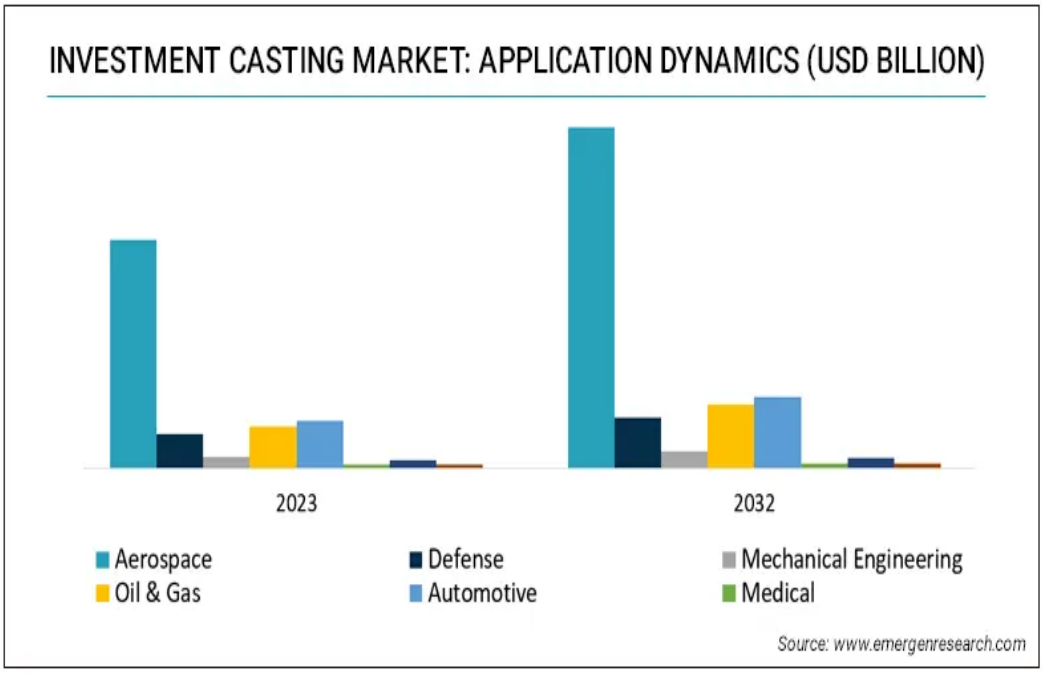

Figure 18: Market for investment casting by sector for 2023 and prediction for 2032 [9]

As automotive industries increasingly adopt electric vehicles and more fuel-efficient aircraft, demand for lightweight, high-performance cast parts is expected to surge

even more [72]. Anticipated growth in air passenger traffic is set to drive the production of new commercial aircraft, positively impacting demand for investment cast products [73]. This surge is fuelled by rising per capita income and favourable global GDP trends, boosting the need for new aircraft and the components used in their construction. Increased demand in sectors such as oil and gas is also contributing to the growth of the investment casting market. Additionally, advancements in materials science and casting technologies are expanding the capabilities of investment casting. These include the development of enhanced ceramic shell materials, more refined control over metal-mould reactions and the rise of high-performance alloys. Moreover, the integration of computational modelling for predictive analysis of mould filling, solidification and shrinkage is leading to fewer trial runs and reduced resource expenditure. This results in higher precision, reduced material waste and lower production costs [72]. Further research in investment casting is crucial to meet the growing demand for high-performance, lightweight components. Research can drive innovations that support these goals while maintaining the high-quality standards required for critical applications.

2.2.2 Investment Casting Process

The following text describes the IC process with reference to figure 22. **Pattern Creation:** The first step in the casting process involves the creation of a wax pattern (figure 22 (a)) [12], which serves as a replica of the actual shape of the part being produced by IC. Investment casting waxes are complex blends of natural or synthetic waxes, resins, solid organic fillers and sometimes water [10]. Figure 19 lists common wax types and their properties.

Sr. No.	Name of wax	Density (gm/cc)	Melting point (°C)	Volumetric shrinkage (%)
1	Bees wax	0.97	65	7.25
2	Paraffin wax	0.78	64	6.20
3	Carnauba wax	0.99	87	4.20
4	Montan wax	1.02	82	2.45

Figure 19: : Properties of the waxes [10]

The creation of the wax pattern begins with injecting molten wax into a die cavity under high pressure. The wax is injected through a nozzle or gate system into the die cavity, filling it completely and reproducing all the intricate features of the part. The wax is then allowed to cool and solidify, after which it is ejected from the die

cavity ready for the next step.

The effectiveness of investment casting can be influenced by one or more characteristics of the wax [12]. For instance, additives may be mixed to improve rigidity and/or strength, blending with different waxes may promote greater surface accuracy and varying the process parameters, such as increasing holding time, may decrease shrinkage. Some common characteristics essential for the wax pattern to be effective, as identified by Craig *et al.* [74], which include:

1. Low thermal expansion to form shapes with the highest dimensional accuracy.

2. Smooth and wettable surface to obtain a smoother surface finish.

3. Low viscosity during the melting away process.

4. Resistance to breakage.

The effectiveness of a wax pattern is assessed based on properties like strength, shrinkage, and volumetric expansion. After solidifying, the wax pattern is removed from the die and dipped in water to harden [75], [12].

Pattern Assembly: Typically, the complete wax pattern is not created in one go due to design constraints, but rather as separate parts that are then assembled together (figure 22 (b)). These individual wax pattern components are attached to a central wax sprue, which serves as the channel through which molten metal will be

poured into the mould. Additionally, during this stage, any fractures that may have occurred during the handling of the pattern are repaired, typically using a repairing wax. [75], [12]

Shell Building: Shell building, is one of the fundamental steps in IC. It involves coating the wax pattern with a refractory material called investment or ceramic slurry, which acts as a binder (figure 22 (c)). The ceramic slurry typically consists of fine ceramic particles suspended in a liquid binder, such as colloidal silica [76, 75]. The purpose of this step is to coat the wax patterns with a thin layer of ceramic slurry. After the initial dip in the ceramic slurry, the wet surface of the wax patterns is coated with a layer of stucco material. Stucco is a refractory material consisting of fine ceramic particles, typically silica, zircon, alumina, etc. [75] mixed with a binder. Figure 20 shows the typical slurry specifications for aluminium shell coating.

Slurry	Binder silica content (%)	Polymer addition (wt.%)	Fibre addition (g/l of binder liquids)	Filler	Refractory loading
Primary	26	6	n/a	200 mesh zircon	77%, 75% zircon, 25% silica
Secondary 1	22	8	n/a	200 mesh alumino-silicate	57%
Secondary 2	22	n/a	20	200 mesh alumino-silicate	57%

Figure 20: Slurry specifications for aluminium shell coating [11]

This stucco layer adds strength and stability to the ceramic shell mould and is the material the liquid metal will be in contact with. Figure 21 shows the typical shell build specifications for aluminium shell coating [11].

Coating	Stucco	Dip time (s)	Drain time (s)	Air speed (ms^{-1})	Dry time (h)
Primary	50/80 Molochite	30	60	0.4	24
Secondary 1	30/80 Molochite	30	60	3	1.5
Secondary 2	30/80 Molochite	30	60	3	1.5
Secondary 3	30/80 Molochite	30	60	3	1.5
Secondary 4	30/80 Molochite	30	60	3	1.5
Seal		30	60	3	24

Figure 21: Shell build specifications for aluminium shell coating [11]

The coating process involves an initial primary coat with 50/80 Molochite, dipped for 30 seconds, drained for 60 seconds, dried at 0.4 m/s airspeed for 24 hours. Four secondary coats with 30/80 Molochite are applied similarly, but with faster air drying (3 m/s) and a shorter drying time of 1.5 hours each. Finally, a seal coat is applied without stucco, with the same dip and drain times, drying at 3 m/s for 24 hours. The two-coating process is repeated layer by layer through dipping, brushing or spraying, allowing each layer to dry before the next one is applied. The coating thickness depends on the metal size, weight and density. Producing a ceramic shell is time-intensive, typically requiring 24–72 hours based on component size [75], [12].

De-waxing: Once cured, the mould is heated to melt and remove the wax, leaving a cavity shaped like the original pattern (figure 22 (d)). The wax is typically recovered, purified and reused for new patterns [12]. De-waxing is traditionally done using methods like autoclave or flash fire de-waxing, with industrial autoclaves commonly used in investment casting. In this process, the ceramic shell is rapidly heated to 180–200°C, allowing molten wax to flow out. However, autoclave de-waxing often leaves the wax heavily contaminated with refractory particles, making recovery and treatment challenging and costly. Additionally, autoclaving does not always ensure complete wax removal. Flash-fire de-waxing, which uses a heatable chamber, an extinguishing chamber, and an inert gas injector, reduces wax contamination issues but has high operating costs, limiting its popularity. Microwave de-waxing, now widely used, provides a cleaner wax recovery and improves product quality [75, 12].

Mould Pre-heating: Pre-heating is the the process in which the mould is heated to temperatures of around $950°\text{C} - 1100°\text{C}$ in a furnace for specified amount of time depending on the ceramic material. Firing may entail multiple heating and cooling stages to reduce thermal shock and ensure even heating across the mould. This is done to remove any residual moisture particles, remove any traces of wax and to strengthen the material. Strengthening allows the mould to withstand high temper-

atures during casting and reduces the chances of shell cracking that may occur due to the difference in temperature of mould and liquid metal [75], [12].

Casting and Solidification: After preheating the ceramic shell, molten metal is poured into the mould cavities at a predetermined temperature and allowed to cool and solidify [75] (figure 22 (e)). During the pouring process, as molten metal enters the mould cavity, it navigates through the sprue system, intricately filling the moulds detailed features and mirroring the original shape of the wax pattern. The design precision of the sprue system and gating is paramount, as it ensures consistent metal flow and prevents the occurrence of turbulence or the entrapment of air bubbles, factors that could otherwise cause defects in the final casting. Various methods, such as gravity, pressure, vacuum and centrifugal techniques are employed to introduce the molten metal into the shells, each with its own pros and cons. The pouring temperature must be carefully controlled; it should not be too high to avoid cracking the ceramic shell, nor too low, as this leads to unsound castings [75]. In addition, pouring temperature can also impact mechanical properties, such as hardness, impact strength and tensile strength as proven by Yadav [77]. Pouring and cooling processes greatly impact the final microstructure so much care must be given to transfer the metal to the mould material [75]. The rate at which cooling

occurs and the subsequent solidification process are pivotal elements that impact the microstructure and characteristics of the eventual casting. Effective management of cooling rates is essential in reducing internal stresses, porosity and other flaws within the casting, thereby ensuring its quality [75, 12].

Mould Removal: Once the metal has solidified and cooled, the ceramic refractory can be removed manually or with a pneumatic vibration machine (see figure 22 (d)). High collapsibility of the refractory aids in easy removal, though impurities or suboptimal refractory properties can complicate this process. Adding alkali salts to earth metals has been found to facilitate shell removal. Figures 22 (g) and (h) show the cutting and final casting, respectively [75], [12].

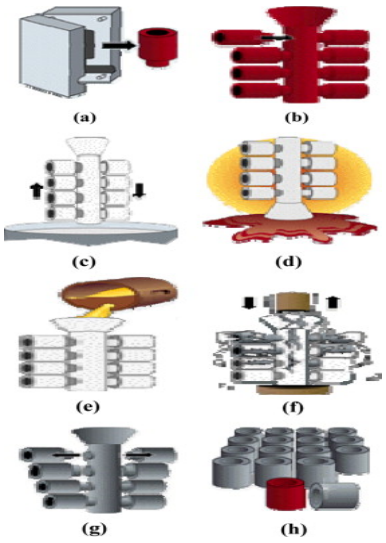

Figure 22: Steps in the investment casting process [12], [13]

2.2.3 Alternatives to Investment Casting

Today, a significant drawback of TiAl is its substantial material cost [78]. Consequently, a crucial economic evaluation metric is the buy-to-fly ratio (BTFR) [14]. This ratio elucidates the balance between the amount of feed-stock material used to manufacture one blade and the weight of the finished Low-Pressure Turbine Blade (LPTB) [14]. For instance, a BTFR of 10 indicates that 1 kilogram of TiAl is required to produce a ready-to-use blade weighing 100 grams [14]. Figure 23 illustrates the potential for process optimization. Notably, the investment casting route exhibits the highest potential owing to near-net-shape casting, with less than 1 millimetre of excess material.

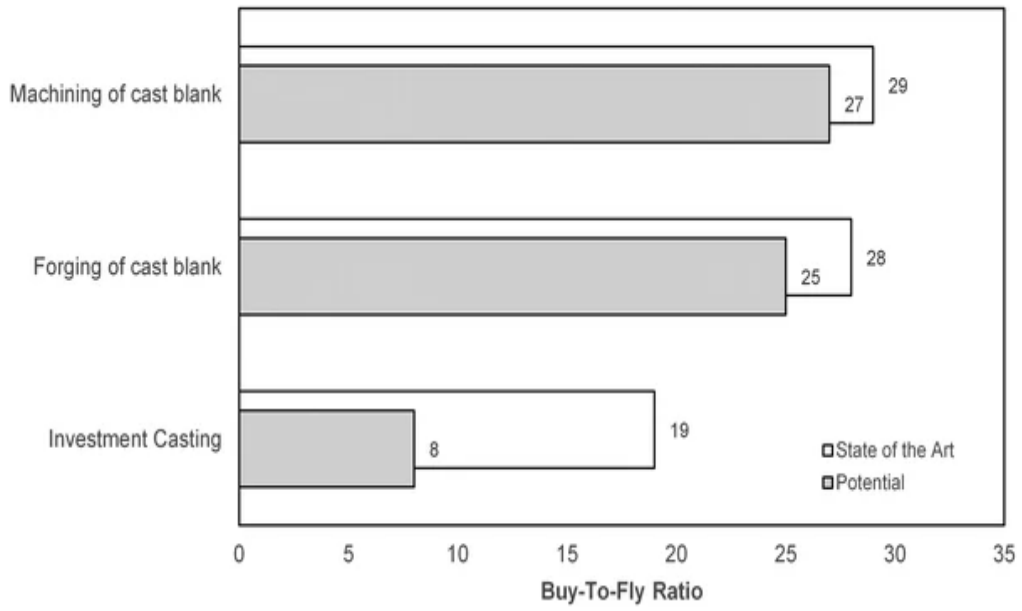

Figure 23: Comparison of buy-to-fly ratio of three manufacturing processes for TiAl-LPTBs [14]

.

2.2.3.1 Vacuum Die-Casting (VDC): Die-cast parts are manufactured by melting the alloy in air and subsequently injecting the liquid metal into a set of reusable moulds under high pressure, which contain the desired shape of the component [15, 14]. In titanium die-casting, a vacuum level below 20 µm is maintained in the melt chamber and die cavity to minimize oxygen contamination in the alloy. Unlike investment casting, products produced through this method are typically close to the final shape, with minimal additional processing or machining. Moreover,

the procedure features swift cycle times, frequently achieving the conversion from molten metal to the final component in less than 15 seconds [15]. One of the biggest advantage of using die-casting instead of investment casting is that it involves fewer processing steps [15]. Figure 24 shows the comparison of processing steps of investment casting and die casting process for a typical, small (<2 kg) aerospace titanium casting [15].

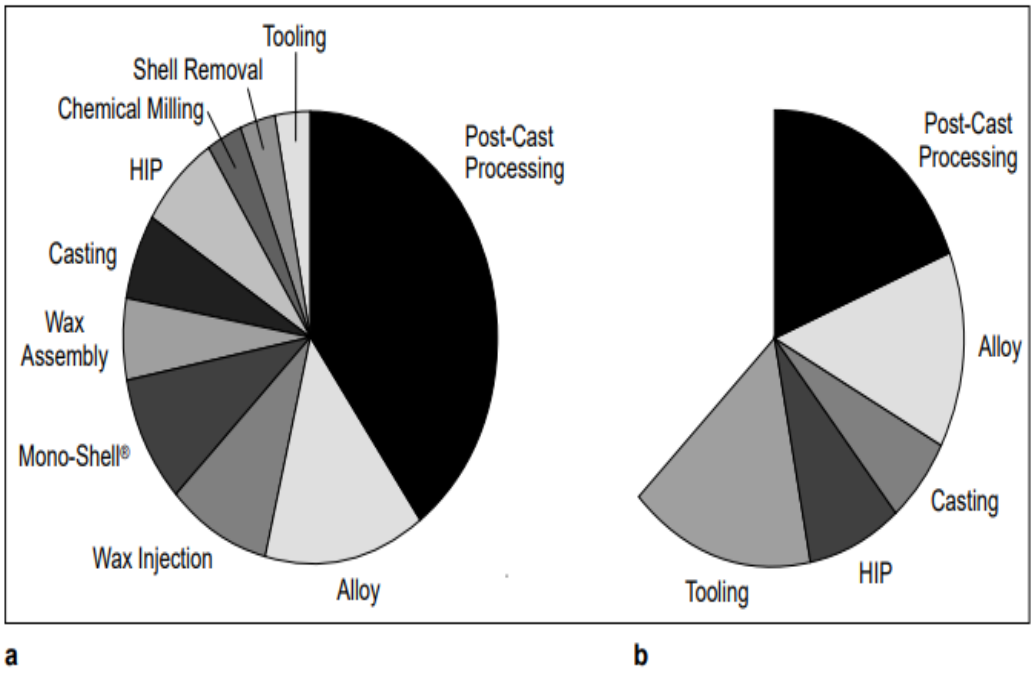

Figure 24: Number of processing steps in IC (a), number of processing steps in die-casting (b) [15]

Through VDC, all wax and shell operations, along with chemical milling, are completely eradicated, effectively reducing the number of processing steps by almost

half. The cost savings resulting from the elimination of these steps can amount to as much as 30% compared to investment casting. Currently, VDC is limited to casting solid, single-plane and simple-shaped titanium components weighing no more than 35 kg. In contrast, investment casting has the capability to produce large parts, highly intricate and hollow geometries. For such reasons, investment casting is largely preferred for large component production.

2.2.3.2 Powder Metallurgy: Titanium powder is typically produced using methods like the hydride-de-hydride (HDH) process, which converts titanium sponge or scrap into fine powder [79]. The powder is then blended with additives like aluminium or vanadium to tailor its properties and shaped under high pressure in a die [80]. The compacted form undergoes sintering, where it is heated just below its melting point in a controlled atmosphere to fuse particles, reducing porosity and enhancing strength [80]. Additional steps such as machining, heat treatment, and surface finishing ensure precise dimensions and surface quality [80].

Powder metallurgy produces less material waste than investment casting, which often involves removing excess material during finishing [81]. It also offers better dimensional consistency, as casting parameters and cooling rates in investment casting can introduce variability [81]. However, powder metallurgy requires expensive and specialized equipment for handling, compaction and sintering, while investment cast-

ing uses simpler tools. Although powder metallurgy may require extra machining for a smooth surface finish, investment casting can achieve this directly. Furthermore, powder metallurgy is limited in producing large or heavy parts, while investment casting accommodates a wider range of sizes and weights [80].

2.2.3.3 Forging: Forging is a process in which a metal is configured by applying compressive forces through tools such as hammers, presses or dies [82]. Typically performed at elevated temperatures, forging improves the mechanical properties of the metal by refining its grain structure, resulting in improved strength, toughness and ductility [82]. The high temperatures facilitate easier deformation while minimizing the risk of cracking and the controlled compression aligns the grain structure, yielding components with superior durability and performance under stress [82]. However, forging has limitations in shape complexity, especially with open-die forging, where the metal is pressed between flat or simple-shaped dies, producing components with relatively straightforward geometries [83]. Closed-die forging allows for moderate complexity through the use of shaped dies, but it generally cannot achieve the level of intricacy possible with casting. Casting enables more intricate and precise shapes due to its ability to create complex internal geometries in a single pour. Additionally, forging often incurs higher production costs, particularly in closed-die forging, where complex dies require significant investment [84].

2.2.3.4 Additive Manufacturing: Titanium additive manufacturing (3D printing) constructs objects layer by layer, starting with a CAD-designed 3D model sliced into layers [85]. A high-powered laser or electron beam melts titanium powder or wire, following the sliced layers to build the part gradually. Post-processing, such as heat treatment and machining, improves accuracy and mechanical properties [85]. This method excels in creating intricate geometries and allows design modifications without costly tooling changes, offering flexibility and customization. It minimizes material waste compared to investment casting and reduces lead times by eliminating mould creation. However, additive manufacturing can be less cost-effective for large-scale production, with higher porosity and rougher finishes than investment casting. Additionally, the high cost of equipment and titanium powder poses challenges, particularly for high-performance applications [86]. Other Ti-Al alloy manufacturing processes include centrifugal chill casting, as used by Safran for the LEAP engine [87], and forging, employed by MTU for the Geared Turbofan [88]. GE has pioneered 3D printing of TiAl low-pressure turbine blades for the GE9X engine, standing as the only OEM utilizing printed TiAl blades [89].

Investment casting stands out as the superior option for manufacturing titanium components compared to other methods due to its unparalleled ability to produce

intricate and precise geometries, including hollow and complex internal structures, in a single process. Unlike Vacuum Die-Casting (VDC), which is limited to simpler shapes and smaller components, investment casting can handle larger parts with high dimensional accuracy. While powder metallurgy offers material efficiency and consistency, it is constrained by size limitations and requires extensive post-processing to achieve comparable surface finishes and mechanical properties. Forging, though excellent for strength and durability, struggles with producing complex shapes and incurs higher costs for tooling and operations. Similarly, while additive manufacturing excels in design flexibility and waste minimization, it faces challenges with scalability, surface finish, and porosity, making it less viable for large-scale production. Investment casting also minimizes issues associated with high-temperature materials, offering a cost-effective and reliable solution for aerospace and industrial applications, where precision, complexity, and material performance are critical.

2.3 Industrial Challenges in Casting Ti-Al Alloys

2.3.1 Chemical Interaction Between Ti Melt and Crucible Ceramics: Alpha Case Layer

While oxide ceramics generally demonstrate higher stability compared to other ceramics like borides and nitrides, it is crucial to acknowledge that even the most stable

ceramic oxides are susceptible to reacting with liquid titanium during the melting and casting of Ti-alloys. This susceptibility has been substantiated by numerous experimental studies investigating oxide-Ti interactions [19], [36], [90]. Consequently, it becomes imperative to comprehensively understand the findings derived from these experimental studies and draw meaningful conclusions which can further aid in targeted research and identify gaps in knowledge. Xu *et al.* [16], conducted an investigation into the interaction between Y_2O_3 (face coat) and Ti-64 alloy. A sample Ti64 alloy measuring 10mm x 10mm x 10mm was melted to above 1973 K and cast using the gravity casting technique. Following casting, the metal-shell interface was examined using an optical microscope while the surface compositions were analysed using an X-ray diffractometer and the micro-hardness profile at the metal-mould interface was acquired utilizing a micro-hardness tester [16]. Figure 25 shows the surface of the as-cast alloy extending from where the metal-mould surface would have been all the way to the interior of the metal.

It can be clearly seen that there are two different microstructures that are present in the alloy. The metal-mould interface microstructure is drastically different from the lamellar microstructure that is observed within the bulk of the metal. This microstructure is often distinguished as the interaction layer where the exchange of chemical mass transfer has occurred between the metal and the mould during the

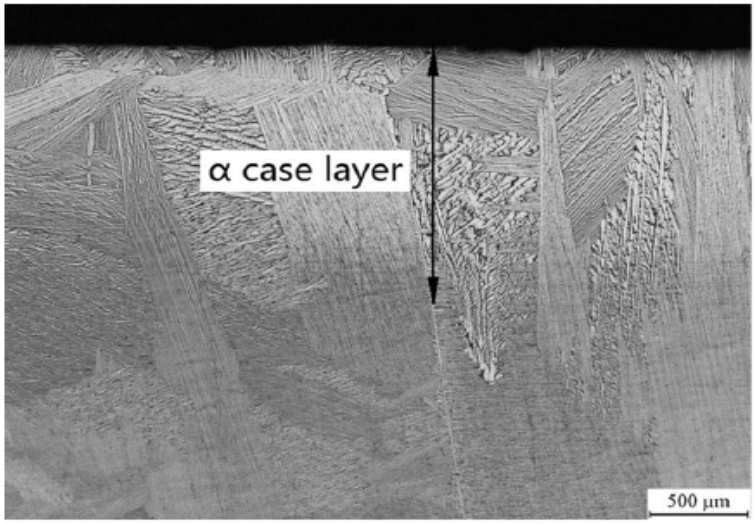

Figure 25: Formed Alpha Case Layer on Ti-64 alloy cast with Y_2O_3. The bottom half showing $\alpha + \beta$ phase and the top part (layer with bright contrast) showing coarsened alpha-case layer due to metal-mould interaction [16]

casting process. Within the interaction layer there exists an alpha case layer often associated with the presence of high oxygen concentration.

Figure 26 shows the predicted oxygen concentration from the metal-mould interface to the interior of the metal as a function of interface distance.

The determined thickness of the alpha case layer with respect to oxygen is estimated to be approximately 1367 μm. Further projections indicate a hardened layer thickness of approximately 1450 μm and an oxygen penetration distance of approximately 1665 μm. The compositional analysis of the alpha case layer indicates a significant concentration of oxygen to be present and the primary source of oxygen

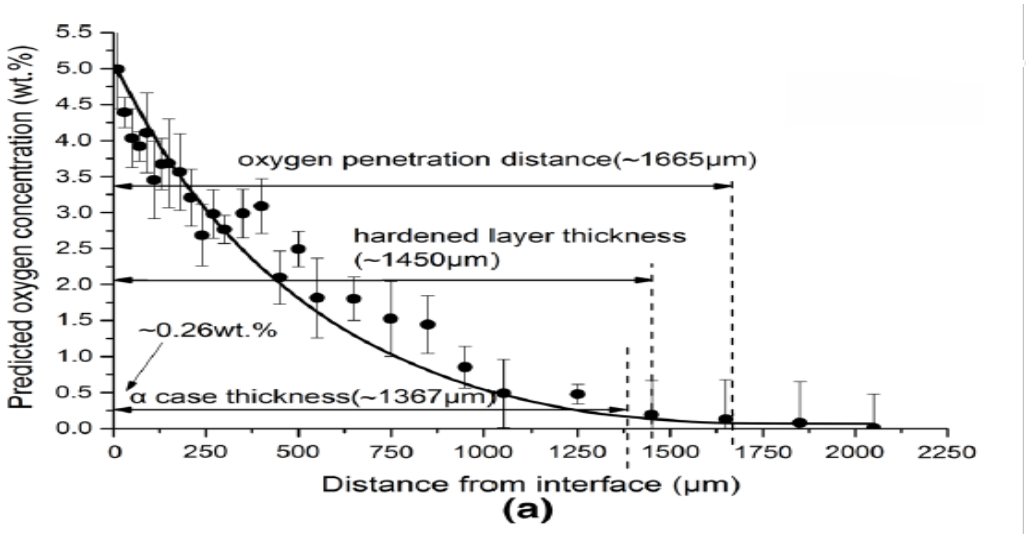

Figure 26: Predicted oxygen concentration from the metal-mould interface to the interior of Ti-64 cast with Y_2O_3 [16]

that enters the metal is predicted to have originated from the mould itself. The development of the alpha case layer, characterized by elevated oxygen levels, is a direct consequence of an unstable mould undergoing chemical interaction with the molten metal during the casting process [16]. The alpha case primarily consists of alpha titanium (alpha-Ti), which is the hexagonal close-packed (HCP) phase of titanium as illustrated in figure 5. The microstructure of the alpha case is often characterized by fine equiaxed grains [91]. It is understood that the alpha case layer serves as a protective barrier against further oxidation [16].

Formation of alpha case layers are a serious concern in casting metals. Alpha case at the surface of metals tends to be more brittle compared to the bulk, leading to a re-

duction in ductility, embrittlement and compromises the fatigue strength of titanium alloys [92, 93, 94]. This phenomenon holds significant implications for their practical applications, especially in critical areas such as aircraft engines. The growth of alpha-case is influenced by several factors, including impurity level of oxygen, metal-mould exposure time, temperature and pressure. To illustrate the effects of alpha case on the properties of Ti-alloys, Chan proposed a micromechanical model to study the impact of alpha-case thickness on the tensile ductility of Ti castings [17]. Figure 27 displays the computed plastic strain at fracture (tensile ductility) relative to alpha-case thickness for both CP-Ti and Ti-6Al-4V [17].

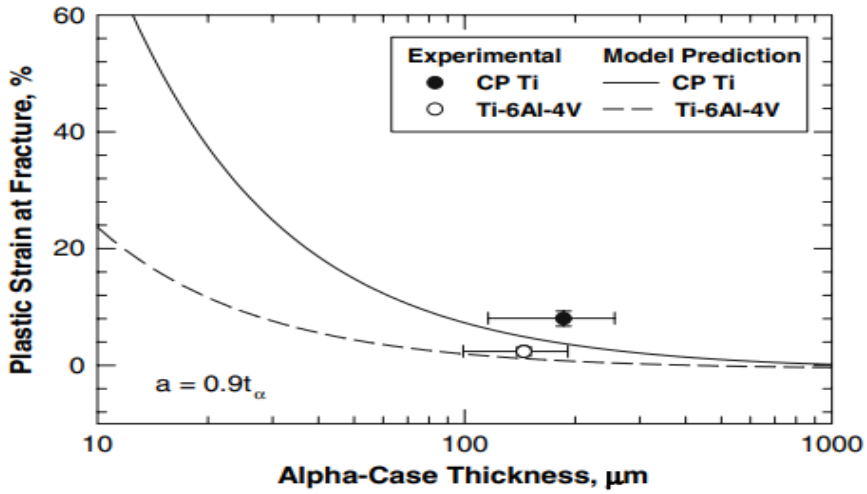

Figure 27: Impact of alpha-case on ductility of CP-Ti and Ti-6Al-4V [17].

The general trend is that ductility decreases as the alpha case increases. The tensile ductility of commercially pure titanium (CP-Ti) is approximately 75% at

an alpha-case thickness of 10 μm, but decreases rapidly with increasing alpha-case thickness [17]. For Ti-6Al-4V, tensile ductility is around 23.7% at an alpha-case thickness of 10 µm, decreasing sharply as alpha-case thickness increases. In the context of turbine blades, decreased ductility increases the risk of rendering the blades more susceptible to cracking or failure under cyclic loading which is highly common in turbine applications [95]. In addition, alpha case layers can serve as initiation sites for stress corrosion cracking [22], particularly in the presence of aggressive environments. Turbines commonly operate in conditions where corrosion is a concern and the presence of an alpha case layer can exacerbate the susceptibility to stress corrosion cracking. For such reasons, alpha case layers are often removed from the primary castings using various methods. Surface coating, laser ablation, cathodic de-oxygenation, and acid pickling are among the techniques used to effectively eliminate alpha case layers [96]. However, these techniques can be challenging so it is best to employ prevention methods rather than dealing with the aftermath.

2.3.2 Modelling Alpha Case Layer

Boettinger *et al.* [97], performed a one-dimensional analysis of alpha case formation in titanium (Ti) castings, focusing on oxygen diffusion into the beta phase during solidification. Their study emphasizes that oxygen diffusion in the liquid phase is

often neglected, with the diffusion in the solid (β) phase typically being considered the rate-limiting step for alpha case formation. In their model, the outer surface of the casting is defined at $x = 0$, and the interior at $x = \infty$ [97]. The oxygen concentration in the beta phase, denoted as $C(x, t)$, is governed by the following diffusion equation [97]:

$$\frac{\partial C}{\partial t} = \frac{\partial}{\partial x}\left(D\frac{\partial C}{\partial x}\right) \tag{1}$$

The boundary conditions for this diffusion process are specified as $C(0, t) = C_0$ at the casting surface and $C(\infty, t) = C_\infty$ at the midsection (bulk) [97]. The initial oxygen concentration at the surface is considered equivalent to that of the bulk, leading to the condition $C(x, 0) = C_\infty$ at $t = 0$. For various temperatures during the cooling phase, the solution to the governing equation under these boundary conditions is expressed as follows:

$$C = C_0 - (C_0 - C_\infty)\,\mathrm{erf}\left(\frac{x}{2t^{1/2}}\right) \tag{2}$$

Chan *et al.* [17] found that micro-hardness, is directly proportional to oxygen content according to the expression given by:

$$H_V = b_0 + b_1 C \tag{3}$$

where, Hv is the Vickers hardness constant, b0 and b1 are empirical constants. Figure

28 shows the modelled relationship between micro-hardness and oxygen concentration to follow equation 3.

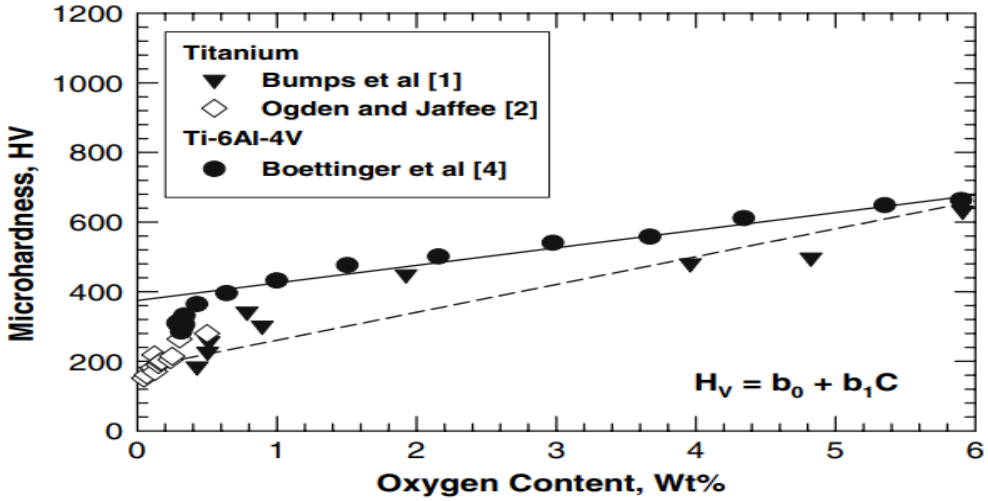

Figure 28: Comparison of micro-hardness as a function of oxygen content for 6-mm-thick Ti-6Al-4V (cast plate) and as-cast titanium [17].

Using equations 2 and 3, Chan [17] modelled the micro-hardness of the alpha-case layer in 0.5, 0.75, 1, and 2-mm thick CP-Ti and Ti-6Al-4V castings and subsequently compared the results with experimental data. The outcomes of these calculations for 1 mm thick castings are illustrated in figure 29.

The computed micro-hardness aligns well with experimental measurements, with only marginal differences that do not significantly affect the overall hardness profile. Several key findings can be drawn from this study. As oxygen acts as an interstitial element in titanium, its presence strengthens the metal by impeding dislocation

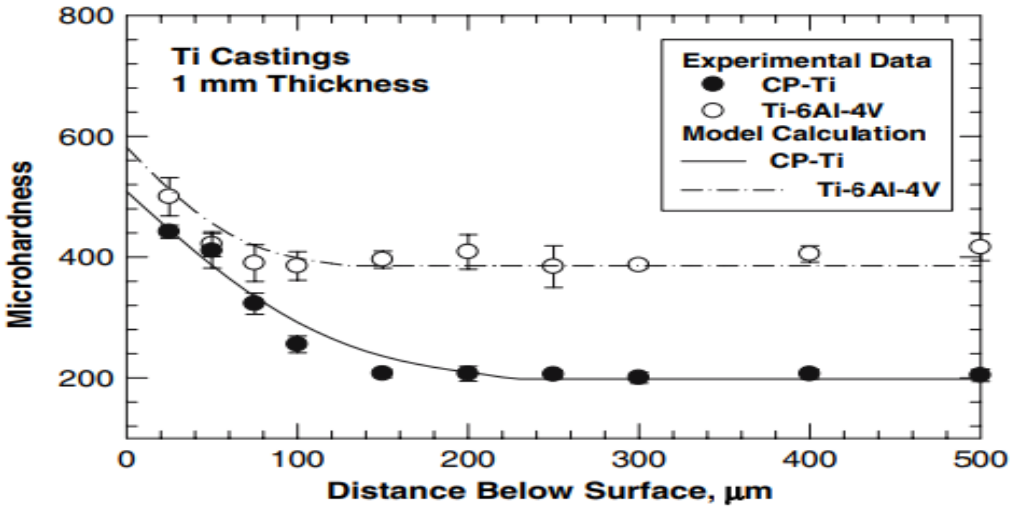

Figure 29: Comparison of Modelled Micro-hardness vs Experimental Micro-hardness [17].

movement, thereby increasing hardness. Oxygen proves to be a potent solid solution strengthener in titanium, as even a small increase in oxygen concentration significantly boosts micro-hardness. The model predicts the depth of the alpha-case layer to be approximately 220 micrometers for CP-Ti and 110 micrometers for the Ti-6Al-4V alloy. The thicker alpha-case layer in CP-Ti, compared to Ti-6Al-4V, is attributed to the higher oxygen diffusivity in CP-Ti. Chan also observed that as the metal thickness increased from 0.5 mm, the alpha-case thickness similarly increased.

2.3.3 Formation of Reaction Layer

Meijia Liu *et al.* [18], investigated the formation of a reaction layer (alpha case) through the sintering of Al_2O_3 powder to Ti metal at temperatures of 1150°C, 1250°C,

1350°C, 1400°C, 1420°C, and 1450°C for different holding times (from 1.5 to 2.5 h) under a pressure of 30 MPa. Despite the focus on solid-state diffusion in this experiment, the formation and development of the reaction layer are distinctly observable. BSEM images and EDS analysis of the Ti-Al_2O_3 interfaces at various temperatures are shown in figure 30 [98]. From the provided figures, it is evident that as the temper-

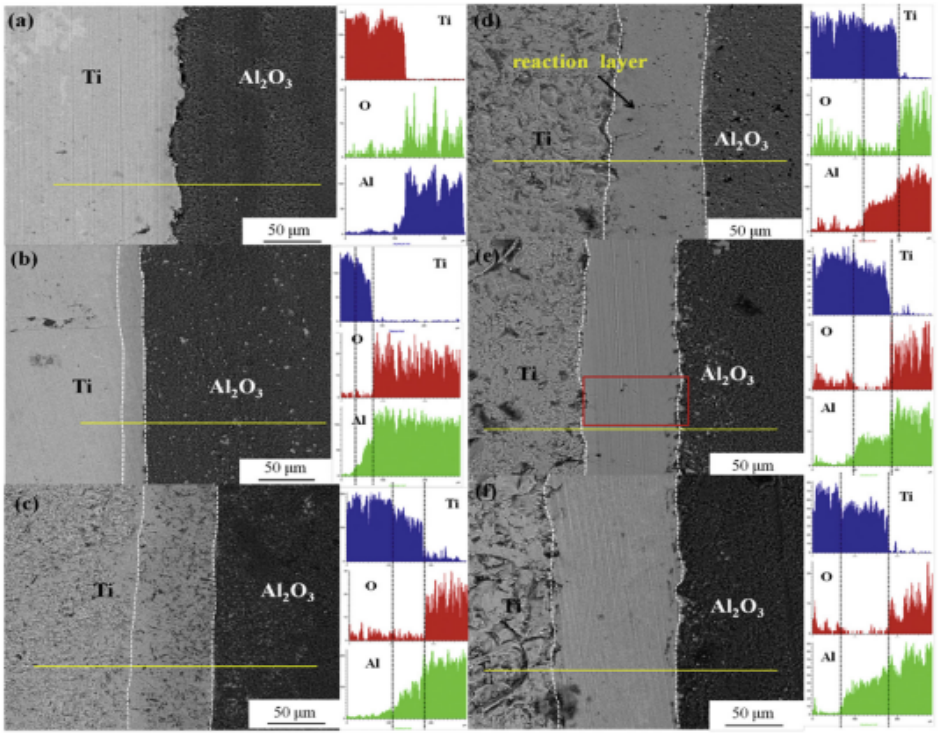

Figure 30: Ti-Al_2O_3 composite sintered at different temperature for 1.5 h: (a) 1150°C; (b) 1250°C; (c) 1350°C; (d) 1400°C; (e) 1420°C; (f) 1450°C [18]

ature increases, Al_2O_3 diffuses into the pure Ti, resulting in notable alterations to the interfacial microstructures. The thickness of the reaction layers exhibits significant

growth within the temperature range of 1150°C to 1450°C, underscoring the influential role of temperature in expediting the expansion of the reaction layer. At the lower temperature of 1150°C, a linear scan along the yellow lines in figure 30 reveals an absence of an apparent reaction layer. Analysis of element concentrations (Al, O, and Ti) at the interfaces indicates a sharp reduction, implying limited diffusion of elements at lower temperatures. Nevertheless, Al and O elements have diffused into the Ti phase, initiating the formation of the reaction layer at this temperature [18]. As the temperature rises, clearly visible reaction layers emerge at the interfaces, indicative of pronounced interactive solid diffusion across the interface driven by higher atomic average kinetic energies associated with elevated temperatures. The thicknesses of the reaction layers progressively increase to approximately 28.6 mm, 65.3 mm, 78.2 mm, 91.7 mm, and 112.2 mm at 1250°C, 1350°C, 1400°C, 1420°C and 1450°C, respectively [18]. Moreover, the microstructures of the reaction layers become notably dense, with pores disappearing at 1420°C and 1450°C. However, defects become apparent at the Ti zones at 1450°C. This study clearly demonstrates that the formation of reaction layer is significantly influenced by temperature. Moreover, it is anticipated that the thickness of the reaction layer will further increase when the titanium is in a molten state. Meijia [18] developed a kinetic equation for the growth of the reaction layer as a function of time and temperature, shown in equation 4,

where d is the layer thickness, K is the reaction rate constant, t is the holding time, and n is the kinetic exponent [18].

$$d = Kt^n \tag{4}$$

Reaction rate constant K can be obtained from the general Arrhenius equation given in equation 5.

$$K = K_0 \exp\left(-\frac{E}{RT}\right) \tag{5}$$

where K_0 is the pre-exponent factor, R is gas constant, E is the reaction activation energy and T is the absolute temperature. Combining equation 4 and equation 5 the overall growth of the reaction layer can be described according to equation 6 [18].

$$d = K_0 \exp\left(-\frac{E}{RT}\right) t^n \tag{6}$$

2.3.4 Metal-Mould Reaction Mechanisms

2.3.4.1 Chemical and Physical Erosion Kung *et al.* [19, 21] suggested that the interaction between the mould and metal encompasses both chemical reactions and physical erosion. Figure 31 illustrates the process Kuang proposed upon melt-mould contact [19]. During melting, when the metal becomes sufficiently fluid, strong

wetting between the melt and crucible enables capillary forces to draw the melt into the crucible, targeting the grain boundaries. This process makes it easier for refractory particles to become entrained into the melt through mechanical actions, the dashed arrow on the left shows how a particle is eroded from the crucible and enters the melt. Once entrained, as shown on the right, the particle is fully surrounded by the melt, which promotes further chemical dissolution due to the increased contact area between the melt and crucible material (indicated by red lines) [19]. Additionally, mass transfer is enhanced, as it is no longer restricted by the limited conductivity of melt-filled channels in the porous crucible. The removal of particles also leads to the expansion of these channels (represented by the pink background), which facilitates deeper melt penetration into the pores. This, in turn, weakens the bonds of neighbouring particles, making them more likely to be entrained into the melt. The eroded ceramic particles may either dissolve or remain suspended in the melt, depending on factors such as holding times and super-heat levels [19, 21]. In this interplay, erosion complements chemical attack by exposing fresh surfaces that are susceptible to chemical reactions with the molten metal. Conversely, chemical attack weakens the structure of the refractory, facilitating further erosion [19].

Kuang, also suggested that this behaviour becomes notably more pronounced during the induction melting of Ti-alloys, as the electromagnetic stirring induces

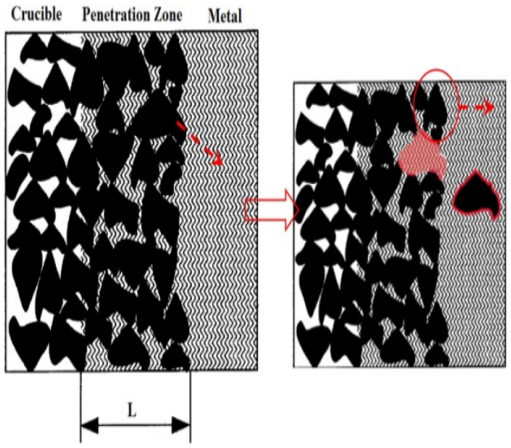

Figure 31: Schematic representation of melt penetration into crucible and entrainment of the crucible particles into the melt [19]. Adapted by Fashu [20]

continuous changes to the metal-mould interface [19]. This perpetual stirring action effectively removes reaction products, consistently exposing fresh surfaces for subsequent chemical attacks. Moreover, the particles that are removed through this process can diffuse into the metal, contributing to their presence as inclusions. Studies by Cui [28] and Gao [99] also made similar conclusions attributing the dissolution to be largely driven by physical erosion.

Figure 32 [21] shows the microstructure at the interface between the crucible (mullite) (left side) and the TiAl alloy (right side). The figure shows that mullite significantly reacted with the TiAl alloy. This was particularly evident after a 60-minute exposure at 1550°C (figure 32 (c)), where the metal sample almost entirely reacted with

the mullite crucible. The microstructure of the metal consisted of both particles and a matrix phase, differing from the typical as-cast lamellar α_2/γ structure of the γ-TiAl alloy [21]. The combination of X-ray diffraction data and SEM-EDX analysis revealed that the particles were α_2-Ti_3Al (Ti = 71.2 ± 0.3 at%, Al = 24.3 ± 0.2 at%), and the matrix phase was γ-TiAl (Ti = 48.0 ± 0.4 at%, Al = 47.6 ± 0.3 at%). Kuang and Harding [21], attributed the unusual microstructure to two factors: the metal absorbed a significant amount of oxygen from the crucible, stabilizing both the α and α_2 phases, as oxygen is known to do. Additionally, the slow cooling rate in the carbon resistance furnace (10°C/min) enabled the growth of these phases during cooling.

Chemical and physical erosion of oxides can be minimised through microstructure strengthening techniques, which aim to enhance mechanical properties like hardness, toughness and thermal stability. Given that oxides are typically brittle ceramics, these methods focus on refining grain structure, controlling phase distributions, and minimizing intrinsic flaws. Common strengthening techniques include grain size reduction, precipitation hardening, doping, alloying and porosity control [100]. Together, these approaches improve the oxide microstructure, making it more resilient and suitable for applications such as titanium casting.

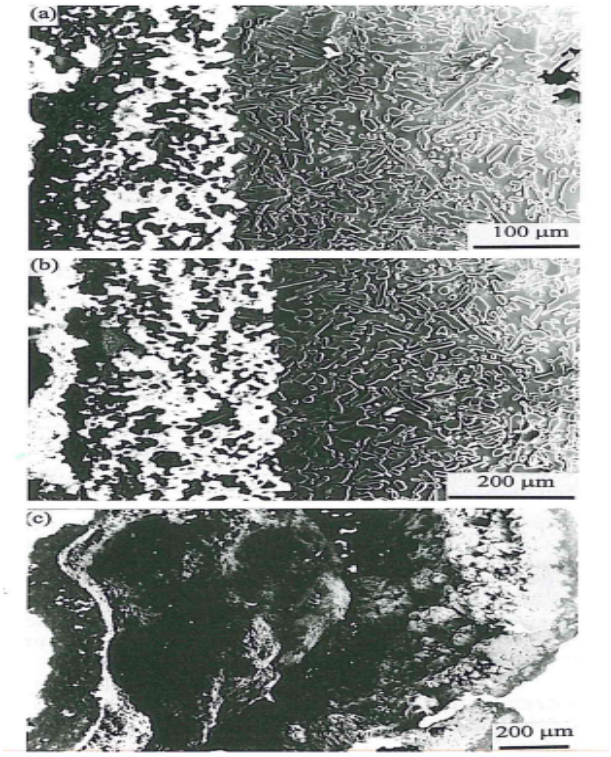

Figure 32: SEM secondary electron micrographs of the interacted mullite crucibles: (a) 1550°C/15 min, VFOP (Volume Fraction of Open Porosity) = 7.5% (b) 1550°C/30 min, VFOP = 7.5% (c) 1550°C/60 min, VFOP = 7.5% [21].

2.3.5 Oxidation of Ti and Ti-Alloys

To comprehend fully the nature of the chemical interactions resulting in the formation of an oxygen-enriched reaction layer, it is imperative to elucidate the oxidation behaviour exhibited by titanium. Titanium exhibits a high affinity for oxygen and readily reacts when exposed to oxidizing environments [101]. At room temperature, the interaction between titanium and oxygen leads to the formation of a thin oxide

layer (TiO_2), which serves as a protective barrier for the metal surface, preventing further oxidation and corrosion [22]. At temperatures exceeding 300°C, particularly in oxygen-rich environments, titanium undergo rapid oxidation (rapid growth of oxide layer) [101, 22]. Numerous studies have presented oxidation behaviour of Ti and Ti-alloys at elevated temperatures [102, 103, 104]. The most significant investigations into the oxidation of titanium in oxygen at atmospheric pressures and a wide temperature range have been conducted by Kofstad *et al.* [105] and more recently Hasan Guleryuz [106]. These studies report different oxidation behaviours of titanium, primarily dependent on temperature and time. Figure 33 shows the oxidation kinetics of CP-titanium at various temperatures [22]. At temperatures below 400°C,

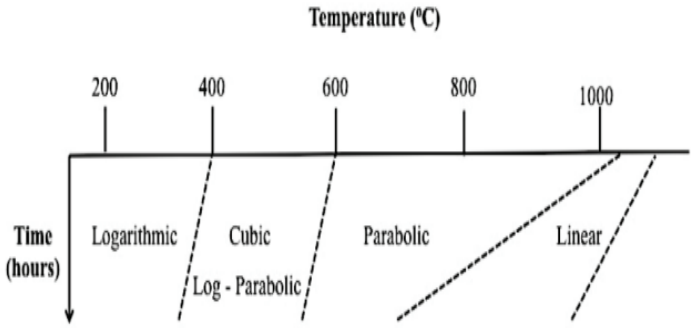

Figure 33: Rate equations observed in the oxidation of titanium [22].

the oxidation rate follows a logarithmic law, while between 400°C and 600°C it follows a cubic law and between 600°C and 700°C a parabolic law [22]. Moreover, it has been noted that with prolonged oxidation times, there is a transition from the

parabolic rate to a linear rate. At temperatures above 900°C, linear growth has been observed. The logarithmic oxidation primarily leads to the formation of a thin oxide scale, mainly TiO_2 (existing either as rutile or anatase) phase [22]. In contrast, cubic and parabolic rates are linked to both oxide scale formation and oxygen diffusion into the titanium metal [22]. The diffusion of oxygen results in the creation of a brittle and hard oxygen-enriched layer beneath the oxide scale. This is the layer known as the α-case that has been observed to form on metal surfaces as a result of Ti-casting.

For TiAl alloys, oxidation behaviour shares similarities with that of CP titanium but also exhibits key differences due to the presence of aluminium. While CP titanium typically follows a logarithmic or parabolic oxidation law at lower temperatures, indicating the formation of a protective oxide film, TiAl alloys generally form a more protective alumina (Al_2O_3) layer at elevated temperatures [107], which improves oxidation resistance. However, several differences emerge:

Lower Temperature Oxidation: TiAl alloys also exhibit logarithmic and parabolic oxidation behaviours (below 800°C), but the presence of aluminium promotes the formation of alumina, which is more protective than the TiO_2 layer (typically formed on pure titanium) [22].

Higher Temperature Oxidation: Above 800°C, TiAl alloys can form both alumina and titanium oxides. The oxidation rate may transition toward a linear or

breakaway regime, depending on factors such as alloy composition, microstructure, and environmental conditions. The oxidation behaviour becomes more complex due to the interaction between the TiO_2 and Al_2O_3 layers [22].

2.3.5.1 Wagners Oxidation Model Wagner's model, shown in Figure 34, describes the simultaneous formation of oxide scale and α-case by modelling the oxygen concentration profile in oxidized titanium [22]. According to Wagner's model, the oxygen concentration profile consists of two distinct regions: one for the oxide layer (TiO_2) and the other for the oxygen diffusion layer, known as the α-case layer [22]. Each concentration profile has distinct thicknesses: the TiO_2 layer with a thickness denoted as z and the α-case layer with a thickness denoted as x.

The thickness of the α-case layer is dependent on the solubility of oxygen in titanium, with the highest concentration observed at point C_{sl}, representing the oxide-metal interface [22]. The thickness extends to distance C_{so}, corresponding to the bulk concentration of oxygen in the metal. Observations indicate that at temperatures exceeding 600°C, an increase in the oxidation rate results in the formation of a thicker oxide layer. However, this increase in the oxidation rate also leads to the development of defects in the oxide layer, such as porosity [22]. The presence of porosity facilitates easier penetration of oxygen into the bulk metal, causing the α-case layer to widen. As the temperature exceeds 800°C, the oxide layer further

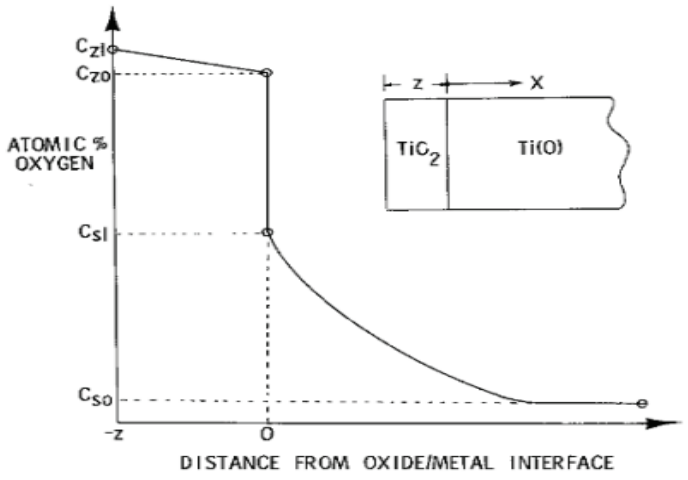

Figure 34: Oxygen Concentration Profile of Oxidized Titanium According to Wagner's model [22].

degrades, contributing to an even greater thickness of the α-case layer [22].

Oxidation of Ti-Al alloys becomes more complex due to the presence of β-phase, which results from β-stabilizers such as aluminium. The addition of aluminium considerably enhances the oxidation resistance of titanium by forming the more thermodynamically stable protective α-Al_2O_3 phase. As mentioned earlier, at temperatures exceeding 600°C, the TiO_2 oxide layer becomes defective as porosity arises, but α-Al_2O_3 offers higher resistance [22]. Hence, Ti-Al alloys exhibit better oxidation resistance than pure titanium alloys. Frangini *et al.* [108], conducted a study on the oxidation behaviour of the Ti–6Al–4V alloy within the temperature range

of 600–700°C in air, with exposure times up to 300 hours. Their findings revealed that the oxidation kinetics in this temperature range primarily followed a parabolic behaviour [108]. Interestingly, a transition to linear behaviour was noted at 700°C after 50 hours of exposure. This is due to changes in the oxide scale morphology. The oxide scale is dense and compact at lower temperatures, while it is porous and prone to spalling when at higher temperatures [108, 22]. The oxide scales also exhibit a multi-layered structure, consisting of TiO_2 and Al_2O_3 layers [22]. Du *et al.* [109] and Sefer [22], observed this structure in oxide scales at temperatures ranging from 650–850°C, noting that the number of Al_2O_3 layers increases with higher temperatures or prolonged reaction times. The problem with high temperature oxidation arises at above 850°C, where the protective oxide layer weaken or even disappears, exposing the large diffuse layer for oxygen to penetrate. This is the reason for the appearance of reaction layer observed by Liu in figure 30. Regardless of the type of oxide scale formed under the solidus temperature, the oxide scale is no longer present when the metal/alloy is molten. This is one of the prime causes of oxygen contamination during the casting of TiAl alloy, since there is no longer a protective layer to restrict oxygen diffusion.

The crystal structure and the extent of alpha case layer formation can be unveiled through the examination of the Ti-O phase diagram. Figure 35 illustrates

the Ti-O phase diagram, highlighting significant regions such as multiple Ti-oxide phases—TiO, TiO_2, Ti_2O_3—and two primary solid solutions, namely alpha titanium and beta titanium.

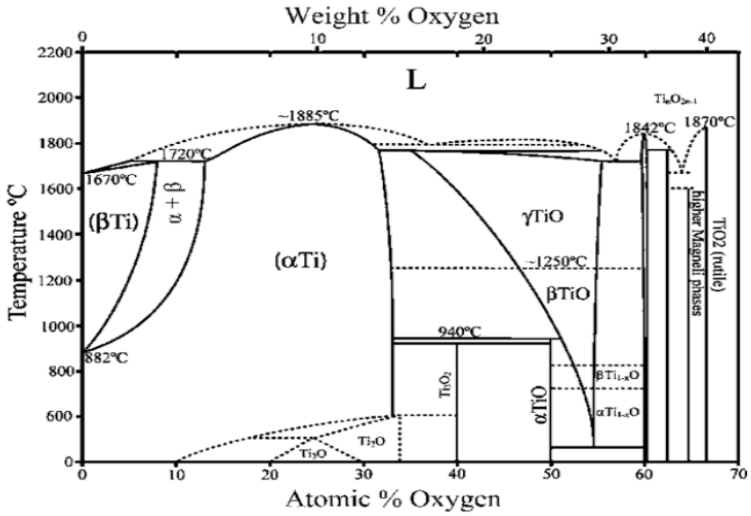

Figure 35: Ti-O Phase Diagram [23].

In α-Ti, the solubility of oxygen is notably high, approximately 33 atomic percent, with minimal variations observed across temperature changes. In contrast, the solubility of oxygen in β-titanium exhibits an increasing trend with temperature, peaking at 8 atomic percent at 1700°C. In analysing the diagram, it can be hypothesised that the formation of the alpha case layer is due to the higher solubility of oxygen in α-titanium (approximately 14.5 wt.%) and the strong affinity of titanium to absorb oxygen. The absorbed oxygen instantaneously reacts and stabilises the alpha phase, leading to the development of the alpha case layer.

2.4 Conventional Prevention Techniques of Alpha-Case Formation and Oxygen Contamination

2.4.1 Impact of Sintering Elements on Metal-Mould Reaction

Prevention of alpha case and oxygen contamination in the melt can be achieved by selecting suitable mould materials. Yttria with its high melting temperature (around 2683 K (2410°C)), requires a high sintering temperature (1773 K or 1500°C) to achieve a dense structure [34]. Investment casting moulds are commonly sintered at temperatures around 1473 K (1200°C). This results in numerous yttria inclusions at the casting surface, leading to degradation of mechanical properties in the casting [34]. To improve sintering properties of yttria at lower temperatures, common sintering additives such as B_2O_3, TiO_2, Al_2O_3, ZrO_2 and fluorides like CaF_2 or LiF are added to yttria [34]. This promotes mass diffusion at lower temperatures, effectively reducing the powder sintering temperature. Nevertheless, these additives can affect the chemical inertness of the mould material due to the formation of new microstructures resulting from the change in chemical composition. Study by Chen *et al*. [34], the chemical inertness of three different face coat systems based on the yttria-alumina-zirconia system (Y_2O_3-0.5 wt.% Al_2O_3-0.5 wt.% ZrO_2), a yttria-fluoride system (Y_2O_3-0.15 wt.% YF_3), and a yttria-boride system (Y_2O_3-0.15 wt.%

B_2O_3) was investigated. The interaction layer thickness was found to vary with different additive inclusions in the yttria coating [34]. Pure yttria (yttria + sol) exhibited the lowest reaction layer thickness at 4 μm, followed by YAZ (yttria-alumina-zirconia system) with just over 4 μm, the fluoride system reaching over 5 μm, and 6 μm for the yttria-boride system [34].

Hardness testing of the cast metal revealed that metal cast with pure yttria had the smallest hardened layer thickness, measuring less than 15 μm [34]. YB and YF exhibited similar hardened layer thicknesses of around 25 μm. The stability ranking from most stable to least stable is Yttria > YAZ > YF > YB. Studies such as these show that chemical formulations of moulds are critical in maintaining the chemical stability of the mould. Although the addition of additives improves mechanical properties, it can certainly affect the chemical inertness of the mould. By selecting appropriate sintering agents, the reaction layer thickness can be controlled.

2.4.1.1 High-Temperature Oxidation Layers One of the prime causes of diffusion of oxygen into the liquid metal from the ceramic is the absence of protective oxide layer. Few studies have highlighted the possibility of forming a protective layer across the metal-mould interface to limit the diffusion of oxygen from the mould and into the metal. Cheng *et al.* [24], conducted a study on the interactions between a high Nb-containing TiAl alloy and a yttria face-coat during investment casting. Their

findings indicated that the addition of a high concentration of Nb into TiAl resulted in much thinner oxidation layers and reduced hardened layer thickness [24]. Figure 36 shows the backscattered image of the metal mould interface of Ti–46Al–8Nb–B alloy [24]. The TiAl alloy showed clear alpha and beta lamellar microstructure with the face-coat (bright) still attached to the metal surface. At the interface, two main types

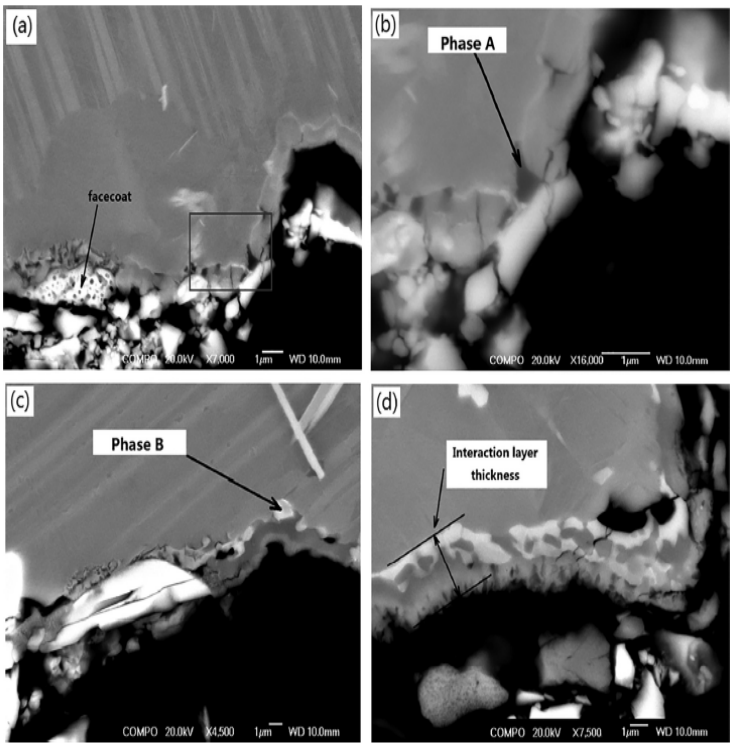

Figure 36: Backscattered image of the metal/shell interface in a Ti–46Al–8Nb–B alloy [24].

of interaction phases were identified, namely 'Phase A' (dark color) and 'Phase B' (bright). Phase A is predominantly observed in the gamma phase within the lamellar structure of the Ti–46Al–8Nb–1B alloy, while Phase B appeared some distance away

from the interface. The Energy Dispersive X-ray (EDX) analysis results revealed that 'Phase A' contains a significant amount of Al and O, suggesting the presence of Al_2O_3. On the other hand, Phase B contains a substantial amount of Ti, Nb, and O, resembling the composition of the reported $(Ti,Nb)_xO_y$ phase. Cheng proposed a more intricate oxidation behaviour occurring at the metal-mould interface. A schematic diagram illustrating the oxidation mechanism suggested by Cheng is presented in figure 37.

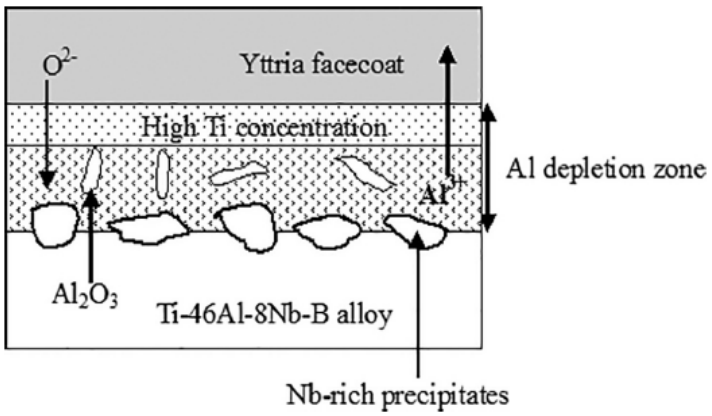

Figure 37: Schematic of possible oxidation mechanisms of Nb containing TiAl alloy [24].

Initially, Y_2O_3 decomposition continuously saturates the liquid metal with oxygen, leading to an interfacial microstructure in high Nb-TiAl alloy that forms Al_2O_3 phase islands in the outer interaction layer and $(Ti,Nb)_xO_y$ in the inner layer, as shown in figure 37 [24]. Cheng suggested that the formation of this Nb-rich precipitates hinders the continuous diffusion of oxygen from the mould, thereby reducing

the thickness of the hardened layer. The formation of a protective oxide layer rich in Nb has also been suggested by Lin *et al.* [110] but at lower temperatures. The creation of protective oxide layers that impede the diffusion of oxygen from the mould represents another approach to reducing the interaction layer thickness. However, the formation of protective oxide layers has rarely been observed at high temperatures by other researchers, especially when Ti-alloys are involved. This is a fairly new field of study, and much research is required to fully understand the development of oxide layers for titanium close to melting temperatures.

2.4.2 Nb-Added TiAl

Many studies have shown Nb additions improve oxidation resistance in TiAl alloys. Yang [25] studied the as-cast microstructure of alloys with varying Nb levels compared to binary Ti–47Al alloy. Figure 38 depicts the microstructure of TiAl alloy with varying amounts of Nb in the metal, specifically 2, 5, and 8% compared to Ti47Al. The microstructure transitions from being 'nearly full-layered' (a) to 'fully layered' (d), with increasing percentages of Nb. Additionally, the colony sizes increase as the Nb percentage increases, while the layered voids become refined.

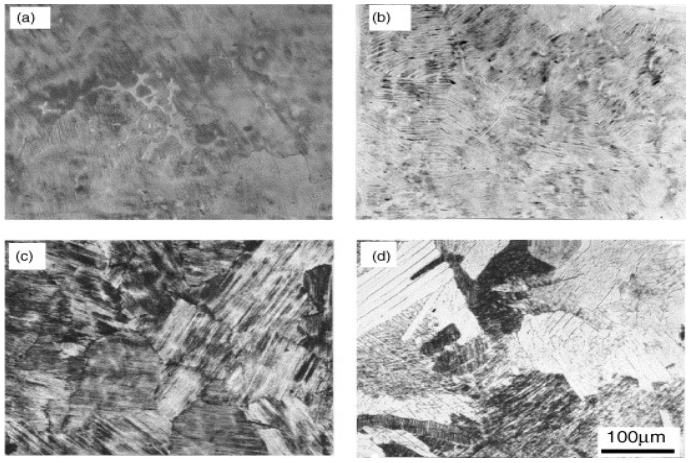

Figure 38: SEM micrographs showing as-cast microstructures of (a) Ti–47Al; (b) Ti–47Al–2Nb; (c) Ti–47Al–5Nb; (d) Ti–44.2Al–8Nb [25]

Firstly, Nb acts as a dopant in the TiAl alloy, Nb has a higher valency than Ti, its presence decreases the concentration of oxygen vacancies in titanium dioxide lattice (this is the protective oxide layer) [25]. This reduction in vacancies inhibits oxygen diffusion within the lattice preventing further oxidation. Nb also increases the activity and diffusivity of aluminium within the alloy. As a consequence, this facilitates the formation of a protective alumina (Al_2O_3) layer on the surface of the alloy which again serves as a barrier against further oxidation of the metal. Nb addition reduces the solubility of oxygen in the TiAl alloy, thereby restraining internal oxidation which can weaken its structure. The effectiveness of oxidation resistance can be quantified by measuring the thickness of the oxidation layers, which

is indicated by the total mass gain of the metal, as depicted in figure 39. For cast alloys, cyclic heat treatment can be used to refine the lamellar colony size [25]. Effect of heat-treatment on oxidation also depicted in figure 39 [25].

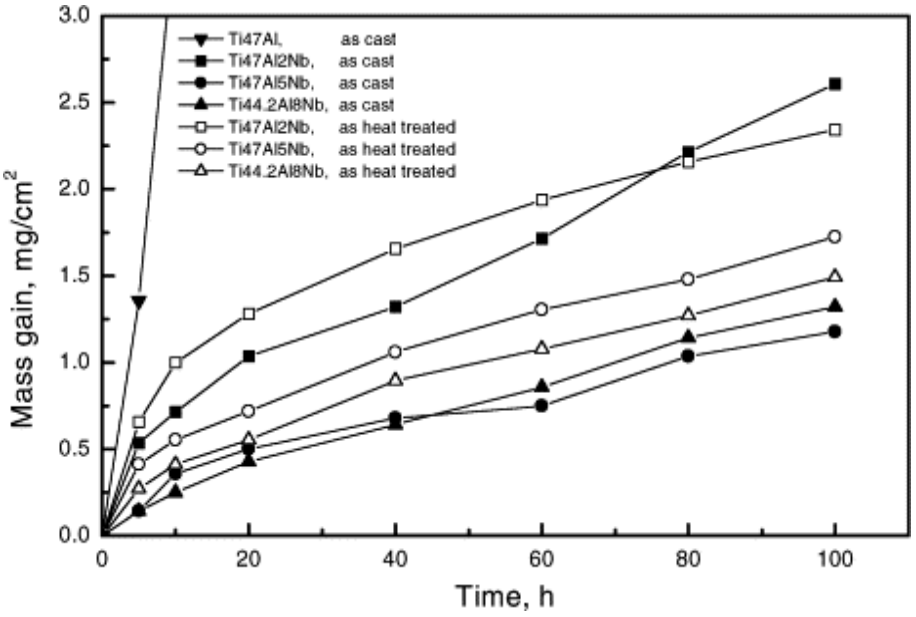

Figure 39: Isotherman Oxidation of Ti–47Al; Ti–47Al–2Nb; Ti–47Al–5Nb; Ti–44.2Al–8Nb, both as-cast and heat-treated [25]

A larger mass gain corresponds to a greater oxide layer thickness, and consequently, indicates greater resistance towards oxidation. As the results show that increase in Nb composition does contribute to greater mass gain attributed to protective oxide growth.

2.4.2.1 Impact of Back-up Coating on Metal-Mould Reaction Moulds like yttria have poor thermal shock resistance, risking cracking and delamination during shell-making and casting. Therefore, backup coats are used to ensure strength, permeability and dimensional accuracy [16]. However, silicon (Si) in backup coats can infiltrate the face coat during mould firing and high-temperature casting, compromising the chemical inertness of the mould material. Study by Cheng [16], investigated the chemical interaction of Y_2O_3 moulds using two different backup coat formulations. The first was mullite (Al_2O_3-SiO_2), and the other was Ti-added mullite (MTi). Figure 40 shows the oxygen penetration and hardness profile of the cast metal with mullite and Ti-added mullite backup coats (yttria as a facecoat).

The oxygen penetration distance for mullite (M) is approximately 1665 μm, while for MTi, it is reduced to 990 μm. The alpha-case thickness is predicted to be approximately 1367 μm for M and 803 μm for MTi. Similarly, the hardened layer thickness for the M backup coat was 1450 μm and 850 μm for MTi. It is clearly evident that the use of Ti powders in mullite has significantly improved the chemical inertness of the mould, as reflected in the interaction layer thicknesses.

Xu concluded that Ti powder undergoes a dual reaction process during firing. Firstly, it forms TiO_2 according to the reaction $Ti + 2O \rightarrow TiO_2$, and then interacts with silicon coming from the decomposition of the silica binder and mullite powder,

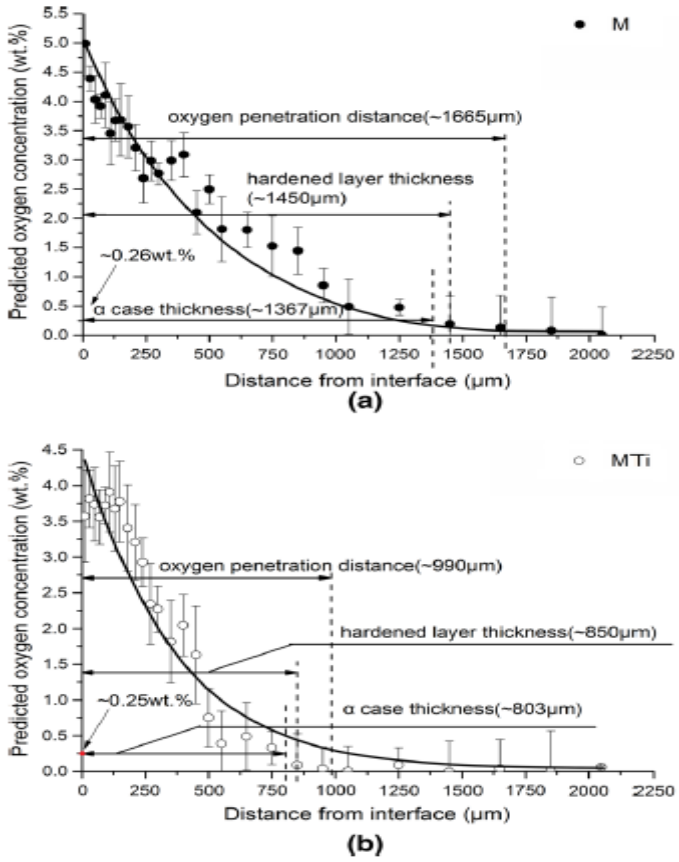

Figure 40: Predicted oxygen penetration distance in Ti64 alloy castings using different backup coat materials: (a) M backup coat and (b) MTi backup coat [16].

resulting in the formation of a silicon-rich layer outside the Ti particles. The likely reaction between Ti and Si is $5\text{Ti} + 3\text{Si} \rightarrow \text{Ti}_5\text{Si}_3$ [16].

Due to the reactions promoted by Ti within the backup coat, titanium powder oxidizes and interacts with Si and O in the mullite shell, which reduces both the Si penetration distance and the oxygen penetration distance [16]. Consequently, the

thicknesses of both the alpha case and the hardened layers of the alloy are shorter when utilizing the MTi shell compared to those obtained using M shells [16].

2.4.2.2 Impact of Mould Pre-heat Temperature on Metal-Mould Reaction Before the casting process commences, the mould undergoes preheating, with preheat temperatures for casting titanium alloys ranging 800°C to 1200°C. Studies have revealed that pre-heat temperature of the mould affect the overall chemical inertness. In a study conducted by Chen [111], the hardness of the Ti-46Al-8Nb-1B alloy was tested under two different mould preheat temperatures (500°C and 1200°C). The average thickness of the hardened layer was 73 micrometers with a mould preheat temperature of 500°C, and about 261 micrometers with a preheat of 1200°C. Clearly, indicating that higher pre-heat temperatures lead to larger reaction layer. In another study by Chen [112], the CaO-stabilized zirconia face coat was investigated at various mould preheat temperatures. Chen reported that the thickness of the hardened layers was approximately 100 micrometers when preheated at temperatures of 500°C and 1000°C. The thickness increased to around 150 micrometers when the preheat temperature was elevated to 1200°C. This is one other instance where, preheat temperatures can also affect the metal-mould interaction. Chen concluded that raising the mould preheat temperature from 500°C to 1200°C led to a substantial increase in solidification time. This extended time allows for more prolonged

contact between the molten metal and the ceramic mould, promoting metal-mould interactions. In addition the diffusion of elements is enhanced by the higher preheat temperature, this results in a faster growth of the reaction layer, as the diffusion of reactive species like oxygen become more efficient at elevated temperatures.

2.4.2.3 Impact of Alloying Additions on Metal-Mould Reaction De-oxidation of the Ti melt is one such technique, where the process generally involves the addition of a deoxidizing agent that reacts with oxygen in the liquid to form a stable compound, which can then be removed or reduced in concentration. For example, Yahata *et al*. [113], employed the de-oxidation process by adding excess aluminium into the melt. The oxygen reacts with aluminium to form Al_2O_3, which rises as a gas phase and escape from the surface of the melt when in a high-temperature, low-pressure environment (such as in vacuum arc remelting or other vacuum processes). Similarly, study by Suzuki explored the de-oxidation behaviour of solid titanium with calcium (Ca) [114]. Additionally, Okabe [115], investigated the de-oxidation behaviour of rare earth metals on β titanium. Okabe showed that a highly reducing atmosphere was obtained pertaining to an oxygen partial pressure of 10^{-41}, using Y/Y_2O_3 promoting the decrease in concentration in titanium to 200 ppm [115]. Other oxide removal techniques include vapour phase removal, skimming, centrifugal separation, filtration, and remelting. Vapour phase removal vaporizes oxides under vacuum.

Skimming relies on oxides rising to the surface due to density differences and being physically removed. Centrifugal separation spins molten titanium to separate oxides by density, forcing heavier ones outward. Filtration uses ceramic or mesh filters to trap fine oxide particles during casting. Remelting involves repeated melting to float oxides to the surface or trap them in slag, refining the metal over multiple cycles. The problem with these approaches is that they focus on treating the consequences of metal-mould interactions rather than preventing them. Techniques like oxide removal deal with oxides that have already formed, increasing processing time and costs. A better approach would be to prevent these reactions by developing more stable mould materials or coatings, reducing the need for extensive oxide removal and improving overall efficiency and product integrity.

2.5 Moulds For Casting Ti-Alloys

2.5.1 Ceramic Shells for Casting Ti-Alloys

Jones and Yuan [11], stressed the importance of 7 specific requirements that the ceramic shell in investment casting must meet to successfully cast the desired component. These include sufficient green strength, adequate fired strength, high thermal shock resistance, high chemical stability, sufficient permeability, adequate thermal conductivity and limited creep. Amongst these thermal shock resistance and chemi-

cal inertness are among the most critical factors in selecting and designing crucibles for melting titanium alloys. During processing, large thermal gradients arise as manufacturers aim to minimize contact time between the crucible and molten titanium to prevent unwanted reactions. Consequently, crucible materials must withstand rapid temperature changes without cracking while maintaining high chemical inertness to avoid contamination from reactions with the molten titanium. The challenge becomes more pronounced with larger crucibles, where the thermal stresses are amplified due to the greater size and surface area, increasing the risk of cracking or failure. Therefore, materials with high thermal shock resistance are essential for ensuring the durability and performance of crucibles in such demanding conditions [20], [116]. Often, high thermal shock-resistant ceramics are those which exhibit low thermal expansion coefficients and high thermal conductivity [20]. In traditional ceramic oxides, a trade-off frequently exists between thermal shock resistance and chemical inertness to molten titanium [20]. Materials with better shock resistance, like Al_2O_3 and MgO, are generally less thermodynamically stable in comparison to more inert materials such as ZrO_2, CaO and Y_2O_3 [20], [117], [118]. To mitigate this, an Al_2O_3 crucible with a Y_2O_3 coating has been used, which combines good thermal shock resistance, cost-effectiveness and improved inertness to molten titanium [119], [120]. However, Y_2O_3 coatings present challenges, including a short slurry shelf life,

low sinterability and weak adhesion to many substrates.

Methods to improve these aspects, such as adding low-melting-point additives like SiO_2, may enhance slurry stability [19, 121] but can compromise inertness, increasing susceptibility to titanium reactions. Optimizing crucible thickness can improve shock resistance, durability and reduce thermal cracking; however, further research is needed to determine the ideal coating thickness for optimal shock resistance and inertness [122, 123]. Another crucial factor in crucible design is the porosity of the mould material [124, 125, 126]. Higher porosity enhances surface wettability and allows for greater melt infiltration, which can accelerate erosion and lead to premature cracking when infiltrated melt solidifies within the pores [20]. However, porosity also improves thermal shock resistance and can aid in coating adhesion to the substrate [20]. Thus, selecting an optimal porosity level is essential for balancing durability, shock resistance, and coating stability, making it a key consideration in crucible design for molten titanium processing. The crucible material must have a melting and softening point above superheated titanium (1668°C) to effectively contain the molten metal [20]. SiO_2 has a melting point of 1710°C but unsuitable for melting titanium because it softens at around 1280°C [20]. This softening leads to structural instability and contamination of the titanium, making it an inadequate choice for crucibles used in high-temperature titanium alloy processing.

Composite ceramic oxides have gained much attention as they have demonstrated high thermal stability when in contact with Ti-alloys. An advantage in using composite oxides as mould is that they can be more cost effective for instance, $Y_2O_3$is identified as the least reactive material for casting titanium however, it is also the most expensive. In such instances, composite oxides are a viable solution as less Y_2O_3 is present in the mould. Calcia-stabilized zirconia ($CaZrO_3$) composite showed low corrosion properties similar to CaO [127], [128]. $BaZrO_3$ is another example of composite system shown to exhibit high inertness [129]. Doping is also another technique in which higher inertness can be achieved whilst being economic. Figure 41 shows the method in which Y_2O_3 is used to dope ZrO_2.

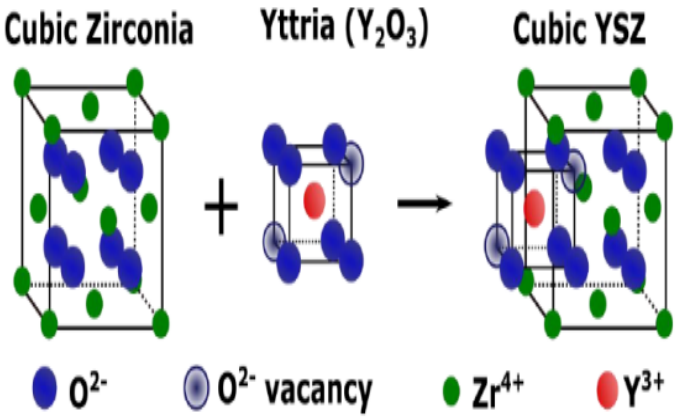

Figure 41: Schematic illustration of Yttria-Doped-Zirconia [26].

ZrO_2 exists in three different structures including monoclinic, tetragonal and fluorite. The monoclinic structure is stable up to 1170°C, the tetragonal and fluorite

structures are stable at higher temperatures. Specifically, the fluorite structure, stable from 1170°C to 2370°C and more thermodynamically stable. The addition of yttrium oxide (Y_2O_3) to zirconia stabilizes the high-temperature fluorite phase, enhancing its stability. Typically, 8-10 mol percent yttria is used to stabilize the cubic phase across all temperatures, preventing disruptive phase transformations and associated volume changes.

Research into mould development for titanium casting can be traced back to the 1950s, where a study by Saha [130] reported that authors Eastwood and Craighead studied various refractory compounds and metals, finding that all, except zirconia, to be reactive. In the early 1960s, the US Bureau of Mines [131] tested various binary and ternary oxides, carbides and nitrides as mould materials for casting titanium. These studies used thermodynamic analysis, comparing the formation free energies of refractory oxides (such as SiO_2, zirconia, Al_2O_3, MgO etc.) with corresponding titanium phases (TiO, TiO_2, TiC) [131]. However, no material was identified as completely inert to molten titanium, although some exhibited reduced reactivity. Among the least reactive oxides identified during the 1960s to 1980s were Al_2O_3, ZrO_2, CaO and Y_2O_3. Despite these findings, no substantial developments have been made in this field, as these oxides remain the common materials used in titanium casting today. Nevertheless, $CaZrO_3$ [20], Yttria-Stabilised-Zirconia [132], $BaZrO_3$

[133] are novel oxides system that have gained much attention recently due to their enhanced stability by combining multiple phases like ZrO_2 and CaO.

Much more recently, ceramic systems such as carbides, nitrides and oxides have been the subject of extensive research especially, for high temperature applications (>1700°C) [134, 135]. Jet engines, industrial gas turbines and nuclear reactors often require ceramic materials that can withstand temperatures greater than 1700°C without being subject to oxidation or reduction. Casting of Ti-alloys also require mould materials operating at temperatures greater than to 1700°C as the melting temperature of pure titanium is approximately 1700°C. Many studies have identified oxide ceramics such as Y_2O_3, Al_2O_3, ZrO_2 and CaO to be suitable mould materials for casting Ti-alloys in comparison to carbides, nitrides and borides; largely due to their lower reactivity towards molten titanium [136, 137, 138, 139, 140]. Backman investigated equilibrium oxide phases and the free energy of formation of oxides and their carbides, nitrides and borides for group IV, V and VI refractory metals [136]. Backman concluded that oxide ceramics to be most stable as they have the highest free energy of formation. Kartavyk investigated the interaction between aluminium nitride ceramic (AIN) and boron nitride and concluded that the reaction aids the formation of Ti_2AlN and (Ti,Nb)B micro-precipitates at the expense of the liquid metal [139]. The reaction is thus: Ti_3Al +(Nb)+BN $\rightarrow$ Ti_2AlN+(Ti,Nb)B. Glasson

found that boride and carbide coatings generally have poor resistance in air or oxygen therefore, have poor oxidation resistance [138]. Formation energies, interaction products, liquid contamination by the mould and resistance to reduction and oxidation are few criteria used in the above studies to test the suitability of ceramics for casting Ti-alloys. Studies such as these prove that oxide ceramics have been found to be superior compared to carbides, nitrides and borides. Ceramic oxides are less reactive due to their high resistivity to air and oxygen [141], while non-oxide ceramics (carbides, borides, nitrides) have lower resistance and depend on oxide formation for high-temperature stability [142]. Ceramic oxides also have low chemical solubility in liquid metal [143], giving them greater resistance to chemical attack and corrosion.

2.5.2 Design and Selection of Oxide Ceramics

A more prominent approach to this problem is to identify or design for oxide materials that exhibit the highest resistance towards liquid titanium. An example of this is SiO_2, where the reaction between SiO_2 and Ti forms TiSi as a by-product. Such reactions cause SiO_2 to fail prematurely forming TiSi as a by-product [144]. SiO_2 in this case will be considered thermodynamically unstable since, the precipitation of TiSi is favoured. A better alternative would be to use CaO, Y_2O_3 or mullite (a composite of Al_2O_3 and SiO_2 with a chemical formula $2Al_2O_3SiO_2$) where, the side reaction form-

ing TiSi is eliminated. Experimental studies determine the thermodynamic stability of oxides in contact with TiAl melt through reaction layer thickness, and oxygen diffusion into the liquid from the ceramic mould. Fashu [20] gathered empirical data on the thickness of interaction layers and oxygen contamination specifically for Ti-Al alloys in contact with various mould oxides at melting temperatures. The data is presented in the appendix 7.5.6. Based on this assessment, a stability ranking of oxides, determined by both interaction layer thickness and oxygen contamination, is presented below. This criterion will serve as a benchmark for comparison with the results obtained in this study.

$$Y_2O_3 > CaO > ZrO_2 > Al_2O_3 > SiO_2$$

Though there are many experimental studies on identifying stable oxide systems, there are few computational studies that are able to identify stable shell systems without the need for experiments. Moreover, a plethora of studies has delved into the realms of oxygen saturation and the consequential formation of reaction layers during the contact between titanium and moulds of diverse compositions.

It is interesting to note that irrespective of the oxide used, all oxides are prone to dissolution, resulting in the formation of the reaction layer. However, the extent of reaction layer thickness and oxygen contamination in the metal varies depending on the specific type of oxide utilized. Y_2O_3 and CaO exhibit the lowest levels of oxygen

contamination and reaction layer thickness when compared to oxides like Al_2O_3, MgO, and ZrO_2. It is noteworthy that a higher level of oxygen contamination does not necessarily align with a larger reaction layer thickness. As an example, $CaZrO_3$, when used as a mould material, displays very low oxygen contamination; however, the reaction layer thickness is substantially larger, falling within the range of 300-350 μm.

2.6 Thermodynamics of Metal-Mould Reactions

In addition to studying the metal-mould interfaces, it is also imperative to analyse the behaviour of the bulk liquid metal for several reasons: i) Alloying elements can be added to titanium to improve mechanical properties and these alloying additions significantly affects how the alloy interacts with the mould. For instance, the presence of Nb in TiAl resulted in smaller reaction layer thickness [24]. ii) The dissolution of oxides leads to the release of solutes such as oxygen into the liquid metal. This ongoing process continuously alters the composition of the metal, thereby changing the way the metal interacts with the mould. Quantifying the reactivity of Ti as a function of varying composition is a crucial aspect in understanding metal-mould behaviour. Understanding the factors that increase or decrease the reactivity of titanium can greatly aid in comprehending the problem at hand.

2.6.1 Mass Action Law

The mass action law, also known as the law of mass action, is a principle that describes the equilibrium relationship between the concentrations of reactants and products in a chemical reaction [145]. It is fundamental for understanding chemical equilibria and predicting the direction in which a particular reaction will proceed under certain conditions. The principle applies to any type of reaction whether decomposition, dissolution, displacement or combustion. The mass action equation given in equation 8 provides a quantitative measure of thermodynamic stability known as change in free energy (ΔG_r),

$$\Delta G_r = R \cdot T \cdot ln(K) \tag{7}$$

where R is the gas constant J/(mol·K), T is the temperature (Kelvin) and K is the equilibrium constant. The sign of ΔG_r is indicative of the direction in which a reaction will proceed and the magnitude shows the intensity of the reaction as illustrated below.

$+\Delta G_r$ = Reverse Reaction Favoured

$-\Delta G_r$ = Forward Reaction Favoured

$\Delta G_r = 0$ (neither forward nor reverse reaction is favoured)

Calculations of ΔG_r have been in effect for over a century in practices such as combustion, electrochemistry, reduction and oxidation of metals, and many more [146], [147], [148]. When choosing oxide materials for casting, the concept of mass action plays a crucial role in determining favourable and unfavourable reactions based on the above criteria. For instance, a negative ΔG_r value for a metal-oxide reaction may indicate the oxide is unstable and therefore not suitable for casting, whereas a positive ΔG_r can indicate a stable oxide and therefore suitable for casting Ti-alloys. This understanding enables the selection of suitable materials, narrowly avoiding unwanted reactions that destabilize the mould during contact with molten titanium.

2.6.1.1 Free Energy of Formation Formation energies are widely used in extraction metallurgy to facilitate the reduction or oxidation of metals. The formation energy, is a thermodynamic property that indicates the amount of energy released or absorbed when a compound is formed from its elements in their standard states [149] as shown in Equation 8.

$$\Delta G_f^o = R \cdot T \cdot ln(pO_2) \tag{8}$$

where, ΔG_f^o is the free energy of formation of a substance and pO_2 is the partial pressure of oxygen. The difference in the formation energies of two different substance

or oxides determines the ΔG_r for a reaction as shown in equation 9. The equation simply states that a more stable oxide will displace the less stable one.

$$\Delta G_r = \Delta G_f^o(M_xO_y) - \Delta G_f^o(N_xO_y) \tag{9}$$

The Ellingham diagram, developed by Harold Ellingham in the mid-1940s, is a graphical representation that plots the Gibbs free energy change of formation (ΔG_f^o) for oxides (and other compounds) as a function of temperature. This tool has been instrumental in predicting when a metal can reduce an oxide or displace another metal. The selection of crucible materials for casting Ti-alloys largely relies on the Ellingham method, guiding the choice of materials based on their thermodynamic stability. Figure 42 shows a typical Ellingham Diagram for some of the common mould oxides.

Slope: The slope of a line on the Ellingham diagram indicates the entropy change (ΔS) associated with the formation of the oxide. A steeper slope indicates a greater entropy change.

Intercept: The intercept on the y-axis, where $T = 0$, is the enthalpy of formation ΔH_f of the oxide. The lower the intercept, the more stable the oxide is at high temperatures as they release more energy when forming from their elements

Material Selection: The feasibility of a reaction between a metal and oxygen

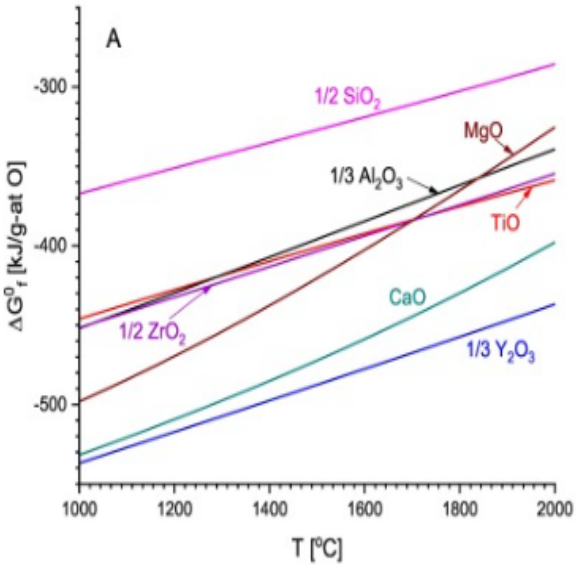

Figure 42: Gibbs free energy of formation of different binary oxide as a function of temperature [20], data adapted from [27]

to form its oxide can be assessed by comparing the Ellingham plots of the respective metals involved according to equation in 9. A metal positioned lower on the diagram, characterized by a more negative ΔG_f^o value, possesses greater thermodynamic driving force and can thereby, reduce the oxides of metals situated above it on the diagram. For instance, figure 42, shows that Y_2O_3 is situated below TiO showing that Y_2O_3 is more stable TiO. Through this analysis, it was possible to compare the stability one oxide to another.

2.6.1.2 Limitations in using Free Energy of Formation

Numerous studies have used the Ellingham method to select oxide materials for casting titanium alloys [136], [19]. These studies found that stability rankings based on reaction layer thickness and/or oxygen contamination generally align with rankings derived from formation energies. However, several investigations have highlighted inconsistencies with the stability predictions provided by this approach [150], [28]. A more elaborate study was conducted by Saha [150] on the thermodynamic stability of rare earth oxide face coats in contact with liquid titanium. The relative stability of rare earth oxides was assessed by determining the micro-hardness of as-cast samples and analysing concentration profiles of oxygen in investment cast titanium rods. These analyses were conducted at the melting point of titanium, approximately 1941 K, as well as at a temperatures above its melting point, around 1943 K and 1963 K. Stability ranking predicted by Saha through formation energy from decreasing stability (1941 K):

$$Y_2O_3 > Gd_2O_3 > Sm_2O_3 > Nd_2O_3 > ZrO_2 > CeO_2$$

Stability ranking established through experimental data based on oxygen contamination and micro-hardness profile from decreasing stability:

$$Y_2O_3 > Nd_2O_3 > Gd_2O_3 > Sm_2O_3 > ZrO_2 > CeO_2$$

As in the case above, the two rankings show disagreements between the stability of Nd_2O_3, Sm_2O_3, and Gd_2O_3. Calculations from formation energies indicate Gd_2O_3 and Sm_2O_3 to be more stable than Nd_2O_3, whereas experiments show Nd_2O_3 to be more stable than Sm_2O_3 and Gd_2O_3, showing there are disagreements between predictions. Saha also found that the increase in the standard Gibbs energy of formation of Sm_2O_3 with temperature was steeper than that of Gd_2O_3, suggesting inferior performance of Gd_2O_3 at higher temperatures. Furthermore, Saha also observed that the metallic content in the as-cast sample was notably lower than oxygen. This disparity likely arises from the incomplete dissolution of mould oxides in the liquid titanium, with metallic components remaining in the moulds, likely as lower oxides for instance $M_{x-z}O_y$. Saha proposed that the solubility of metallic species also plays a significant role in determining stability, suggesting that better predictions could be achieved by considering the solubility of metallic species.

Although the Ellingham method serves as a valuable tool for the initial screening of oxide materials for casting titanium alloys, its predictions do not always align perfectly with experimental observations. This can result in the selection of the wrong oxide, such as choosing Sm_2O_3 or Gd_2O_3 over Nd_2O_3 or anticipating Al_2O_3 to be completely stable when in reality, becomes unstable. Relying solely on the Ellingham method for selecting mould oxides is not always a reliable approach.

2.6.1.3 Modified Formation Energy Few studies have highlighted that formation energies are idealistic values calculated assuming standard state conditions, in other words, bulk thermodynamics. In light of this, Chidambaram [151] suggested accounting for surface energy effects by adding an excess term (ΔG_{xs}) to the free energy of formation, as shown in Equation 10.

$$\Delta G_{surf} = \Delta G_f + \Delta G_{xs} \tag{10}$$

Another study by Cui [28] modified formation energy by accounting for realistic values of solute free energy in the liquid melt. This was done by calculating individual contributions of free energy from the overall reaction equation as shown below.

Overall formation reaction of M_xO_y oxide is described as:

$$xM(s) + \frac{y}{2}O_2(g) \rightarrow M_xO_y(s) \qquad \Delta G_1 \tag{11}$$

The non-standard state dissolution of the metal in liquid can be written as:

$$xM(s) \rightarrow x[\text{M}] \text{ in TiAl melt} \qquad \Delta G_2 \tag{12}$$

The non-standard state dissolution of oxygen in liquid can be written as:

$$\frac{y}{2}O_2(g) \rightarrow y[\text{O}] \text{ in TiAl melt} \qquad \Delta G_3 \tag{13}$$

The modified formation energy can be obtained by the summation of ΔG values calculated from equations 12 and 13 minus the ideal formation energy in equation 11.

$$\Delta G_f^o = \Delta G_2 + \Delta G_3 - \Delta G_1 \tag{14}$$

$$\Delta G_2 = x \sum a_i \cdot RT \cdot ln \frac{M_i}{100 M_M} \gamma_M^0 \tag{15}$$

$$\Delta G_3 = y(\sum x_i \Delta G_i + RT \sum x_i \cdot ln \gamma_i)/2 \tag{16}$$

Figure 43 shows the new formation energy predicted by this method for temperatures ranging from 1800K to 2300K, which is significantly lower than the conventional method of predicting formation energy.

The advantage of this method is the activity of metallic species (M) and and (O) are taken into consideration but activities are calculated using the Miedema method, which considers only binary interactions, resulting in some level of inaccuracy.

2.6.1.4 Kostov Model Kostov studied dissolution of mould oxides in liquid titanium whilst accounting for non-deal behaviour of the liquid phase[27]. According to the Kostov model, the direction in which the dissolution reaction is favoured

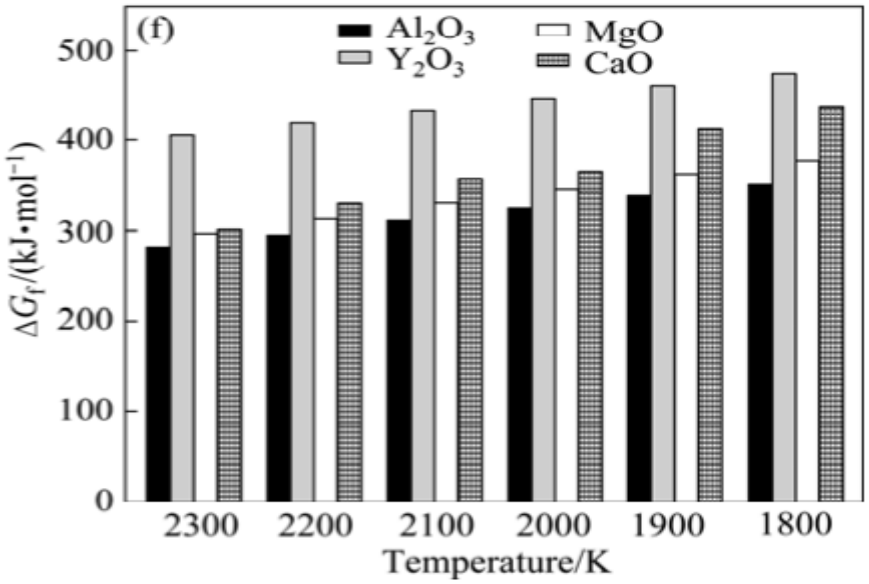

Figure 43: Modified formation energy predicted by Cui Renji for 1800K to 2300K [28].

depends entirely on the activity of oxygen in the liquid melt. The dissolution of oxides will proceed if the chemical potential of oxygen is sufficiently reduced in the liquid melt. At this juncture, the system will endeavour to establish a new equilibrium state to rectify the imbalance of oxygen potential. Figure 44 shows the ΔG_r for the dissolution of various mould oxides in TiAl alloy melt.

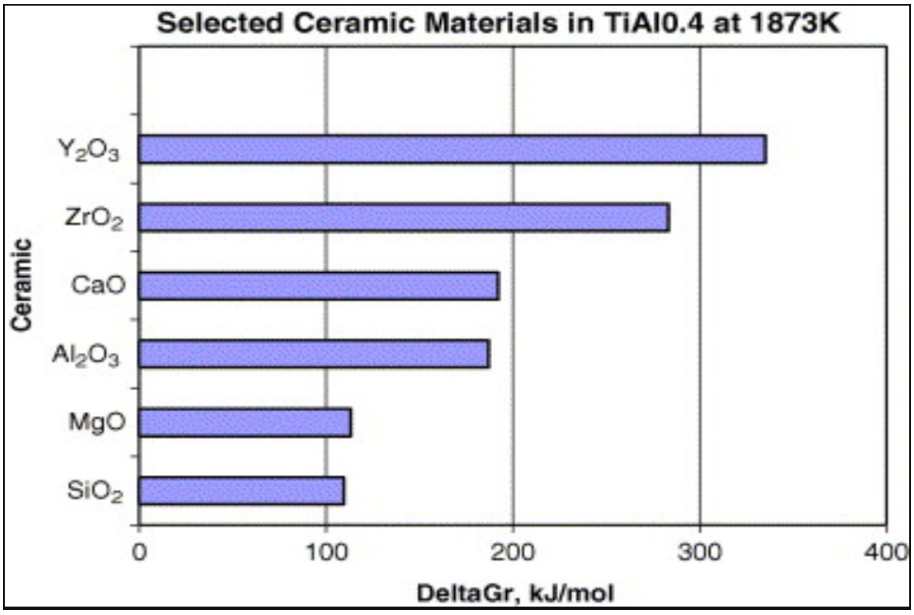

Figure 44: ΔG values predicted by Kostov for various oxides at (1873 K) [27]

The results indicate that all oxides are predicted to be stable, as evidenced by a positive change in free energy. Y_2O_3 is predicted to be the most stable oxide, while SiO_2 is the least stable. The stability ranking aligns closely with the experimental ranking established earlier in section 2.5.2, though ZrO_2 is predicted to be more stable than CaO. A few questions remain unanswered: first, the highly positive ΔG_r does not fully explain the extensive reactions observed between the metal and the mold. Second, the reasons behind the formation of the alpha case layer, as observed in experiments, are still unclear.

2.6.2 Challenges in Predicting ΔG_r

There are three main limitations that have been found in computational predictions of ΔG_r whether using Formation Energies or the Kostov model:

1. Extent of Metal-Mould Reaction: The highly positive ΔG_r implies stability but does not fully capture the significant extent of reaction between the metal and the mould observed experimentally.

2. Alpha Case Formation: The model does not reveal the mechanism behind the formation of an alpha case layer, as documented in experiments.

3. The occasional mis-ordering of oxide stability as observed by Saha [150].

Computational predictions of ΔG_r seem to over-estimate the stability of oxides in Ti than what has been observed in experiments. Computational predictions of ΔG_r from the above studies utilise the mass action law to model the energy changes of a reaction. However, some simplification to the complete mass action law was introduced to compensate for the lack of thermodynamic data. Such simplifications can cause inconsistencies in accurately determining free energy change of reactions. In summary, reactions between mould oxides and Ti-alloys pose a serious concern to mould stability and metal purity during casting. Many techniques are available to extent the stability of the mould but a better approach is to select moulds that

exhibit the highest stability. However, in literature all mould oxides have been found to react with Ti-alloys and much of the computational predictions of stability are inconsistent. This underscores the need for a deeper investigation into the problem.

2.6.3 Thermodynamic Behaviour of Alloying Elements and Dissolved Solutes in Ti Melt

2.6.3.1 Thermodynamic Behaviour of Ti and Al in Ti-Al Melt Kostov *et al*.. modelled the chemical activity of titanium and aluminium in a Ti-Al melt using the Factsage database. Figure 45 illustrates the activity diagram for titanium and aluminium in the Ti-Al melt as a function of Ti-Al composition, at 1973 K. On the x-axis, the left end represents pure aluminium, while the right end represents pure titanium. At the pure titanium end, the activity of titanium is 1, whereas at the pure aluminium end, the activity of titanium is always 0. Several assumptions can be made regarding the behaviour of titanium and aluminium in the liquid phase: 1) As the composition of aluminium increases, the reactivity of titanium decreases and vice versa. 2) The activities exhibit negative deviation from ideal behaviour, indicating strong inter-metallic interaction between titanium and aluminium. Since the activity of Ti decreases with increasing Al content the ΔG_r for the reaction should also decrease with increasing Al content. This is illustrated by the Kostov

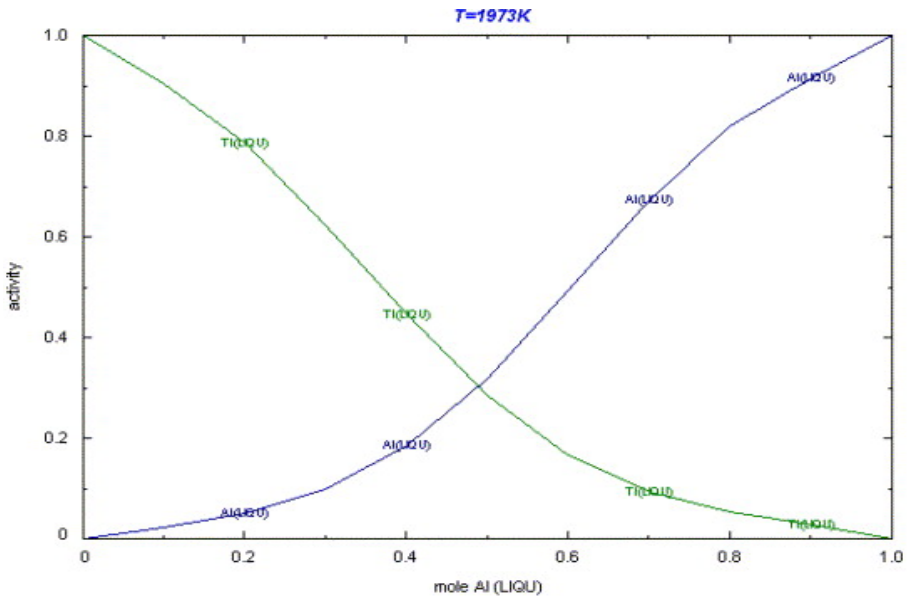

Figure 45: Activity of Ti and Al in Ti-Al melt [27].

model as shown in figure 46 for the dissolution of Al_2O_3 in Ti-Al melt. The significant decrease in chemical activity of Ti can be explained by the presence of inter-metallic phases between Ti and Al. These include gamma-TiAl, Ti_3Al, Ti_2Al etc.

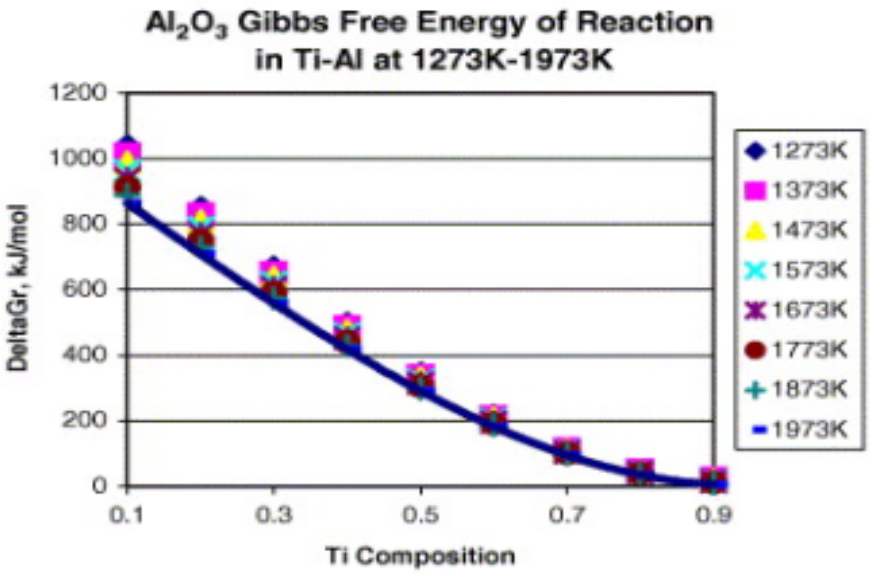

Figure 46: ΔG_r for the dissolution reaction of Al_2O_3 in Ti-Al melt [27].

At higher titanium composition, ΔG_r of the reaction approaches 0, whereas at low titanium composition, the ΔG_r is relatively high. This result suggests that Al_2O_3 is stable at all titanium compositions ranging from 0.1 mol fraction of titanium to 0.9 mol fraction of titanium.

2.6.3.2 Wetting Thermodynamics Studying chemical activities is one method in which the reactivity of an element can be quantified in relation to another alloying element, but it may provide limited insight into the impact it can have on the mould oxide. A well-known method for quantifying the reactivity of a liquid metal in contact with a ceramic substrate is wetting [151]. When a liquid droplet comes into

contact with a solid surface, it can either spread exhibiting wetting behaviour or not spread leading to non-wetting behaviour [151]. When a droplet of liquid sits on a solid surface, it forms an angle with the solid surface known as the contact angle, through which it is possible to deduce the degree of wetting. Many experiments have been conducted to measure the contact angle between liquid and solid substrates using the sessile drop technique, as compiled by Arroyave [30]. The results reveal a clear relationship between oxide dissolution and the contact angle at the ceramic-metal interface, illustrated in figure 47.[30, 29]. The degree of wetting of liquid

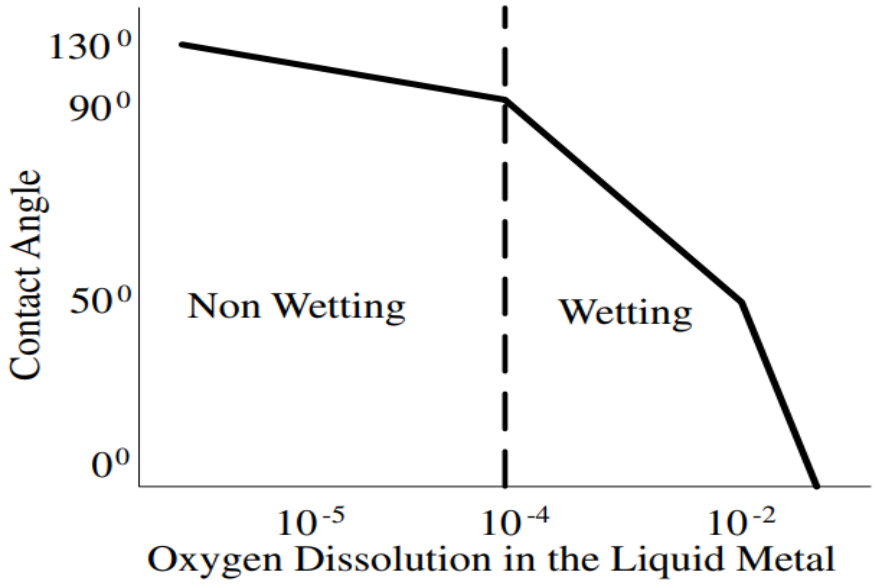

Figure 47: Schematic of experimental compilation by Eustathopoulos *et al.* [29, 30].

metal over a solid substrate can indeed provide valuable information on the extent of a metal-mould reaction. In the regime where non-wetting behaviour is observed,

with a contact angle greater than 90 degrees, is considered a non-reactive region. Conversely, in the regime where wetting is observed, with a contact angle less than 90 degrees, it indicates a reactive region. The transition between wetting and non wetting takes place when oxygen dissolution is greater than 10^{-4} mol fraction. Figure 48 shows the contact angle measured by Li *et al.* for various mould oxides in contact with Ti50Al alloy.

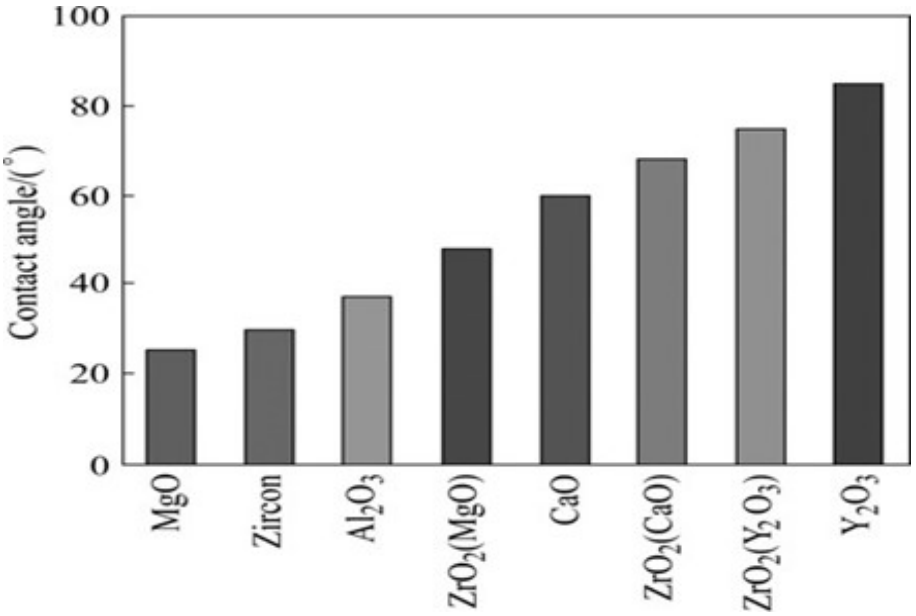

Figure 48: Contact angle between liquid Ti50Al and different mould materials [31].

The results show that all oxides have a contact angle that is less than 90 degrees, indicating that the metal-mould interaction is likely to be reactive. Y_2O_3 has the largest contact angle and therefore, the least reactive whereas, MgO has the smallest contact angle and therefore most reactive. In addition, Wang *et al.* studied the

evolution of contact angle over time for Cu-11Ti alloy on a Al_2O_3 substrate and the results from this study is given in figure 49. The initial contact angle starts at

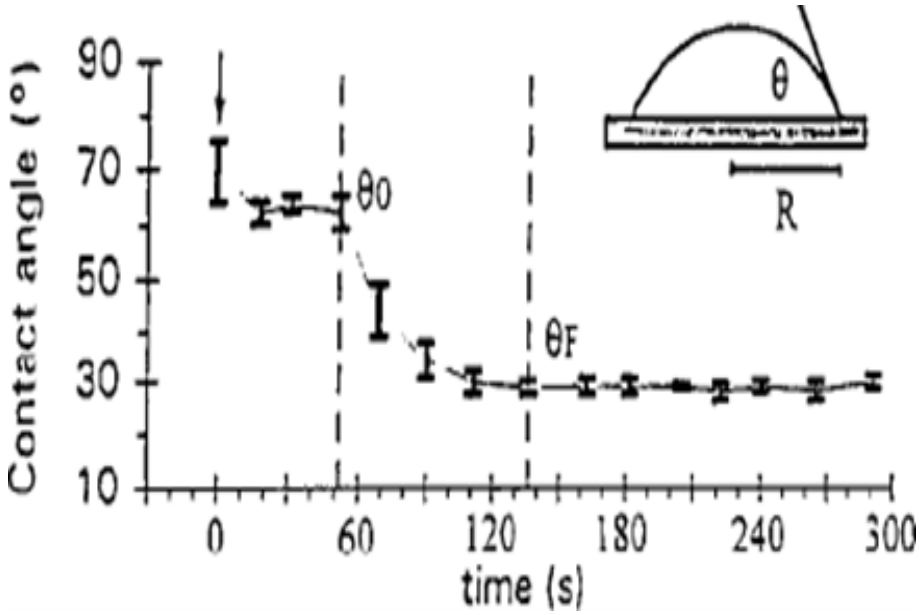

Figure 49: Evolution of contact angle of Cu-11Ti alloy on an Al_2O_3 ceramic substrate [31].

approximately 70 degrees and remains constant for approximately 60 seconds. This behaviour could be attributed to the formation of reaction products at the interface. After 60 seconds, the contact angle rapidly decreases to below 30 degrees, where the equilibrium contact angle is reached. The outcome from these studies show that the Ti-liquid in contact with any oxide ceramic exhibits reactive behaviour, therefore should be treated as a reactive system when undertaking calculations. There are various factors that affect the contact angle formed between the liquid droplet and the substrate such as temperature, alloy composition, atmosphere but for relevancy

will not be discussed in this thesis. Wetting behaviour is much more useful when surface energy of contributions are generally high. These results contrast with the ΔG_r values predicted by formation energies and the Kostov model, which suggest a reactive oxide-metal interaction. It is possible that significant interface contributions drive the reaction towards oxide dissolution. The discrepancies may stem from computational models not accounting for surface energy contributions

2.6.3.3 Thermodynamic Behaviour of Solutes in Ti-Al Melt It is also critical to assess the behaviour of solutes that may be present along with titanium and aluminium. These solutes may originate from the dissolution of oxides into the liquid metal or added as alloying additions to promote specific properties. Understanding how these solutes interact with the titanium-aluminium system and the impact it has on metal-mould reaction is of paramount importance. Yoshinao *et al*.. investigated the interaction between yttrium and oxygen present in a Ti-Al melt resulting from the dissolution of Y_2O_3 into the liquid metal [32]. Figure 50 shows the effect of oxygen has on excess yttrium added to TiAl melt.

The results indicate that as the yttrium composition increases in the melt, the oxygen content decreases significantly. This suggests that yttrium possesses deoxidation properties, which could be valuable for reducing the oxygen content in the metal after the casting process. The results also indicate that at higher temperatures,

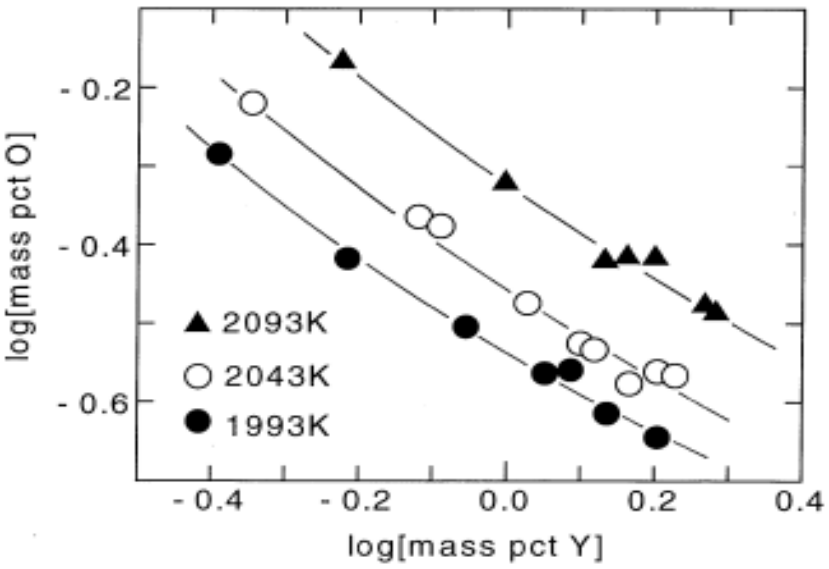

Figure 50: Interaction between Y and O in Ti-Al melt [32]

there is a higher content of oxygen left behind in the melt. This observation is reasonable because a greater dissolution of the oxide is expected at higher temperatures, as the reactivity of titanium will be higher under these conditions. Tsukihashi *et al.* conducted a similar experiment on the dissolution of CaO in a Ti-Al melt and found that calcium is thermodynamically more effective than yttrium for de-oxidation [152]. When selecting oxide materials for casting, it is reasonable to conclude that the type of metal, M, in the oxide (M_xO_y) plays a significant role in determining the activity of oxygen in the liquid. This suggests that oxygen can be removed from the Ti melt by adding excess yttrium or calcium or by using an oxide containing Ca and Y, such as CaO or Y_2O_3. To quantify the behaviour of yttrium-oxygen in Ti melt, Yoshinoa

et al. calulated the interaction parameter between oxygen and yttrium whose results are reported in figure 51. The interaction between Y and O is found to be negative

Solvent	Temperature (K)	Log K	e_Y^O
Ti	1991	−2.14	−0.589
	2042	−1.73	−0.421
	2093	−1.40	−0.377
Ti_3Al	1993	−2.16	−0.478
	2043	−1.81	−0.359
	2093	−1.53	−0.375
TiAl	1793	−4.96	−2.41
	1843	−4.26	−1.32
	1893	−3.74	−0.508

Figure 51: Interaction Coefficient of Y to O [32].

indicating favourable interaction between the two molecules. The attractive forces between the two molecules leads to enhanced mixing behaviour compared to ideal solutions and is the reason for lower oxygen activity as a consequence of increasing yttrium. As temperature increases the interaction parameters approach zero which indicates that yttrium and oxygen behave more ideally at high temperatures.

2.7 Reaction Kinetics

2.7.1 Importance of Reaction Kinetics in Metal-Mould Reactions

In addition to thermodynamics, kinetics of metal-mould reactions are also of paramount importance in modelling metal-mould interaction. The following summary highlights the significant influence of reaction kinetics on the stability of oxides in Ti-Al melt, underscoring the importance of considering kinetics alongside thermodynamics when selecting oxides for casting Ti-alloys.

- Higher the melt temperature, greater the oxygen contamination
- Longer the contact time between the metal and the mould, greater the interaction layer and oxygen contamination
- Type of oxide affects the rate at which the reaction proceeds, determines reaction layer thickness and amount of oxygen contamination
- Alloy composition also affects reaction layer thickness and oxygen contamination
- Reaction layer thickness is observed to increase with melt temperature and holding time

These findings emphasize the multifaceted nature of metal-mould interactions and

highlight the need to consider various factors, including temperature, time, oxide type and alloy composition, when evaluating the stability of oxides in Ti-alloy melt. To quantify these observations, the reaction rate constant (k) is commonly used [153]. The reaction rate constant provides a quantitative measure of the rate at which a reaction occurs by, helping to characterize the kinetics of the metal-mould interaction and its impact on oxide stability. For decades, the rates of chemical reactions have been studied through the rate law given in equation 17 [153], where k is the reaction rate constant and M_xO_y representing the concentration of any oxide.

$$rate = -k[M_xO_y] \tag{17}$$

Kung *et al.* [19], investigated the suitability of MgO, CaO, Al_2O_3, and Y_2O_3 by utilizing small crucibles for the melting and casting of a small quantity of Ti-alloy. Kung documented the impact of holding time on metal oxygen content, penetration distance and microstructure. Figure 52 shows the oxygen content in the melt as a function of time during metal mould contact. Among the studied oxides, Y_2O_3 exhibited the highest kinetic stability, followed by CaO, MgO and Al_2O_3, for a holding time of 60 minutes at 1550°C. This kinetic ranking aligns with the predicted thermodynamic ranking based on the free energy of formation by Backman [136], Kuang [33] and also the Kostov model [27]. Similar kinetic analysis by Tetsui [154], Harding

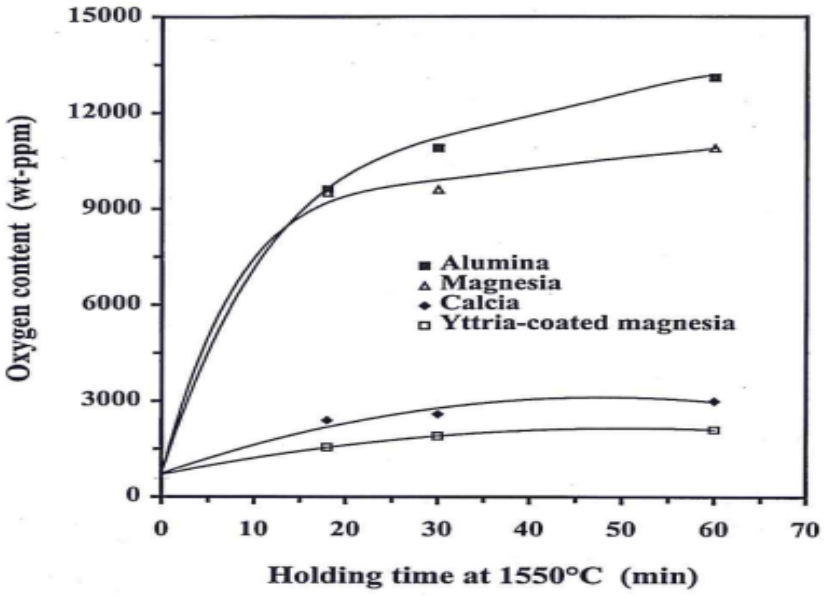

Figure 52: Impact of Holding Time on Oxygen Contamination in the Liquid Melt, Based on Various Oxides. [33]

[21] also confirm the same kinetic ranking.

Studies conducted Cui [28] and Liu [18] have demonstrated that the reaction between oxide and the metal adheres to the Arrhenius law, as depicted in equation 18, where, K_0 is the pre-exponential factor, Q_0 is the activation energy, R is the gas constant and T is temperature. The Arrhenius equation provides an insightful framework for understanding the temperature dependence of reaction rates in chemical processes. Each term within the equation serves a distinct function in showing how temperature influences the rate of a chemical reaction. Below are a description of each term within the equation.

$$k = K_0 \cdot exp(\frac{-Q_0}{RT}) \tag{18}$$

Rate constant (k): Describes the rate at which a chemical reaction occurs. It depends on aspects such as the nature of the reactants, the presence of a catalyst and temperature. **Pre-exponential Factor (K_0)**: Represents the frequency of collisions and orientation of molecules in a chemical reaction that result in a successful reaction. Higher values of A indicate a greater likelihood of successful collisions. **Activation Energy (Q)**: This term represents the minimum energy required for a chemical reaction to occur, as molecules must reach this energy level to overcome the barrier and initiate the reaction. **R and T**: R is used to ensure that all units in the equation are compatible. Temperature (T) affects the reaction rate by increasing the kinetic energy of reactant molecules. Molecules collide more frequently and energetically at higher temperature, thereby increasing the reaction rate.

In the realm of metal mould reactions during casting, the optimal outcome is characterized by the slowest possible dissolution rate of oxides. Therefore, it is imperative for research efforts to concentrate on attaining the lowest achievable reaction rate. These reaction rate constants can also serve as a factor that can be compared with computational rate constants.

2.7.2 Experimental Rate Constants

2.7.2.1 Kinetics From Ficks' First Law Rate constants are critical in determining oxide stability, often proving more important than thermodynamic stability, as oxides that react at the slowest rate are always preferred. They also serve as a bridge between experimental and modelling results, offering a basis for validating models against experimental data. Numerous experimental methods exist for calculating rate constants, some of which are outlined below. R.J. Cui [36], reported the experimental reaction rate constant (k) for Y_2O_3 in Ti–47Al–2Cr–2Nb melt through observing oxygen dissolution in the liquid over time, using Fick's first law given in equation 19 [153]. In this equation, D represents the diffusion coefficient ($mol/m \cdot s$), $\partial C/\partial t$ represents the change in concentration over change in time and ∂x represents the change in distance where diffusion of solute take place.

$$\frac{\partial C}{\partial t} = -D \cdot \frac{\partial C}{\partial x} \tag{19}$$

Equation 19, can be rewritten as equation 20

$$\frac{dC_t}{dt} = -K \cdot \frac{A}{V} \cdot (C_0 - C_s) \tag{20}$$

Here, A represents the interfacial area (m^2) (mould-metal) V is the volume of the melt (m^3), C_t denotes the oxygen concentration in the melt at time t, and C_s is the oxygen saturation concentration in the melt [36]. The rate constant of mass transfer, K, follows an Arrhenius-type expression, as shown in equation 18 [36].

Further integrating equation 20 gives equation 21

$$ln(\frac{C_s - C_0}{C_s - C_t}) = K \cdot \frac{A}{V} \cdot t \tag{21}$$

Renjis experiment [36] involved, a metal with dimensions of 15 mm diameter × 18 mm height was brought into contact with a Y_2O_3 crucible with the dimensions of 20 mm height and a wall thickness of approx. 3.5 mm. Upon interaction, the build-up of oxygen in the liquid melt was measured over time by the inert gas infrared-thermal conductivity technique and the results are shown in figure 53.

The concentrations of oxygen over time can now be substituted for C_t in Equation 21 and can be solved to obtain the rate constant (k). Renji reported rate constants of 6.05, 1.51, and 2.12 for temperatures of 1550 K, 1600 K, and 1650 K, respectively, and the activation energy for the reaction to be 366.8 kJ/mol [36]. A similar study was conducted by Lapin *et al.* [155], who calculated the activation energy for the increase of oxygen content for the Ti–46Al–8Nb alloy to be 412.1 kJ/mol. The increase in activation energy found by Lapin predicted the reaction to be much less intense. One

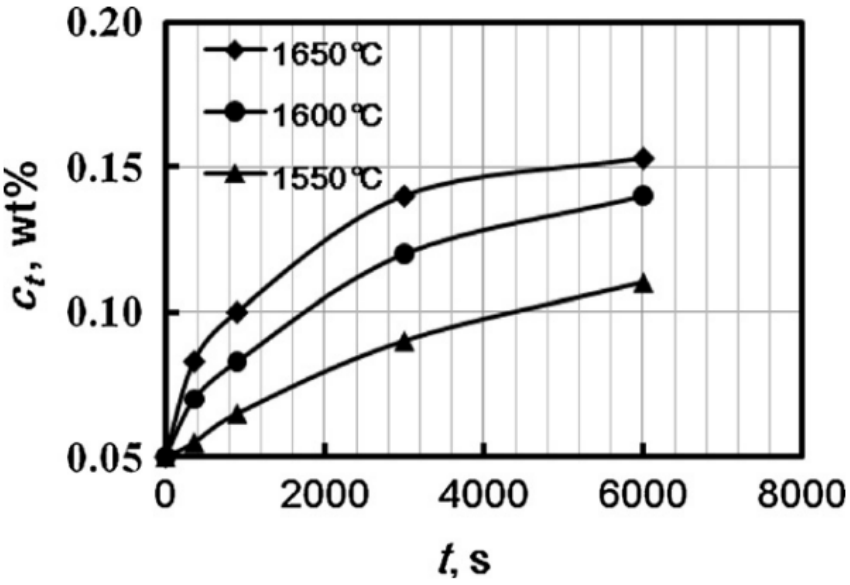

Figure 53: Oxygen concentration build-up in Ti-Al melt in contact with Y_2O_3, measured with inert gas infrared-thermal conductivity technique [28].

possible explanation for such differences between Renji and Lapin can be attributed to the differences in Nb composition in both the experiments. With the increase in Nb, the chemical reactivity of the melts decreases, which directly increases the stability of the Y_2O_3 in contact with the melts, consequently decreasing the alloy contamination, yielding higher activation energy reported by Lapin [36].

2.7.2.2 Kinetics From Reaction Layer Growth In the absence of oxygen dissolution data, Meijia *et al.* reported reaction rate constant by measuring the growth of reaction layer thickness with time for the dissolution of Al_2O_3 in pure Ti.

This is assuming that the rate of growth of reaction later thickness is proportional to the rate of overall reaction. The kinetic equation for reaction layer growth can be describe with equation 22, where d is the thickness of the reaction layer, k is the reaction rate constant described by Arrhenius equation given in equation 18, t is the contact time between the oxide and the melt and n is the exponent.

$$d = kt^n \tag{22}$$

By combining equation 18 and equation 22, Meijia *et al.* obtained the following equation where E is the activation energy.

$$d = K_0 \cdot exp^{(-E/RT)t^n} \tag{23}$$

Then taking the natural log of both sides the following equation can be obtained:

$$ln(d) = -E/RT + nlnt + lnK_0 \tag{24}$$

To work out E and k_0, Meijia plotted the reaction layer thickness with temperature as shown in figure 54.

The slope and intercept of the line are $-E/R$ and $n \ln t + \ln K_0$, allowing calculation of the activation energy E and the pre-exponential factor k_0. For Al_2O_3 dissolution in Ti melt, E is 153.1 kJ/mol and k_0 is 1286.4 m/s^n. These rate constants are useful for validating and comparing computational predictions.

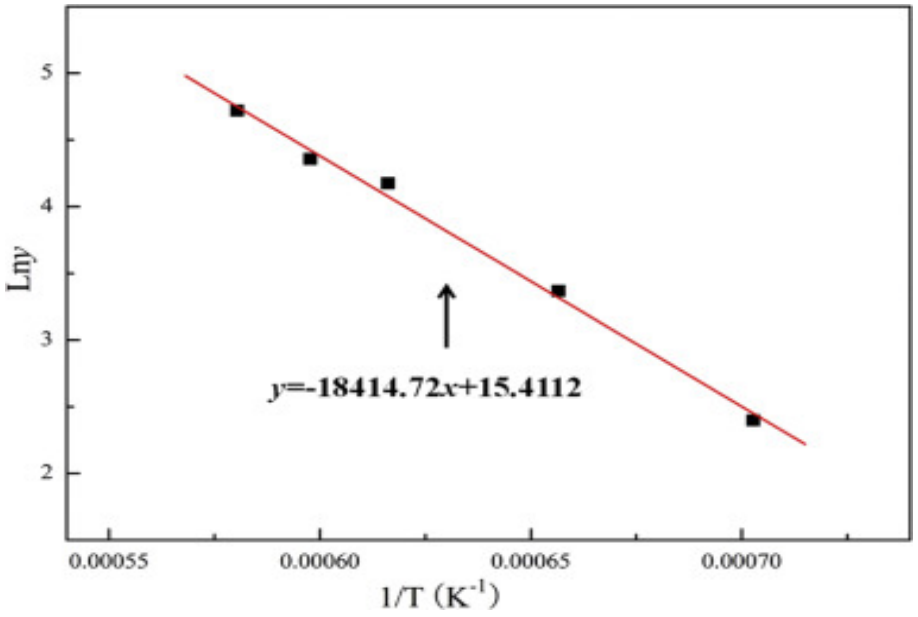

Figure 54: Meijia Plot of reaction layer thickness versus temperature for Al_2O_3 in contact with pure Ti [18].

2.7.2.3 Kinetics From Wetting Dynamics As evaluated in the thermodynamics section, sessile drop experiments can be very useful to study surface interaction of metal and mould. In addition to this, it can also be used to study kinetics of metal-mould interaction. Chen *et al.* [34] studied the kinetics of metal-mould interaction through the spreading behaviour of the metal droplet on a ceramic surface. The spreading rate of a metal droplet on an oxide surface follows Arrhenius law and can be written as shown in equation 25,

$$\frac{dr}{dt} = k \cdot exp^{(\frac{-E}{RT})} \tag{25}$$

where r is diameter of the sessile drop and dr/dt is the rate of sessile drop spreading. Taking the log of both side the following equation can be obtained.

$$ln\frac{dr}{dt} = lnk - exp(\frac{-E}{RT}) \tag{26}$$

Therefore, by plotting the logarithms of dr/dt against (1/T), the metal spreading activation energy was calculated from the slope of the line as shown in figure 55.

Actiavation energy calculated for YB (yttria + 0.15 wt% B_2O_3), YF (yttria + 0.15 wt% YF3), YAZ (Y_2O_3-0.5 wt% Al_2O_3-0.5 wt% ZrO_2) and pure yttria (Y) are 879.6, 397.4, 144.7 and 24.9 kJ/mol respectively. The high activation energies observed for YF 0.15 and YB 0.15 face coats suggest that wetting is primarily driven by interfacial chemical reactions between the metal and shell surface. However, the activation energy of the metal on the shell surface reflects the system's interfacial chemistry more than the strength of the chemical interactions. In other words, while the activation energy reflects the energy barrier associated with the reaction, it does not necessarily quantify the strength or magnitude of the chemical interactions taking place at the interface.

Few other studies have also reported reaction rates between mould oxides and

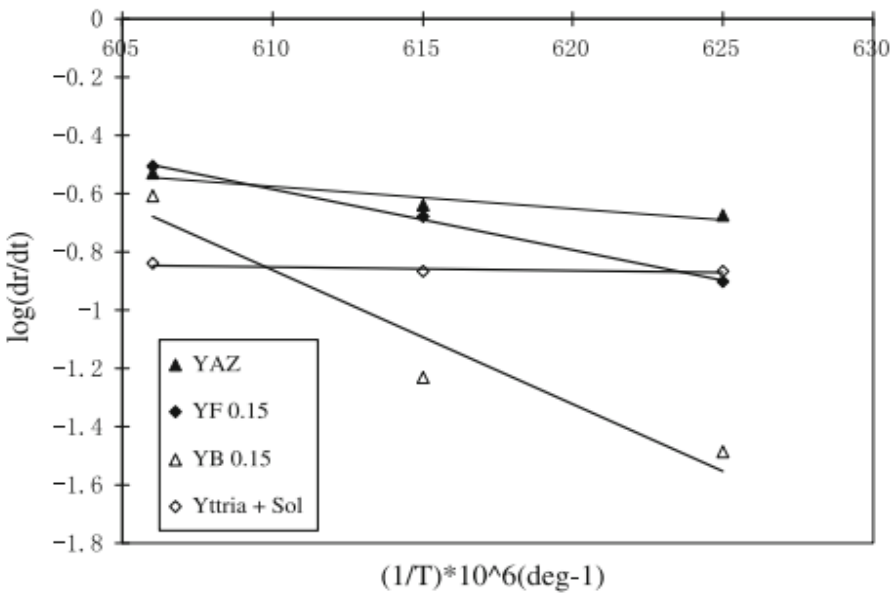

Figure 55: Plot of dr/dt of a Ti-45Al-2Mn-2Nb-0.2B metal droplet YB (yttria + 0.15 wt% B2O3), YF (yttria + 0.15 wt% YF3), YAZ (Y_2O_3-0.5 wt % Al_2O_3-0.5 wt% ZrO2), Pure yttria (Y). Melt dimensions: 6-mm height and 10-mm diameter, placed on the face coat of ceramic plates of dimensions around 2 x 4 x 0.5 cm [34].

liquid titanium [156, 157, 34]. As mentioned earlier experimental studies have reported reaction rate constants based on studies of reaction layer thickness and oxygen composition overtime however, these experiments are often challenging as they have to be conducted at high liquidus temperature. Modelling reaction rates instead will impose less dependency on experiments and offers the liberty of conducting targeted experiments based on modelling results. In this project the kinetics of reaction was also considered for a complete understanding of metal-mould interactions. Since

reaction rates are critical in selecting oxides materials for casting Ti-alloy, a thorough understanding of how reaction rates can be manipulated will allow to develop ceramics that exhibit slower reaction rates.

2.8 Thermodynamic Data

Thermodynamic data form the foundation for accurately predicting the stability of materials and chemical reactions. Various methods are available to calculate key properties such as Gibbs free energy, formation energies, enthalpy, and chemical activities which are essential for studying chemical reactions. The choice of method depends on the specific system being studied and the desired level of accuracy. These methods include First-Principles (Ab Initio) approaches, empirical and semi-empirical models, molecular dynamics simulations, experimental techniques and more recently, machine learning models [158, 159, 160, 161]. Each method offers unique advantages and is selected based on the complexity and precision required for the analysis.

2.8.1 First Principles (Ab-initio) Calculations

First-principles methods, also known as ab initio methods, use quantum mechanical calculations to predict formation energies and other material properties without relying on experimental data [158]. Among these methods, Density Functional Theory (DFT) is one of the most widely utilized techniques, serving as a cornerstone for calculating the electronic structure of materials [162]. DFT enables the estimation of various thermodynamic properties, such as Gibbs free energy, formation energies, chemical potentials and enthalpy, by calculating the total energy of a system and incorporating additional contributions from entropy (vibrational, electronic, and configurational) and pressure-volume work [162]. DFT can also be applied to calculate the formation energies of defects, including vacancies, interstitials, and substitutions. These defects play a crucial role in altering the thermodynamic stability of materials and significantly affect chemical reactions. DFT-derived Gibbs free energy changes (ΔG_r) are particularly valuable for calculating equilibrium constants for chemical reactions across a range of temperatures. This capability is essential for predicting shifts in the equilibrium position of reactions, allowing for the accurate modelling of temperature-dependent processes in materials design.

2.8.2 Empirical and Semi-Empirical Methods

Empirical methods use experimental data to create relationships or models without relying on basic principles. They rely on observations to develop equations. In contrast, semi-empirical methods mix experimental data with theoretical ideas. They often simplify complicated theories by adding empirical parameters based on the data. The CALPHAD (Computer Coupling of Phase Diagrams and Thermochemistry) approach is a semi-emperical method that generates thermodynamic data through a step-by-step process [159]. It starts by gathering experimental data on phase balances and properties like enthalpy, entropy, and Gibbs free energy. Next, suitable models are chosen to explain the Gibbs free energy of each phase, considering both ideal and non-ideal mixing. Numerical techniques are then used to adjust these models based on the collected data, creating a consistent set of thermodynamic parameters stored in databases. Once these parameters are refined, they allow for the calculation of Gibbs energy, which helps predict other thermodynamic properties and phase diagrams by minimizing total Gibbs free energy. Finally, the predicted results are checked against new experimental data to improve the models, ensuring the accuracy of the thermodynamic data produced[98]. The Miedema Model is another example of a semi-empirical model already described in the methods section, commonly used to estimate the formation energies of alloys and intermetallic compounds, particularly

useful for transition metals. However, it has been replaced by newer, more accurate methods like DFT.

2.8.3 Molecular Dynamics

Molecular dynamics (MD) simulations use interatomic potentials, like Lennard-Jones or Embedded Atom Model potentials, to estimate formation energies and free energies by calculating the total energies of atomic arrangements [160]. Ab Initio Molecular Dynamics (AIMD) combines molecular dynamics with quantum mechanics, usually using density functional theory (DFT), to give more precise energy estimates. These are generally restricted to simpler systems like binary and more suited to systems that are closer to ideal behaviour [160].

2.8.4 Experimental Methods

Experimental methods for predicting thermodynamic data involve measuring key properties such as enthalpy, entropy, Gibbs free energy and heat capacity directly from physical systems [161]. Techniques like calorimetry (measuring heat changes during reactions), phase equilibrium studies (observing phase transitions), and electromotive force (EMF) measurements (for determining Gibbs free energy) are commonly used. Additionally, high-temperature experiments, such as Knudsen effusion [163] for vapour pressures and calorimetric methods like differential scanning

calorimetry (DSC) [164], provide critical thermodynamic parameters. Techniques like thermal analysis (e.g., DTA, TGA) and X-ray diffraction (XRD) [165] can be used to identify phase boundaries by tracking the temperature at which phase changes occur. High-Temperature Reaction Calorimetry are used to study reactions at elevated temperatures [166], providing enthalpy and heat capacity data for solid-state systems and high-temperature reaction.

3 Thermodynamics of Reactions

3.1 Method

The first and foremost requirement for identifying appropriate oxide systems is a quantitative measure of thermodynamic stability. Such information will allow to select appropriate oxide materials and prevent unwanted chemical reactions. For any chemical reaction the quantitative measure of thermodynamic stability is determined through the calculation of free energy changes of reaction (ΔG_r). This is based on the principle that any dynamic system is likely to approach an equilibrium state that is lowest in energy. This allows to distinguish between favourable and unfavorable chemical reactions. Calculations of ΔG_r have been in effect for over a century in practices such as combustion, electrochemistry, reduction and oxidation of metals and many more [167, 168, 169]. For many of these applications, it has been pivotal in predicting the equilibrium state of a dynamic system.

For any dissolution reaction as represented by equation 57, a rigorous approach for modelling the free energy changes of reaction (ΔG_r) is through the mass action law given in equation 28.

$$M_xO_y \rightleftharpoons xM + yO \tag{27}$$

$$\Delta G_r = \underbrace{R \cdot T \cdot ln\left(\frac{a^e_{M_xO_y}}{a^e_{O^y} \cdot a^e_{M^x}}\right)} + \overbrace{R \cdot T \cdot ln\left(\frac{a_{O^y} \cdot a_{M^x}}{a_{M_xO_y}}\right)} \tag{28}$$

The first term in equation 28 (bottom bracket) represents the free energy of formation of Al_2O_3 under standard state conditions and the second term (over bracket) accounts for the deviation from standard state condition. All the terms from the first part of the equation remains fixed at all times, whereas the activities of oxygen and aluminium in the second term corresponds to activities in the liquid melt and is the independent variable. The activity of the metal oxide ($a_{M_xO_y}$) is taken to be 1 at all time. The magnitude of ΔG_r provides an indication of the extent of reaction and the sign in front determines the position of the equilibrium. For any reaction the position of the equilibrium is determined by the sign of ΔG_r as described in section 2.6.1.

To implement the mass action law given in equation 28, chemical activities of M and O in the liquid phase are required. Elemental activities are defined as the effective concentration of a species in a solution or simply a measure of degree of presence of a species in a mixture. Activities are measured with a scale ranging from 0 to 1; 1 being pure metal (greatest reactivity) and 0 corresponding to the absence of the element therefore, low or no reactivity. When the activity of an element is 1, it is considered to exhibit ideal behavior described using Raoults law shown in

equation 29. Where, P_A^o is the vapor pressure of Ti, X_A and P^o are the mole fraction and the standard state vapour pressure of Ti respectively. Under ideal conditions the mole fraction of Ti is equal to its activity, under non-standard state the activity of an element is not equal to its mole fraction and is described by equation 30.

$$P_{Ti} = X_{Ti} \cdot P_{Ti}^o \tag{29}$$

$$a_{Ti} = \frac{P_{Ti}}{P_{Ti}^o} \tag{30}$$

Determining elemental activities are highly challenging and very few computational models accurately model elemental activities. Activity data is even more limited for multi-component systems consisting of more than two elements such as in the case of Al_3O_3 in Ti-Al melt. Experimental measurements of activities are extremely sensitive and frequently necessitate the use of extremely sensitive measuring devices. Using Knudsen effusion mass spectrometry, Spathara et al assessed the activity of elements in Ni-based superalloys [170]. Data from such investigations is essential for studying metal oxidation at high temperatures. Equation 31, shows the complexity of obtaining activity data for oxygen, similar equation are also true for metallic elements such as Al, Ti, Y in liquid phase.

Activity coefficient of oxygen ($\gamma(O)$) in Ti-Al-O melt can be derived from interaction parameters (ϵ) as shown in equation 31 [171].

$$ln(\gamma(O)) = (\epsilon_O^O \cdot xO) + (\epsilon_{Ti}^O \cdot xO) + (\epsilon_O^{Ti} \cdot xTi)$$
$$+(\epsilon_{Al}^O \cdot xO) + (\epsilon_O^{Al} \cdot xAl) + (\epsilon_{Al}^{Ti} \cdot xTi) + (\epsilon_{Ti}^{Al} \cdot xAl) \quad (31)$$

The activity coefficient of oxygen is determined by the interactions of oxygen with itself and with each other element in the liquid metal. ϵ_O^O represents the interaction between oxygen-oxygen molecules, ϵ_{Ti}^O represents the interaction of oxygen with Ti, ϵ_O^{Ti} represents the interaction of Ti with oxygen and so on. Few experimental studies have reported interaction parameter for inclusions in liquid Ti [172, 32, 173] however, these methods are not feasible for alloy composition beyond a ternary system. The interaction parameters stated in equation 31 for first order, second and third order interactions could also be considered for even more rigorous estimation of activities. For such reasons activity data predicted by models or through experiments can vary drastically giving varied predictions of ΔG_r. It is possible for activity data from one source to predict a positive ΔG_r value whilst another sources to predict a negative ΔG_r value.

Due to the lack of quality thermodynamic data, various approximations to the mass action law have been devised in the past to reduce the need for rigorous chemical activity data. In the following sections, these approximations was revisited and examined with the intention of comparing and contrasting ΔG_r predictions and the

stability ranking of oxides. As there are many inconsistencies between computational and experimental predictions of stability ranking of oxides, each of the approaches have been compared to experimental ranking established in section 2.5.2 to identify the approach that resembles closely with experimental ranking of oxides. It is also discussed how appropriate activity data for known and unknown alloys/oxide systems can be obtained from various sources. In addition, the impact of data in predicting ΔG_r was also studied.

3.1.1 Sources of Activity Data: Miedema Model

The Miedema model, also known as the Miedema's semi-empirical model, is a theoretical framework used to predict and understand the formation and stability of inter-metallic compounds and alloys. Roelof Miedema [174] developed the model in the late 1970s, and it has since been used in materials science and metallurgy. The Miedema model is based on the concept of 'binary atomic interaction parameters' and uses a semi-empirical approach to calculate the formation enthalpies of intermetallic compounds. It takes into account the electronic and atomic characteristics of the constituent elements in a binary alloy system. The Miedema model is based on the notion of 'binary atomic interaction parameters' and employs a semi-empirical technique to determine intermetallic compound formation enthalpies. It considers

the electrical and atomic properties of the component elements in a binary alloy system. The model proposes that an intermetallic compound's formation enthalpy may be described as a sum of contributions from several atomic interactions. Atomic size mismatch, electronegativity differential, electron concentration, and chemical bonding effects are examples of these interactions. The atomic size mismatch factor accounts for the atomic size variation in the alloy, whereas the electronegativity difference term indicates the variation in electron distribution. The electron concentration notion takes into account the electronic structure and occupation of various energy levels, whereas the chemical bonding term indicates the strength of the connection between the atoms. The Miedema model estimates the formation enthalpy of an intermetallic compounds by combining these components. Once the formation enthalpy is known the activities of elements in the binary system can easily be derived. The working principle of the model and the equations are outlined in the paper by Miedema [174] and [28]. In this study Miedema model was used to calculate the activity of Ti in Ti-Al melt as suggested by R.J Cui [28]. Newer, more accurate models like Density Functional Theory (DFT) are available; however, they require extensive calculations, making them computationally demanding. In contrast, the Miedema model offers a simpler and more efficient approach, providing fast results with a reasonable level of accuracy.

3.1.2 Sources of Activity Data: CALPHAD Data

A more rigorous source of activity data can be calulated from CALPHAD databases. The CALPHAD technique is founded on thermodynamic and statistical mechanics concepts. To construct phase diagrams and thermodynamic characteristics of complicated multi-component systems, it integrates experimental data, such as phase equilibria and thermodynamic parameters, with theoretical models. The CALPHAD technique provides information about the energetic and characteristics of individual phases, as well as the interactions between distinct phases in a material system, through the calculation of free energy of system (G). These databases are then utilised to compute phase diagrams and other thermodynamic features in computational models.

3.1.3 Mass Action Law - Standard State Approximation

As established in the previous section, obtaining non-ideal activities of elements in liquid melt is challenging. In the absence of quality thermodynamic data the stability (ΔG_r) of an oxide can still be studied with the mass action law under standard state conditions (at 2000K, 1 atm pressure). In reference to the mass action law in equation 28, under ideal conditions the non-ideal activities of elements in the second term ($a_O,\ a_M$) (over bracket) can be taken as 1 such that the entire second term

becomes 0. This ensures that ΔG_r is now equal to ΔG_f (Formation Energy) as shown in equation 32. ΔG_f is just the first term of the mass action law (bottom bracket).

$$\Delta G_r = \Delta G_f + 0 \tag{32}$$

Using this approach the stability (ΔG_r) of oxides can be calculated by comparing the free energies of formation of mould oxides to that of Ti-oxides as given in reaction equation 34, the assumption being the dissolution of mould oxides causes the precipitation of Ti-oxide as given in equation 33. M_xO_y represents any mould oxide and Ti_zO_y represents Ti-oxide. If Ti-oxides are more stable than the mould oxides, the mould will react with Ti to form the more stable Ti-oxide and this can be identified using the sign of ΔG_r. A negative ΔGr anticipates the reaction to proceed in the forward direction (with reference to the reaction in equation 33) suggesting the mould oxide is unstable (or Ti-oxide is stable). Whereas, a positive ΔG_r predicts the reverse reaction is favourable therefore, the mould oxide is stable (or Ti-oxide is unstable) and is suitable for casting titanium.

$$M_xO_y + zTi \rightleftharpoons Ti_zO_y + xM \tag{33}$$

$$\Delta G_r^o = \Delta G_f^o(Ti_zO_y) - \Delta G_f^o(M_xO_y) \tag{34}$$

The standard state approximation was applied to calculate ΔG_r of mould oxides including CaO, SiO_2, ZrO_2, Al_2O_3 and Y_2O_3 according to reaction in equation 33. These mould oxides were chosen as they have been found to be least reactive with Ti through literature studies. Ti-oxides including TiO, TiO_2 and Ti_2O_3 was chosen as by-products as their free energy of formation are highly negative (table 6) and therefore, are most likely precipitation products. The likely reactions that could take place for each oxide are given in table 4; all reactions were studied at 2000K with formation energy of oxides obtained from various CALPHAD databases including TCTI3, TCOX11 and TCFE7.

Reactions
$Ti + CaO = TiO + Ca$
$Ti + SiO_2 = TiO_2 + Si$
$Ti + ZrO_2 = TiO_2 + Zr$
$2Ti + Al_2O_3 = Ti_2O_3 + 2Al$
$2Ti + Y_2O_3 = Ti_2O_3 + 2Y$

Table 4: Likely reactions to take place between mould-oxides and Ti-oxides

3.1.4 Mass Action Law - Kostov Approximation

As established earlier, calculating activities of any one component in the liquid phase is highly challenging therefore, some approximations can be made to calculate activities of elements in the liquid phase. One such approximation to the mass action law was implemented by Kostov *et al.* [27] to calculate ΔG_r. Kostov's approximation is shown in equation 35 where, $\Delta G_f(M_xO_y)$ represents the formation energy of any ceramic oxide and $yG_o(Ti - Al)$ represents the free energy of oxygen in Ti-Al melt.

$$\Delta G_r = yG_o(Ti - Al) - \Delta G_f(M_xO_y) \tag{35}$$

The approximation here states: that the dissolution of any oxide is solely dependant on the free energy of oxygen (or oxygen activity) in Ti-Al melt. The free energy of oxygen (G_O) in the liquid phase was calculated from the formation energy of TiO ($\Delta G_f(TiO)$) minus the free energy of titanium (G_{Ti}) in Ti-Al melt as shown in equation 36. The free energy of Ti in Ti-Al melt was calculated with equation 37, where R is the gas constant, T is the temperature in Kelvin and a_{Ti} is the activity of titanium in Ti-Al melt.

$$G_O(Ti - Al) = \Delta G(TiO) - G_{Ti} \tag{36}$$

$$\mu_i = \mu_i^\circ + RT \ln(a_i) \tag{37}$$

The oxide dissolution will take place if the free energy of oxygen (or oxygen activity) in the Ti-Al melt is sufficiently low. At which point, the system will attempt to reach a new equilibrium state through the dissolution of the ceramic oxide to compensate for the imbalance of oxygen potential in the liquid melt. It is at this point where the mould oxide is said to become unstable evident by the change in sign of ΔG_r from positive to negative.

Study by Kostov was replicated in this study at 2000 K, for the dissolution of

oxides including CaO, Al_2O_3, ZrO_2, Y_2O_3 and SiO_2. The methodology is stated below:

- Activity data of Ti in Ti-Al melt was calculated at 2000 K from various CALPHAD databases (TCOX11, TCTI3 and TCFE7), a semi-imperical model developed by Meidema and a Ti-Al-O open database developed by Maria Illastovkakia [35].

- With the obtained activity data, the free energy of Ti in Ti-Al melt was calculated according to equation 37.

- Using free energy of Ti, the free energy of oxygen in Ti-Al melt was calculated according to equation 36.

- Finally, ΔG_r was calculated according to equation 35 as the free energy of oxygen in Ti-Al melt is now known and the $\Delta G_f(M_xO_y)$ of mould oxides were obtained from the same databases as the activity data. For the Miedema model the $\Delta G_f(M_xO_y)$ was taken from the open database (Ilatovskaia, 2017)

3.1.5 Mass Action Law - Modified Kostov Approximation

One of the drawbacks of the Kostov model was the method in which the free energy of oxygen was calculated. Free energy of oxygen was calculated with a reference

oxide (TiO) as shown in equation 36. Using TiO as reference introduces the assumption that a certain amount of oxygen is already present in the melt. For TiO, this corresponds to approximately 0.25 mol fraction of oxygen in Ti-Al melt (according to TCTI3 database at 2000K) because this is the concentration TiO is stable in the liquid melt. Since the equilibrium will only shift to the direction of dissolution if the oxygen content in the melt is sufficiently low, this approximation significantly limits the accuracy of ΔG_r by assuming 0.25 mol fraction of oxygen in already present in the melt. To solve this problem, oxygen free energy must be modified to account for actual concentration of oxygen in the liquid. Ideally, this composition has to be as close to 0.

To get improved predictions from the Kostov approximation, equation 36 was modified to account for actual saturation of oxygen in the melt. This involved adding an excess term to equation to adjust for the oxygen concentration in the melt as shown in equation 38. The way in which the modification was introduced is given below:

- Equation 36 was modified to include an excess energy term as shown in equation 38, to account for the excess free energy contribution from the saturation of oxygen in Ti-Al melt.

- The total free energy of oxygen is now given by equation 38 where, X_O is the actual oxygen concentration in the melt and X_s is the saturation of oxygen as

a result of the reference phase TiO.

- The saturation limit of oxygen was taken to be 0.25 mol fraction as this is the minimum oxygen composition required for TiO phase to be stable in Ti-Al melt.

- X_O was then changed manually from 0.25 to as low as 0.01 in the Ti-Al melt and the predicted ΔG_r was recorded.

$$G_O(Ti - Al) = \Delta G_f(TiO) - G_{Ti}) + RTln(\frac{X_o}{X_s}) \tag{38}$$

The modified equation was then used in the same way as the original Kostov model for the dissolution of CaO, ZrO_2, MgO, SiO_2, Y_2O_3 and Al_2O_3 in Ti-Al melt at 2000 K. The methodology is as follows:

- The activity data of Ti in Ti-Al melt and the solubility of oxygen in Ti-Al melt was calculated at 2000 K from TCTI3 CALPHAD database.

- With the obtained activity data the free energy of Ti in Ti-Al melt was calculated according to equation 37.

- Using free energy of Ti, the free energy of oxygen in Ti-Al melt was calculated according to equation 38.

- Concentration of oxygen was varied from 0.5 mol fraction to as low as 0.01 mol fraction of oxygen depending on the oxide and ΔG_r was recorded for all Ti compositions.

3.1.6 Mass Action Law - CALPHAD Data

A rigorous approach for obtaining realistic activity data is from the CALPHAD databases. CALPHAD databases provide a readily available source of data for multi-component, multi-phase systems. Activity data calculated from these databases can readily be applied to the mass action law to determine free energy changes of reaction without having to make any approximation to the mass action law. The mass action law was applied to the dissolution reaction of CaO, ZrO_2, SiO_2, Y_2O_3 and Al_2O_3. The activity data was obtained from various CALPHAD databases including TCOX11, TCTI3 and TCFE7 and a Ti-Al-O database developed by Maria Illastovkakia. The methodology for Al_2O_3 is stated below, the same it also true for CaO, Al_2O_3, ZrO_2, Y_2O_3 and SiO_2 systems.

- Firstly, a ternary meta-stable phase calculation of the liquid phase containing Ti, Al and O was calculated at 2000 K with the use of Thermo-Calc software whilst, all the other phases was suspended. The databases used include TCOX11, TCTI3 and TCFE7 and a Ti-Al-O database developed by Maria

Illastovkakia [35]. For oxides other than Al_2O_3, Al was replaced with either Zr, Y, Ca or Si depending on the oxide. So, the system remains as a ternary (table 5).

- Following an equilibrium calculation through Thermo-Calc, the non-standard state activities of Al and O in the liquid phase and the formation energy for Al_2O_3 was obtained as input, for the mass action law from each of the databases. For other oxides this was the activities of Zr, Y, Ca or Si instead of Al.

- Al composition was fixed at 0.1, 0.4 and 0.5 mol fraction in the system and Ti and O compositions was varied. ΔG_r was calculated as the composition of Ti and O was varied in the system. For other oxides the fixed compositions are given in table 5. These metallic compositions were specifically chosen so that the change in ΔG_r sign can be observed clearly.

System	Fixed Metal Composition in Liquid Melt
Ti, Al, O	Al: 0.1, 0.4, 0.5
Ti, Zr, O	Zr: 0.2, 0.4, 0.6
Ti, Ca, O	Ca: 0.4, 0.6
Ti, Y, O	Y: 0.2, 0.4, 0.6
Ti, Si, O	Si: 0.2, 0.4, 0.5

Table 5: Shows the ternary system chosen to calculate ΔG_r. For each system the composition of Zr, Y, Ca and Si was fixed and the Ti and O compositions were varied in the system.

3.2 Results

3.2.1 Comparison of Activity Data from Various Sources

Figure 56 presents the activity data for Ti as a function of Ti-Al composition, calculated through various sources. The left end of the x-axis represents pure Al, while the right end corresponds to pure Ti. At the pure Ti end, the activity of Ti is 1, and at the pure Al end, the activity of Ti is 0. Under ideal conditions, the activity of Ti follows Raoult's Law, as shown in equation 29.

Several general trends in the activity diagram remain consistent across different data sources, allowing for key observations to be made. First, the activity of Ti exhibits a pronounced negative deviation from ideal behaviour with the addition of Al. The extent of this deviation varies with Ti-Al composition, creating a characteristic 'S-shaped' curve. As the system becomes saturated with Al, the activity of Ti meaning the reactivity of Ti is reduced. At low Ti compositions, the deviation from ideal behaviour is most pronounced. However, as the Ti content increases, its activity gradually approaches ideal behaviour. Despite these general trends, some variations in activity data exist depending on the data source. For example, the Ti-Al-O database by Ilatovskaia predicts a larger deviation from ideal behavior, while the TCOX11 and TCFE7 databases show relatively similar activity values. The Miedema model, in contrast, predicts higher activity values, suggesting behavior closer to ideal condi-

tions. Notably, the Miedema model shows a small positive deviation at around 0.8 mol fraction of Ti, which is absent in the other systems.

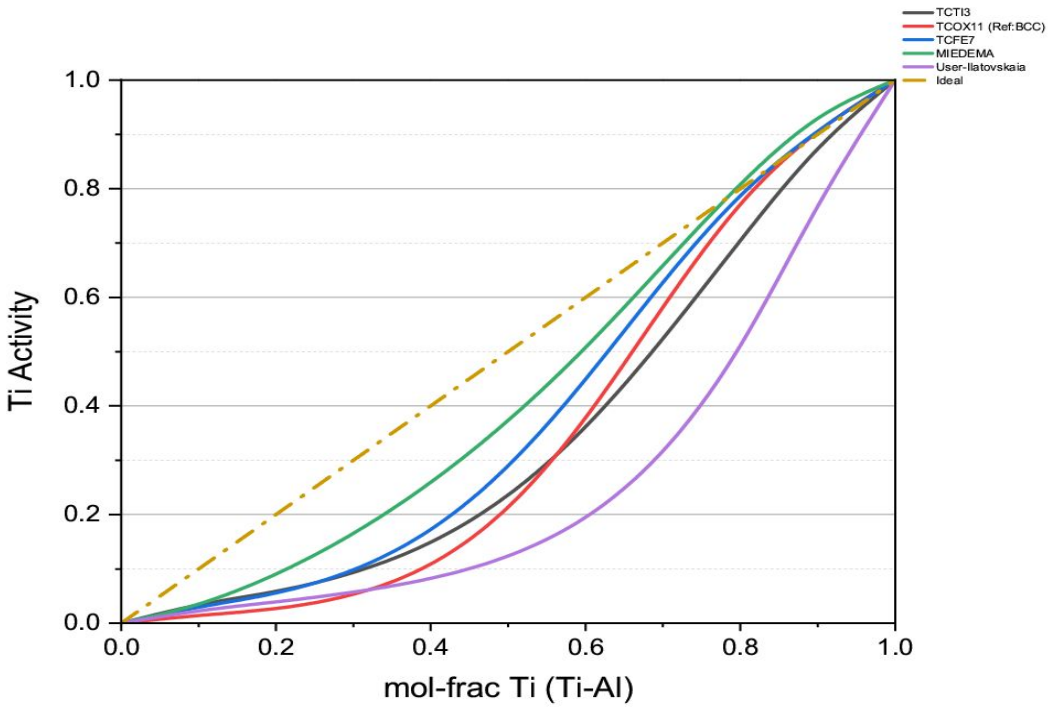

Figure 56: Activity of Ti in Ti-Al melt as a function of Ti mol fraction at 2000K, calculated from five different sources

3.2.2 Mass Action Law - Standard State Approximation Results

Table 6 lists the formation energies of oxides, including CaO, SiO_2, ZrO_2, Al_2O_3, and Y_2O_3, at 2000 K from various databases. The formation energies from TCOX11 and TCFE7 are generally in close agreement, though notable differences arise when compared with the TCTI3 database. The TCTI3 database predicts more negative formation energies, indicating a much higher stability for these oxides. Among the

mould oxides, Y_2O_3 exhibits the most negative free energy of formation, while SiO_2 has the least. Similarly, for the reaction products, Ti_2O_3 shows the most negative free energy of formation, whereas TiO shows the least.

Oxide	TCOX11 (ΔG_f)	TCTI3 (ΔG_f)	TCFE7 (ΔG_f)	User-Ilatovskaia (2017) (ΔG_f)
CaO	-420.127	-	-420.246	
SiO_2	-550.450	-610.719	-550.708	-
ZrO_2	-726.163	-785.438	-726.402	
Al_2O_3	-1033.254	-1123.835	-1033.692	-1033.878
Y_2O_3	-1362.640	-1453.015	-	
TiO	-344.839	-377.452	-347.446	
TiO_2	-568.006	-568.139	-560.631	-
Ti_2O_3	-996.549	-1052.640	-962.623	

Table 6: Free Energy of Formation of Oxides ((ΔG_f)) (kJ/mol) caluclated by various databases at 2000K

Table 7 lists the ΔG_r values for reactions involving mould oxides and Ti-oxides, with data sourced from Table 6. With the exception of SiO_2, all oxides are predicted to have a positive ΔG_r, indicating they are stable for casting titanium. They have been identified to be stable because no titanium oxides are expected to form upon

metal-mould contact. However, in the case of SiO_2, a displacement reaction is likely to occur, forming the more stable TiO_2 at the expense of SiO_2. Although data from the TCTI3 database suggest that SiO_2 may remain stable due to its positive ΔG_r, this highlights a case where oxide selection could suffer from inaccuracies and/or disagreements due to differences in thermodynamic data.

Reaction	TCTI3 (ΔG_r)	TCOX11 (ΔG_r)	TCFE7 (ΔG_r)
$Ti + CaO = TiO + Ca$	-	75.288	72.801
$Ti + SiO_2 = TiO_2 + Si$	42.580	-17.555	-9.924
$Ti + ZrO_2 = TiO_2 + Zr$	217.299	158.158	165.770
$2Ti + Al_2O_3 = Ti_2O_3 + 2Al$	71.195	36.705	71.069
$2Ti + Y_2O_3 = Ti_2O_3 + 2Y$	400.375	366.091	-

Table 7: Free energy change of reaction (kJ/mol) calculated from formation energy at 2000 K for various oxides from three different databases

According to ΔG_r predictions from the three databases, Y_2O_3 is the most stable oxide for casting titanium, followed by ZrO_2, CaO, Al_2O_3, and SiO_2. This ranking closely aligns with the experimental results in section 2.5.2, although ZrO_2 is predicted to be more stable than CaO. While the TCTI3 database suggests that SiO_2 is unstable, its ranking is consistent with the predictions from the other two databases.

Stability ranking based on free energy of formation:

$$Y_2O_3 > ZrO_2 > CaO > Al_2O_3 > SiO_2$$

3.2.3 Mass Action Law - Kostov Approximation Results

Figure 57 presents the findings from the Kostov approximation, where the free energy change of reaction (ΔG_r) is shown on the y-axis and the mol fraction of Ti in the Ti-Al melt is plotted on the x-axis. The left end of the x-axis represents pure aluminum, while the right end represents pure titanium. Several key observations can be drawn from all the results. First, as the Ti content in the Ti-Al melt increases, ΔG_r decreases, indicating that the mould becomes progressively less stable with higher Ti content. The addition of Al significantly reduces the activity/reactivity of Ti, resulting in higher ΔG_r values. This observation aligns with figure 56, where the addition of Al is shown to lower titanium's activity substantially. Consequently, mould oxides are expected to become more stable as the Al content in the melt increases. The decrease in ΔG_r as Ti composition rises follows a parabolic trend, with the largest reduction occurring at higher Ti compositions, while the rate of decrease slows as Al content increases. Except for SiO_2, all other oxides are predicted to remain stable across all Ti compositions, as reflected by their positive free energy change of reaction. SiO_2 remains stable up to a 0.7 mol fraction of Ti but becomes increasingly unstable at higher Ti compositions. However, the TCTI3 database predicts SiO_2 to remain stable up to a 0.8 mol fraction of Ti.

The results originally published by Kostov were largely unaffected by the findings

replicated in this study, affirming that all oxides remain stable regardless of the different data sources used. The differences in these results primarily arise in the magnitude of ΔG_r; for instance, ΔG_r calculated using the Miedema model predicted much lower values compared to those from the CALPHAD databases. This trend aligns with the activity data shown in figure 56, where the Miedema model predicts the highest activities for titanium, resulting in lower ΔG_r values, while the TCTI3 database predicts lower activities for Ti, leading to higher ΔG_r values. The results seem to indicate that the high stability predicted by Kostov is not due to the lack of quality thermodynamic data.

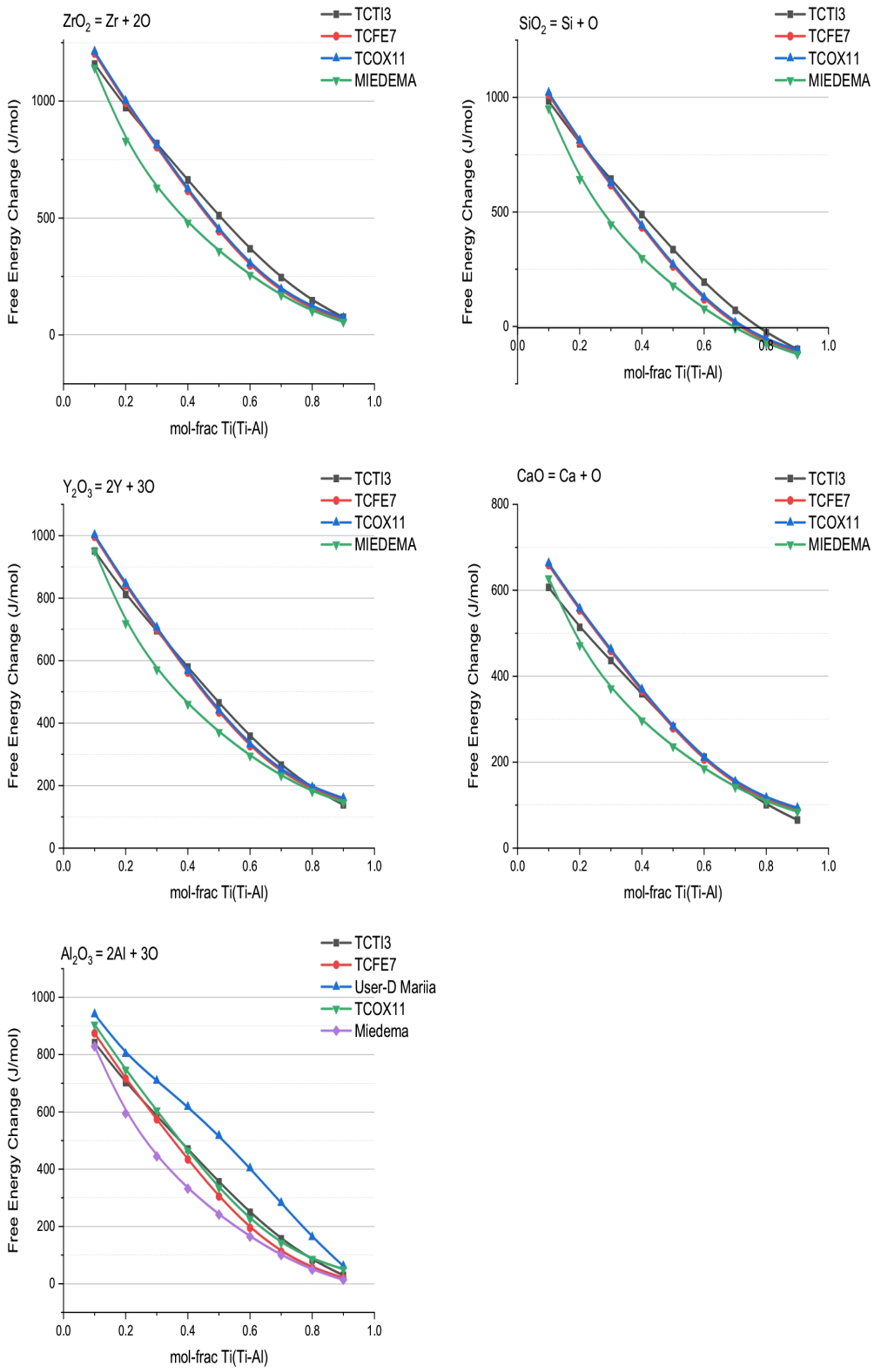

Figure 57: Kostov approximation predicting ΔG_r, replicated with data from various CALPHAD databases and Miedema model at (2000K) for oxides including ZrO_2, SiO_2, Y_2O_3, CaO and Al_2O_3

The stability ranking from Kostov approximation is in agreement with the ranking established through formation energy. ZrO_2 is again predicted to be more stable than CaO contrary to the experimental ranking established in section 2.5.2.

The stability ranking established by Kostov approximation:

$$Y_2O_3 > ZrO_2 > CaO > Al_2O_3 > SiO_2$$

Results in figure 57 is reproduced in figure 58 with each figure representing ΔG_r for different oxides from the same database. The stability of oxides overlap as the composition of Ti changes. At certain composition of Ti, particular oxides seems to exhibit higher stability than others. For instance, at low Ti composition ZrO_2 is predicted to be the most stable oxide. At higher composition of Ti close to 0.8 mol fraction Y_2O_3 is predicted to be the most stable oxide. Some overlapping of reaction lines are observed as shown in figure 58, stating that at certain Ti composition the stability of oxides may vary. For instance, results from TCTI3 database shows that SiO_2 is more stable at lower Ti-compositions (at about 0.1 mol fraction of Ti) than CaO and Al_2O_3 but as Ti composition increases and reaches around 0.8 mol fraction of Ti, SiO_2 is the least stable oxide. Showing that stability of oxides vary depending on the composition of the alloy. The overall trend predicted by each database for each oxide is similar. These results show that oxide stability may vary depending on Ti-composition. Though ZrO_2 is predicted to be the most stable at high Ti

composition, it becomes less stable than Y_2O_3 at low Ti composition.

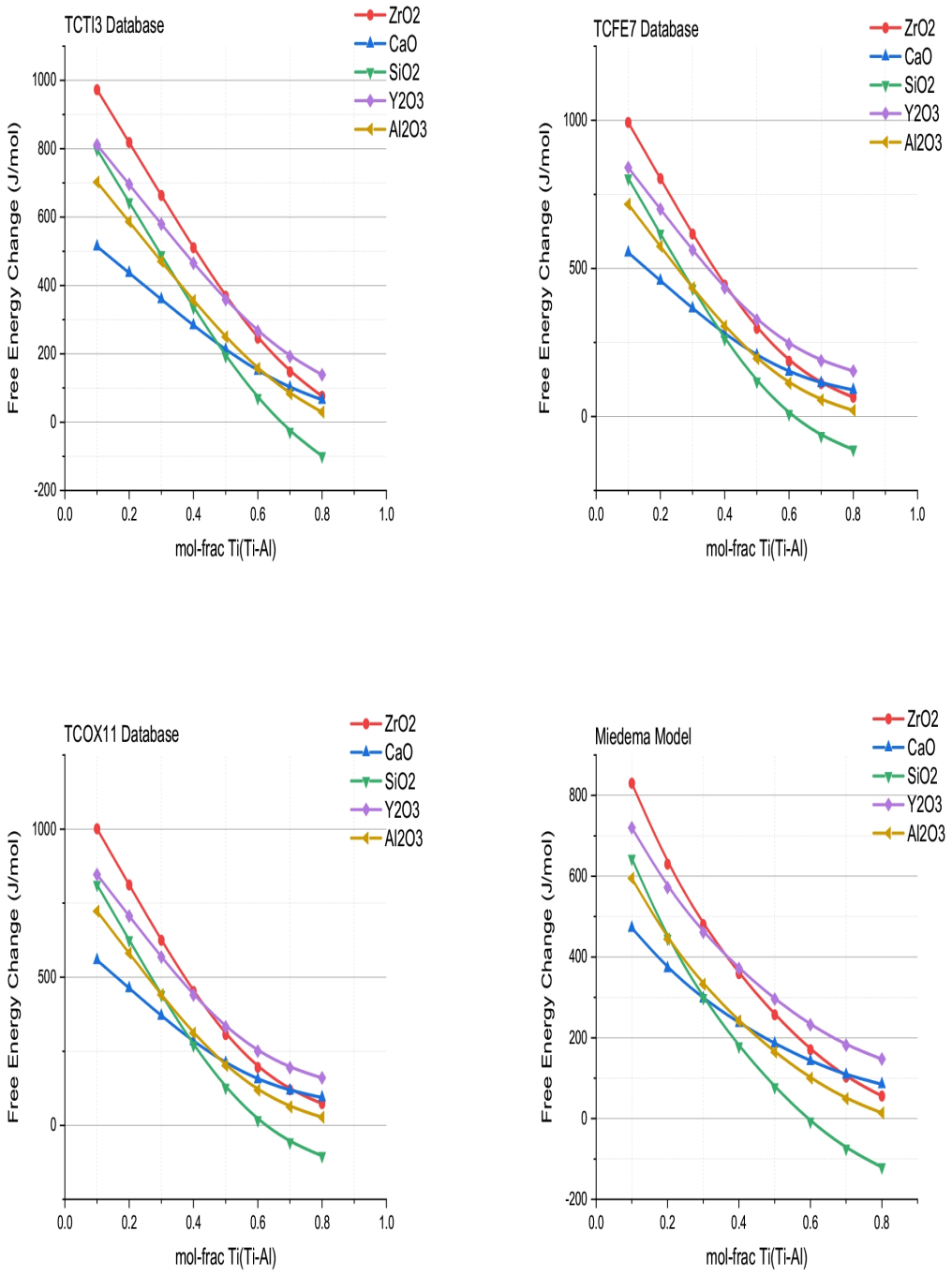

Figure 58: Kostov approximation - Comparison of the ΔG_r of different oxides calculated with data from respective databases

3.2.4 Kostov Approximation: Oxygen Activity

Figure 59 shows the free energy of oxygen as predicted by Kostov, while figure 60 presents the corresponding oxygen activity in the liquid. The x mark in both figures represents the dissolution point of SiO_2, where the sign of ΔG_r changes from positive to negative, as shown in figure 57. The mark indicates that the oxygen content in the liquid must be sufficiently low for the oxide to become unstable. Among the oxides studied, only SiO_2 becomes unstable due to the low enough oxygen activity in the liquid to destabilize it. Interestingly, both the predicted oxygen free energy and the corresponding oxygen activity in the liquid are significantly higher than expected. Since the dissolution of oxides only occurs when oxygen activity is low in the melt, the ΔG_r values for all reactions remain extremely high. This suggests that the approximation used to predict oxygen free energy may be inaccurate. It appears that the high ΔG_r values predicted by the Kostov model may not be due to poor thermodynamic data but rather to the approximations used in calculating oxygen activity. More realistic oxygen activity data could have a substantial impact on the results.

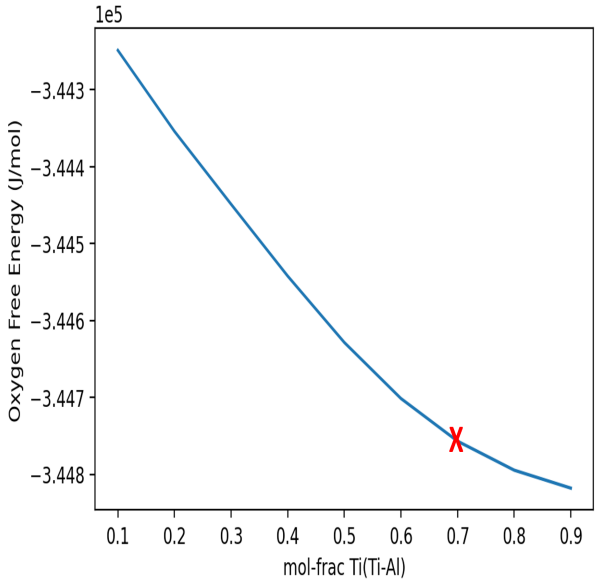

Figure 59: Free energy of oxygen in Ti-Al melt predicted by Kostov model

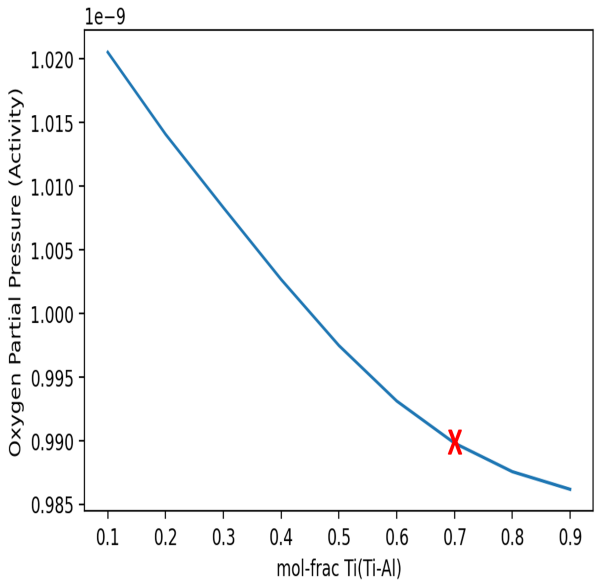

Figure 60: Activity of oxygen in Ti-Al melt as predicted by Kostov

3.2.5 Mass Action Law - Modified Kostov Approximation Results

Accounting for the solubility of oxygen in the Kostov approximation had a substantial impact on the magnitude and sign of ΔG_r as shown in figure 61. The results demonstrates that if the oxygen content in the melt is sufficiently lowered, all oxides are subject to instability, at which point the free energy change curve crosses the x-axis as shown in figure 61. This intersection reflects the minimal oxygen activity necessary for an oxide to be stable; below which the oxide will begin to dissolute. This is observed to be different for each oxide. The dissolution of Y_2O_3 is observed at 0.8 mol fraction of Ti and at fixed oxygen composition in the melt of 0.1 mol fraction. Stating that Y_2O_3 is stable up-to 0.8 mol fraction of Ti with an oxygen composition of 0.1 mol fraction. Beyond 0.8 mol fraction of Ti the oxygen activity becomes too low, causing the equilibrium to favour dissolution. The dissolution will continue until the activity of oxygen in both phases (liquid and the oxide) is in equilibrium with each other. Similar conclusions can be drawn from other graphs.

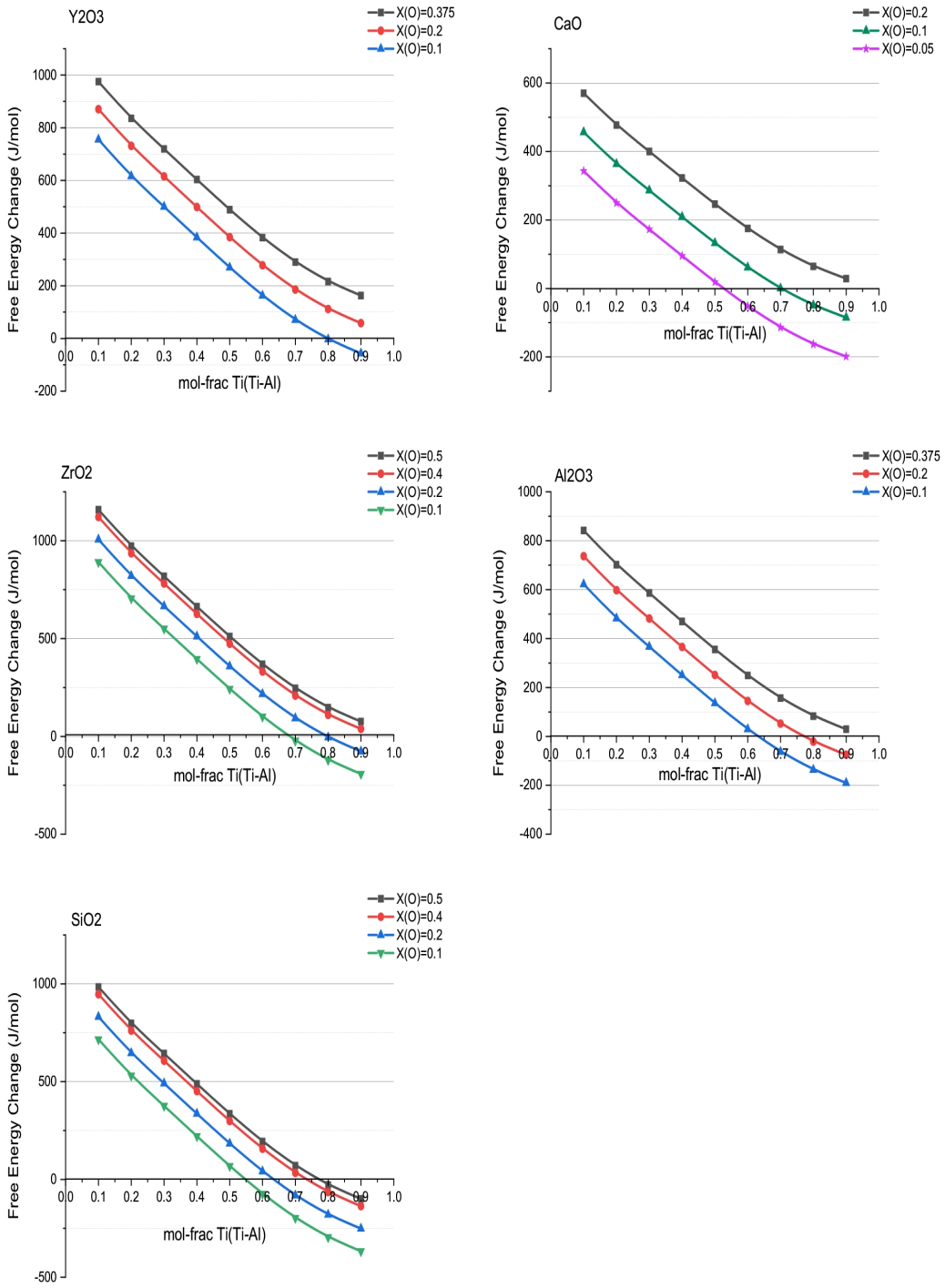

Figure 61: Modified Kostov approximation predicting ΔG_r for oxides including Y_2O_3, CaO, ZrO_2, Al_2O_3 and SiO_2. Data obtained from TCTI3 database at (2000 K)

Stability Ranking for the Modified Model:

$$Y_2O_3 > CaO > ZrO_2 > Al_2O_3 > SiO_2$$

Y_2O_3 has been observed to be the most stable since, the dissolution only occurs at 0.8 mol fraction of Ti with an oxygen composition as low as 0.1 mol fraction in the melt. SiO_2 is the least stable since, the dissolution of SiO_2 is predicted to occur at 0.6 mol fraction of Ti for an oxygen content of 0.1 mol fraction in the melt. This approximation predicts CaO to be more stable than ZrO_2 (although the stability of both are almost identical) which is in agreement with experimental ranking, whereas the original Kostov model and formation energies predicted the opposite.

3.2.6 Mass Action Law - Complete Treatment Results

The meta-stable phase diagram of the liquid phase is shown in figure 62 and the meta-stable phase diagram of both the liquid and the corundum phase (Al_2O_3) at 2000 K is shown in 63. Figure 63 clearly shows separation of two regions where Al_2O_3 (corundum phase) is present (stable) and the other region where the oxide is absent (unstable). From which it is clear that Al_2O_3 is not stable at all composition of Ti compositions. This information was then replicated quantitatively using the mass action law which yields ΔG_r. The same approach was also applied to other oxides under consideration (CaO, Y_2O_3, SiO_2, ZrO_2) with data taken from four different databases. The results are reported in figures 64 to 68.

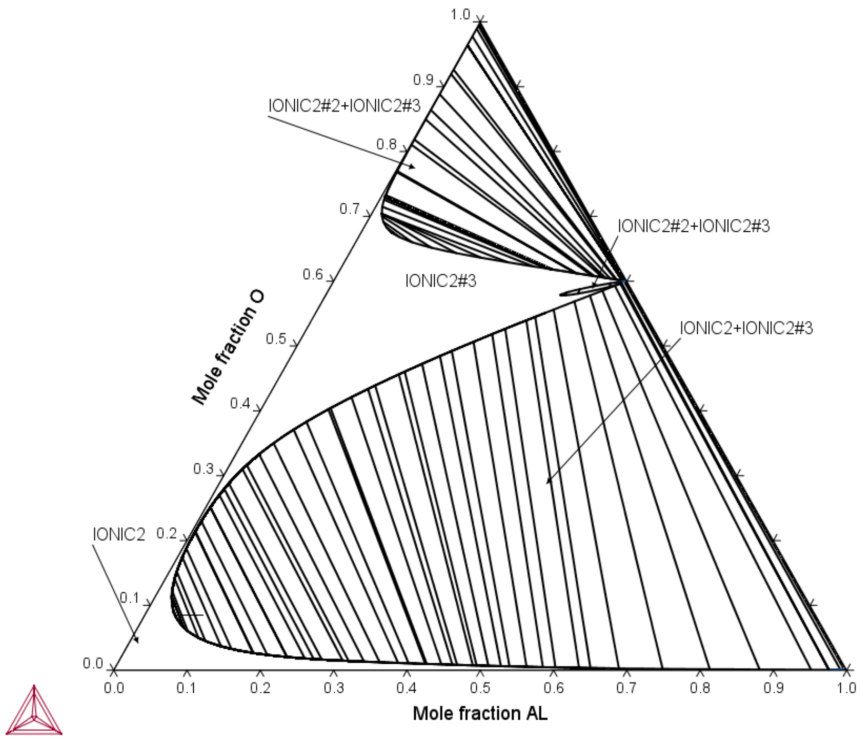

Figure 62: Meta-stable liquid Phase Diagram of Ti-Al-O system at 2000K, only the liquid phase is stabilised and all other phases are suspended. Data from Ilatovskaia 2017 [35]

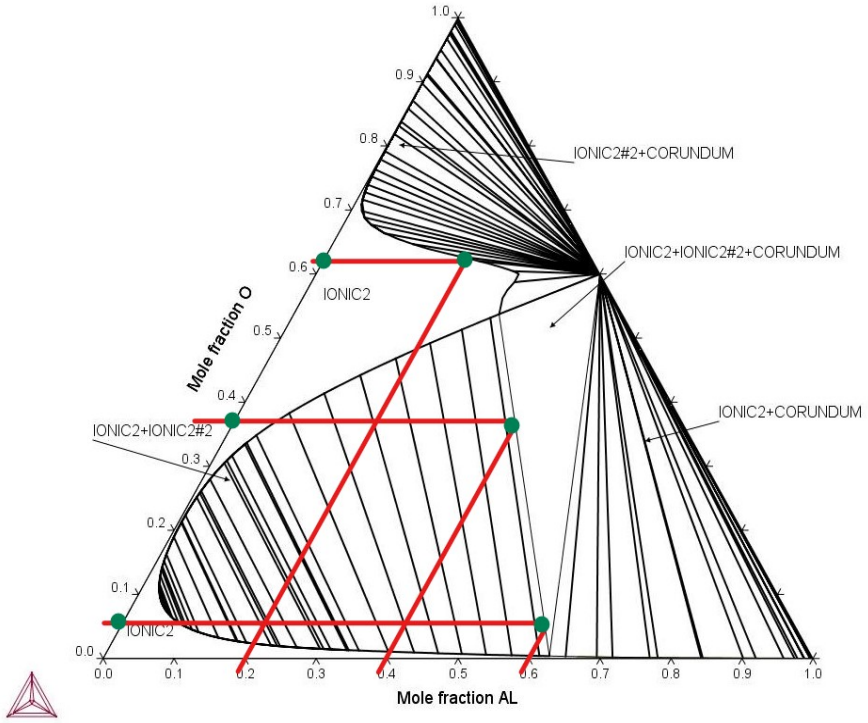

Figure 63: Meta-stable liquid-Al_2O_3 Diagram of Ti-Al-O system at 2000K, only the liquid and Al_2O_3 phases are stabilised and all other phases suspended. Data from Ilatovskaia 2017 [35]

Figures from 64 to 68 shows the calculations from the of the mass action law calculated with CALPHAD data. The results show that all oxides are prone to dissolution at certain Ti mol fraction. This is usually when the mol fraction of Ti is high and the oxygen composition is low in the melt. The point where the x-axis is intersected by the ΔG_r curve, corresponds to a ΔG_r value of 0. It also indicates the minimum composition of oxygen required in the Ti melt before the equilibrium shifts to the direction of dissolution. Oxide in equilibrium with the least amount of oxygen is considered to be the most stable. From the results shown in figure 64 to 68, the oxide in equilibrium with a minimal amount of oxygen is Y_2O_3 followed by CaO, ZrO_2, Al_2O_3 and SiO_2.

Stability Ranking from Complete Treatment of Mass Action Law - CALPHAD Data :

$$Y_2O_3 > CaO > ZrO_2 > Al_2O_3 > SiO_2$$

Taking Al_2O_3 as an example, the x-intersect from in figure 64 (a) can also be located on the meta-stable phase diagram in figure 63. The x-intersection is the red line marked in figure 63. Any composition to the right of the red line corresponds to a positive ΔG_r value and any composition to the left of the diagram corresponds to negative ΔG_r value. Any composition that falls on the red line corresponds to a ΔG_r value of 0. Casting an alloy with Ti-60 and Al-40 using Al_2O_3, needs around 0.35 mole fraction of oxygen in the Ti-Al melt for the Al_2O_3 to be stable in the melt. Any oxygen content less than this value promotes oxide dissolution. This observation is also true for the other oxides.

The minimal oxygen concentration required for Al_2O_3 to be stable decreases as the Al content increases from 0.2 to 0.6 mol fraction as demonstrated in figure 64. A similar pattern is also observed for CaO and ZrO_2 although the Al is replaced by Ca and Zr in Ti melt. Overall stability ranking of each of the mass action approach is summarised in table 5.

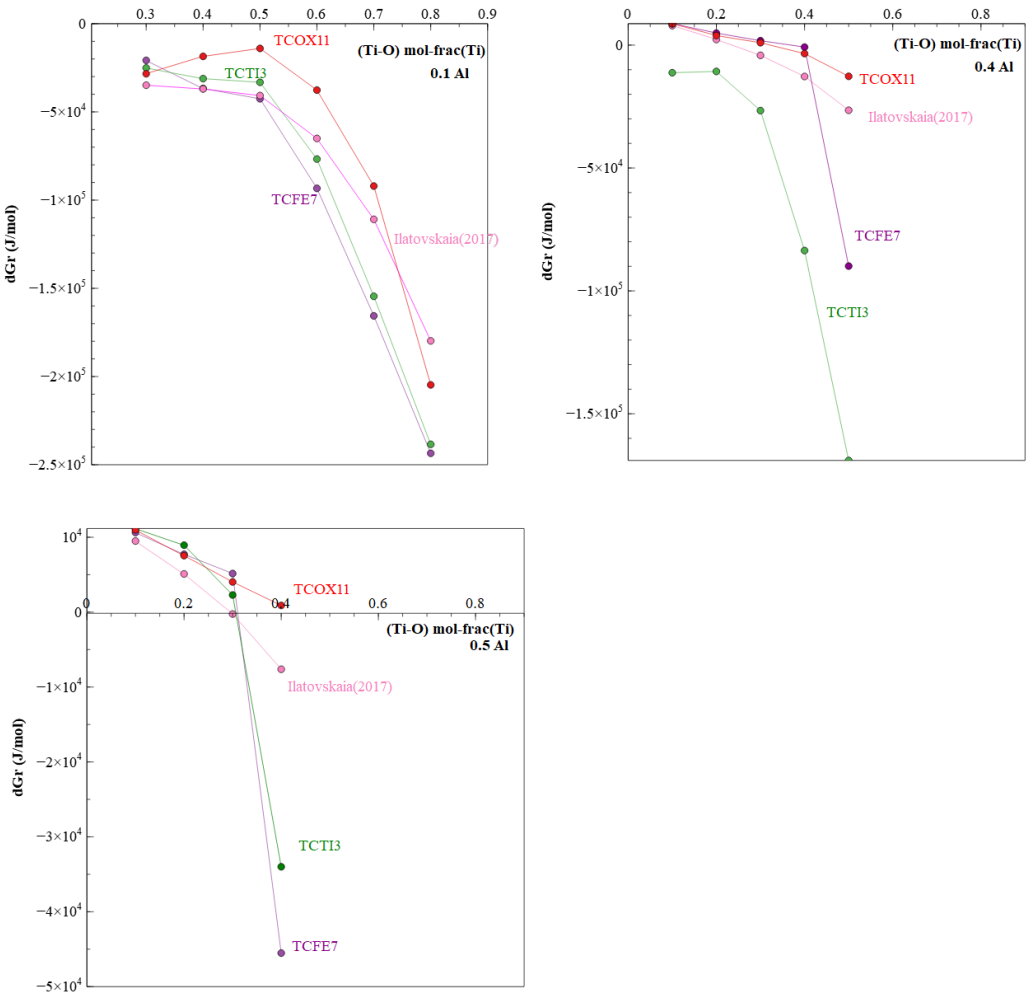

Figure 64: Calculated ΔG_r for Al_2O_3 in Ti-Al-O melt, predicted through the mass action law with activity data taken from various databases at 2000K, figures (a), (b) and (c) shows a fixed mol fraction of Al in the melt at 0.1, 0.4 and 0.5 respectively whilst Ti and O mol fraction are varied in the melt

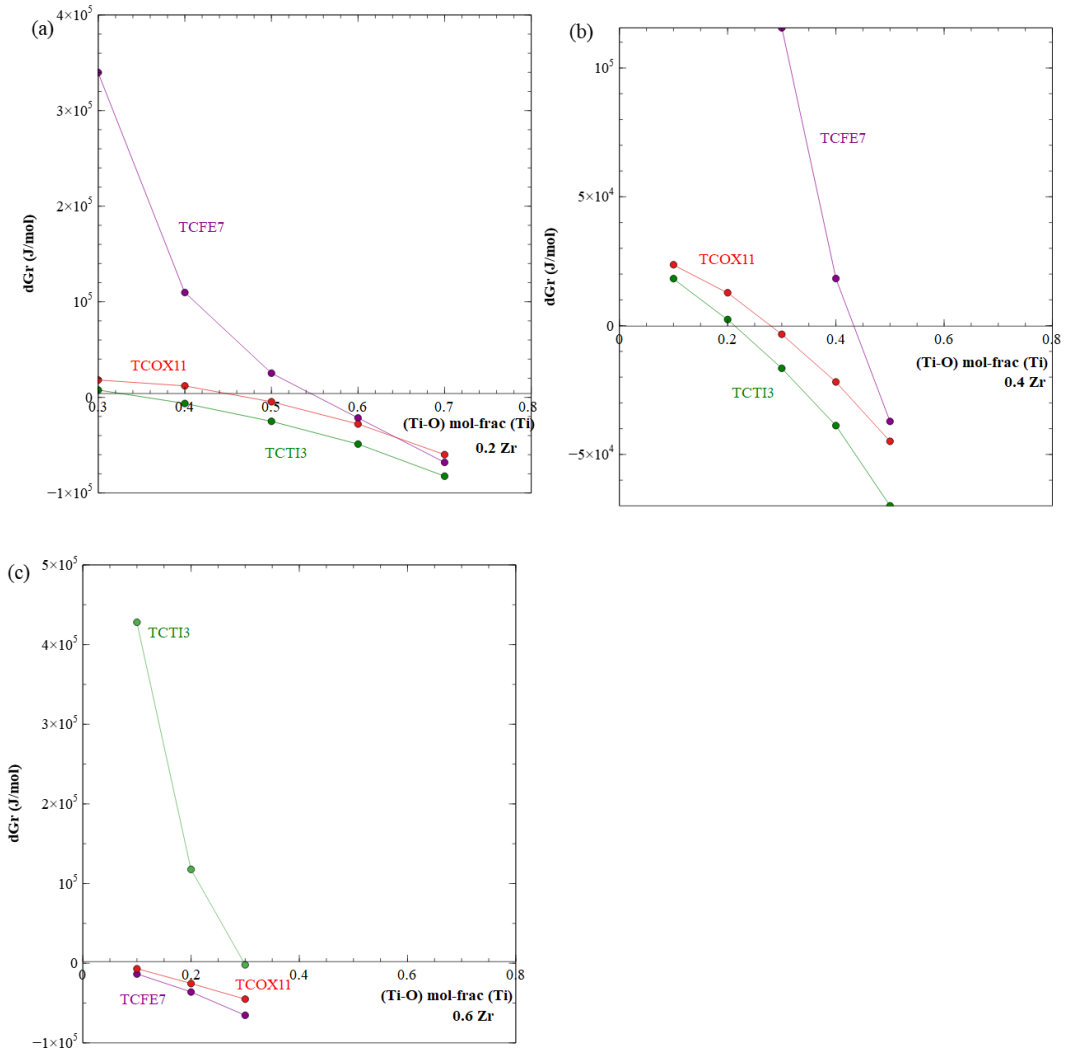

Figure 65: Calculated ΔG_r for ZrO_2 in Ti-Zr-O melt, predicted through the mass action law with activity data taken from various databases at 2000K, figures (a), (b) and (c) shows a fixed mol fraction of Zr in the melt at 0.2, 0.4 and 0.6 respectively whilst Ti and O mol fraction are varied in the melt

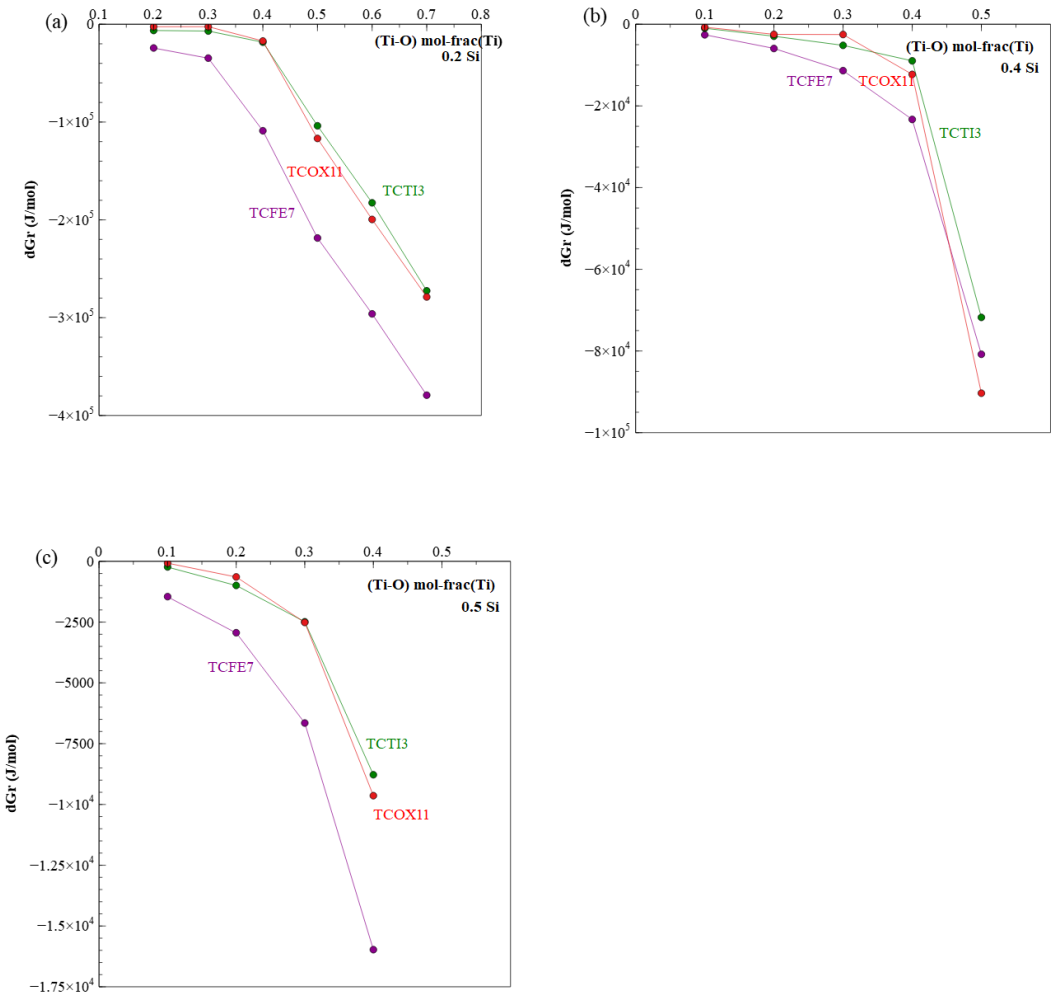

Figure 66: Calulated ΔG_r for SiO_2 in Ti-Si-O melt, predicted through the mass action law with activity data taken from various databases at 2000K, figures (a), (b) and (c) shows a fixed mol fraction of Si in the melt at 0.2, 0.4 and 0.5 respectively whilst Ti and O mol fraction are varied in the melt

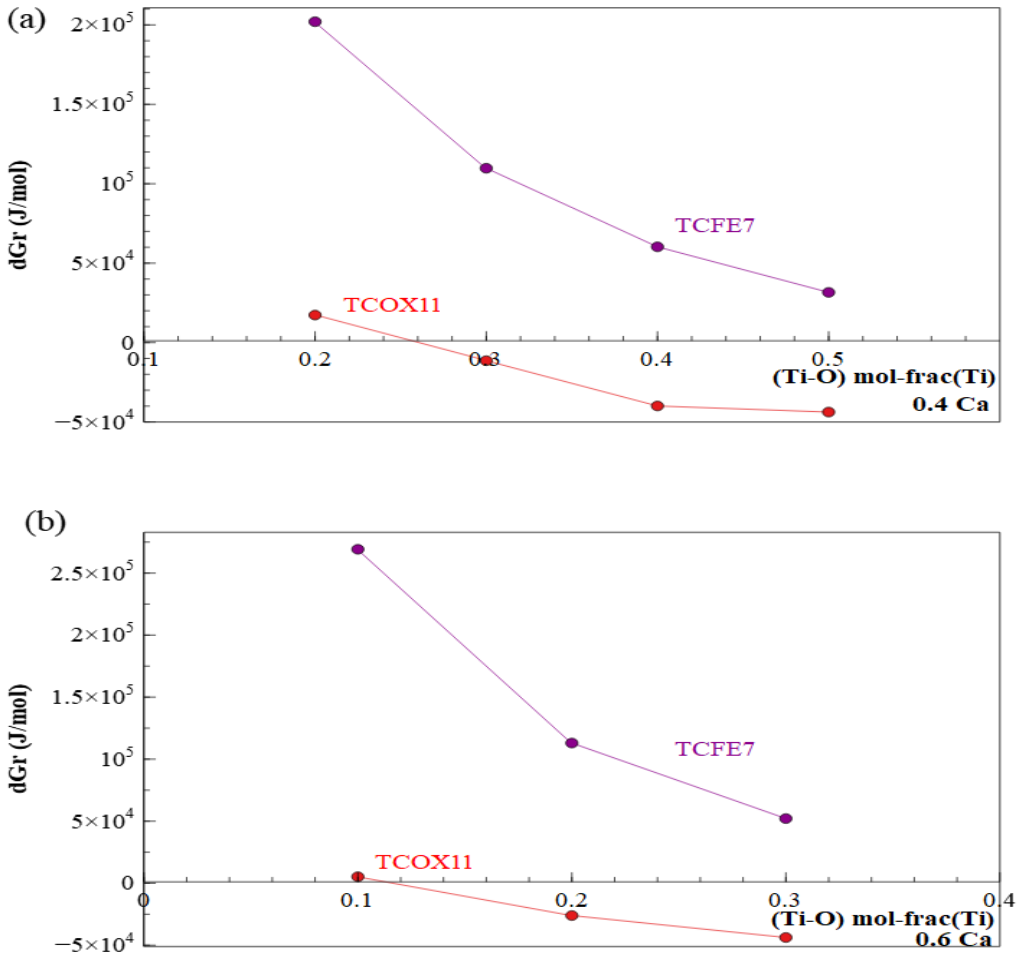

Figure 67: Calculated ΔG_r for CaO in Ti-Ca- O melt, predicted through the mass action law with activity data taken from various databases at 2000K, figures (a) and (b) shows a fixed mol fraction of Ca in the melt at 0.4 and 0.6 respectively whilst Ti and O mol fraction are varied in the melt

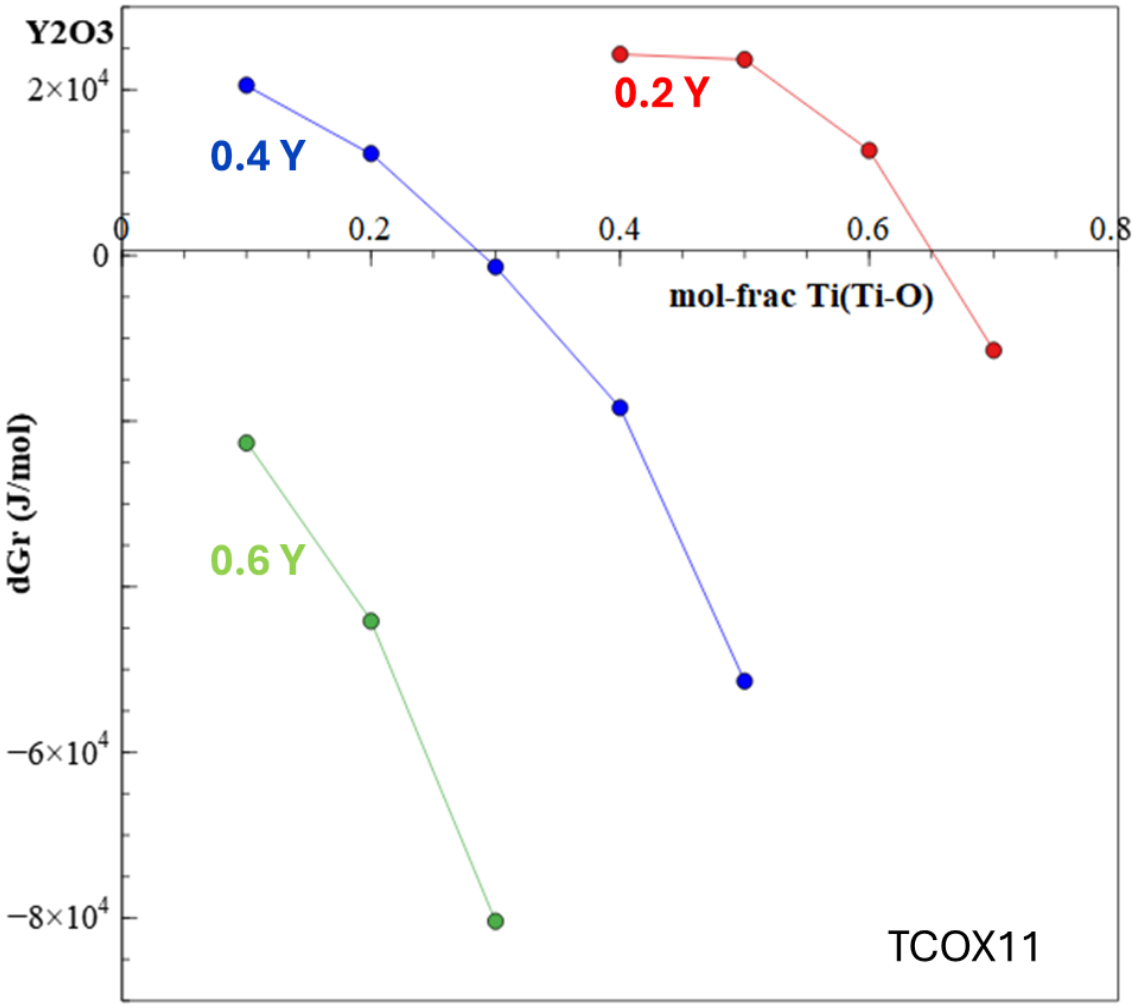

Figure 68: Calculated ΔG_r at 2000 K for Y_2O_3 in a Ti-Y-O melt. The three curves represent fixed yttrium saturation levels in the melt at 0.2, 0.4, and 0.6 (mole fraction), while the titanium and oxygen mole fractions are varied. Data from TCOX11 database

3.3 Chapter 3 Discussion

3.3.1 Thermodynamic Behaviour of Ti-Al System

The activity diagram (figure 56) reveals the thermodynamic behaviour of the liquid phase at 2000K. The negative deviation from ideal behaviour indicates strong intermetallic interactions between Ti and Al, suggesting the potential formation of intermetallic phases. This observation aligns with the phase diagram (figure 8), where several intermetallic phases of Ti and Al have been identified. Due to these interactions, the activity of Ti is significantly reduced, which in turn lowers its overall reactivity.

3.3.2 Mass Action Law: Standard State Approximation

The formation energies (Table 7) reveal both agreements and discrepancies between the databases. These variations may arise from the CALPHAD methodology itself, including differences in thermodynamic models used for data optimization, the assumptions and approximations made during the fitting process, the underlying experimental datasets, and the methods employed for extrapolating multi-component systems from binary or ternary subsystems. Each of these factors can influence the final data. These are one of the drawback of the methodology that data may not always be in close agreement. Despite these challenges, it is still possible to identify

reliable databases for oxides. The TCOX11 CALPHAD database employs thermodynamic models specifically tailored for oxide phases, including metal oxides and complex oxide compounds (e.g., spinels, perovskites). These models are optimized to capture the unique chemical interactions, bonding, and phase behaviour characteristic of oxide systems. In contrast, the TCTI3 database is specifically designed for conventional Ti-based alloys and newly emerging gamma-TiAl-based alloys. It is optimized for metal-metal interactions and may not adequately address oxygen-metal interactions, making it less suitable for predicting the behaviour of oxide phases or phase transformations involving oxygen. The same limitations apply to the TCFE7 database. In addition, TCOX11 has undergone several updates incorporating improvements based on new data or feedback from the scientific community further increasing its reliability. This ongoing refinement provides a high level of confidence in the accuracy of the data, as it has been carefully scrutinized, optimized and validated by experts. In addition, all the oxides selected for this study are assessed in TCOX11 and TCTI3 database. In TCFE7, only Al_2O_3 and SiO_2 are assessed.

CaO, Y_2O_3, Al_2O_3, and ZrO_2 have all been identified as stable and suitable for casting titanium under standard state conditions due to their positive ΔG_r. This prediction is consistent with multiple studies [19], [136], [21], which have consistently

shown that ΔG_r, calculated through formation energies, identifies these oxides as suitable. Additionally, experimental studies have reported that no titanium oxides have formed as a result of Ti-mould contact [175, 34]. This is likely because a significant amount of oxygen is required in the Ti melt before any titanium oxides can stabilise. This observation is supported by Ti-O phase studies, where the Ti-O phase diagram indicates that a saturation level of approximately 0.25 mol fraction is necessary to stabilise the Ti_2O_3 oxide. Even higher oxygen levels are required for the stabilisation of TiO and TiO_2. Such elevated oxygen concentrations are not expected to be extracted from the mould oxides, given their highly negative free energies of formation. Only SiO_2 is expected to react intensely enough to render the formation of TiO_2 thermodynamically favourable. This has been confirmed by a few studies.

These results do not fully explain the substantial damage caused by molten metal observed in experiments, nor do they account for the level of oxygen dissolution found in the liquid melt. Furthermore, the formation of the alpha case, which has been consistently reported in the literature, cannot be explained by these findings. One potential reason is that these calculations were computed exclusively for Ti-oxides, while the formation of intermetallic phases, spinels or unknown Ti-oxides could still contribute to mould failure. Moreover, the reactions were studied exclusively under

standard state conditions, which can be a broad assumption, especially for a reactive system involving titanium. Under non-ideal condition the behaviour could be drastically different and deviate significantly from ideal behaviour. Such behaviour is not captured under standard state conditions.

Nevertheless, the stability ranking generally aligns with the experimental ranking; however, ZrO_2 is predicted to be more stable than CaO. Several studies, including measurements of interaction layer thickness, hardness, and oxygen contamination, have clearly demonstrated that CaO is superior to ZrO_2. This discrepancy in grading was also noted in investigations by [150], where the experimental grading did not correlate with the formation energies. This can happen especially when a thermodynamic system deviates significantly from ideal behaviour. Ti for instance is a highly reactive metal which can cause significant deviation from ideal behaviour.

The advantage of this approach is that all calculations can rely on readily available free energies of formation, and the stability ranking is generally consistent with the experimental rankings established in Section 2.5.2. While this method can still be valid for identifying suitable oxide systems, inconsistencies may arise, such as a inconsistent ordering of oxides that fails to align with experimental observations. Additionally, many unanswered questions remain regarding the reasons behind the reactions of the oxides and the formation of a larger alpha case layer at the inter-

face. To effectively address these questions, it is crucial to study the system under non-ideal conditions.

3.3.3 Mass Action Law: Kostov Approximation

Approximation to the mass action law by Kostov indicated that; with the exception of SiO_2 all oxides have been found to be stable (figure 57). Additionally, the predicted ΔG_r values are significantly higher than expected. This discrepancy arises from one of the approximations used by Kostov to estimate the activity of oxygen in the Ti-Al melt. Due to the lack of solubility data for oxygen, the oxygen free energy (activity) was calculated using a reference oxide, specifically TiO. This approximation assumes that the liquid is already saturated with oxygen to a degree where the reference oxide (Ti-oxide) is stable. According to the TCTI3 database, this oxygen saturation limit was found to be 0.25 mol fraction for TiO, while the saturation limits for TiO_2 and Ti_2O_3 vary depending on their stoichiometry. The issue with this assumption is that, according to the mass action law, oxides will only dissolve if the oxygen activity in the liquid metal is sufficiently low (i.e., the chemical potential is unequal). By using TiO as a reference oxide, Kostov's approximation enforces a high concentration of oxygen already present in the melt, thereby shifting the equilibrium toward stability.

This compromises the accuracy of the ΔG_r values, leading to the overestimation of oxide stability.

The stability ranking determined by Kostov was the same as the ranking established by formation energy. Both approaches show that ZrO_2 is more stable than CaO, which contradicts experimental ranking in section 2.5.2. The most commendable attribute of the Kostov model is its simplicity in predicting the free energy of oxygen (activity) in Ti-Al melt. However, such approximation also introduce constraints which reduce the accuracy of predictions. For instance, ΔG_r is solely determined by the composition of oxygen in the Ti melt whilst ignoring the effects of metallic species such as Y, Zr, Ca, Al, Mg and Si which are also a product of oxide dissolution and can shift the position of the equilibrium reaction. Nonetheless, it is reasonable to assume that oxygen alone determines the position of the equilibrium since, Ti has the greatest affinity for oxygen but lower affinity for metallic species.

3.3.4 Mass Action Law: Modified Kostov Approximation

Modifying the Kostov model to account for oxygen saturation in Ti-Al melt had a substantial effect on ΔG_r as shown in figure 61. Adding a correction to oxygen (equation 38) saturation ensured the amount of oxygen in the melt can be manually controlled from 0.25 mol fraction to as low as possible in the melt. When the oxygen

concentration was lowered to a particular concentration, the sign of ΔG_r changed and the equilibrium shifted to the right to indicate dissolution. The stability ranking is more in line with experimental ranking, CaO is predicted to be more stable than ZrO_2 using this method, which was not the case with formation energies nor from the original Kostov model. Accounting for oxygen solubility has modified the oxide grading to be more consistent with experiments.

The method also shows that all oxides are subjected to dissolution once the oxygen composition in the melt is sufficiently lowered. The original Kostov model could not account for this tendency due to the presumption that the melt is already saturated with high level of oxygen. These results are evident that solubility of oxygen plays a significant role in determining stability of oxides in Ti-Al melt mainly due to the high solubility of oxygen in Ti. However, a draw back of this model is the approximation introduced to calculated free energy of oxygen; even better predictions can be obtained with realistic activities of oxygen. Furthermore, the position of the equilibrium is solely determined by the activity of oxygen in the melt. The effects of the dissolved metals such as (Y, Si, Ca, Al, Zr) is not taken into consideration. The dissolving metals can also impact the position of the equilibrium.

3.3.5 Mass Action Law: Complete Treatment of the Mass Action Law

Figure 64 shows the ΔG_r for the dissolution of Al_2O_3 calculated through the mass action law with data from various CALPHAD databases. At a fixed composition of 0.1 mol fraction of Al (figure 64 (a)), Al_2O_3 is predicted to be unstable at all Ti-compositions evident by negative ΔG_r even at oxygen compositions as high as 0.6 mol fraction. Although the composition of oxygen is high, the low Al composition (0.1 mol fraction) in the melt impedes the oxide from being stable which is evident that Al composition is also critical to oxide stability. At Al composition of 0.4 mol fraction (figure 64(b)), the Al_2O_3 phase is beginning to be stable at relatively high oxygen composition of 0.5 mol fraction. At 0.5 mol fraction of Al (figure 64 (c)) in the melt, less oxygen is required in the melt for Al_2O_3 to be stable.

In the approximation by Kostov and modified Kostov model, the stability of oxides was solely determined by composition of oxygen and so the results did not account for dissolved elements such as Y, Al, Si, Ca and Zr in the melt. With data from CALPHAD solubility of metallic species in the melt was considered, accounting for the solubility of metallic elements has a significant impact on the stability of oxides, which is not observable from the approximations.

Similar trend is observed for all other oxides considered in this study but Y_2O_3. The trend predicted for Y_2O_3 is not the same as the other oxides. As more yttrium is added to the melt, more oxygen is required for Y_2O_3 phase to be stable as shown in figure 68. Y_2O_3 is stable even at high Ti-compositions which is not the case for other oxide systems.

Results from the mass action law suggests that a high composition of oxygen is required in Ti melt for all the oxides to be stable. Y_2O_3 requires the lowest concentration of oxygen in the melt to be stable followed by CaO, ZrO_2 and Al_2O_3. SiO_2 is unstable up-to 0.5 mol fraction of Si in the melt. There seems to exist a large difference in oxygen chemical potential when oxides are bought into contact with Ti melt due to the high solubility of oxygen. The result of which causes the oxides to dissolute. This can be explained by figure 69.

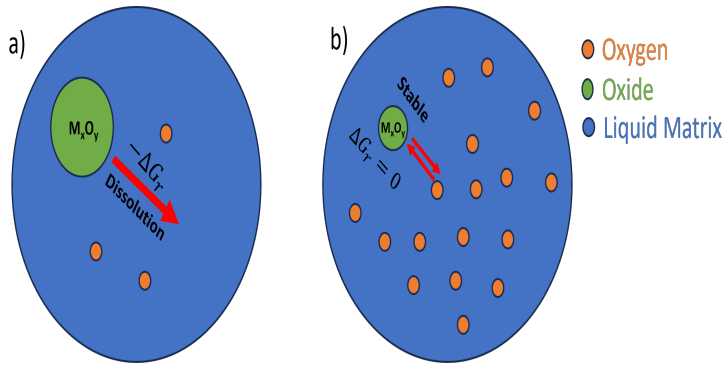

Figure 69: Illustration of Oxide Dissolution Driven by Under-Saturation of Oxygen. a) Unstable oxide due to low oxygen concentration in the liquid, b) Oxide establishing equilibrium with liquid matrix after dissolution, saturating the liquid with oxygen

Under-saturation of oxygen (a) in the liquid prompts the oxide to release oxygen, saturating the liquid and thereby destabilizing the oxide. Once the solubility limit of oxygen is reached (b), the oxide attains stability, and the free energy change, ΔG_r, approaches zero. The solubility limit of oxygen varies based on both the alloy composition and the specific oxide in contact with the liquid.

The stability ranking predicted by the complete treatment of the mass action law is in agreement with literature ranking is section 2.5.2. Compared to the prior methods, the CALPHAD approach accounts for realistic activities of all dissolved elements in the melt. A complete representation of oxide stability was obtained. The stability of CaO is predicted to be more stable than ZrO_2 unlike formation energies and the original Kostov model. However, for the method to work quality thermody-

namic data is required.

Some disagreements with results was revealed when the mass action law was implemented. For instance, ΔG_r for Al_2O_3 shown in figure 64 revealed some disagreement. For a fixed composition of 0.4 and 0.5 mol fraction of Al (figure 64 (b) and (c)), the magnitude of ΔG_r predicted by the model is contrasting. As the fraction of Ti is increased, the TCTI3 database seem to indicate that Al_2O_3 is unstable whereas, the other databases clearly predict a positive ΔG_r at Ti composition higher than 0.2 mol fraction. Another discrepancy with data was observed with ZrO_2 in figure 65. The ΔG_r predicted from TCFE7 for instance is significantly higher than that of TCOX11 and TCTI3. Data from TCFE7 seems to indicate that ZrO_2 is significantly more stable than data from TCOX11 and TCTI3. Considering the ΔG_r calculated using CALPHAD data, it is clear that a high composition of oxygen is required in the melt for any of the oxides to be stable. It is therefore, not a surprise that all oxides are reacting with Ti as observed in experiments. Y_2O_3 is the most stable oxide as it requires the least amount of oxygen in the liquid melt to be stable.

Simplified approaches to the mass action law for ranking oxides as published in the open literature are an asset in terms of its ability to both rank and predict oxide stability. However, it is found that calculations on the mass action law, taking

into account high quality thermodynamic data from CALPHAD assessment have the biggest potential to accurately predict oxide stability. This is particularly critical for selecting oxide materials for casting titanium/alloys. One of the biggest drawbacks of the using the approximation to the mass action law is that the stability rankings may inter-change like in the case with ZrO_2 and CaO. Nevertheless, these approximations are still fairly reliable when data becomes scarce.

3.3.6 Selecting Suitable Mould Oxides

Based on the thermodynamic results there are four ultimate strategies in which suitable oxides can be selected or their stability potentially increased. Figure 70 shows the representation of oxide mould in contact with liquid titanium. As established earlier, the primary cause of oxide dissolution is the substantial chemical potential difference ($\Delta\mu$) between the alloy and the oxide as illustrated in figure 70. To improve oxide stability, several strategies can be implemented:

1. **Select oxides with a minimal chemical potential difference ($\Delta\mu$) between the oxide and the melt**. This reduces the driving force for dissolution.

2. **Choose oxides with low reaction rates**, thereby limiting the rate of oxygen saturation over time, which requires a kinetic model.

3. **Introduce alloying elements into the melt** to reduce the solubility of

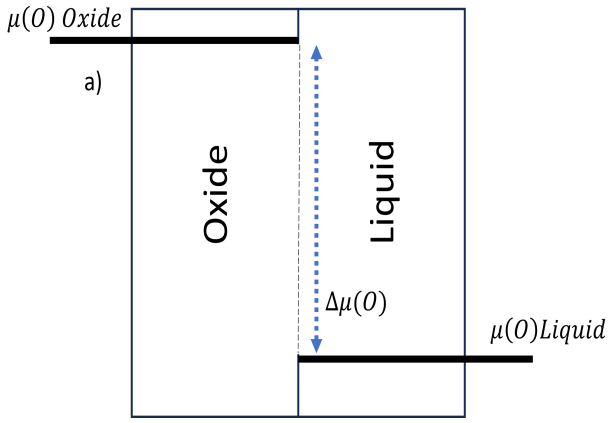

Figure 70: 2D Representation of Metal-Mould Contact Showing the Large Difference in Chemical Potential ($\Delta\mu$) Between the Two Phases

oxygen in the liquid, consequently decreasing $\Delta\mu$.

4. **Combine oxides (e.g., 50/50 M_xO_y-N_xO_y)** to lower the oxygen solubility limit and enhance overall oxide stability.

Much of the literature have heavily focused on the first point but in the following chapters all these points will be considered in detail with the development of a kinetic model.

4 Modelling Reaction Kinetics

4.1 Challenges in Modelling Metal-Mould Reactions

In the previous calculations, the thermodynamic stability of oxides was based on a static system. However, it is also important to study the rates at which the system approaches thermodynamic equilibrium. Experimental studies from the literature have shown that all oxides are subject to dissolution, but different oxides react at varying rates. In such cases, the oxide that reacts at the slowest rate is preferred as a mould oxide. The aim of this chapter is to develop a kinetic model that can capture both the thermodynamics and kinetics of metal-oxide interactions.

There are several challenges in modelling the rates of Ti-mould reactions. A suitable model must meet the following criteria, which are based on the thermodynamic calculations from the previous section and literature review:

1) **Driving Force:** Thermodynamic calculations in the previous section have shown that the dissolution of oxides occurs due to the large difference in chemical potential between the oxide and the liquid Ti-Al melt. This is the primary cause for oxides dissociating.

2) **Reaction Kinetics:** Studies by Kung [19], [36], [120] demonstrate that the reaction proceeds at the fastest rate at the beginning of the reaction and slows over

time as the liquid becomes saturated with oxygen or other solutes. This results in a parabolic reaction curve that eventually heads towards or reaches equilibrium. The kinetic model should reflect this.

3) **Composition-Dependent Dissolution Rate:** The dissolution rate of the oxide should depend on the composition of the elements in the liquid melt. As the particle dissolves, the liquid metal becomes increasingly saturated with impurities coming from the oxide. The reaction rate is expected to evolve as a function of compositional changes in the liquid.

4) **Alpha Case Formation:** The dissolution of high levels of oxygen leads to the formation of the alpha case layer, as documented in literature. Accurately predicting when the alpha case forms, and when it does not, would be a strong indicator of stability.

5) **External Factors:** The model should also account for external factors that influence reaction rates such as temperature, surface area, volume and pressure.

6) **Multi-Component Systems:** The kinetic model must account for interactions in multi-component systems. For example, the dissolution of Al_2O_3 in a Ti-Al melt involves a ternary system containing oxygen, aluminium, and titanium. In such cases, the reaction rate depends not only on the concentration of oxygen but also on the interactions between aluminium, titanium, and other elements. This complex-

ity increases further when alloying additions are introduced into the melt or more complex oxides, such as spinels, are involved.

7) **Multi-Phase Reactions:** The reactions often involve multiple phases, such as the nucleation of reaction products. The model must be capable of handling multi-phase interactions, which directly impact the reaction rate. Additionally, the simultaneous growth and dissolution of phases should be incorporated into the model to accurately model their kinetics.

4.2 Method

4.2.1 Frozen Gradient Approximation

Studying rates of reactions purely from a computational perspective is challenging since reaction rates are generally determined through experimental studies. However, some approximations can be made to estimate reaction rates through computation. The frozen gradient approximation is such a model that uses approximations to model the evolution of any spherical particle in a supersaturated matrix [176]. The set-up of this model is visually illustrated in figure 71 where a spherical solid particle (M_xO_y) is placed inside a spherical liquid matrix. The interaction between the liquid melt

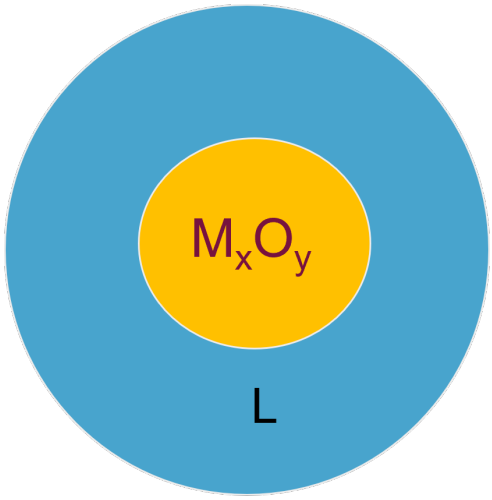

Figure 71: 2D graphical illustration of a 3D spherical oxide (M_xO_y) particle surrounded by spherical Ti-alloy melt

and the solid particle is studied through response of solid particle to the composition

in the liquid melt; that is how the radius of the particle changes in response to the liquid composition. The particle could be subject to growth or dissolution in response to the composition of the liquid phase. The frozen gradient approximation for the growth of a spherical particle in a supersaturated matrix is described by the differential equation 39. In this equation, $\frac{dr}{dt}$ represents the rate of change in the particle's radius, where D (in $\frac{m^2}{s}$) is the diffusion coefficient, indicating the rate at which solutes in the liquid are transported to the solid. The variable r (in meters) represents the particle's radius at time t and S is the dimensionless supersaturation, also referred to as the driving force for growth.

$$\frac{dr}{dt} = \frac{D}{r} \cdot [S] \tag{39}$$

The 'supersaturation' driving force is described as: 40.

$$S = \frac{(C_m - C_l)}{(C_{M_xO_y} - C_l)} \tag{40}$$

where, C_m is the current matrix composition of solute (i.e oxygen) in the liquid at time t, $C_{(M_xO_y)}$ is the fixed stoichiometric composition of the oxide particle and C_l is the equilibrium composition of the liquid phase. The values of C_l and $C_{(M_xO_y)}$ are can be extracted from phase data like phase diagrams and the only variable is C_m, which changes as the particle evolves over time and needs to be updated at each

time-step.

The initial composition of the matrix C_m could either be greater than or less than the equilibrium composition C_l. If $C_m >$ than C_l, the driving force becomes positive and the particle begins to grow. Whereas If $C_m <$ than C_l, the driving force becomes negative and the particle dissolves. When C_m is equal to C_l, the system reaches thermodynamic equilibrium and no change will take place in the system. The matrix composition (C_m) is updated at each time-step through conservation of mass given by equation 41, which relates the fraction of phases to the composition of the liquid matrix. This equation ensures conservation of mass is maintained throughout the simulation and gives the current composition of elements like oxygen in the liquid phase as the particle grows.

$$C_0(i) = C_{lq} \cdot f_l + C_{M_xO_y} \cdot f_{M_xO_y} \tag{41}$$

$$C_{lq}(i) = \frac{C_0 - C_{M_xO_y} \cdot f_{M_xO_y}}{f_l} \tag{42}$$

In equation 41, C_0 is the total alloy composition of the entire system chosen at the beginning of the simulation, C_{lq} is the matrix composition of element (i.e oxygen) in the liquid, $C_{(M_xO_y)}$ is the fixed composition of the oxide particle and $f_{M_xO_y}$ and f_l

are the fraction of the oxide phase and the liquid phase in the system. The equation can be rearranged to get the liquid composition C_lq, which then becomes the matrix composition C_m. The variables in equation are the phase fraction (f) which can be obtained from the updated radius of the particle at each time-step through equation 43 where ($V_{M_xO_y}$) is the volume of the solid particle and V_T is the total volume of the system. Volume of the solid is simply the volume of the sphere as given in equation 44.

$$X_{M_xO_y} = \frac{V_{M_xO_y}}{V_T} \tag{43}$$

$$V_{M_xO_y} = \frac{4}{3}\pi r^3 \tag{44}$$

The thermodynamic data for the simulations have been taken from CALPHAD databases. The reason for choosing CALPHAD methodology is that it provides a broader thermodynamic framework that can handle multicomponent systems and predict phase equilibria and transformations across a wide range of compositions, temperatures, and pressures, whereas abinitio methods like DFT are often limited to simpler systems. The Miedema model is limited to ternary systems. CALPHAD also relies on empirical data combined with thermodynamic modelling, making it highly

accurate when experimental data is available. Since, the model needs some form of validation this would be ideal. Another main reason is CALPHAD is computationally efficient because it relies on pre-existing thermodynamic databases, making it faster to apply to larger systems or simulations. Other methods like DFT may be computationally intensive and time-consuming, especially for large or multi-component systems. For the current task, a rapid and efficient approach to multi-component data is essential, making the CALPHAD method particularly well-suited.

The TCOX11 database [177] has been selected for the forthcoming simulations due to its specific focus on oxide materials and several key advantages. It offers comprehensive coverage of a broad range of elements and their oxides, ensuring applicability to various oxide systems. The database has assessed oxide systems such as those of interest in this study for instance, Al_2O_3, Y_2O_3, CaO among many other ternary oxide systems [177]. Additionally, new and updated versions of the TCOX database incorporate recent research findings and improvements to the underlying thermodynamic models, ensuring access to the latest data and methodologies. By leveraging this database, the simulations can effectively capture the complex interactions and behaviours of oxide systems, allowing for robust analysis of metal-mould interaction and the stability of oxide particles within liquid matrices.

4.2.2 Numerical Simulation of Ti_2O_3 Growth in Ti-O Melt, Using the Frozen Gradient Approximation with Supersaturation as the Driving force

In this section, the frozen gradient approximation introduced earlier was applied to model the growth of Ti_2O_3 particles in a Ti-O liquid matrix. This approach was employed to establish a deeper understanding of the model's operation, preparing it for potential application to metal-mould reactions. The model is designed primarily for binary systems, so Ti_2O_3 was selected as it forms one of the simplest binary systems with titanium oxide in a Ti-O melt. A numerical solution to the frozen temperature approximation, as outlined in equation 39, is presented in equation 45. The particle's growth rate is determined by the change in the particle's radius over time ($\dot{r}$), as given in equation 46.

$$\begin{aligned} dr &= \frac{D}{r} \cdot [S] \cdot dt \\ r' &= r + dr \end{aligned} \tag{45}$$

$$growth\ rate = \frac{dr}{dt} \tag{46}$$

The following paragraph outlines the steps taken to set up the simulation. A flow diagram of the simulation process is provided in figure 72 and the setup is described

below.

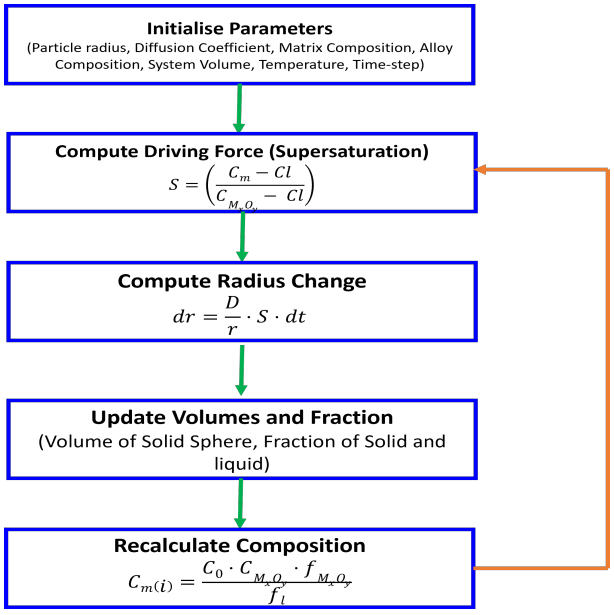

Figure 72: Frozen Gradient Approximation simulation flow diagram

To initialise the simulation conditions/parameters, a Ti-O binary phase diagram was calculated using the (TCOX11) CALPHAD database in Thermo-Calc. The complete calculated phase diagram is given in figure 73.

4.3 Ti-O Phase Diagram

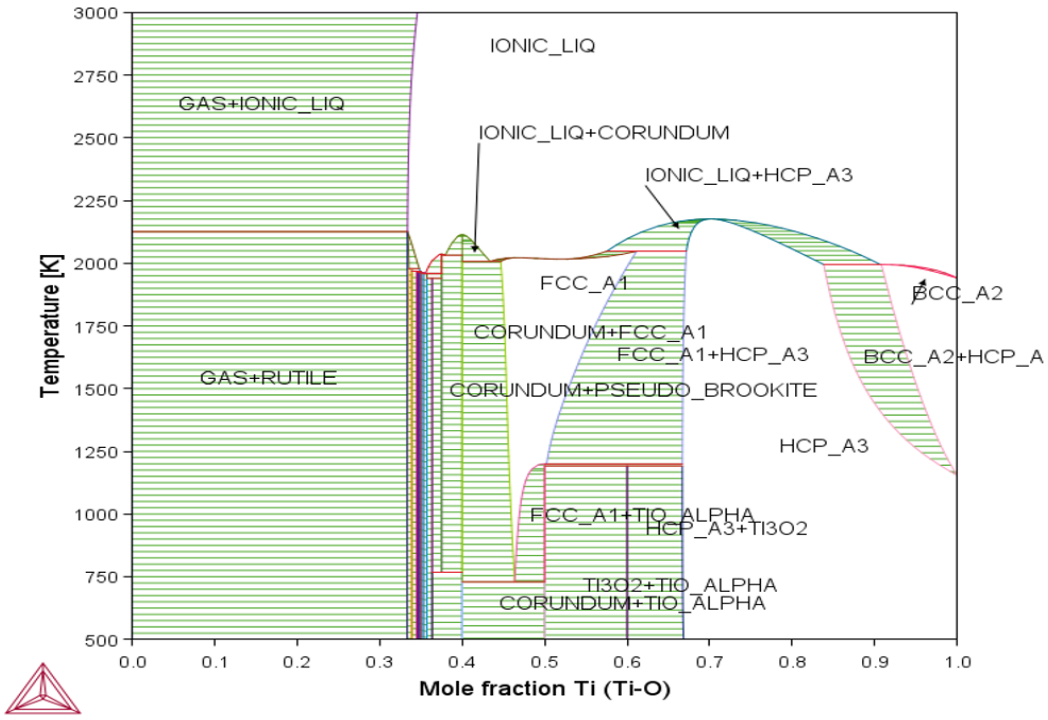

Figure 73: Ti-O Phase Diagram (TCOX11 Database), Thermo-Calc

Figure 74 illustrates a section of the Ti-O phase diagram, highlighting the two-phase region consisting of Ti_2O_3 and liquid. A single tie-line in this region, corresponding to a temperature of just under 2100 K, was selected. This temperature was chosen because it is higher than typical casting temperatures for titanium, though other tie-lines could also be used. The simulation was set up with boundaries (C_l, C_0, and $C_{M_xO_y}$) derived from this tie-line, as represented in figure 74.

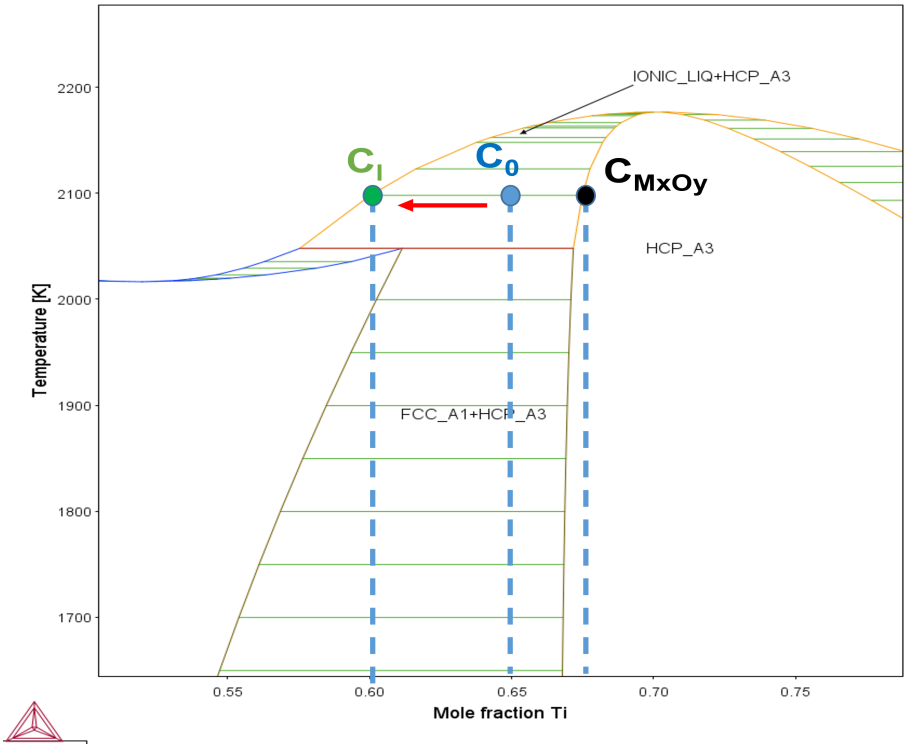

Figure 74: Ti-O Binary Phase Diagram, calculated with TCOX11 database using Thermo-Calc, showing a section of the phase diagram where a liquid and HCP phase (Ti_2O_3) are stable

Since no nucleation model was incorporated, it was assumed that a small precipitate particle with a radius of $0.18 \cdot 10^{-5}$ m had already nucleated. The simulation was designed to model the growth kinetics of the solid particle, assuming the liquid phase makes up the majority of the system, with a volume fraction of approximately 0.998. This corresponds to a total system volume of $2.0943 \cdot 10^{-14}$ $\mathbf{m^3}$. A diffusion coefficient of $1.00 \cdot 10^{-8}$ $\mathbf{m^2}$/s was selected, as the diffusion of solutes in the liquid phase typically falls between $1.00 \cdot 10^{-8}$ and $1.00 \cdot 10^{-9}$ $\mathbf{m^2}$/s [178]. The highest diffu-

sion coefficient was chosen such that the most extreme conditions can be modelled. Table 8 summarizes the simulation conditions.

Parameter	**Value**
Total System Size (m^3)	2.09×10^{-14}
Initial Particle Radius (m)	0.18×10^{-5}
Oxygen Alloy Composition (C_0)	0.35
Fixed Particle Composition $C_{(M_xO_y)}$	0.326
Equilibrium Liquid Composition (C_l)	0.4
Time Step (s)	1.00×10^{-4}
Diffusion Coefficient (m^2/s)	1.00×10^{-8}
Temperature (K)	2100

Table 8: System Parameters and Composition Values for the Growth of Ti_2O_3 Particle in a Supersaturated Matrix

Next, the supersaturation driving force was calculated using equations 39 through 46. Based on this driving force, the change in the solid particle's radius was calculated using equation 45. With the updated radius, the volume fractions of the solid and liquid phases were recalculated. Using these volume fractions, the composition of oxygen in the matrix was determined (equation 42).

The simulation loop, as depicted in figure 72, was then repeated for a 1000 iterations each iteration corresponding to $1 \cdot 10^{-4}$ s. At each time step, the composition evolved from C_0 toward C_l as the particle grew, as indicated by the red arrow in figure 74. This shows the progression from an almost pure liquid (C_0) toward equilibrium at C_l. At the end of the simulation a curve fit was performed using python on the particle radius over time to get the reaction rate constant. The fitted function is the Avrami equation (Eq. 47), widely used to model phase transformations in materials [179]. An exponential term A is added to capture deviations from ideal behaviour. The fit outputs the pre-exponential A and the the reaction rate constant k. The exponent is n is taken as 1, as the reaction corresponds to first order kinetic process. An exponential term A is included to account for deviations from ideal behaviour. The fit yields the pre-exponential factor A and the reaction rate constant k. The exponent n, is taken as 1 as the process follows first-order kinetics.

$$f(t) = A \cdot (1 - \exp(-kt^n)) \tag{47}$$

4.3.1 Development of the Frozen Gradient Approximation with ΔG_r as Driving Force

The frozen gradient approximation was taken as the base to study the evolution of spherical oxide particles in Ti-alloy melt. In its original form there are some limitations that need to be addressed for the model to be effective. There are three limitations which needs to be overcome and they are listed below.

- The approximation limits the model to a binary system
- This approach can only model growth but not dissolution
- Can only have a maximum of two phases in the system

The approximation limits the model to a binary system. In the following sections, new modifications have been introduced into the frozen gradient approximation to overcome these limitations. When interface kinetics is not considered, the model assumes that the process is purely diffusion-limited. This means the following assumptions are true: The concentration of species at the interface, such as a particle surface, reaches equilibrium immediately without any reaction resistance or delay. Under this assumption, the rate of growth, dissolution, or reaction is controlled primarily by the rate at which atoms or molecules diffuse to or away from the interface, neglecting any possible slow surface reactions. Additionally, the model does not

consider the effects of interfacial structure or energy on the reaction rate or mass transfer, assuming these factors have no impact.

As mentioned earlier, the frozen gradient approximation has a few limitations that need to be overcome to make the model more suitable to study metal-mould reactions. Firstly, growth or dissolution of oxide particles should be studied from a reaction perspective; that is representing growth or dissolution in terms of a reaction equation. Whereas the driving force [S] is not reaction specific as it does not consider interactions of alloying elements and its impact on the rate of reaction. Secondly, for a binary system such as the case with Ti and O, the driving force for growth can be calculated with the supersaturation however, for higher order systems with more than two elements present in the melt, supersaturation is inadequate since, the impact of other alloying elements on the position of the equilibrium is not considered. Furthermore, the model is specifically designed to model growth of precipitate particles and dissolution is not yet possible which is essential in this project. In this case, an approach is required, wherein the growth or dissolution of solids in liquid melt is driven by reaction kinetics, able to account for interaction of multiple elements in the melt and be able to model dissolution of oxides. This requires modification to the driving force (supersaturation) such that the above limitations can be overcome.

Firstly, reaction equation for an oxide (M_x O_y) in contact with liquid metal (Ti)

with some oxygen saturation is given in equation 48

$$M_xO_y = xM(Ti-O) + yO(Ti-O) \tag{48}$$

where, $xM(Ti-O)$ represents the concentration of metal M in liquid Ti-O melt and $yO(Ti-O)$ represents the concentration of oxygen in Ti-O melt. With reference to the reaction equation 48, the oxide particle (M_xO_y) could either grow or shrink depending on the position of the equilibrium (whether forward or reverse reaction is favoured). The reaction is favoured to the left if the chemical potential of Ti or O is high in the liquid melt, leading to growth of TiO. If the chemical potential is low in the melt the reaction shifts to the right causing dissolution. ΔG_r for the reaction in 48 is given in equation 49.

$$\Delta G_r = RT \cdot ln\left(\frac{1}{a^e_{M^x} \cdot a^e_{O^y}}\right) + RT \cdot ln\left(\frac{a_{M^x} \cdot a_{O^y}}{1}\right) \tag{49}$$

Incorporating ΔG_r into the frozen gradient approximation as the driving force is appropriate since, many of the challenges outlined at the start of the chapter can be addressed. Some of these are listed below:

- Growth or dissolution can be studied through reaction equations
- Any number of alloying elements can be added to the melt

- Considers interaction of alloying elements and their influence on the position of equilibrium
- Both dissolution and growth can be modelled with respect to the direction of reaction
- Multiple phases can also be present in the liquid as ΔG_r for each phase is different depending on ΔG_f

In the original frozen gradient approximation given in equation 39, the driving force (supersaturation) was unit-less but the units of ΔG_r are J/mol K. To be able to incorporate ΔG_r directly into the model, ΔG_r was divided by $(R \cdot T)$ to make it a unit-less driving force as given in equation 50.

$$\frac{\Delta G_r}{RT} = ln\left(\frac{a_{M^x} \cdot a_{O^y}}{a^e_{M^x} \cdot a^e_{O^y}}\right) \tag{50}$$

As the driving force is now unit-less, ΔG_r is directly substituted into the model as shown in equation 51. Here the assumption is that supersaturation [S] is in some way equivalent to $\frac{\Delta G_r}{RT}$ as defined in equation 52.

$$\frac{dr}{dt} = \frac{D}{r} \cdot \left[\frac{\Delta G_{r(M_xO_y)}}{RT}\right] \tag{51}$$

$$[S] \equiv \frac{\Delta G_r}{RT} \tag{52}$$

The rate of change of radius of an oxide particle in liquid melt is now driven by ΔG_r. The rest of the simulations steps remains unchanged and the updated simulation flow diagram is presented in figure 75.

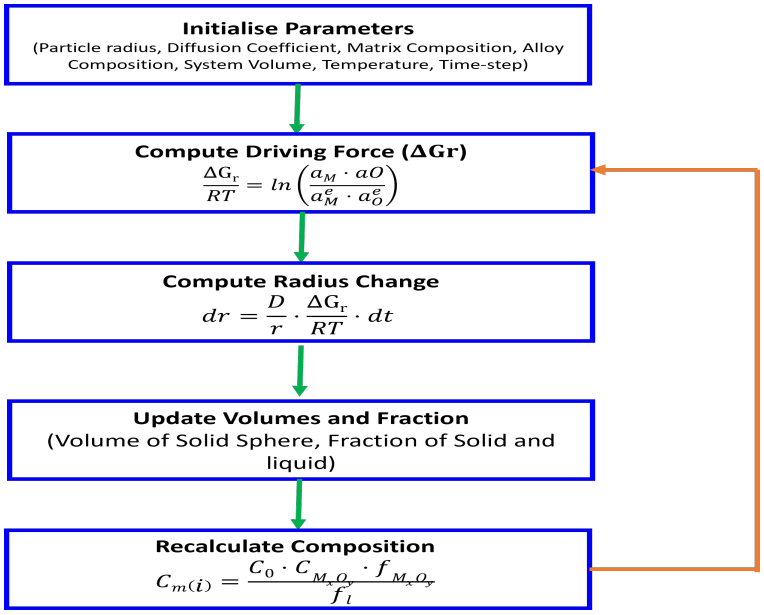

Figure 75: Algorithm showing the simulation steps for a single particle evolution using the ΔG_r approach

.

For a system with multiple phases in the liquid, the ΔG_r corresponding to the second phase is introduced based on the standard free energy of formation as ref-

erence. The flow diagram for a two different oxide particles is illustrated in figure 76.

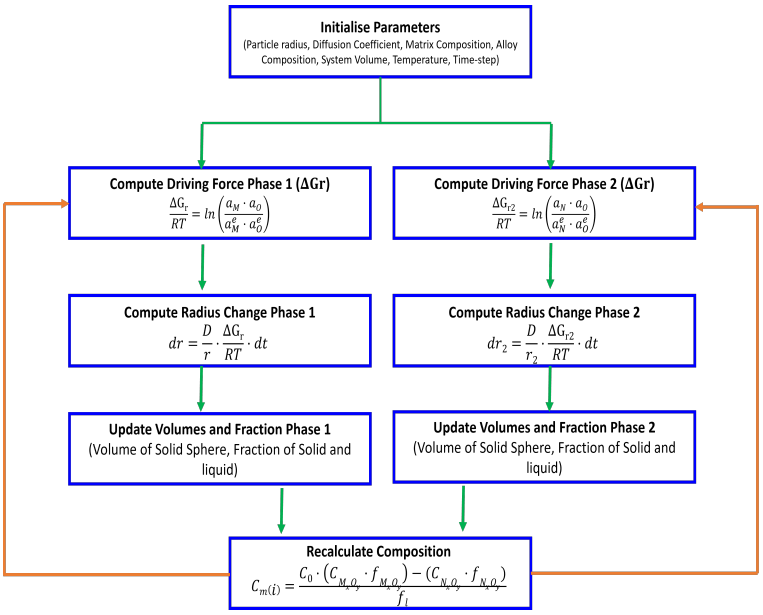

Figure 76: Algorithm illustrating the simulation steps for the evolution of particles from two distinct phases using the ΔG_r approach

4.3.2 Comparison of Growth Kinetics of Ti_2O_3 Particle in Ti-O Matrix with ΔG_r and Supersaturation as the Driving Force

The modified FGA model, using ΔG_r as the driving force, as shown in Equation 51, was tested with Ti_2O_3 in a Ti-O melt. The same set of thermodynamic parameters used for supersaturation (see Table 8) was also applied in this study to allow for a direct comparison between the two driving forces and to highlight their similarities

and differences.

For simplicity, the activities of elements in the liquid phase as required to calculate the driving force ΔG_r were assumed to be ideal, meaning the activity of any element was taken to be equal to its mole fraction, as shown in Equation 53.

$$a_{(i)} = x_{(i)} \tag{53}$$

This comparison allows for establishing similarities and differences between the two approaches and identify where the limitation of using ΔG_r.

.

4.3.3 Comparison of Growth Kinetics of Al_2O_3 Particle in Ti-Al-O (Ternary) Matrix using the modified ΔG_r model and the Unmodified Supersaturation Model

In this section two simulations comparing the growth kinetics of Al_2O_3 particle in Ti-Al-O liquid matrix was simulated. The first using the unmodified supersaturation model as the driving force then using the modified ΔG_r approach. The comparison of both these approaches will allow conclusions to be drawn on the differences and similarities when a ternary system is selected. The thermodynamic conditions for the simulations are listed in table 7.2. The tie-line chosen for this simulation is depicted in the Ti-Al-O phase diagram given in the Appendix 7.1. The phase diagram was calculated to only include the Al_2O_3 and the liquid phase, to simplify the calculations. The simulation steps follow those in figure 72 for the Supersaturation approach and figure 75 for the ΔG_r approach. The simulation parameters and tie-line boundaries are given in Appendix 7.2.

4.3.4 Comparison of Al_2O_3 Dissolution Kinetics in Ti-Al-O Matrix using Supersaturation and ΔG_r as Driving Force

The thermodynamic conditions are similar to those used for the growth simulation, but in this case, the particle radius was set to a value larger than the equilibrium radius identified in the previous simulation, which was reached at $1.29 \cdot 10^{-5} m$. By fixing the initial radius slightly above this equilibrium value, the driving force for the system becomes negative, promoting particle dissolution until the equilibrium radius is attained. The initial radius in this case is set to approximately $1.60 \cdot 10^{-5} m$. This setup ensures that the matrix composition falls outside the tie-line, as illustrated in figure Appendix 7.3, in contrast to the growth cases where the matrix composition lies within the tie-line boundaries. The simulation steps follow those outlined in figures 72 and 75, with the simulation parameters listed in Appendix 7.4.

4.3.5 ΔG_r Model Testing

The ΔG_r approach outlined in the previous section was tested under a variety of conditions to assess both its strengths and limitations. This evaluation is crucial for enhancing the understanding of metal-mould reactions, particularly in relation to reaction rates. These rates are influenced by several key factors, including the particle count in the liquid, initial particle size, surface area-to-volume ratio, temperature

and nucleation events. Simulations were conducted to explore the impact of these variables. It is worth noting that these effects have already been explored extensively in literature but the purpose in this study is to evaluate the model's accuracy in capturing them.

For these simulations, the same tie-line from previous studies, corresponding to the Al_2O_3 + liquid phase region (illustrated in appendix 7.1), was used. The following conditions were tested:

- **Number of Particles (1–8):** The effect of varying the number of particles (ranging from 1 to 8) was investigated by conducting a series of eight simulations, each featuring a different particle count. As the number of particles was increased in the liquid so, did the volume fraction of solid. Such that there was an increasing volume fraction of solid and decreasing volume fraction of liquid upon adding particles. Additionally, the rate constants for particle dissolution were calculated to further analyze the impact of particle number on dissolution behavior.

- **Surface Area-to-Volume Ratio:** The effects of the surface area-to-volume ratio on reaction rates were explored. A set of 8 simulations with number of particles ranging from 1-8 was set-up. Unlike in the previous scenario, a constant solid-to-liquid volume fraction was maintained for each simulation.

Consequently, the initial particle radii was adjusted to reflect this constraint. This allowed to compare the effects of increased surface area to volume and how this affects reaction rates.

- **Varying Initial Radii:** Four different initial particle radii was selected to observe their impact on reaction rates. These include $1.443 \cdot 10^{-5}$, $1.515 \cdot 10^{-5}$, $1.591 \cdot 10^{-5}$ and $1.671 \cdot 10^{-5}$ m. The resulting rate constants for each condition was also plotted with respect to number of particles.

- **Varying Casting Temperatures:** Four different casting temperatures were tested to identify their influence on the reaction rates. In this scenario the only change that takes place is the liquid boundary of the tie-line (C_l) which moves with respect to temperature changes. This is updated at each temperature considered.

- **Nucleation:** Although nucleation was not the primary focus of this study, its effects were investigated using the model. In this scenario, a new Al_2O_3 particle was nucleated every $4 \cdot 10^{-4}$ s, and the impact of this nucleation was analyzed.

4.3.6 Non-Equilibrium, Non-Standard State Reactions

Previous simulations provided a general understanding of the model's workings and aspects that needs to be considered when using the model. However, it did not accurately capture the extreme conditions experienced by the oxide during metal-mould contact in real casting scenarios. The following simulations are set-up to reflect the most extreme conditions likely encountered by the mould oxide. The assumptions are therefore listed below:

- The simulations are conducted under non-equilibrium conditions. Instead of selecting a particular tie-line, pure TiAl liquid is brought brought directly into contact with the oxide.
- The oxygen concentration is set to 0.0001, to reflect the minimal initial oxygen concentration.
- The activity of elements in the liquid is considered to be non-ideal, with activity data obtained from the TCOX11 CALPHAD database.

The primary objective of these simulations is to identify the conditions and oxide combinations that exhibit the lowest reactivity and better stability.

4.3.6.1 Dissolution of Single Oxides Under Non-Equilibrium, Non-Ideal and Low Initial Oxygen Composition For this simulation, several common

conditions have been established to ensure consistency. First, the TiAl alloy has been selected as the main alloy for this study, based on a literature review that highlights its growing potential for use in turbine blades and other critical components. However, for comparative purposes, Ti6Al4V and pure Ti were also included in the simulation set-up. These additional alloys provide valuable benchmarks to assess how the reaction rates and stability differ when compared to TiAl under the same conditions. Regarding mould oxides, the most commonly used oxides in literature include Y_2O_3, Al_2O_3, CaO, $Y_3Al_5O_{12}$, ZrO_2, along with some novel systems such as YSZ (yttria-stabilized zirconia) and $CaZrO_3$. These oxides will be the focus of the study, with the goal of further enhancing their performance. When it comes to particle size, actual applications may involve sequential coatings using slurries with varying grain sizes, such as an initial coating of 30–60 μm particles, followed by 10–30 μm and finally 1–5 μm particles. However, for the purposes of this study, the dissolution process will be modelled using particles of 10 μm in size, representing a balanced medium between too large and too small. The diffusion coefficient for impurities is set at $1 \cdot 10^{-8}$, aligning with the known diffusion rates in Ti alloys. Finally, the temperature for these simulations is set at 2000 K, which reflects the highest casting temperature typically encountered in titanium alloy casting. The simulation conditions for single oxide dissolution are given in the Appendix 7.5, 7.5.1 and 7.5.2.

The thermodynamic activity data for calculating ΔG_r is considered to be non-ideal such that it follows equation 54.

$$a_i = x_i \cdot \gamma_i \tag{54}$$

where, a_i is the activity of element i in the liquid phase and γ_i is the activity coefficient of element i. The activity coefficient are obtained from TCOX11 database. A stability ranking based on reaction rate constant, thermodynamic stability and equilibrium oxygen content was established. For many of the non-equilibrium cases the dissolution profile may not reflect a linear parabolic curve, which makes it difficult to perform a curve fit. To solve this, phase fractions of oxides are chosen to perform a curve fit as they exhibit a parabolic dissolution curve making the fit easier. The curve fit is performed with reference to equation 55.

$$A \cdot e^{(-k \cdot t)} + C \tag{55}$$

where, A is the pre-exponential factor, k is the rate constant, t is time and C is a constant. Appendix 7.5 to 7.5.2 summarizes the initial conditions used for simulating for the TiAl, Ti6Al4V and pure Ti. These conditions were consistently applied across all simulations for comparative purposes.

4.3.6.2 Non-Equilibrium, Non-Ideal, Multi-Phase Reaction - Al_2O_3 and Y_2O_3 System

In this simulation, a system consisting of both Y_2O_3 and Al_2O_3 particles are simulated. The reaction equation for this system follows equation 56.

$$M_xO_y \overset{k_1}{\rightleftharpoons} L \underset{k_2}{\rightleftharpoons} N_xO_y \tag{56}$$

Combining oxides has not been explored to a great extent in literature but have been reported recently as novel developments but little is known about the role they play in stability with each other. In this study the effects of having multiple phases in the liquid is explored to understand the effects on reaction rates stability and oxygen contamination as opposed to single phase systems. The steps for this simulation are given in figure 76 and the simulation conditions are given in the Appendix 7.5.4.

In this simulation setup, most parameters remain consistent with those used for the single oxide setup, with the key difference being the presence of two distinct phases in the liquid. However, it's important to note that the simulation involving multiple phases is not directly comparable to the single-phase oxide simulations (e.g., Al_2O_3 or Y_2O_3) due to factors such as differences in surface area-to-volume ratios and the increase in solid fraction.

To provide a more accurate comparison, simulations were run with two particles of the same phase and then compared to a system where one of the particles is switched

to a different phase. This approach allows for a direct comparison of the behavior of systems with identical particles to those with mixed phases, offering insight into how different oxides interact under the same conditions. Thus, a simulation involving two to three Al_2O_3 and CaO particles was conducted, where both particles of the same phase were placed in the liquid matrix, and the results were compared with those from a system where one Al_2O_3 particle is replaced by another phase. This comparative analysis highlights the effects of having two identical particles versus two different phases in the liquid matrix. The simulation conditions are given in the appendix 7.5.3.

4.3.6.3 Analytical Solution for the Dissolution of Al_2O_3 and Y_2O_3 in TiAl Melt An analytical solution to dissolution of Al_2O_3 and Y_2O_3 was achieved by formulating differential equations for each phase present in the system, expressed in terms of phase fractions. The square brackets [Phase] represent the fraction of phases present in the liquid.

1. For Al_2O_3:

The fraction of Al_2O_3 decreases over time due to dissolution increasing the fraction of liquid (L) in the system. This follows first-order kinetics:

$$\frac{d[Al_2O_3]}{dt} = -k_1[Al_2O_3]$$

Solving this differential equation gives:

$$[Al_2O_3](t) = [Al_2O_3]_0 e^{-k_1 t}$$

where $[Al_2O_3]_0$ is the initial volume fraction of Al_2O_3.

2. For Y_2O_3:

Similarly, the volume fraction of Y_2O_3 decreases due to its dissolution in liquid, again increasing the fraction of liquid (L), also following first-order kinetics:

$$\frac{d[Y_2O_3]}{dt} = -k_2[Y_2O_3]$$

Solving this differential equation gives:

$$[Y_2O_3](t) = [Y_2O_3]_0 e^{-k_2 t}$$

where $[Y_2O_3]_0$ is the initial volume fraction of Y_2O_3.

3. For L:

The fraction of L increases due to the dissolution of Al_2O_3 and Y_2O_3. Therefore, the rate of change of $[L]$ is the sum of the rates at which Al_2O_3 and Y_2O_3 are consumed:

$$\frac{d[L]}{dt} = k_1[Al_2O_3] + k_2[Y_2O_3]$$

By integrating this equation and using conservation of mass, the fraction of L can be calculated as:

$$[L](t) = 1 - [Al_2O_3](t) - [Y_2O_3](t)$$

Here, we assume that the total volume fraction is conserved and that $[Al_2O_3]_0 + [L]_0 + [Y_2O_3]_0 = 1$. The rate constants ($k_1$ and k_2) for each phase were extracted from curve fits performed on the numerical solutions and subsequently utilized in the analytical solution. This approach served two primary purposes: first, to observe the relationship between the numerical and analytical solutions and assess their consistency; and second, to manipulate the rate constants to evaluate their effects on the position of equilibrium. For this analysis, k_2 (the reaction rate for Y_2O_3 was held constant while k_1 was varied. The altered k_1 values included 0.4, 0.54, 0.6, 0.7, 0.8, and 0.9. These values were selected because the fitted value of k_1 from curve fitting was 0.54, making it logical to explore values in its vicinity. The effects of k_1 on k_2 were then plotted in relation to the phase fractions of Y_2O_3 and the liquid phase as presented in section 4.6.1.

4.3.6.4 Improving Performance of Y_2O_3 via Initial Conditions To improve the stability of Y_2O_3 in the presence of Al_2O_3, one strategy is to shift the equilibrium toward Y_2O_3 formation. According to Le Chatelier's principle [180], this can be achieved by adding an excess amount of yttrium to the system, forcing the equilibrium position to shift towards the formation of Y_2O_3. To explore this, three different initial mole fractions of yttrium were selected: 0.01, 0.05, and 0.07 the changes in yttrium composition was compensated by a decrease in Ti composition,

this changed the Ti compositions to 0.4899, 0.4499 and 0.4299 respectively. The rest of the simulation conditions are the same as those in appendix 7.5.4. The simulations steps are the same as outlined in figure 76.

4.3.6.5 Improving Performance of Y_2O_3 via Alloying Additions As already observed in thermodynamic calculation the additions of alloying elements can minimize the thermodynamic driving force for dissolution. To establish effects it has on reaction rates Ti-Al-0.1Cr-0.1Nb was chosen and Al_2O_3 and Y_2O_3 particles was placed inside its matrix. The initial alloy compositions are: Ti:0.937, Al:0.06, Cr:0.001 and Nb:0.001. The simulation steps follow figure 76 and rest of the system conditions are the same as that in Appendix 7.5.4.

4.3.6.6 Improving Performance of Y_2O_3 via Other Oxides The combination of Y_2O_3 and Al_2O_3 was found to have negative effects on the stability of the oxides, indicating that this is an undesirable combination. To improve oxide stability, one potential approach is to investigate the binary interaction between metallic species in their liquid state. Figure 77 shows the activity of Yttrium with Al, Zr and Ca.

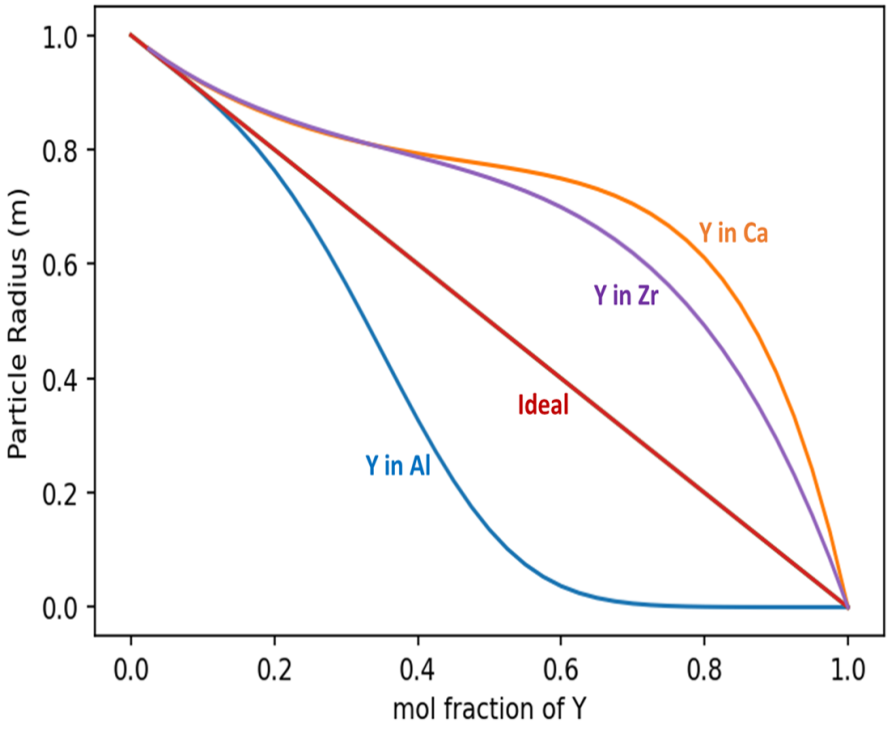

Figure 77: Y-M binary activity diagram

The Y-Al interaction reveals a negative relationship, which is undesirable because it suggests a tendency toward secondary phase formation. In contrast, the Y-Ca and Y-Zr interactions exhibit positive relationships, indicating a repulsive behaviour between elements, which reduces the likelihood of forming reaction products. This positive interaction suggests that systems involving Ca and Zr could be better candidates for enhancing oxide stability when used in combination with Y_2O_3.

For such reasons Ca containing CaO and Zr containing ZrO_2 is chosen as a combi-

nation with Y_2O_3 to model the stability of the system. The simulation set-up follows the set-up shown in figure 76. The simulation conditions are the same as those in Appendix 7.5.

4.3.6.7 More Oxide Combinations Mutual Ions: A few other combination involving oxides that have common ions was also tested. This test was motivated by the fact that oxides that share two or more common ions could establish an equilibrium with each other and achieve mutual stability. For this a few oxides that share common ions was chosen. These are also oxides that exhibit higher stability when present as single phase oxides.

- YAG ($Y_3Al_5O_{12}$) + Al_2O_3 + Y_2O_3
- Mullite ($Al_6Si_2O_{13}$) + Al_2O_3
- Mullite + Al_2O_3 + SiO_2
- ZrO_2 + CaO + $CaZrO_3$

To further investigate the effects of phase composition on the stability of Al_2O_3 particles, a set of simulations involving a combination of mullite ($3Al_2O_3 \cdot 2SiO_2$), Al_2O_3, and SiO_2 was performed. The focus of these simulations was to observe how changes in the volume fraction of mullite and SiO_2 impact the stability and behavior of the Al_2O_3 particles within the system. Three simulations were set up where

the fraction of mullite in the system was progressively increased to 0.3, 0.4, and 0.5. This was done to assess the influence of a higher proportion of mullite on the thermodynamic and kinetic stability of Al_2O_3 particles. Similarly, three other simulations were conducted, with the fraction of SiO_2 being increased to 0.3, 0.4, and 0.5. These setups aimed to test the effects of different SiO_2 proportions on the stability and dissolution kinetics of the Al_2O_3 particle. By systematically altering the volume fractions, it becomes possible to determine whether increasing the concentration of mullite or SiO_2 enhances or weakens the stability of Al_2O_3, providing deeper insights into the inter-phase interactions within the matrix.

Dissimilar Ions: Oxides containing 2 or fewer common ions between them were also tested. Since the CaO-Y_2O_3 system demonstrated improved stability compared to Al_2O_3-Y_2O_3, a new simulation was conducted to observe the behavior when CaO, Y_2O_3, and Al_2O_3 are introduced together in the liquid phase. Additional oxide combinations, listed below, were also tested. Their results are included in the Appendix Section 7.6.1 for reference, as they do not significantly impact the main findings of the thesis.

- Al_2O_3 + YAG
- Al_2O_3 + CaO
- CaO + $CaZrO_3$

- Mullite ($Al_6Si_2O_{13}$)

The simulation conditions for all of these are the same as that in Appendix 7.5.5

4.3.6.8 Identifying Reaction Products and Sequential Oxide Selection Method Previously, in the method section, oxides were selected based on several criteria, including binary interactions between metallic elements, common ions shared between oxides, crystal structure and literature. While these methods provide guidance, they can be time-consuming and do not always guarantee success. A more efficient approach would be to bypass these steps and allow the system to automatically identify the most stable oxide or oxide combination. This can be achieved by identifying the reaction products formed as a result of dissolution and using them as mould materials. Figure 78 illustrates this process.

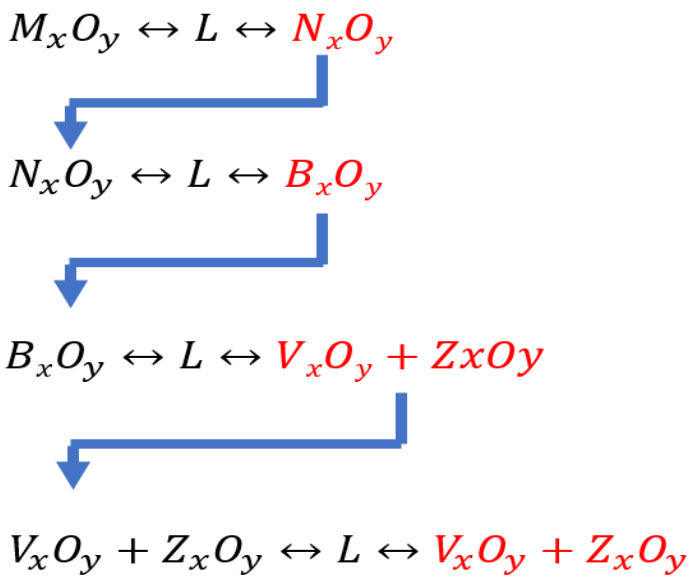

Figure 78: Sequential Oxide Selection Method

In this simulation setup, the process begins with a single oxide (or potentially multiple oxides). Upon dissolution, the oxide reacts with the liquid, yielding a new reaction product denoted as N_xO_y. This newly formed oxide N_xO_y is then selected as the mould material for the next simulation, replacing the initial oxide. The dissolution of N_xO_y subsequently results in another reaction product, B_xO_y, which is again selected as the new mould oxide. The simulation is restarted with B_xO_y as the mould material. This iterative process continues, with each newly formed oxide from dissolution becoming the mould material for the next cycle of simulation. The process repeats until the reaction product in the system becomes the same as

the initial reactant oxide(s). At this point, no further dissolution or changes occur, indicating that the system has reached its most stable oxide combination. In this particular case, the oxides V_xO_y and Z_xO_y are identified as the most stable oxide combination for the system, as no further reaction products are formed from their dissolution. This suggests that V_xO_y and Z_xO_y provide the highest stability for the casting process.

To achieve this, the original flow diagram for the simulation of particle is amended to include additional steps as shown in figure 79.

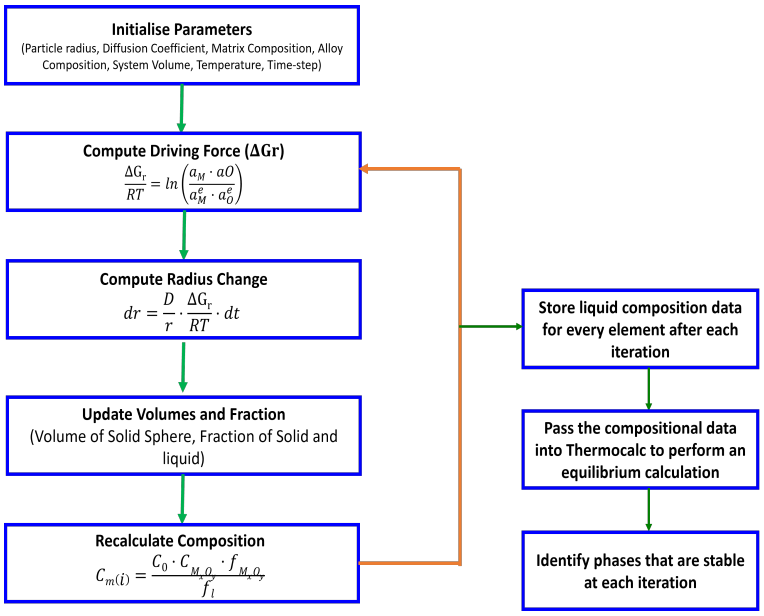

Figure 79: Simulation steps with added simulation step to identify reaction product

At each iteration the chemical composition in the liquid constantly changes due to

dissolution or growth. The changes in composition at each iteration was recorded and then passed into Thermo-Calc to perform an equilibrium calculation. In this instance, all the phases are entered and become part of the equilibrium calculation. Once the equilibrium calculation was the oxides that was became stable is identified as their driving for precipitation will no longer be negative. The reactions products are then chosen as mould oxides and the simulation is restarted with data constituting to the new mould oxide. A representation of choosing mould oxides this way is given below. Two things can be known from this simulation setup: 1) The reaction product can be identified as a result of metal-mould reaction, 2) Stable oxide/s can be identified and used as mould oxides. Table 9 shows all the oxide and oxide combination studied through the sequential oxide selection method. The simulation set-up follows figure 76 with the additional steps from figure 79 also applicable to multi-phase systems. The simulation conditions are available in the Appendix 7.5.5 both for dual and triple particles in the system.

Oxide	Combinations
Al_2O_3	$Al_2O_3 + Y_2O_3$
CaO	Al_2O_3 + Mullite
$CaZrO_3$	Al_2O_3 + Mullite + SiO_2
ZrO_2 (Tetragonal)	$Y_2O_3 + CaO$
ZrO_2 (Monoclinic)	$CaO + CaZrO_3 + ZrO_2$
ZrO_2 (Fluorite)	$CaO + CaZrO_3$
Mullite	$Al_2O_3 + CaO$
YAG	$CaO + Y_2O_3 + Al_2O_3$

Table 9: Single Oxide and Multiple Oxide Combinations Tested with the Sequential Oxide Selection Method

4.3.6.9 Effect of Changing Stoichiometric Coefficients in Reactions The effects of altering the ratios of oxide phases are of particular interest in this study. For this analysis, the Al_2O_3 and Y_2O_3 system was chosen, with the thermodynamic conditions remaining the same as those listed in the Appendix 7.5.4. However, one modification was introduced: the stoichiometric ratios in the reaction equation were adjusted. The following reaction equation illustrates the changes in the reactant stoichiometry:

$$M_xO_y \rightleftharpoons L \rightleftharpoons 2N_xO_y$$

$$M_xO_y \rightleftharpoons L \rightleftharpoons 2N_xO_y$$

This adjustment allows to observe how varying the ratios of Al_2O_3 to Y_2O_3 affects the system's stability and reactivity under the same thermodynamic conditions.

4.4 Results

4.4.1 Numerical Simulation of Ti_2O_3 Growth in Ti-O Melt, Using the Frozen Gradient Approximation with Supersaturation as the Driving force

Figure 80 illustrates the growth dynamics of a Ti_2O_3 particle within a supersaturated Ti-O liquid matrix at 2000K. At the outset, when time $t = 0$, the spherical particle has an initial radius of approximately $0.18 \cdot 10^{-5}$ m. Due to positive driving force generated by the supersaturation, the particle grows steadily until it reaches an equilibrium radius of about $1.45 \cdot 10^{-5}$ m. At this point, the growth of the particle ceases as an equilibrium between the solid and the liquid phase is achieved. The reaction is notably fast, with equilibrium being reached within 0.04 seconds, and the growth rate constant (k) is predicted to be $1.57 \cdot 10^{-2}$.

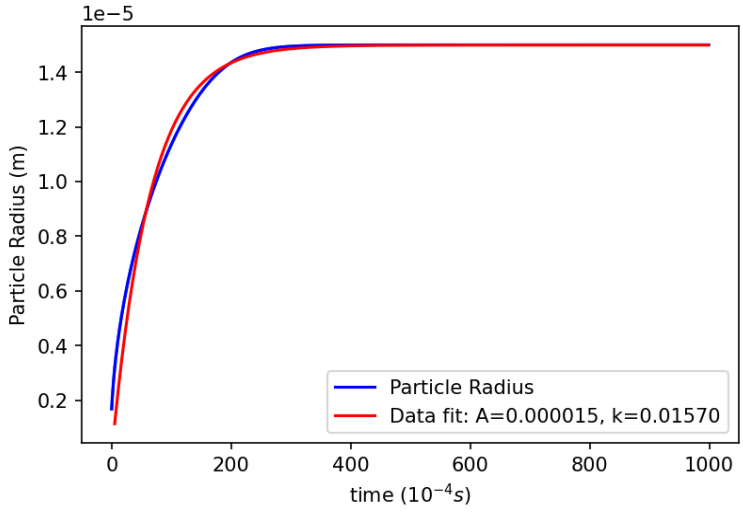

Figure 80: Numerical simulation of change in radius of a Ti_2O_3 particle in Ti-O melt at 2000 K, using the frozen gradient approximation with supersaturation as the driving force. Data sourced from the TCOX11 database.

Figure 81 provides a detailed view of the particle's growth rate over time. The data clearly show that during the initial stages of growth, the Ti_2O_3 particle grows at its highest rate, reaching a maximum rate of approximately $7 \cdot 10^{-7}$ m/s at $t = 0$. As time progresses, the growth rate steadily diminishes, eventually approaching zero, which signifies the system reaching its final equilibrium state. This behaviour results in the characteristic parabolic growth of the particle, as illustrated in figure 80, where the growth is rapid at first and then gradually slows down as the system approaches equilibrium. This behaviour can further be explained in figure 82 which,

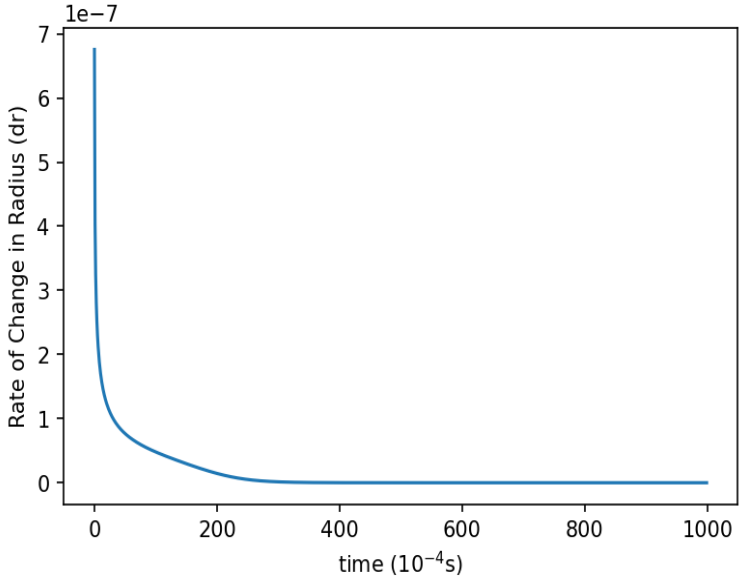

Figure 81: Rate of change in radius of a Ti_2O_3 particle with time in Ti-O melt, at 2000 K, using the frozen gradient approximation with supersaturation as the driving force. Data sourced from the TCOX11 database

provides a visual representation of the reduction in supersaturation as a function of oxygen composition in the liquid. Initially, the system starts with a high supersaturation of approximately 0.69, which gradually decreases as the Ti_2O_3 particle grows. The decrease in driving force is predicted to follow a strictly linear profile with a negative gradient. At equilibrium, the mol fraction of oxygen is predicted to be 0.40, and at this point, the supersaturation is completely eliminated. This absence of supersaturation signifies that the driving force for particle growth has vanished, causing the growth of the particle to cease. Higher initial supersatura-

tion correlates with higher growth rate due to the availability of reactants, which explains the decreasing growth rate observed in figure 81 as the system approaches equilibrium.

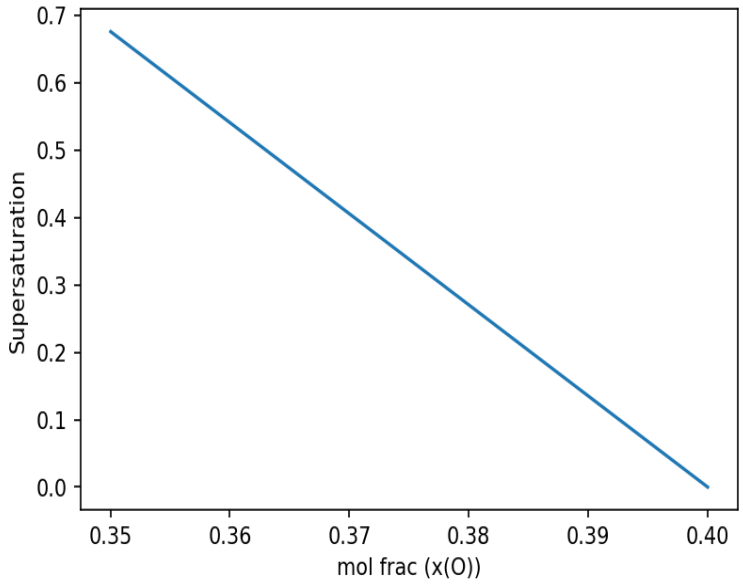

Figure 82: Change in supersaturation driving force as a function of oxygen composition for Ti_2O_3 particle in Ti-O melt, at 2000 K, using the frozen gradient approximation

Figure 83 illustrates the phase fractions of Ti_2O_3 and the liquid phase over time. The oxide phase follows a characteristic sigmoidal growth pattern, contrasting with the parabolic growth curve observed for the particle radius in figure 80. This highlights that phase fraction evolution follows a different profile compared to particle radius growth. The final phase fraction reaching approximately 0.65 for solid, while the liquid phase reduces to around 0.35.

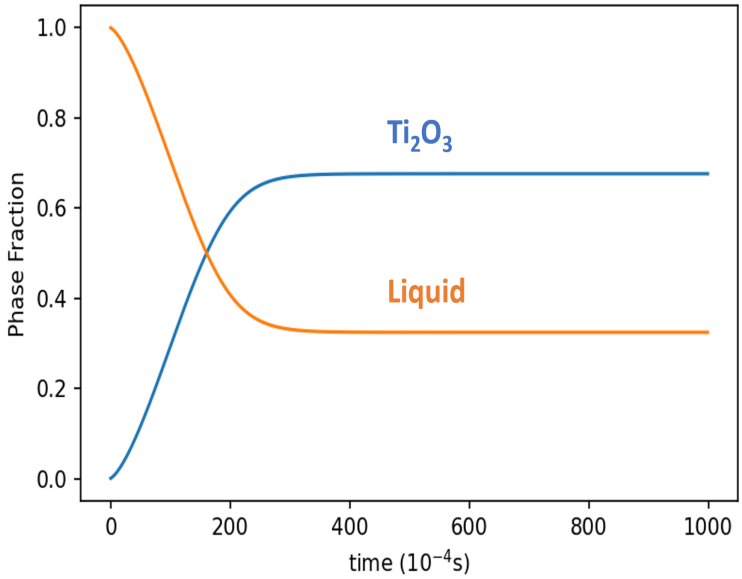

Figure 83: Changes in phase fractions of Ti_2O_3 particle and liquid melt with time at 2000 K, using the frozen gradient approximation with supersaturation as the driving force.

4.4.2 Comparison of Growth kinetics of Ti_2O_3 Using Frozen Gradient Approximation with ΔG_r and Supersaturation as the Driving Force

Figure 84 compares the growth of a Ti_2O_3 particle in a Ti-O melt under two different driving forces: supersaturation and ΔG_r. While the equilibrium radius of the particle is identical for both driving forces, the rate at which the particle reaches equilibrium shows some variation. The growth rate calculated through supersaturation achieves equilibrium sooner, around $300 \cdot 10^{-4}$ s, compared to ΔG_r, which approaches equilibrium around $500 \cdot 10^{-4}$ s. The growth rate predicted for ΔG_r is slower compared

to supersaturation, suggesting that the particle driven by ΔG_r takes longer to reach equilibrium. However, the differences in growth rates are minimal in the overall context. This demonstrates that while the driving force influences the rate of particle growth, both approaches ultimately lead to the same final equilibrium size.

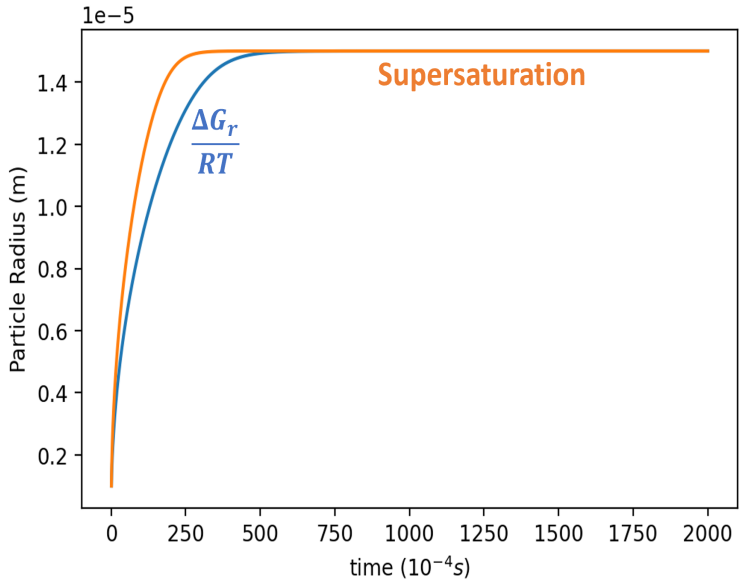

Figure 84: Numerical simulation for the growth of Ti_2O_3 particle in Ti-O melt at 2000 K, calculated using two different driving forces: $\frac{dGr}{RT}$ and supersaturation.

Figure 85 depicts the two driving forces, ΔG_r and supersaturation, as a function of oxygen composition. Both driving forces exhibit a linear decrease as the oxygen composition increases, and they converge at the same equilibrium oxygen composition. However, the initial driving force predicted by supersaturation is higher, starting at 0.7, compared to 0.4 for ΔG_r. This suggests that while both forces lead

to the same equilibrium, supersaturation provides a greater initial driving force, potentially contributing to the faster initial growth rate observed in figure 84. The faster initial growth rate predicted by supersaturation aligns with its higher starting driving force, explaining why the particle using supersaturation reaches equilibrium more quickly compared to the particle driven by ΔG_r as the driving force.

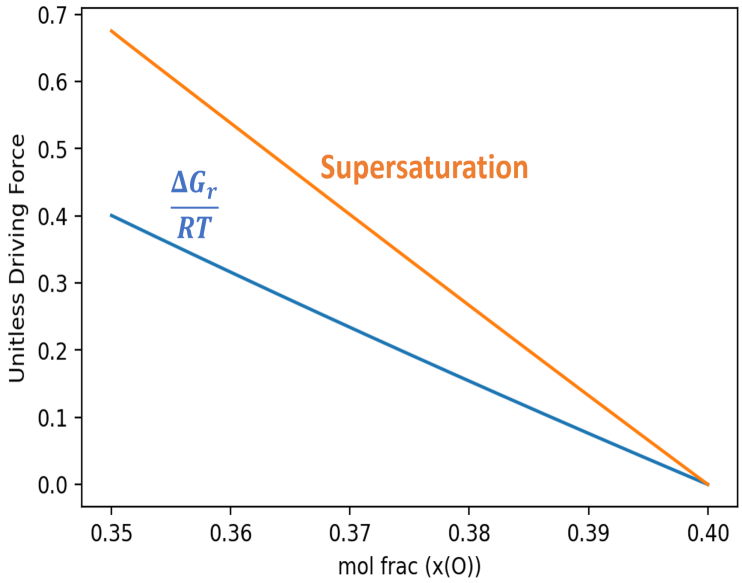

Figure 85: Comparison of driving forces for the growth of Ti_2O_3 particle at 2000 K, calculated using $\frac{\Delta G_r}{RT}$ and supersaturation, plotted against oxygen composition.

4.4.3 Comparison of Al_2O_3 Growth Kinetics in Ti-Al-O Matrix Using Frozen Gradient Approximation with Supersaturation and ΔG_r as Driving Force

Figure 86 compares the growth kinetics of Al_2O_3 particles using ΔG_r and supersaturation as the driving forces. Initially, the growth profiles of Al_2O_3 particles are very similar for both driving forces. However, marginal differences begin to emerge around $50 \cdot 10^{-4}$ seconds as the particles continue to grow. Specifically, the driving force based on ΔG_r leads to a slightly quicker approach to equilibrium compared to the supersaturation-based driving force. The ΔG_r approach predicts an initial driving force of approximately 0.4699, while the supersaturation approach predicts a slightly lower value of 0.4227 as shown in figure 87. This trend mirrors observations from previous simulations involving Ti_2O_3, where supersaturation exhibited a higher initial value than ΔG_r, causing the particle driven by supersaturation to reach equilibrium sooner. In this case, the higher initial value of ΔG_r results in the corresponding particle reaching equilibrium more quickly. Despite these differences, both methods ultimately predict the same equilibrium radius of 1.29×10^{-5} meters. The rate constants for the growth are also quite close, with ΔG_r yielding a rate constant of 0.01974, while supersaturation predicts a rate constant of 0.01624. Compared to the previous simulation, this simulation shows much closer relationship between

supersaturation and ΔG_r.

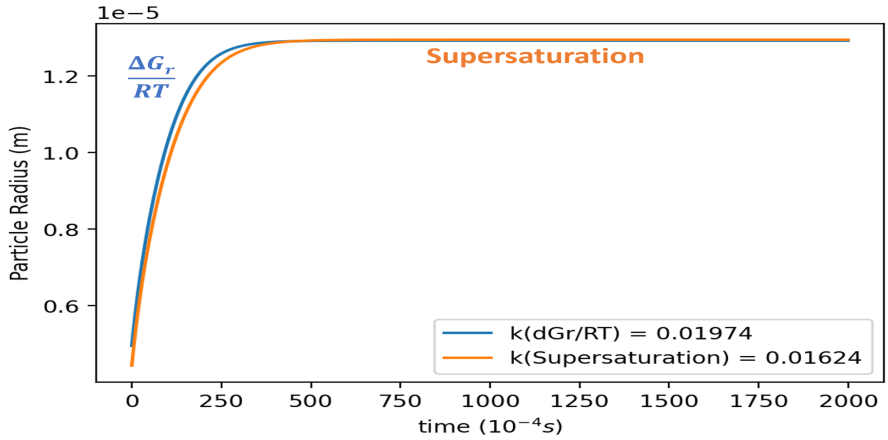

Figure 86: Numerical simulation for the growth of Al_2O_3 particle in Ti-Al-O melt at 2000 K, calculated using two different driving forces: $\frac{\Delta G_r}{RT}$ and supersaturation

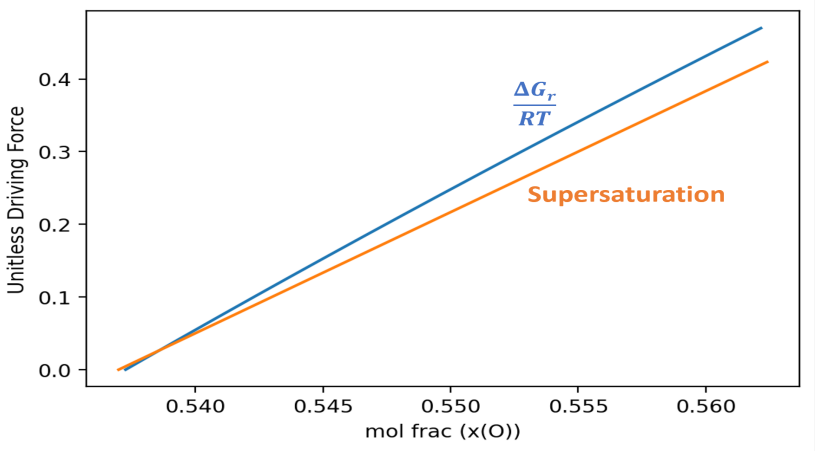

Figure 87: ΔG_r and Supersaturation as a function of oxygen composition for the growth of Al_2O_3 in Ti-Al-O melt (2000K)

4.4.4 Dissolution of Kinetics of Al_2O_3 in Ti-Al melt Using the Frozen Gradient Approximation and ΔG_r as the Driving Force

In addition to modelling the growth of an oxide particle, the dissolution of Al_2O_3 was also simulated using both ΔG_r and supersaturation as the driving forces (figure 88). This simulation follows the same tie-line used to model the growth of the Al_2O_3 in the previous example. The process begins with a particle radius of approximately $1.60 \cdot 10^{-5}$ m, significantly larger than the equilibrium radius identified in the growth simulation. Given that the particle is well above its equilibrium size, it gradually shrinks until it reaches an equilibrium radius of about $1.29 \cdot 10^{-5}$ m for both approaches. The decreasing radius with time is parabolic in nature, indicating the reaction is occurring at the fastest rate during the initial stages of the reaction and slowing down as it approaches equilibrium. Figure 89 shows the driving forces as a function of oxygen composition for both ΔG_r and supersaturation. Initially, both driving forces are negative, which drives the dissolution process. As the system progresses towards equilibrium, the driving forces decrease and gradually approach zero. In both cases the driving forces start with a negative value, indicative of particle dissolution and approach 0 when equilibrium is achieved. While the overall dissolution process is similar under both driving forces, there are minor variations in reaction rates. Specifically, the ΔG_r approach predicts a rate constant of -0.023,

whereas the supersaturation approach yields a rate constant of -0.018. This shows that the ΔG_r method leads to a faster attainment of equilibrium compared to the supersaturation approach. Figure 89 highlights these differences, where for supersaturation, the initial driving force is -2, whereas the ΔG_r approach starts just below -4. It is this difference that causes the particle driven by ΔG_r to approach equilibrium sooner. During the dissolution process, the ΔG_r approach displays a more parabolic change in the driving force, while the supersaturation approach shows a strictly linear approach to equilibrium. Despite minor differences in the dynamics of reaching equilibrium, both approaches ultimately converge to the same equilibrium state. The driving force approaches zero, and the oxygen composition in the liquid stabilizes at a mol fraction of 0.539.

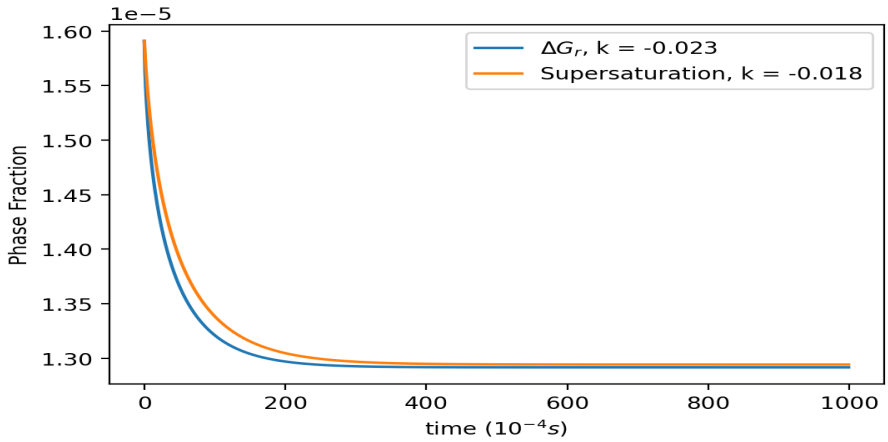

Figure 88: Dissolution of Al_2O_3 in Ti-Al-O melt (2000K)

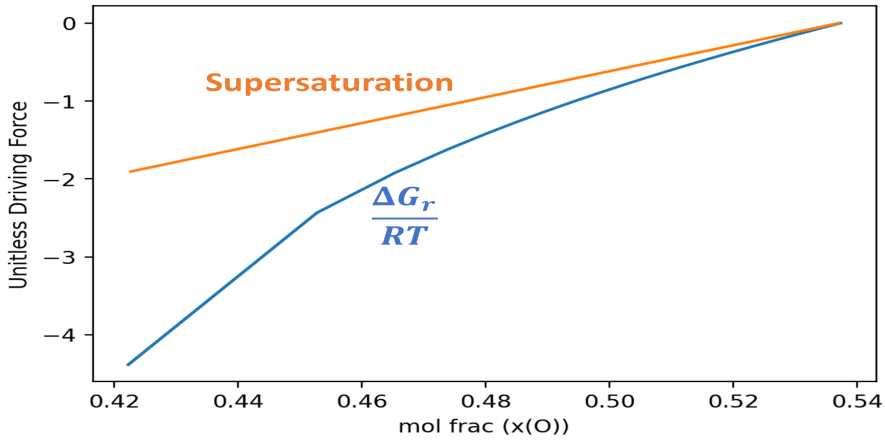

Figure 89: Negative driving force for the dissolution of Al_2O_3 in figure 88, (2000K)

Figure 90 compares the phase fractions of Al_2O_3 during growth and dissolution, as simulated in figures 86 and 88, using the ΔG_r approach. As expected, the equilibrium radius remains consistent due to the same tie-line used for both simulations. However, there are notable differences in the rates of growth and dissolution. The growth of Al_2O_3 exhibits a sigmoid behaviour, while the dissolution shows a more parabolic trend. These differences highlight how the system's approach to equilibrium varies based on the initial conditions.

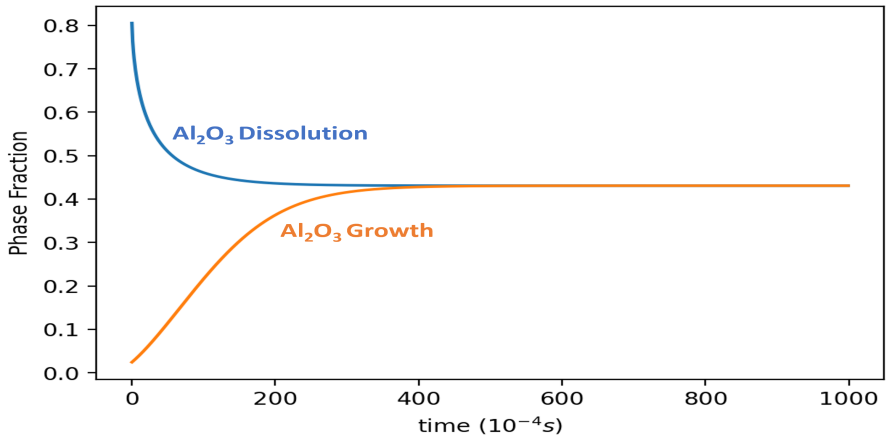

Figure 90: Changes in phase fractions of Al_2O_3 particle and liquid melt at 2000 K

4.4.5 Testing the ΔG_r Approach Under a Range of Conditions

4.4.5.1 Effects of multiple Al_2O_3 oxide particles in Ti-Al-O melt Figure 91 illustrates the kinetics of 1 to 8 alumina particles in a liquid, all starting with the same initial radius. The results show that having up to 4 particles contributes to growth, whereas having more than 4 particles results in their dissolution. Notably, while the presence of multiple particles does not change the final equilibrium state—meaning the equilibrium volume fractions remain the same—the equilibrium radius of each particle varies depending on the number of particles in the liquid. This ensures that the final phase fraction of solid to liquid is consistent, regardless of the number of particles present. Figure 92 illustrates the impact of varying the number of particles on the reaction rate constant, for systems that exhibit dissolution. As the number of particles increases, the rate constant becomes more negative, indicating that the reaction rate is enhanced by the presence of multiple particles. The profile shown in figure 92 is parabolic rather than linear, suggesting that the reaction rate slows down as the number of particles increases.

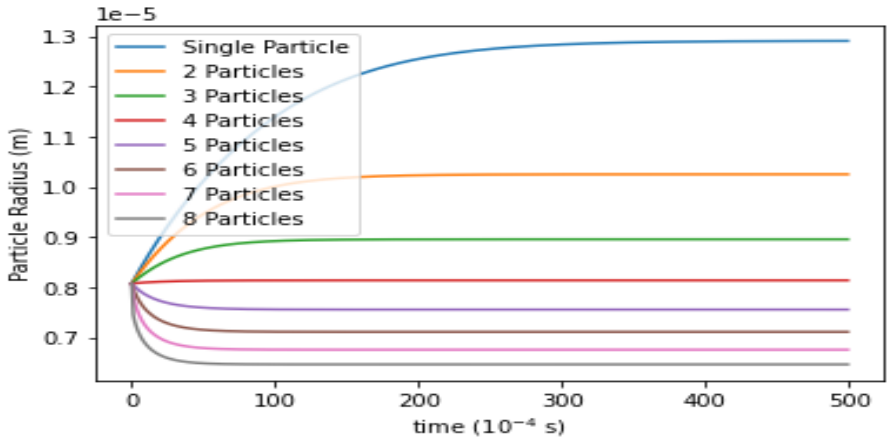

Figure 91: Each curve showing the dissolution of Al_2O_3 in Ti-Al-O melt with varying number of Al_2O_3 particles (2000K), from a single Al_2O_3 particle up-to 8 Al_2O_3 particles in the melt

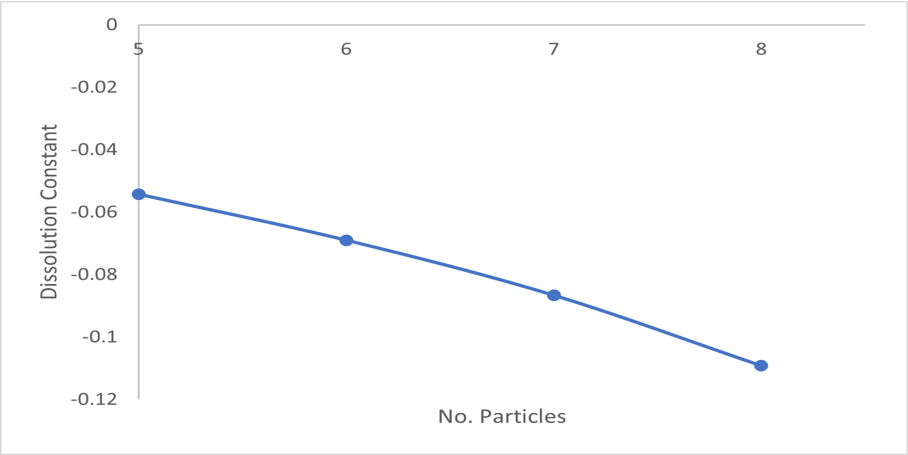

Figure 92: Dissolution constants from figure 91 plotted against its respective number of particles

4.4.6 Effects of Surface-Area to Volume Ratio

In figure 93, the initial volume of the alumina particles is kept constant while varying the number of particles in the liquid. The results show that particles reach a different equilibrium radius depending on the no. of particles in the liquid, yet the equilibrium volume remains the same. Larger particles achieve a larger radius compared to smaller particle in the liquid. The results also show that as the number of particles increases, the dissolution rate becomes more negative, indicating an accelerated reaction. This observation is further supported by figure 94, which demonstrates a linear decrease in the rate constant with an increasing number of particles.

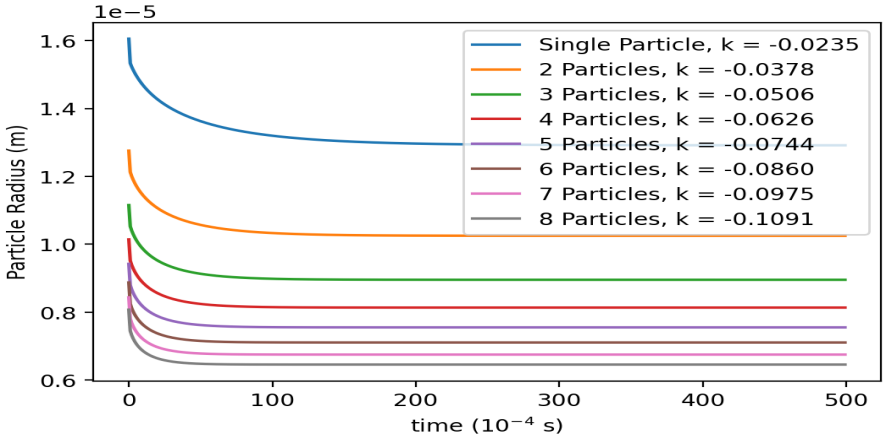

Figure 93: Dissolution of Al_2O_3 particles with varying radii but constant initial volume in Ti-Al-O melt at 2000 K

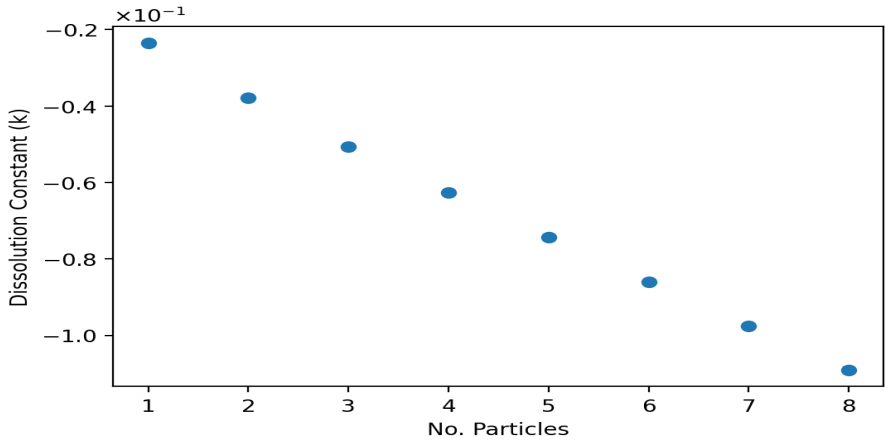

Figure 94: Dissolution constants vs no. particles for simulation in figure 93

4.4.7 Effects of varying initial radii on the reaction rate constant

Figure 95 illustrates the dissolution of four individual Al_2O_3 particles, each with different initial radii. A typical dissolution curve is observed for all particles, regardless of their initial size, and they all eventually reach the same equilibrium radius. However, the reaction rates vary significantly depending on the initial particle radius. Larger particles dissolve at a faster rate but take longer to reach equilibrium, whereas smaller particles dissolve more slowly but reach equilibrium more quickly. The reaction rate constants as plotted against the number of particles (figure 96), clearly indicate that larger particles have higher reaction rate constants compared to smaller ones. The decrease in reaction rate constant is not entirely linear but rather shows a trend approaching parabolic behaviour.

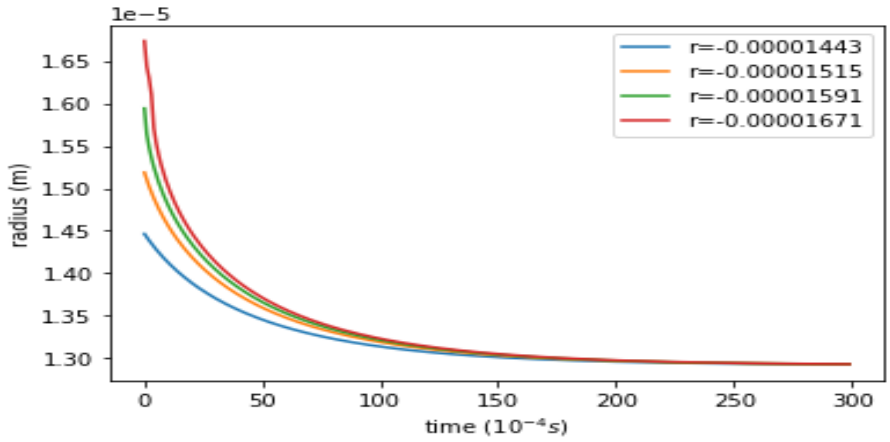

Figure 95: Single Al_2O_3 particle in Ti-Al-O melt but each curve representing different starting radii (2000K)

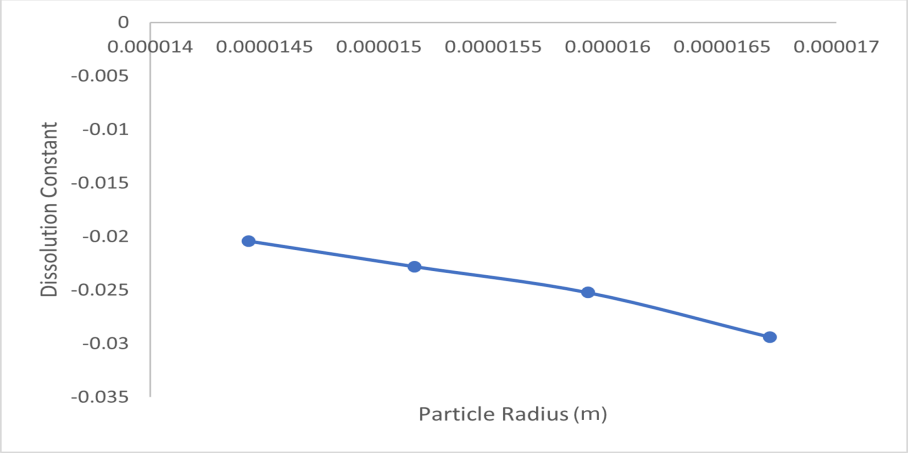

Figure 96: Dissolution constant of various initial radii of Al_2O_3 particle in Ti-Al-O (2000K)

4.4.8 Effects of Temperature on the rates of reaction

Figure 97 illustrates the dissolution behaviour of Al_2O_3 particles at various casting temperatures. The results indicate that particles reach different equilibrium radii depending on the casting temperature, with higher temperatures resulting in smaller equilibrium radii which is indicative of less and less solid in the liquid. Additionally, the reaction rate constant decreases with increasing temperature because, at higher temperatures, the particles attain a smaller equilibrium size, which consequently requires a longer time to reach equilibrium.

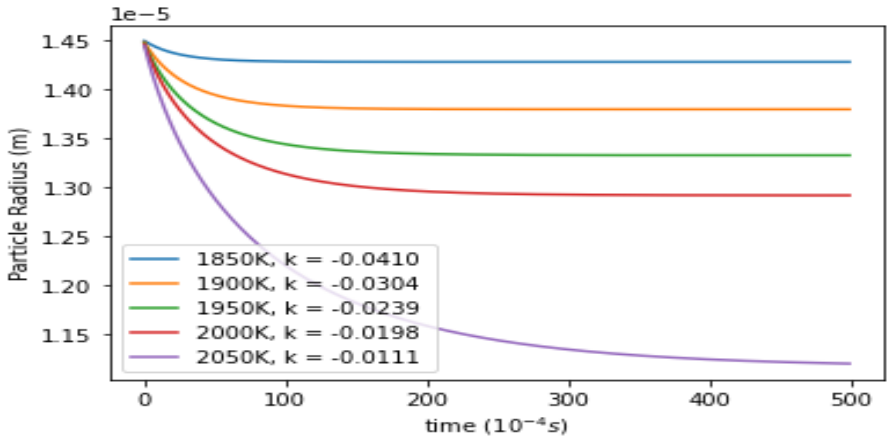

Figure 97: Dissolution of Al_2O_3 particle in Ti-Al-O melt at varying temperatures

4.4.9 Effects of Nucleation

Figure 98 illustrates the effects of nucleating a new particle every 4×10^{-5} s in the matrix. Initially, a particle with a radius of 1×10^{-5} m is nucleated at time $t = 0$ s.

This particle creates a positive driving force for growth, causing it to expand until a second particle, also with a radius of 1×10^{-5} m, is nucleated at $t = 4 \times 10^{-5}$ s. Upon nucleation of the second particle, the driving force for the first particle becomes negative, leading it to begin shrinking at a constant rate. The second particle also starts to dissolve shortly after its nucleation. When the third particle is introduced, the dissolution rates of the first two particles increase, causing them to dissolve even more rapidly. At this stage, all three particles dissolve at different rates depending on their sizes. As the fourth and fifth particles are introduced into the melt, the dissolution rates of the first three particles increase further, causing them to dissolve at an even faster rate. Overall, the trend shows that the dissolution rate accelerates as more particles are introduced at fixed intervals throughout the process.

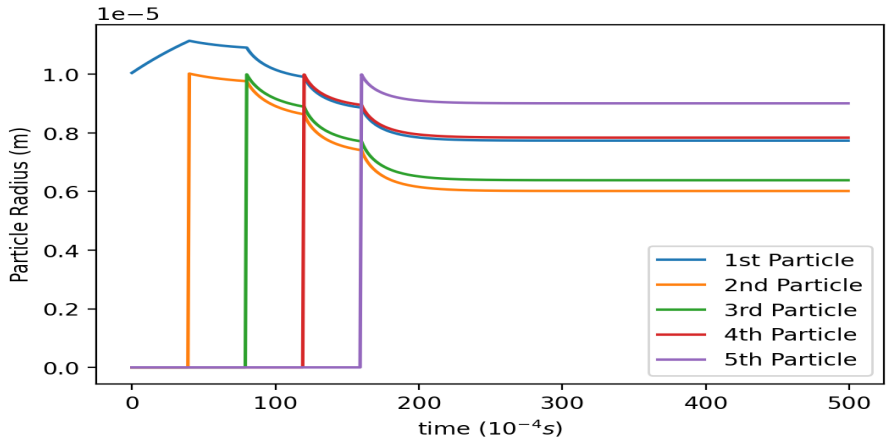

Figure 98: Nucleation of Al_2O_3 particles in Ti-Al-O melt at every 4×10^{-5} s

4.5 Non-Equilibrium, Non-Standard State Reactions

4.5.1 Dissolution of Oxides Under Non-Equilibrium, Non-Ideal and Low Initial Oxygen Composition

Figure 99 illustrates the dissolution behaviour of various single oxides in TiAl melt at 2000 K, showing the reduction in particle size over time. The results show that all oxides listed undergo dissolution at varying rates, eventually stabilizing and reaching an equilibrium state with the liquid. Among these, Y_2O_3 proves to be the most stable, exhibiting minimal reduction in particle size, while Al_2O_3 emerges as the least stable, showing the greatest reduction in particle size.

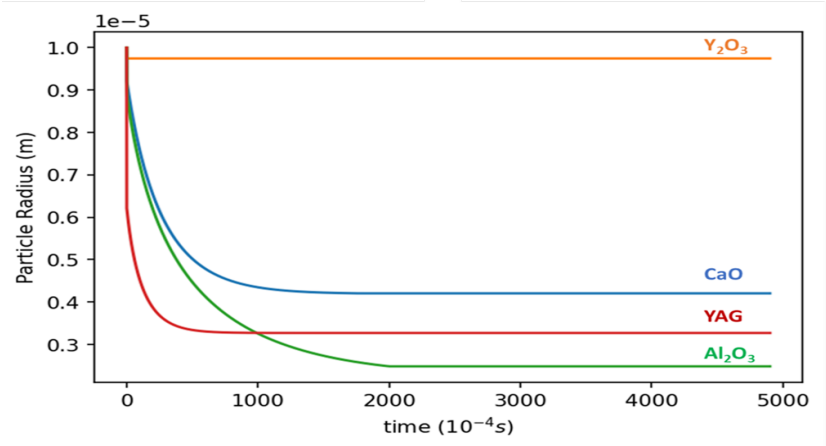

Figure 99: Dissolution of various oxides in Ti-Al Melt at 2000K

In addition, figure 100 presents the dissolution profiles of single CaO and $CaZrO_3$ in TiAl melt at 2000 K. The dissolution behaviour of these oxides is markedly different

from those depicted in figure 99. Unlike the oxides in the previous figure, both ZrO_2 and $CaZrO_3$ completely dissolve into the liquid melt, indicating the absence of an equilibrium state between the oxide and the melt.

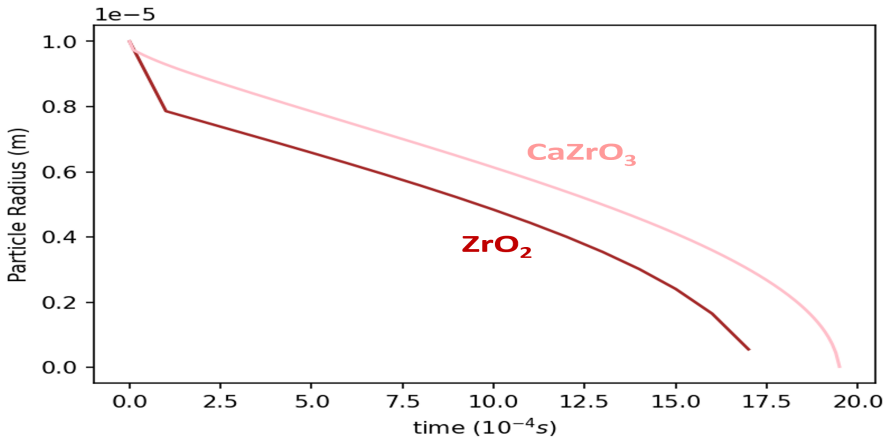

Figure 100: Dissolution of single ZrO_2 and $CaZrO_3$ in Ti-Al melt

The dissolution profiles of ZrO_2 and $CaZrO_3$ exhibit three distinct transitions, which can be analysed by examining the rate of change in particle size over time. Initially, there is a sharp decrease in radius for both particles, with ZrO_2 showing a more significant reduction than $CaZrO_3$. Following this initial stage, the rate of particle size reduction slows down, establishing a more gradual dissolution profile which is almost linear. As the particles become smaller, a third transition occurs, characterized by an accelerated reduction in particle size until the oxides are completely dissolved in the liquid. In this case, ZrO_2 is more unstable than $CaZrO_3$ as

it dissolves first. Both ZrO_2 and $CaZrO_3$ is considered to be more unstable than the oxides in the previous figure. Figure 101 illustrates the relationship between particle radius and surface area-to-volume ratio for $CaZrO_3$ in the context of $CaZrO_3$ dissolution in figure 100. The results indicate that a reduction in particle radius (right to left) leads to an exponential increase in the surface area-to-volume ratio. This rise significantly accelerates the dissolution rate, indicating that smaller particles dissolve much faster than larger ones.

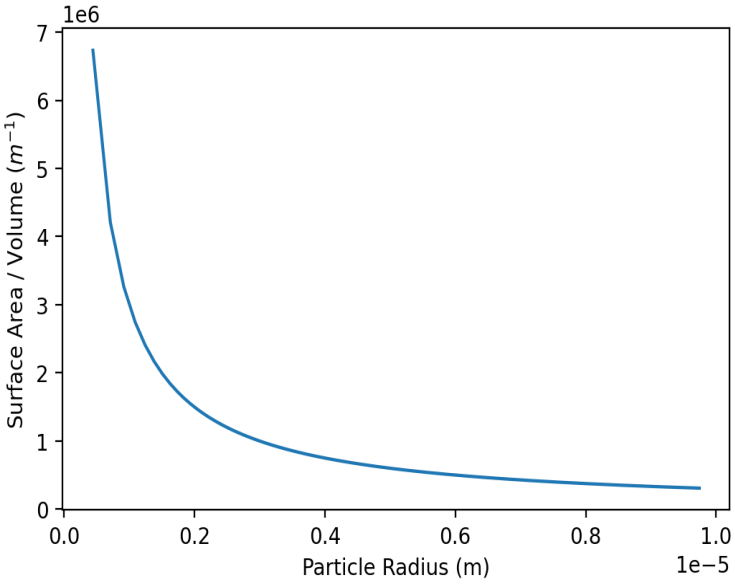

Figure 101: Reaction rate constants of dissolution

Figure 102 shows the equilibrium oxygen contamination in the liquid as a result of oxide dissolution. Y_2O_3 establishes an equilibrium with the liquid with the lest

amount of oxygen followed by CaO, YAG, Al_2O_3, $CaZrO_3$ and ZrO_2. This ranking is somewhat comparable to the kinetic in figure 99, with the exception of YAG and Al_2O_3. ZrO_2 again shows low stability as it saturates the liquid with most amount of oxygen.

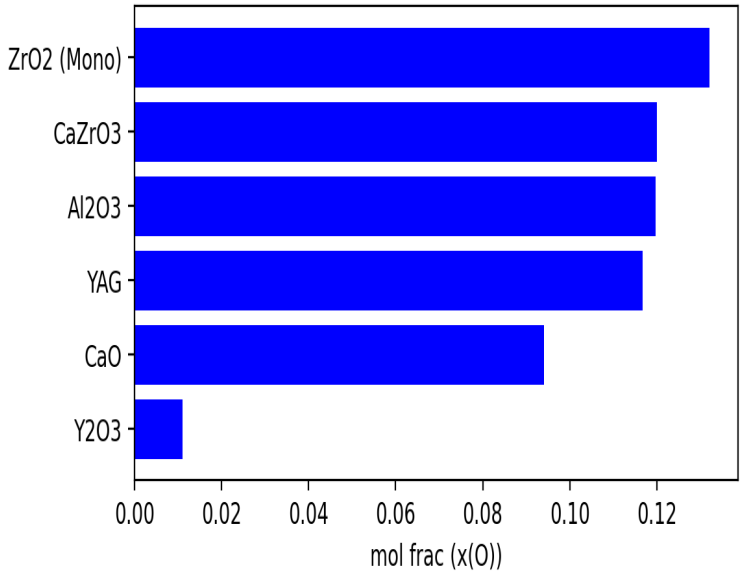

Figure 102: Reaction rate constants of dissolution

The rate constants describing the dissolution rates, presented in figure 103, were derived from the phase fraction data shown in figures 104 and 105. The results clearly demonstrate that, regardless of the type of oxide, the oxides exhibit the greatest instability in pure titanium, followed by Ti6Al4V and then gamma phase. This trend suggests that a higher concentration of titanium in the melt leads to

a more extensive dissolution reaction making oxides less stable. Though Al_2O_3 is the least stable oxide, its reaction rate is much slower compared to YAG. In reality, Al_2O_3 maybe preferred over YAG since, it exhibits a slower reaction rate.

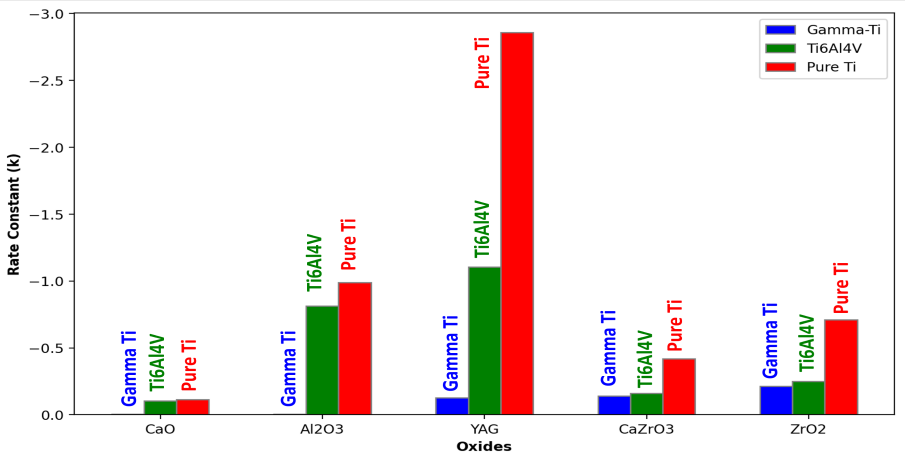

Figure 103: Reaction rate constants of dissolution of oxides in pure Ti, Ti6Al4 and Gamma TiAl 2000K

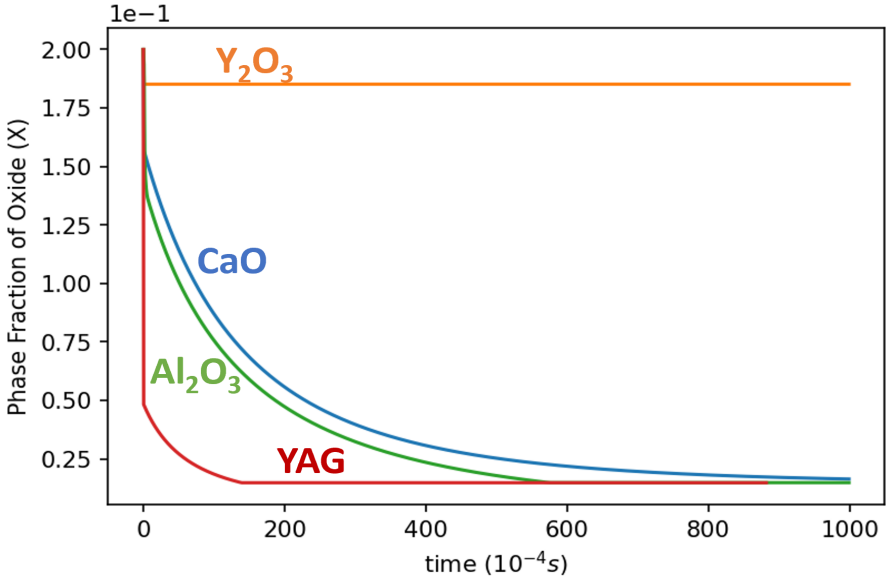

Figure 104: Changes in phase fraction of various oxides in TiAl melt at 2000K

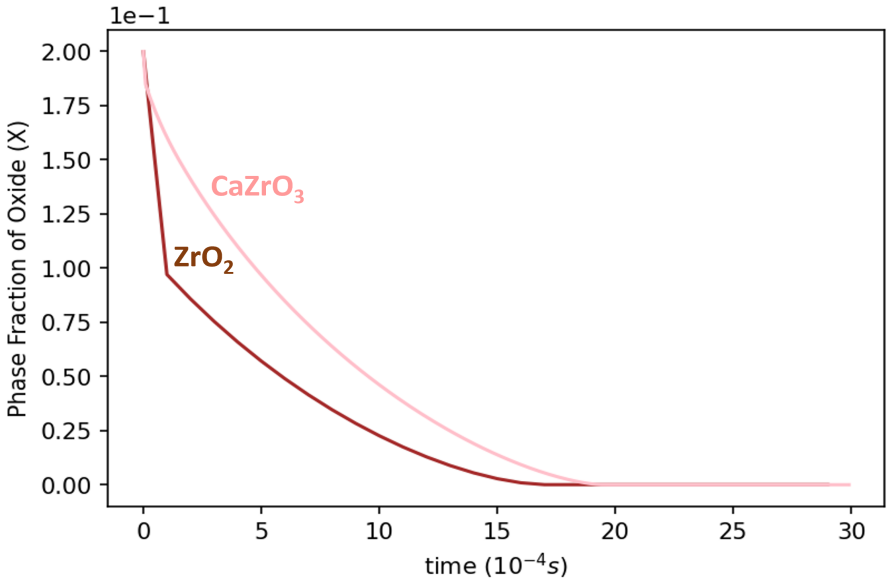

Figure 105: Phase fractions of CaO and $CaZrO_3$ in TiAl melt

Figure 106 presents the dissolution kinetics of three different ZrO_2 structures in a TiAl melt. The results demonstrate that the fluorite structure is the most stable, followed by the tetragonal and monoclinic structures. The fluorite structure shows stability that is second only to Y_2O_3 (as depicted in figure 99). Although tetragonal is more stable than mono-clinic, it still completely dissolves into the liquid.

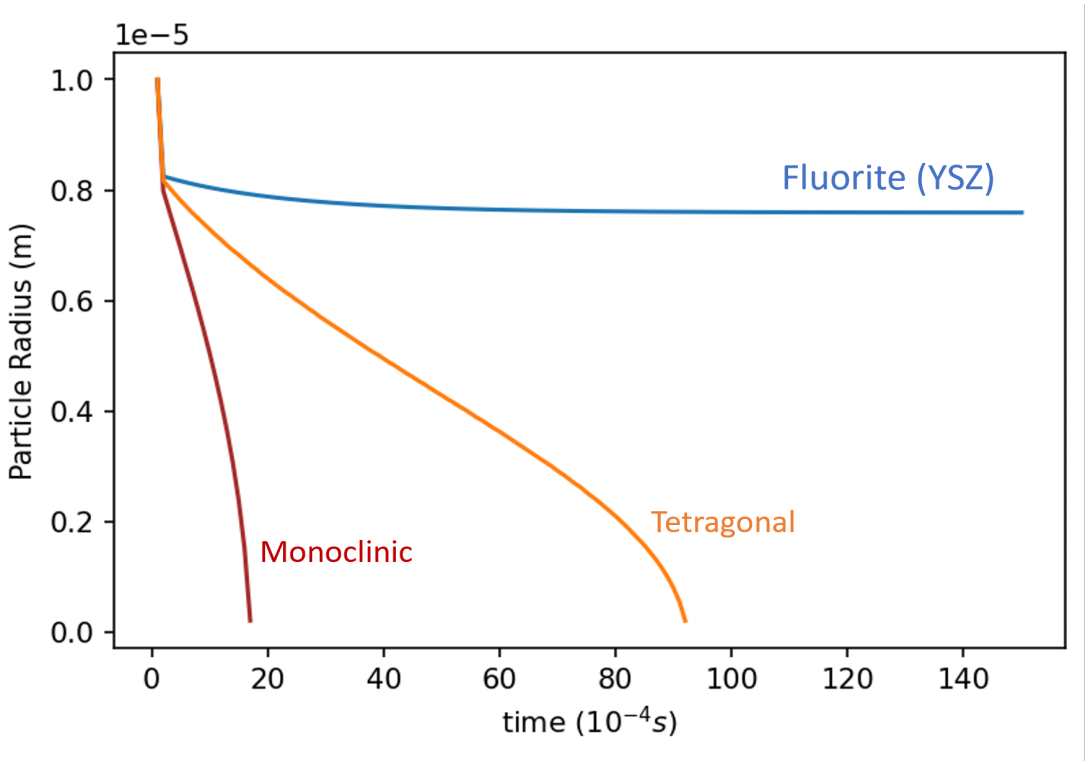

Figure 106: Dissolution profiles of mono-clinic, tetragonal and fluorite ZrO_2 structures in TiAl melt at 2000K

4.6 Non-Equilibrium, Non-Ideal, Multi-Phase Reaction- Al_2O_3 and Y_2O_3 System

Figure 107 presents a simulations of multiple Al_2O_3 and CaO particles (single phase) in TiAl melt, specifically designed to explore the effects when one of the Al_2O_3 particle or CaO particle is replaced with another phase. This simulation allows for a comparative analysis of the behaviour of Al_2O_3 alongside a different oxide phase within the liquid. Similar is also true for single oxides that established an equilibrium with the liquid link in figure 99.

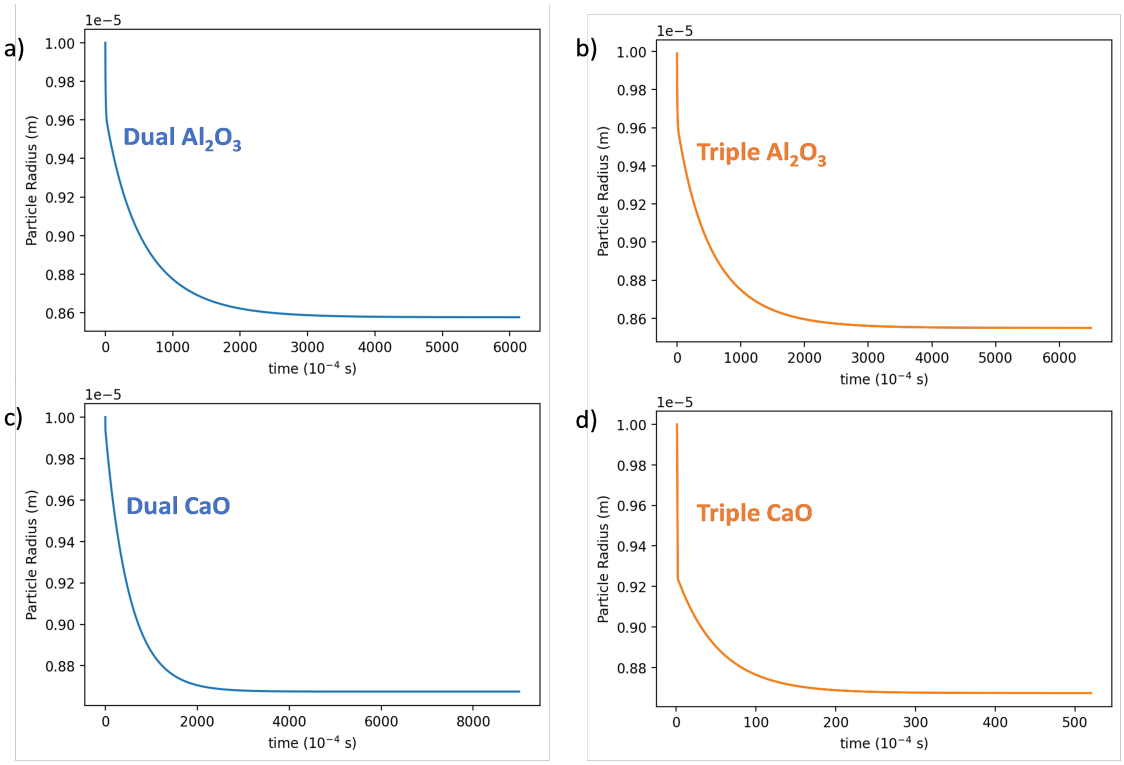

Figure 107: a) Dissolution kinetics of two Al_2O_3 particles in TiAl melt. b) Dissolution kinetics of three Al_2O_3 particles in TiAl melt. c) Dissolution kinetics of two CaO particles in TiAl melt. d) Dissolution kinetics of three CaO particles in TiAl melt.

Figure 108 illustrates the dissolution behaviour of Al_2O_3 and Y_2O_3 particle in a liquid Ti-Al melt. Initially, both Al_2O_3 and Y_2O_3 start with the same particle radius in the liquid but exhibit different dissolution rates. Eventually, both particles completely dissociate into the liquid, with Al_2O_3 dissolving quicker than Y_2O_3. It is noteworthy that this dissolution process occurs rapidly. Furthermore, figure 109 shows the reaction rate constants for the reaction calculated through changes in

phase fraction. The rate constants k1 and k2 indicate the dissolution constants of Al_2O_3 and Y_2O_3 respectively. In contrast to simulation in figure 107, where multiple Al_2O_3 particles reached an equilibrium state. Switching, the Al_2O_3 particle with Y_2O_3 destabilised both the oxides.

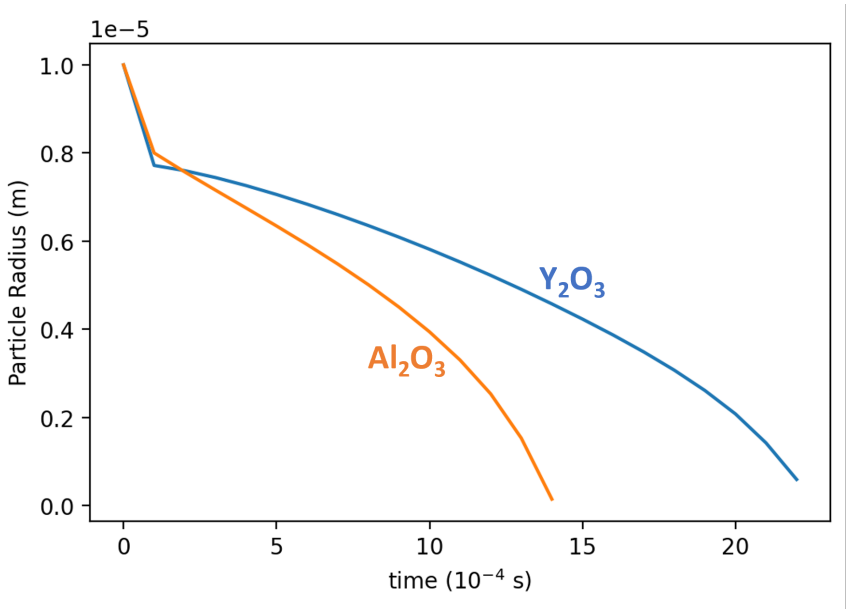

Figure 108: Dissolution of Y_2O_3 and Al_2O_3 multi-phase reaction in Ti-Al melt

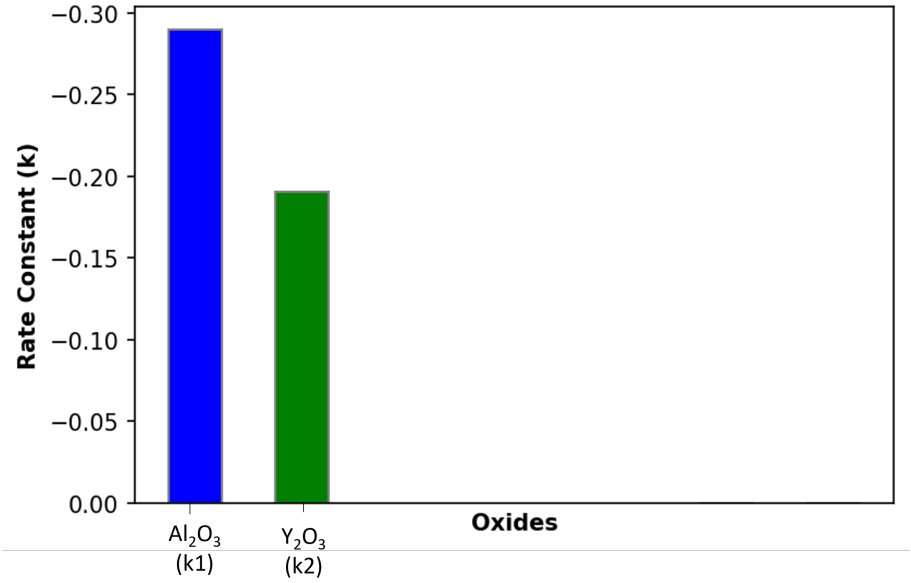

Figure 109: Rate constants for Al_2O_3 (k1) and Y_2O_3 (k2)

Figure 110 illustrates the time-dependent driving forces (ΔG_r) for Y_2O_3 and Al_2O_3. Both particles display negative driving forces, which correspond to their dissolution behaviour. Notably, the ΔG_r values for Al_2O_3 are more negative than those for Y_2O_3, indicating that Al_2O_3 dissolves more rapidly. Interestingly, the driving forces for both oxides exhibit an inverse relationship, where the trends in their ΔG_r values are opposing one another. As Al_2O_3 shows a trend towards stabilization (less negative ΔG_r) during the early stages of the reaction, the Y_2O_3 becomes increasingly unstable (more negative ΔG_r). Conversely, when ΔG_r, for Al_2O_3 drops (tending towards more negative ΔG_r), the Y_2O_3 tends towards stabilization (less

negative ΔG_r).

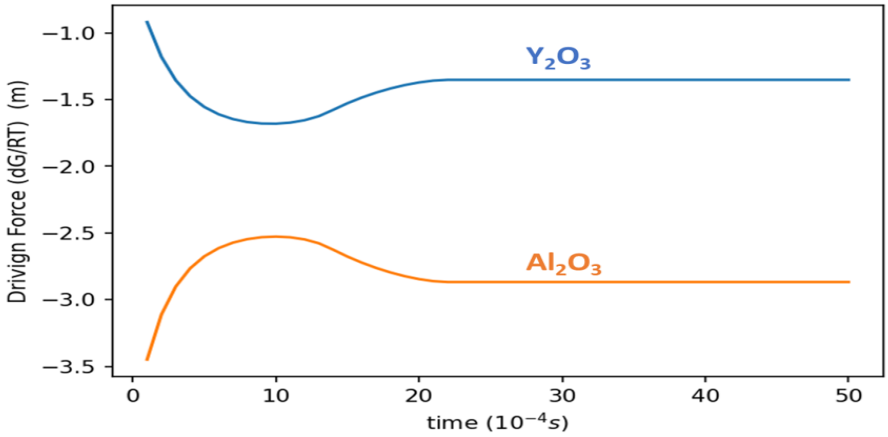

Figure 110: Driving force ΔG_r for Y_2O_3 and Al_2O_3 in Ti-Al melt

As illustrated in figure 111, when the activity of Al increases, the activity of Y decreases proportionally. Conversely, when Al_2O_3 is fully dissolved and the activity of Al is reduced, while the activity of Y in the liquid phase starts to increase. These opposing effects between Y and Al lead to an increased instability of both oxides, causing them to dissolve more readily.

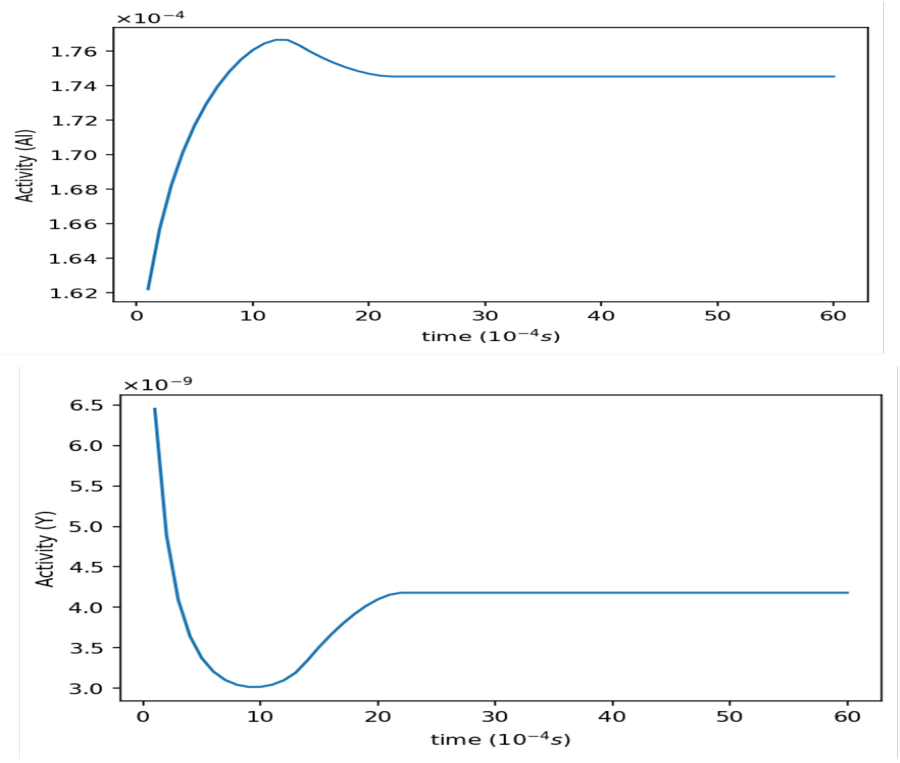

Figure 111: Y and Al activities in the liquid as a result of particle dissolution

Figure 112 illustrates the activity of yttrium across varying aluminium compositions. As the aluminium composition increases, yttrium exhibits a pronounced negative deviation from ideal behaviour. This negative deviation indicates a strong intermetallic interaction between yttrium and aluminium. Consequently, there is potential for the formation of multiple intermetallic phases between these two elements.

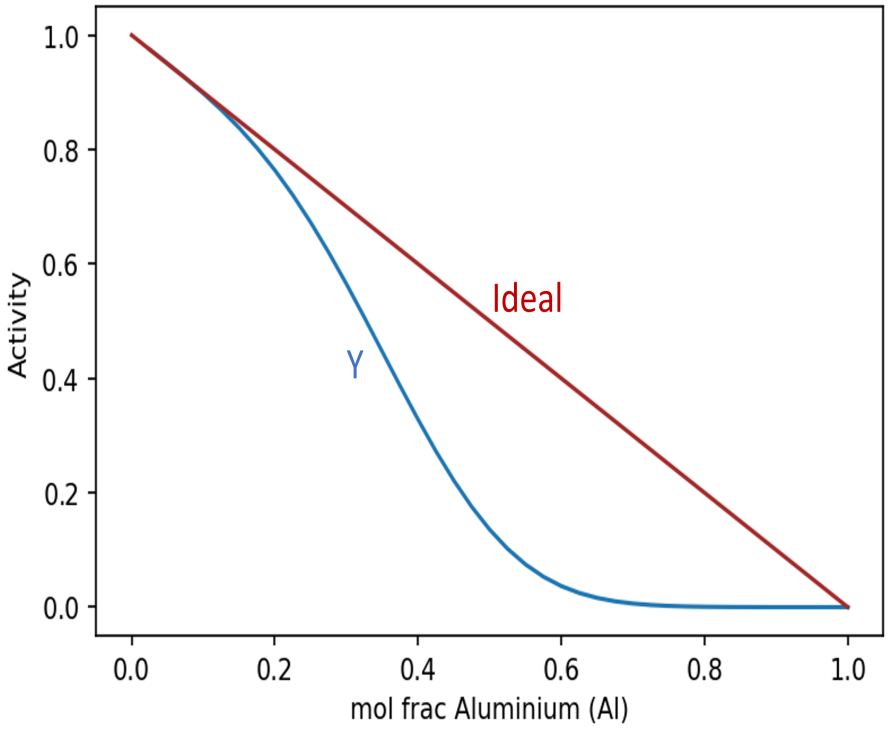

Figure 112: Y and Al binary activity diagram, 2000 K, (TCOX11)

4.6.1 Analytical Solution for the Dissolution of Al_2O_3 and Y_2O_3 in TiAl Melt

Figures 113 to 115 shows the comparison of analytical and numerical solution obtained for the dissolution Al_2O_3 and Y_2O_3 in TiAl. The figures represent the changes in phase fractions of Al_2O_3, Y_2O_3 and liquid during the dissolution reaction. Both the analytical and numerical solutions are in close agreement with minor deviations from each other. The analytical solution exhibits a smoother and more continuous

change in phase fraction, while the numerical solution displays less continuity. This discrepancy is most noticeable during the early stages of the reaction, where the numerical results show sharp changes in phase fraction, resulting in visible kinks across all three cases before transitioning to a more continuous trend. These kinks are numerical artifacts caused by the relatively large time step used in the simulation. Reducing the time step would improve temporal resolution, thereby minimizing these artifacts and producing a smoother phase fraction curve. Nevertheless, both solutions show identical equilibrium state and similar reaction times.

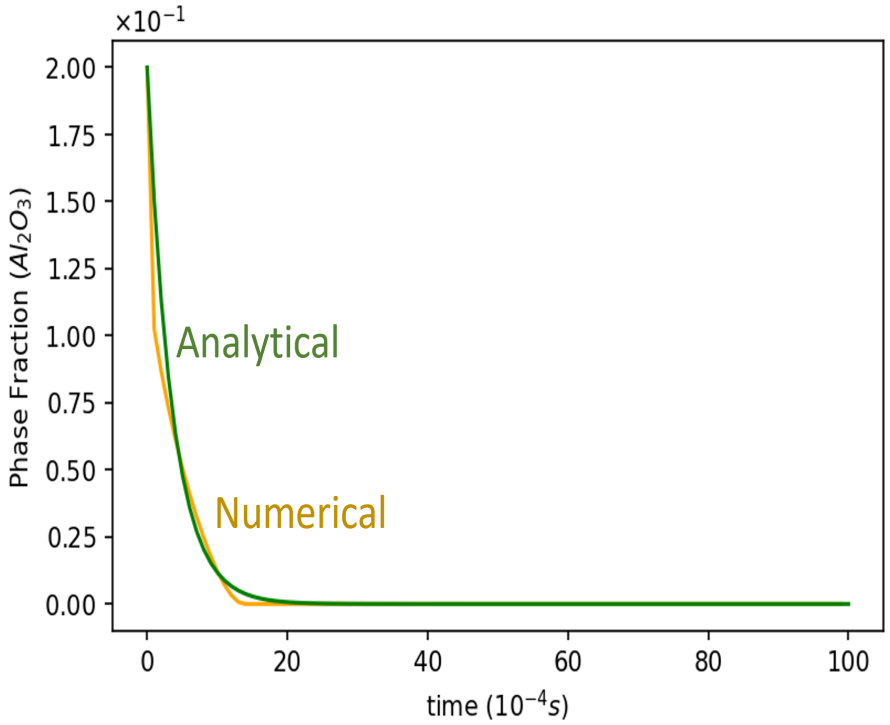

Figure 113: Comparison of analytical and numerical solution of phase fraction of Al_2O_3

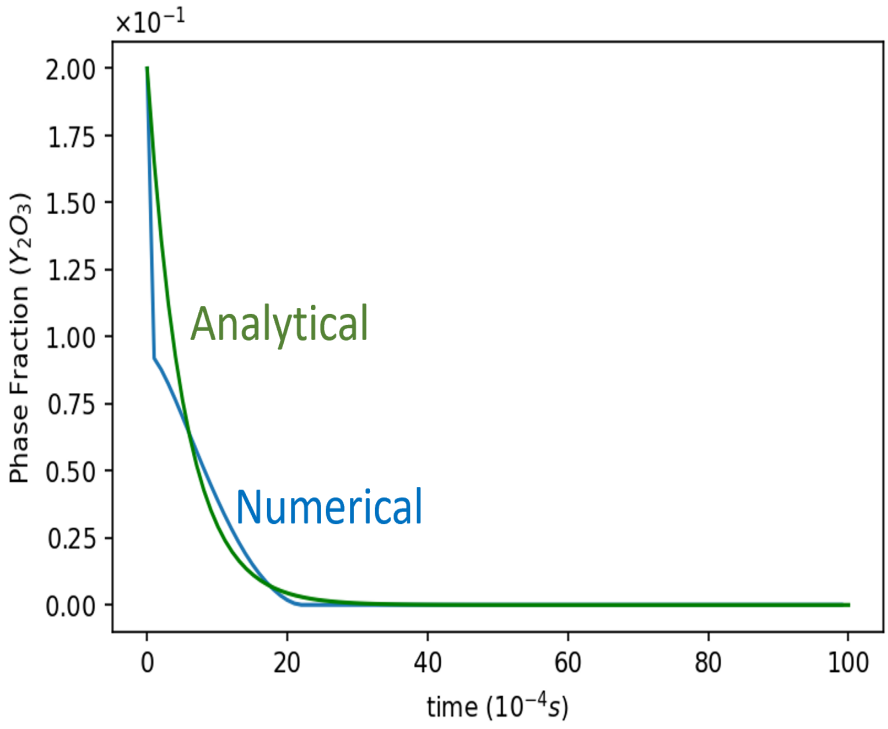

Figure 114: Comparison of analytical and numerical solution of phase fraction of Y_2O_3

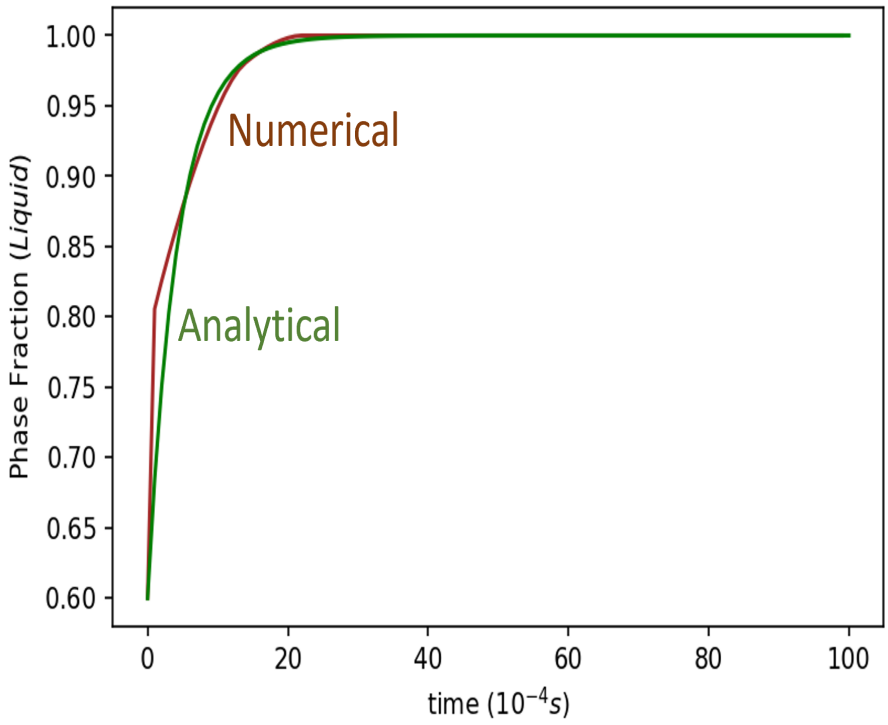

Figure 115: Comparison of analytical and numerical solution of phase fraction of liquid

Figures 116 and 117 show the effects of increasing k_1, which is the dissolution rate of Al_2O_3. As the dissolution of Al_2O_3 increases, k_2, the dissolution rate of Y_2O_3, decreases. Similarly, increased dissolution of Al_2O_3 increases the rate of liquid formation. From these simulations, the interdependence of k_1 and k_2 can clearly be seen. To slow down the dissolution of Y_2O_3, one can increase k_1, and vice versa.

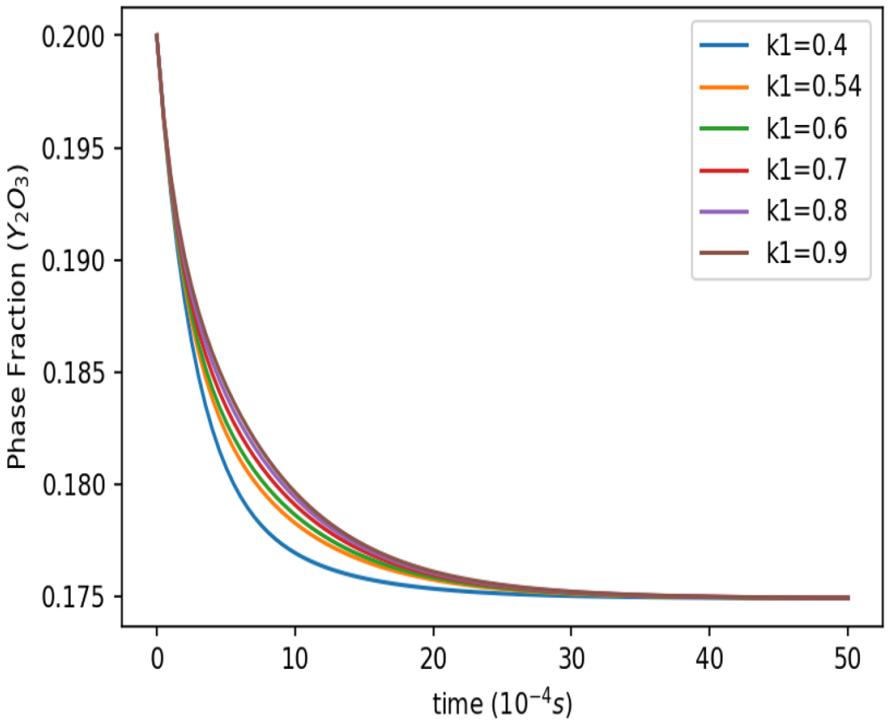

Figure 116: Changes in phase fraction of Y_2O_3 as a result of increasing k1

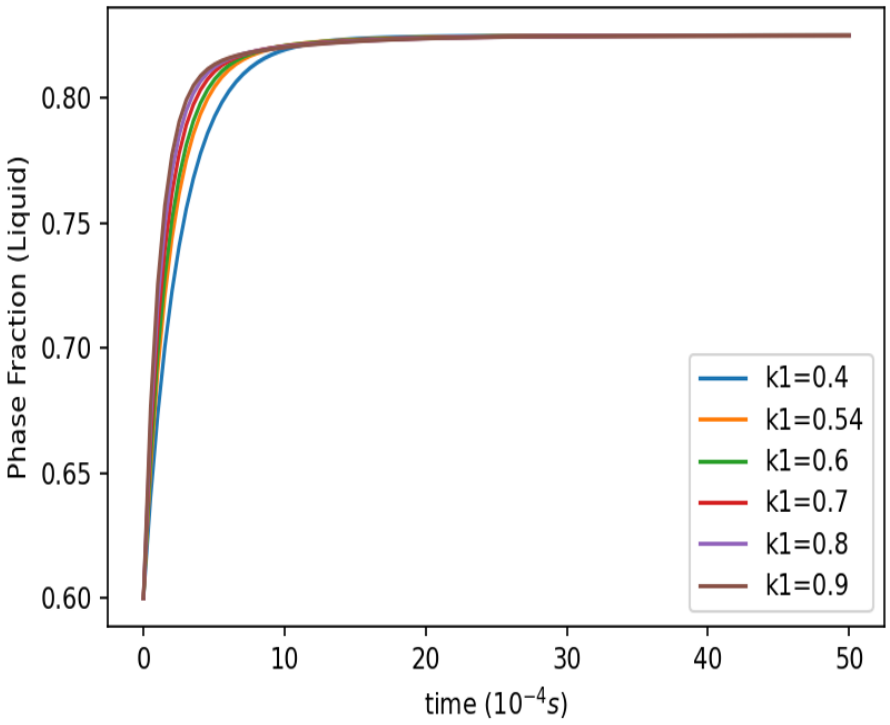

Figure 117: Changes in phase fraction of liquid as a result of increasing k1

4.6.2 Improving Performance of Y_2O_3 via Adjusting Initial Conditions

Figure 118 illustrates the effect of increasing initial yttrium content on the stability of yttrium particles. At lower yttrium compositions of 0.0001 and 0.05, the particles completely dissociates. However, at higher yttrium compositions of 0.07 and 0.1, the Y_2O_3 particle eventually become stable despite some initial dissolution. Increasing the yttrium composition in the melt enhances the stability of Y_2O_3 particles, leading to greater overall stability. It is also imperative to note that during the initial stages

of the reaction, the system is in a state of flux as it attempts to establish a steady state. During this period, the particles experience a combination of growth and dissolution within the first few time steps of the reaction until a steady state is achieved.

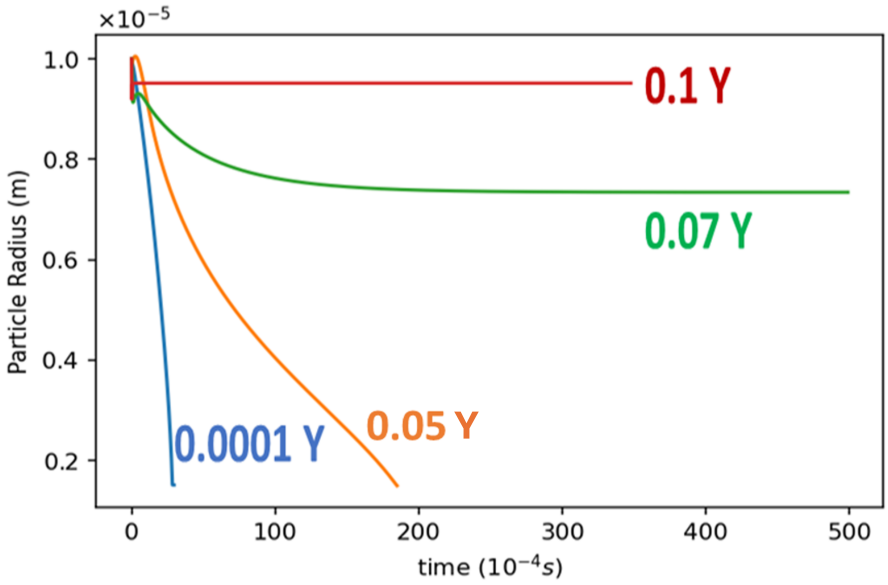

Figure 118: Y_2O_3 Particle stability under various initial compositions of yttrium

Figure 119 illustrates the effect of increasing yttrium content on the driving force of Y_2O_3. As the yttrium content increases, the driving forces become less negative and eventually positive at a yttrium composition of 0.1 mol fraction. Additionally, the depth of the minima decreases with higher Y content, further enhancing the stability of the particle. Minimizing this minima is essential for maintaining particle stability and increasing the initial yttrium content is an effective method to achieve

this.

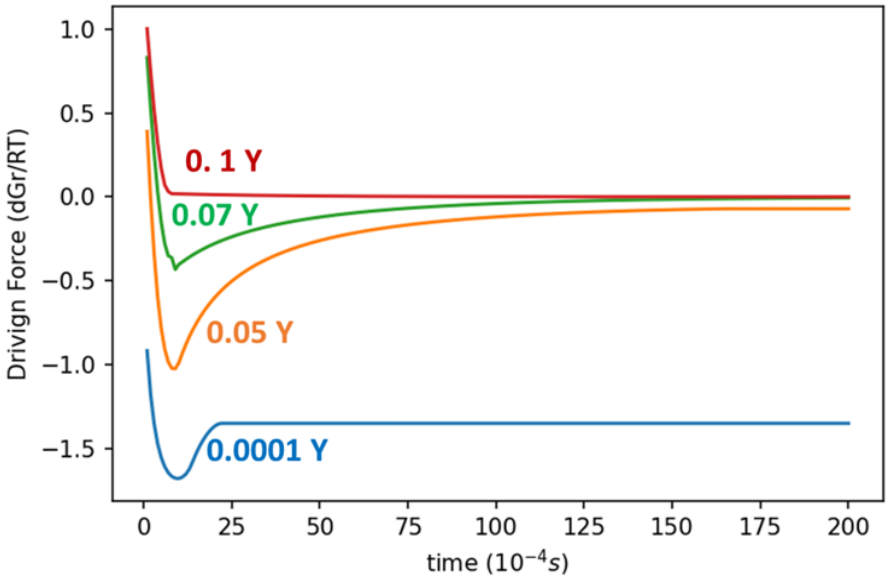

Figure 119: Driving force of Y_2O_3 for various initial yttrium composition in the liquid

Figure 120 illustrates the equilibrium oxygen concentration in the liquid for various initial concentrations of yttrium in the melt. As the yttrium concentration in the liquid increases, the equilibrium concentration of oxygen decreases. This behaviour is anticipated, as increasing the yttrium concentration shifts the reaction equilibrium to the stabilise the Y_2O_3 particle according to Le Chatelier's principle. This demonstrates the deoxidation behaviour of yttrium. The results indicate that lower oxygen concentrations can be achieved by increasing the yttrium content in the liquid.

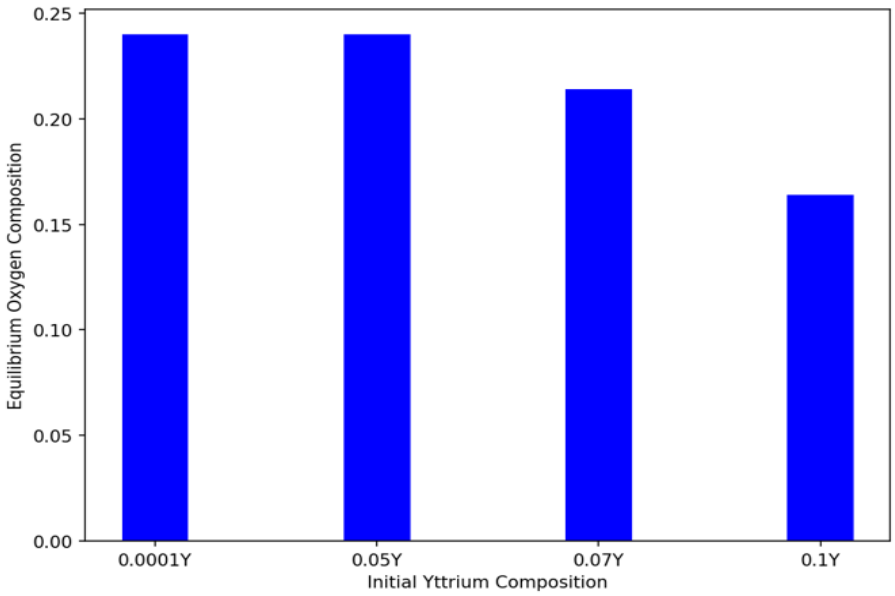

Figure 120: Equilibrium oxygen mol fraction in liquid for various initial concentrations of yttrium in the liquid

Figure 121 presents the reaction rate constants k_1 and k_2 for the multi-phase reaction Al_2O_3, and Y_2O_3, with k_1 and k_2 representing the dissolution rates of these oxides respectively. As the initial concentration of yttrium in the liquid increases, the reaction constant for Al_2O_3 (k_1) also increases, indicating faster dissolution of Al_2O_3 particle. In contrast, the rate constant k_2 decreases indicating a slower reaction rate. This interdependence between k_1 and k_2 shows that an increase in k_1 results in a decrease in k_2, and similarly, an increase in k_2 would decrease k_1. At a yttrium concentration of 0.1, the Y_2O_3 particles exhibit growth due to high activity of Y.

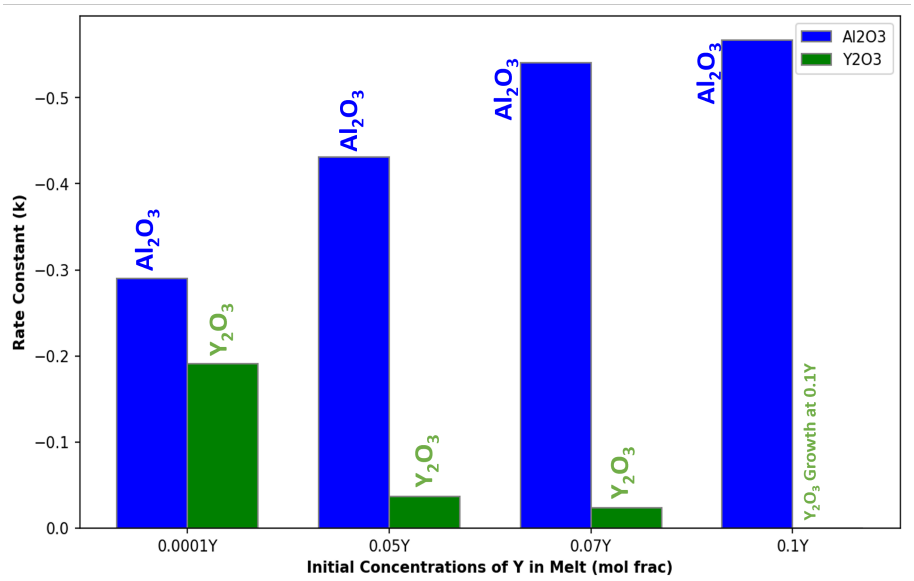

Figure 121: Rate constants for Al_2O_3 (k1) and Y_2O_3 (k2) in Ti-Al melt various initial Y compositions

4.6.3 Improving Stability of Oxides via Alloying Additions

Figure 122 shows the stability of Al_2O_3 and Y_2O_3 particles in a Ti-Al-0.1Cr-0.1Nb alloy, highlighting the impact of Nb and Cr additions on the dissolution behaviour of these oxides. Compared to their stability in pure gamma phase, shown in figure 108, both Al_2O_3 and Y_2O_3 exhibit increased stability in the alloy. Al_2O_3 maintains its stability for over $20 \cdot 10^{-4}$ s, while Y_2O_3 remains stable for around $27 \cdot 10^{-4}$ s. This shows that both reaction rates of Al_2O_3 and Y_2O_3 can be lowered by the addition of Nb and Cr, whereas in the previous instance reaction rate of Al_2O_3

dissolution increased in order to slow down the dissolution of Y_2O_3. Additionally, the large drop in radius observed during the initial stages in pure gamma has been minimized, indicating a lower chemical potential difference between the oxides and the melt. This reduction in chemical potential difference significantly decreases the rate of initial dissolution, implying that the presence of Nb and Cr helps stabilize the oxides in the alloy environment.

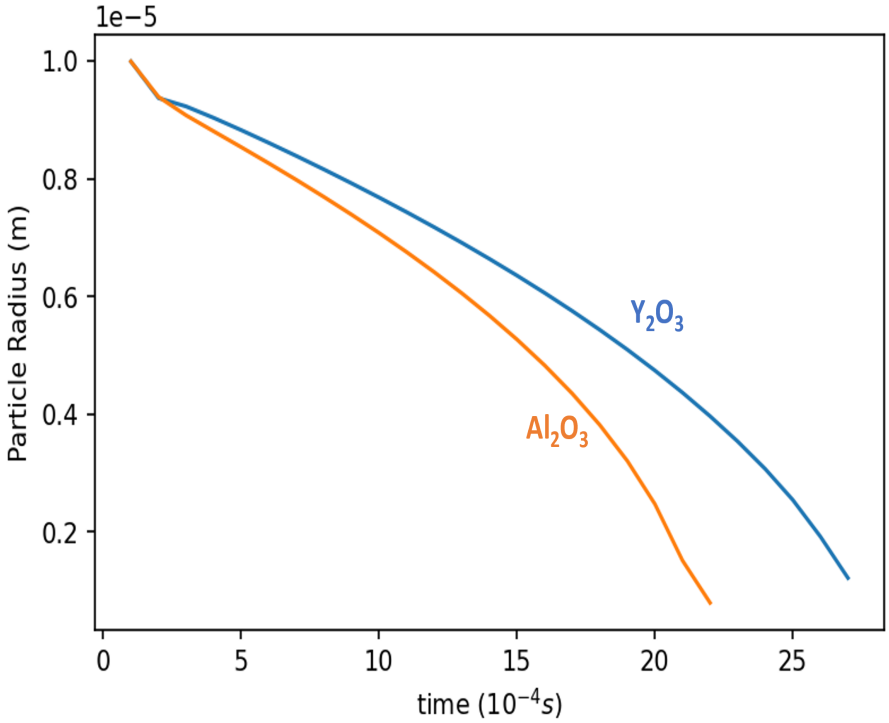

Figure 122: Y_2O_3 and Al_2O_3 particle dissolution in Ti-Al-0.1Cr-0.1Nb alloy

Figure 123 shows the driving forces of Y_2O_3 and Al_2O_3 where the dip and rise

effect still exists but much more flatter and spread out than in figure 110. The flattening of the maxima and the minima leads to slowing down of both the reaction rates.

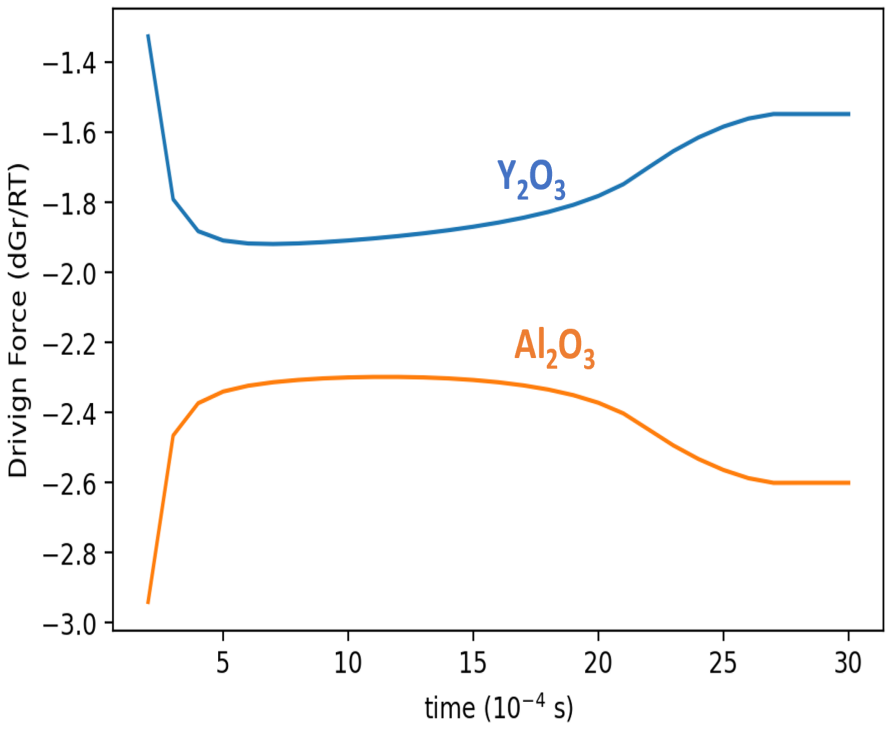

Figure 123: Driving force for Y_2O_3 and Al_2O_3 in Ti-Al-0.1Cr-0.1Nb alloy for the dissolution of Y_2O_3 and Al_2O_3

Activities of elements in the liquid is given in figures 124 to 126 for both Ti-Al and Ti-Al-Nb-Cr system. In Ti-Al-Nb-Cr system the yttrium activity (figure 124) gets lower than in TiAl but the oxygen activity gets higher in Ti-Al-Nb-Cr melt than in TiAl melt (figure 125). Al activity is high in TiAl melt but lowers in Ti-Al-Nb-Cr

alloy (figure 126).

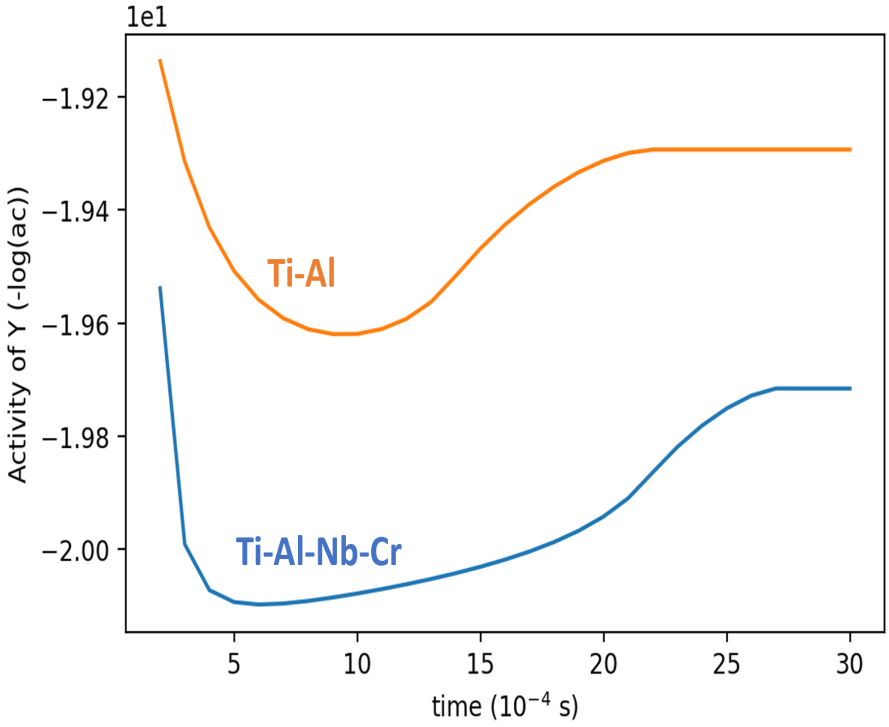

Figure 124: Comparison of activity of yttrium in TiAl and Ti-Al-0.1Cr-0.1Nb alloy for the dissolution of Y_2O_3 and Al_2O_3

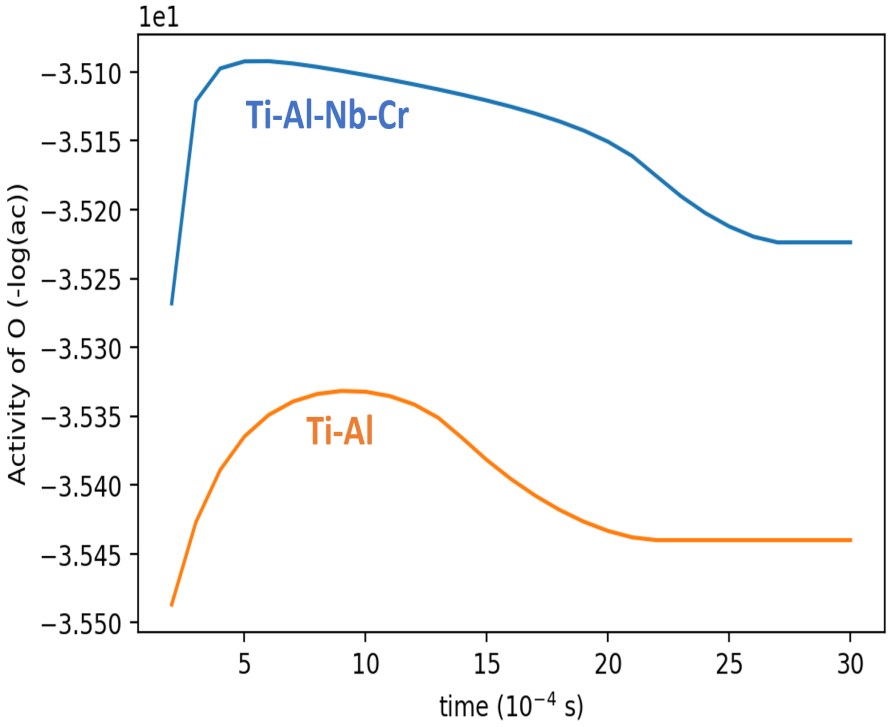

Figure 125: Comparison of the activity of oxygen in TiAl and Ti-Al-0.1Cr-0.1Nb alloy for the dissolution of Y_2O_3 and Al_2O_3

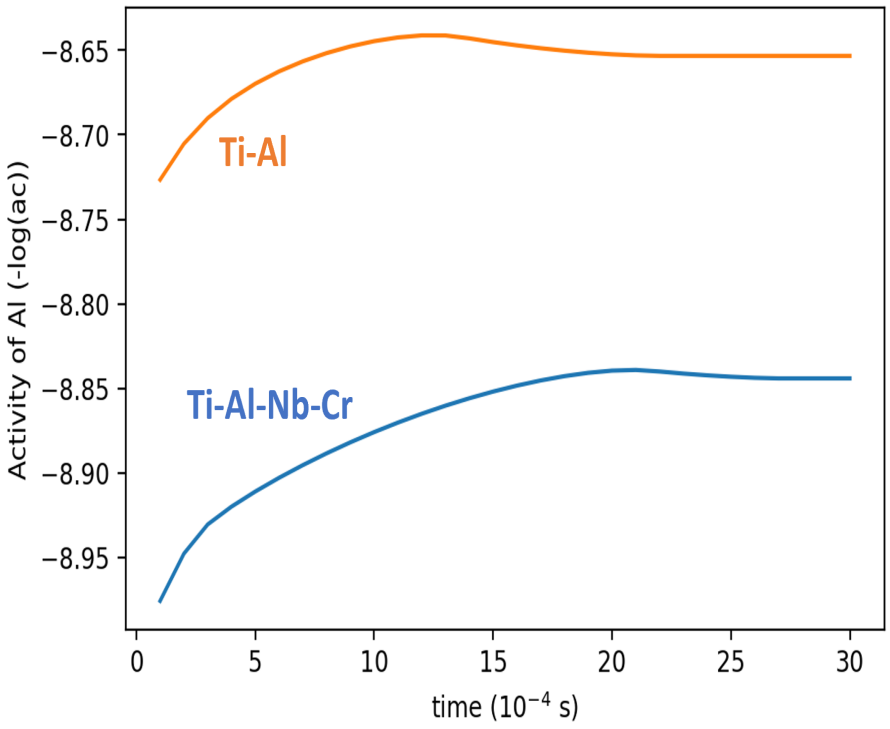

Figure 126: Comparison of the activity of Al in TiAl and Ti-Al-0.1Cr-0.1Nb alloy for the dissolution of Y_2O_3 and Al_2O_3

4.6.4 Improving Performance of Y_2O_3 via Other Oxide Combinations

With reference to the binary activity diagram of yttrium (Y) in aluminium (Al), zirconium (Zr), and calcium (Ca) at 2000 K, as shown earlier in figure 77, the activity of yttrium varies significantly depending on the accompanying element. Yttrium demonstrates a negative deviation from ideal behaviour when alloyed with Al, whereas it shows a positive deviation when combined with either Zr or Ca. A

negative deviation from ideal behaviour suggests a strong inter-metallic interaction between Y and Al, which could result in the formation of Y-Al phases. Conversely, a positive deviation implies a repulsive interaction between the elements, indicating a lower likelihood of phase formation.

In terms of mould selection, negative deviation observed in the Y-Al combination is undesirable due to the strong potential for forming Y-Al phases, which could lead to destabilization, as previously noted. In contrast, the positive deviation in the interactions between Y, Ca, and Zr is advantageous since it indicates a reduced tendency for forming stable phases.

Figure 127 represents the stability of CaO and Y_2O_3 particle in a TiAl melt. During the initial stages of the reaction, both particles begin to dissolve into the liquid melt, but Y_2O_3 reaches an equilibrium state, whereas CaO completely dissociates into the liquid. This behaviour contrasts with previous observations in figure 108, where Al_2O_3 was used instead of CaO. In that instance, both Al_2O_3 and Y_2O_3 dissociated at an accelerated rate without the liquid establishing an equilibrium state with the particles. Conversely, CaO dissolution is significantly slower even though the particle eventually disappears. Y_2O_3 also reacts more slowly compared to the previous instance and eventually stabilises. This slower reaction rate is highly desirable as it significantly reduces the dissolution rate when Al_2O_3 is replaced with

CaO, with the added benefit of a stable yttria particle. However, it is noteworthy that the stability of single phase (CaO and Y_2O_3) particles is higher compared to situations with multiple phases.

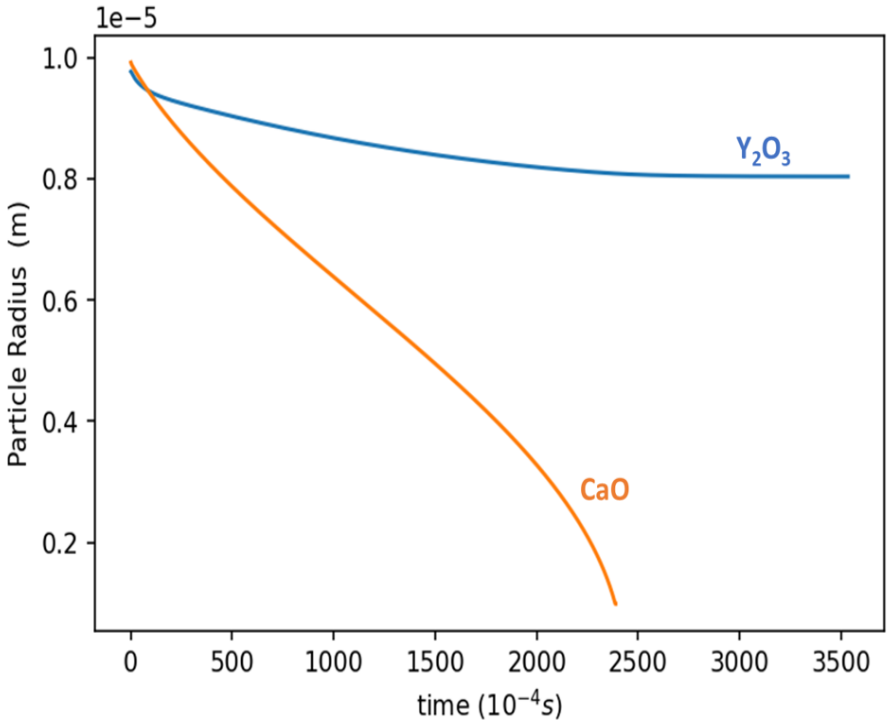

Figure 127: Multi-Phase stability of CaO and Y_2O_3 in TiAl

Figure 128 illustrates the driving forces of CaO and Y_2O_3 system. The driving force for Y_2O_3 converges to zero, signifying equilibrium state, whereas the driving force for CaO remains negative until the particle completely vanishes. This behaviour contrasts with the dip-rise-effect observed in figure 110, where Al_2O_3 was

used instead of CaO. The u-effect, evident with Al_2O_3, does not manifest when CaO is accompanied as a substitute particle.

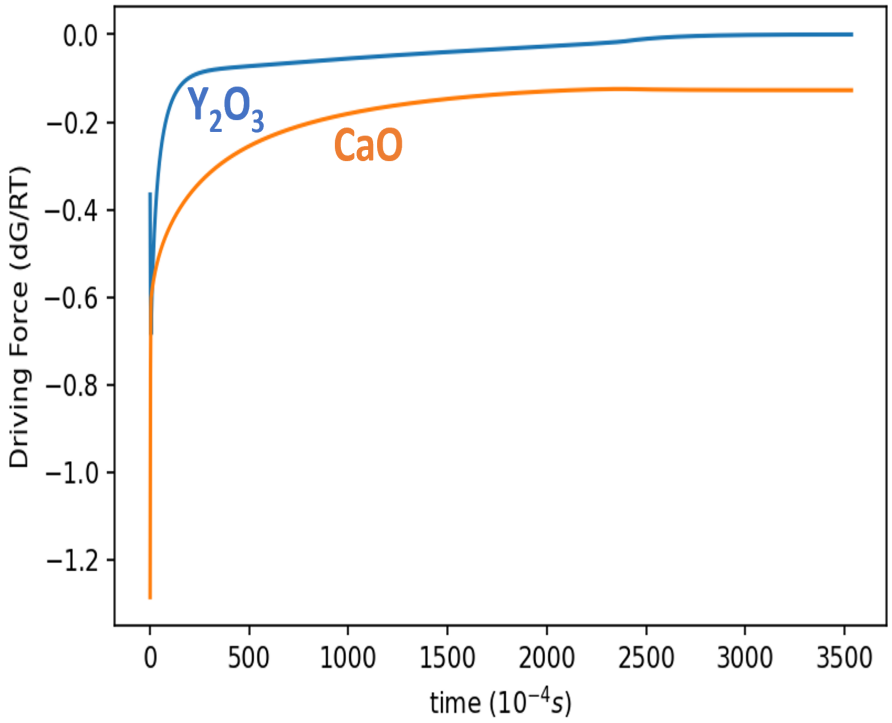

Figure 128: Driving force for the dissolution of Y_2O_3 and CaO particles

Figure 129 illustrates the activity of Y in two different systems. In the system containing CaO, the activity of yttrium in the liquid is substantially higher, which eventually contributes to the stability of Y_2O_3. In contrast, the activity of Y in the Al_2O_3-Y_2O_3 system is much lower, leading to the equilibrium shifting toward complete dissolution.

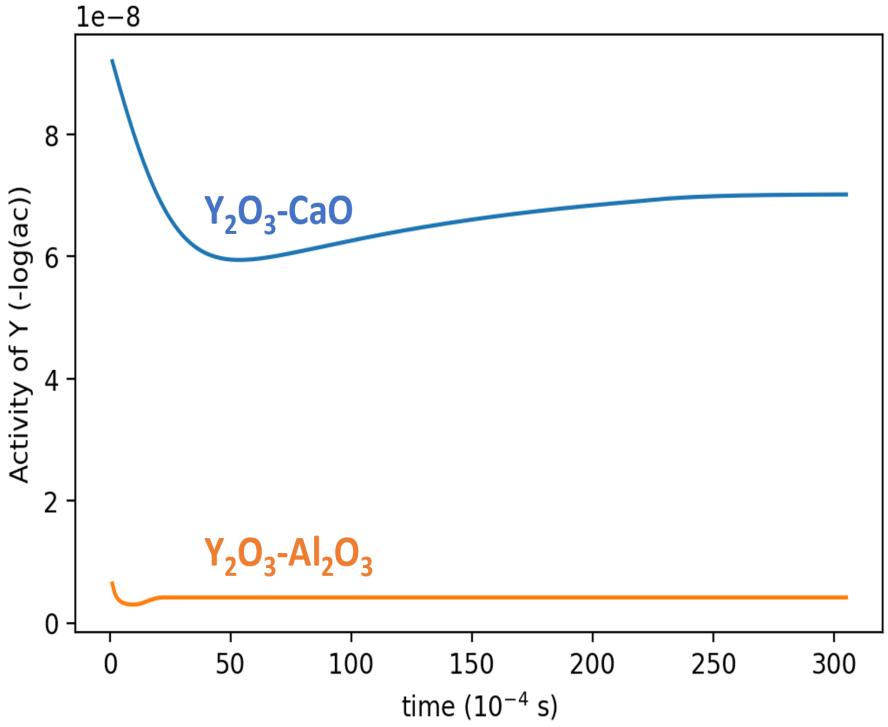

Figure 129: Comparison of the activity of Y in Y_2O_3-Al_2O_3 system vs Y_2O_3-CaO system

4.6.5 Y_2O_3 Destabilising Oxide Combinations

Figure 130 shows the kinetics of Al_2O_3, Y_2O_3, and CaO in a TiAl melt. When all three particles are present in the liquid, they destabilize each other and completely disappear into the liquid. CaO dissolution is the slowest, followed by Y_2O_3 and Al_2O_3. Compared to the previous simulations, this combination is the most undesirable. In contrast, the simulation of CaO and Y_2O_3 in TiAl melt shown in figure 127 indicates that Y_2O_3 eventually stabilizes, with CaO dissolving into the liquid. How-

ever, the presence of the third oxide (Al_2O_3) quickly destabilizes Y_2O_3, even in the presence of CaO. It appears that mixing three unlike oxides completely destabilizes each of them, similar to the effect observed when two dissimilar oxides are present in the liquid.

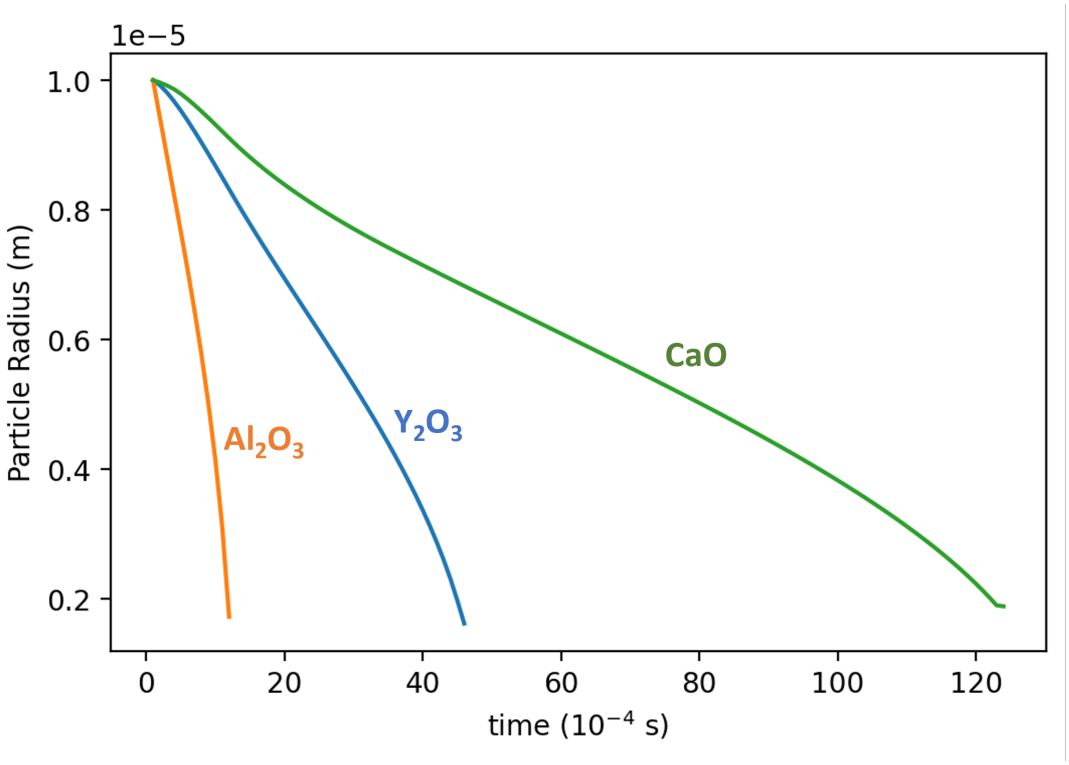

Figure 130: Multi-Phase, CaO-Al_2O_3-Y_2O_3 system stability in TiAl

Figure 131 shows the driving force for CaO, Y_2O_3, and Al_2O_3. The dip-and-rise effect is evident when these oxides are combined, with Al_2O_3 again causing this effect, as seen in the Y_2O_3 and Al_2O_3 system. This interaction explains why all three oxides

become destabilized when present together.

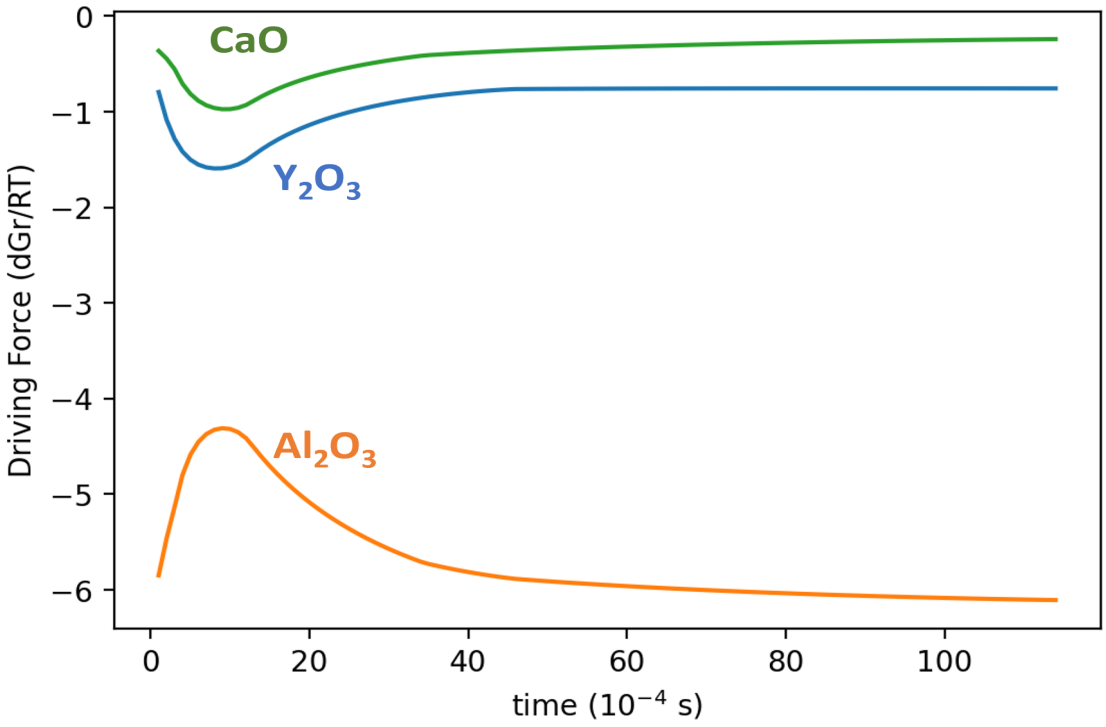

Figure 131: Driving force for dissolution CaO-Y_2O_3-Al_2O_3 in TiAl

Figure 132 shows the dissolution kinetics of Y_2O_3 and YAG in a TiAl melt. In this instance, Y_2O_3 reaches an equilibrium state, whereas the YAG completely dissolves into the liquid. Comparing these simulations to when these oxides are present as single phases (figure 99), both Y_2O_3 and YAG are much more stable and react at a much slower rate. Hence, this combination is undesirable since there is heavy dissolution of the oxide taking place. This can be attributed to the presence

of Al in the liquid and the Al dissolution resulting from the dissolution of YAG. This further destabilizes Y_2O_3, making it an undesirable combination. Although compared to figure 108 where Y_2O_3 and Al_2O_3 are present together in the melt the current combination is much more suitable since, the Y_2O_3 actually ends up becoming stable without completely disappearing into the liquid.

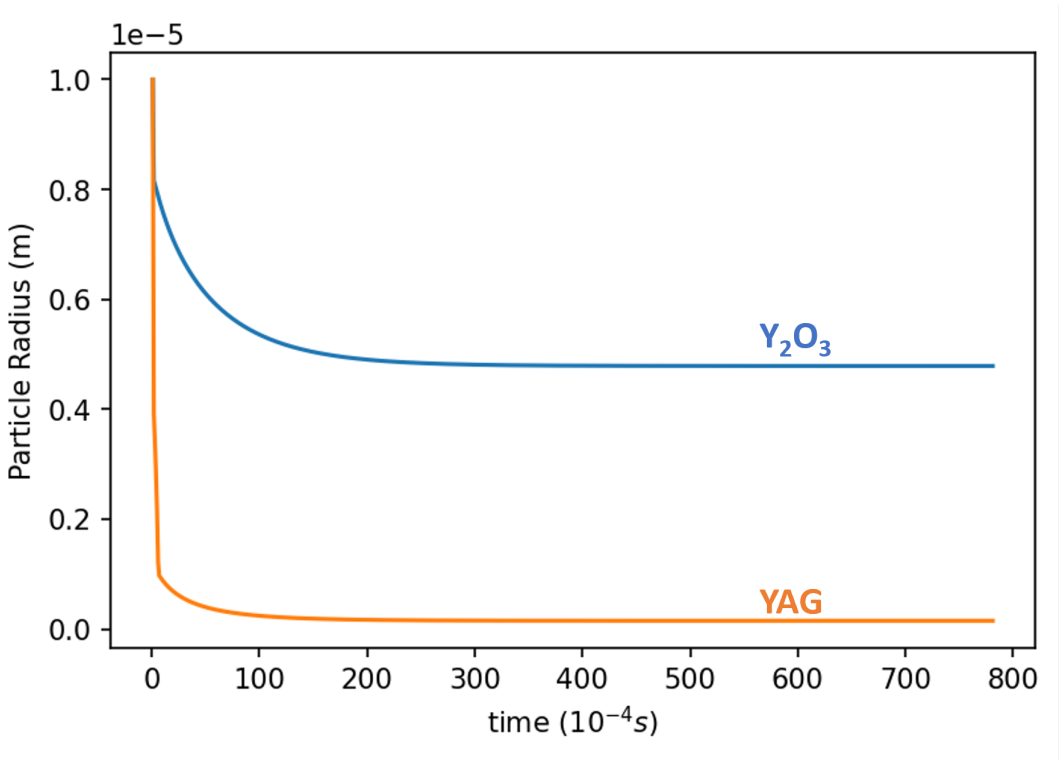

Figure 132: Multi-Phase stability of YAG and Y_2O_3 in TiAl

Figure 133 presents the dissolution kinetics of the Y_2O_3 and ZrO_2 together in TiAl melt. ZrO_2 was specifically chosen because, in the presence of Y, Zr exhibits

a positive deviation from ideal behaviour similar to Ca as shown in figure 77. However, both ZrO_2 and Y_2O_3 dissolve into the liquid, making the combination a highly undesirable combination. This observation is noteworthy since Zr and Ca exhibit similar interaction behaviour with Y, yet Y_2O_3 stabilizes in the presence of CaO but destabilizes in the presence of ZrO_2. Therefore, it is evident that intermetallic interaction is not the sole factor to be considered when selecting oxide combinations.

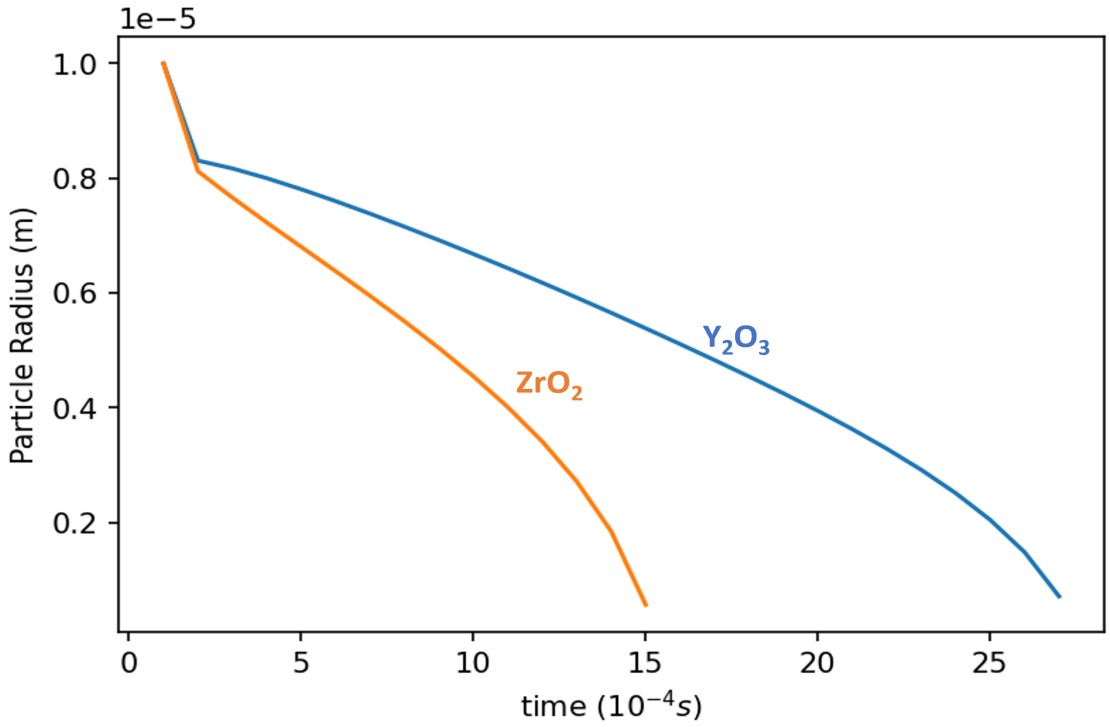

Figure 133: Multi-Phase stability of Y_2O_3 and ZrO_2 in TiAl melt

4.6.6 Stabilising Oxide Combinations

The dissolution kinetics of the system containing Y_2O_3, Al_2O_3, and YAG ($Y_3Al_5O_{12}$) particles in a TiAl melt, as depicted in figure 134, reveal a varied behaviour among the oxides. Both Al_2O_3 and Y_2O_3 particles dissolve completely into the melt, showing no signs of stability or reaching stable equilibrium. In contrast, YAG follows a different dissolution pattern. Initial, dissolution is observed but soon switches to growth very quickly. Initially, all particles, including YAG, undergo dissolution when exposed to the pure Ti-Al melt. This is consistent with prior simulations where all particles, even Y_2O_3, showed dissolution when in contact with pure Ti-Al melt. During this early stage, YAG exhibits the highest dissolution rate. However, after a few time-steps, the liquid becomes saturated with yttrium, aluminium, and oxygen, leading to a shift in equilibrium where YAG begins to stabilise. The elemental requirements for the growth of YAG is being taken from the dissolution of Al_2O_3 and Y_2O_3 particle, this is confirmed in figure 135. In general, YAG stabilizes, at the expense of Y_2O_3 and Al_2O_3. It is important to note that the final equilibrium radius of YAG is still smaller than its starting radius.

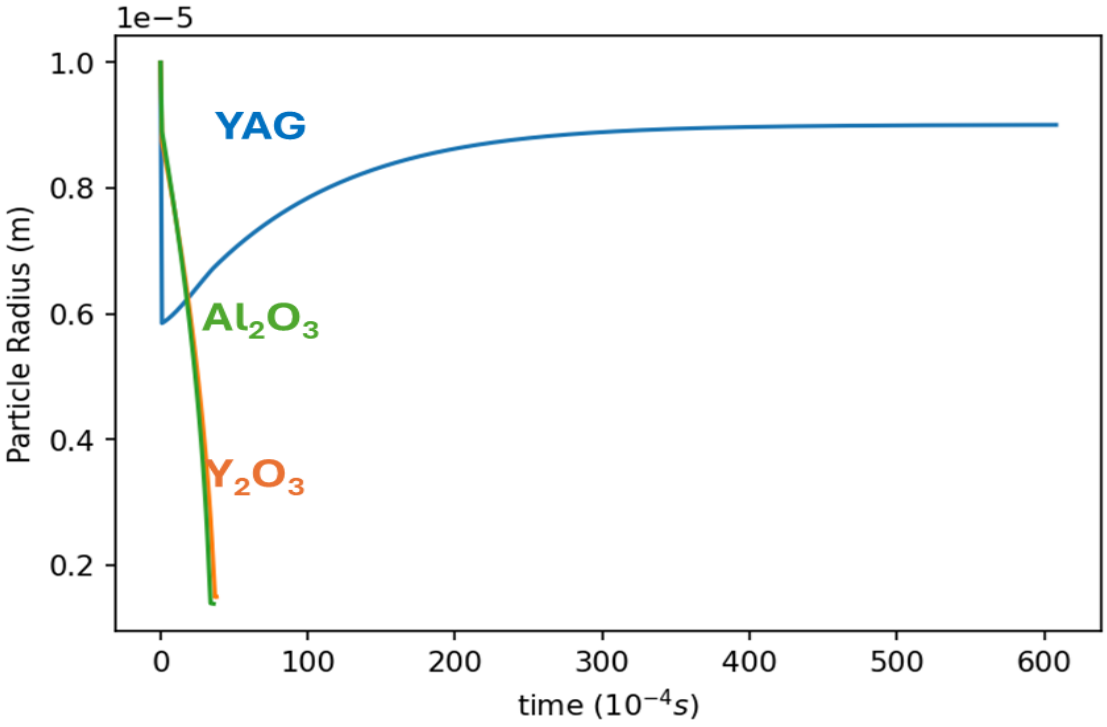

Figure 134: Multi-Phase stability of Al_2O_3, Y_2O_3 and YAG in TiAl melt

Compared to the simulation in figure 99, where YAG is present as a single phase oxide in TiAl melt, it reaches an equilibrium radius of just above $0.3 \cdot 10^{-5}$, significantly lower, than the radius reaches by this three phase system, indicating improved stability of the YAG particle. Interestingly, in figure 132, where YAG and Y_2O_3 are present, the YAG completely disappears, leaving only the Y_2O_3 particle stable. The addition of Al_2O_3 in this scenario completely shifts the equilibrium position, stabilizing the YAG particle. This behaviour can be explained by tracking the elemental

compositions of each particle as shown in figure 135 Al_2O_3 and Y_2O_3 release oxygen into the liquid, while YAG absorbs the oxygen released by these two particles. Notably, the rate of oxygen dissolution is significantly faster in the two particles, indicating that the dissolution of Al_2O_3 and Y_2O_3 finishes much earlier, whereas the growth of the YAG particle takes a longer.

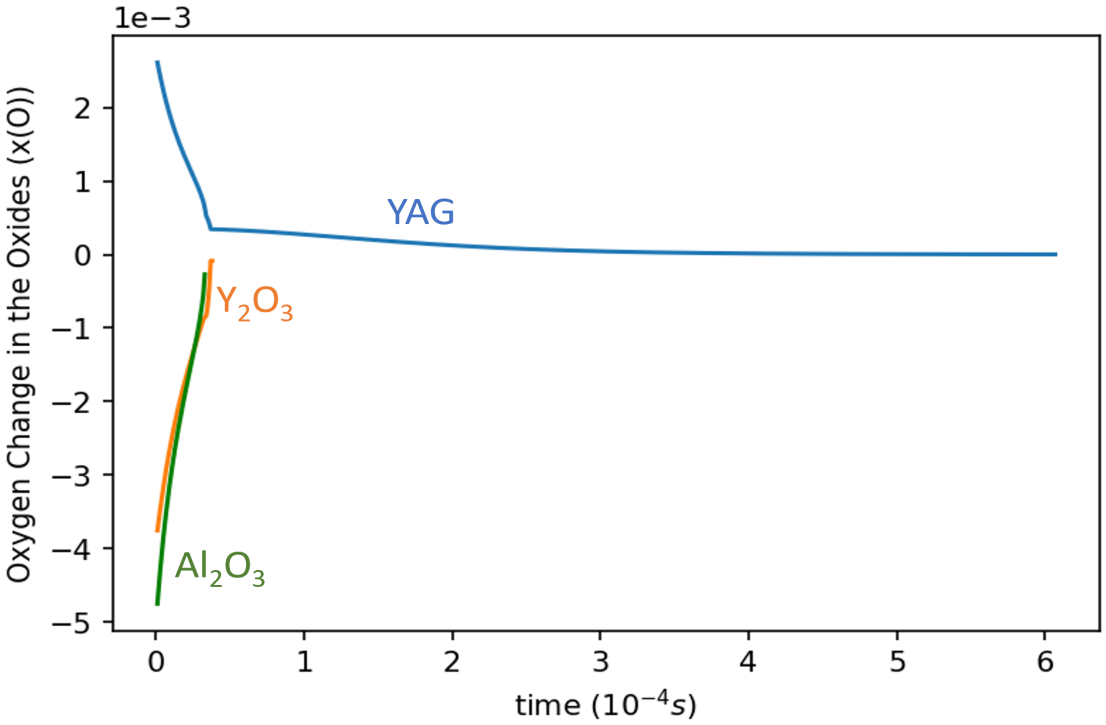

Figure 135: Oxygen exchange in Y_2O_3, Al_2O_3 and YAG

Figure 136 illustrates the kinetics of the system containing Al_2O_3 and mullite. In this instance, the mullite particle rapidly dissolves into the liquid, whereas the Al_2O_3

particle, despite experiencing some initial dissolution, begins to grow and eventually stabilizes at an equilibrium radius of approximately $> 1 \times 10^{-4}$ m, significantly larger than its initial radius of 1×10^{-5} m. This behaviour contrasts with previous simulations, where dissolution typically results in particles reaching an equilibrium radius much smaller than their initial size. Similar to the previous example, mullite acts as a source of oxygen and aluminium, facilitating the growth and stabilization of the Al_2O_3 particle. figure 137 illustrates the diffusion of oxygen into the Al_2O_3 particle. Initially, oxygen diffusion into the solid increases over time until it reaches a peak, after which the rate gradually decreases, eventually reaching zero. Oxygen is supplied by the rapid dissolution of mullite, which quickly saturates the melt with oxygen and aluminium, creating the conditions necessary for the growth of the Al_2O_3 phase

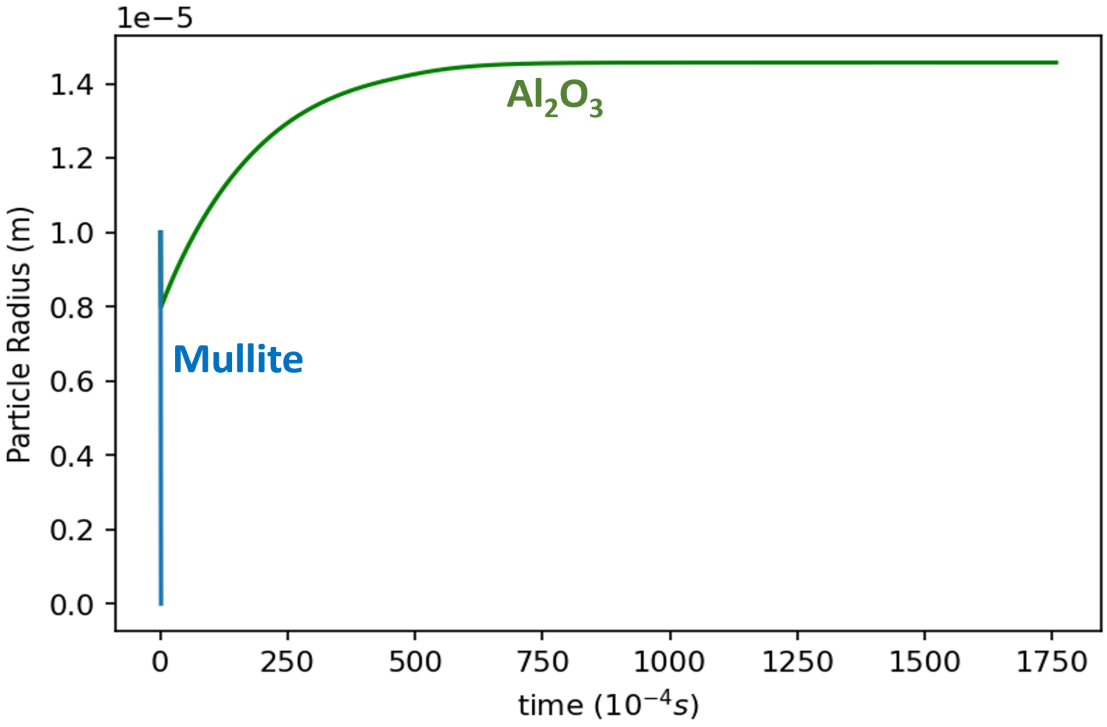

Figure 136: Multi-Phase stability of Al_2O_3 and mullite in TiAl melt

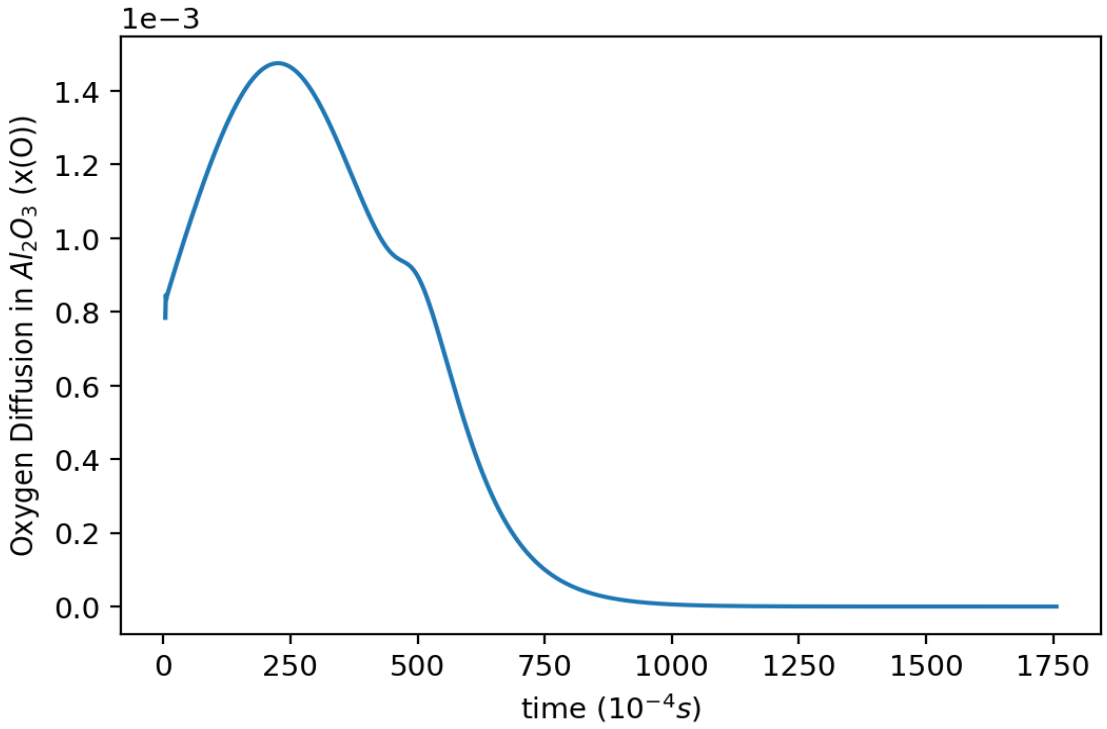

Figure 137: Oxygen diffusion into Al_2O_3 (Al_2O_3-mullite kinetics)

Figure 138 illustrates the influence of SiO_2 on the kinetics of Al_2O_3 and mullite, in contrast to the growth observed in figure 136, which lacked SiO_2. Similar to mullite, the SiO_2 particle dissolves into the liquid, albeit at a slower rate. The addition of SiO_2 significantly accelerates the growth kinetics of Al_2O_3, enabling equilibrium to be reached before 200×10^{-4} seconds, compared to approximately 750×10^{-4} seconds in figure 136. Notably, while the presence of SiO_2 enhances the kinetics, it does not alter the final equilibrium state of the system.

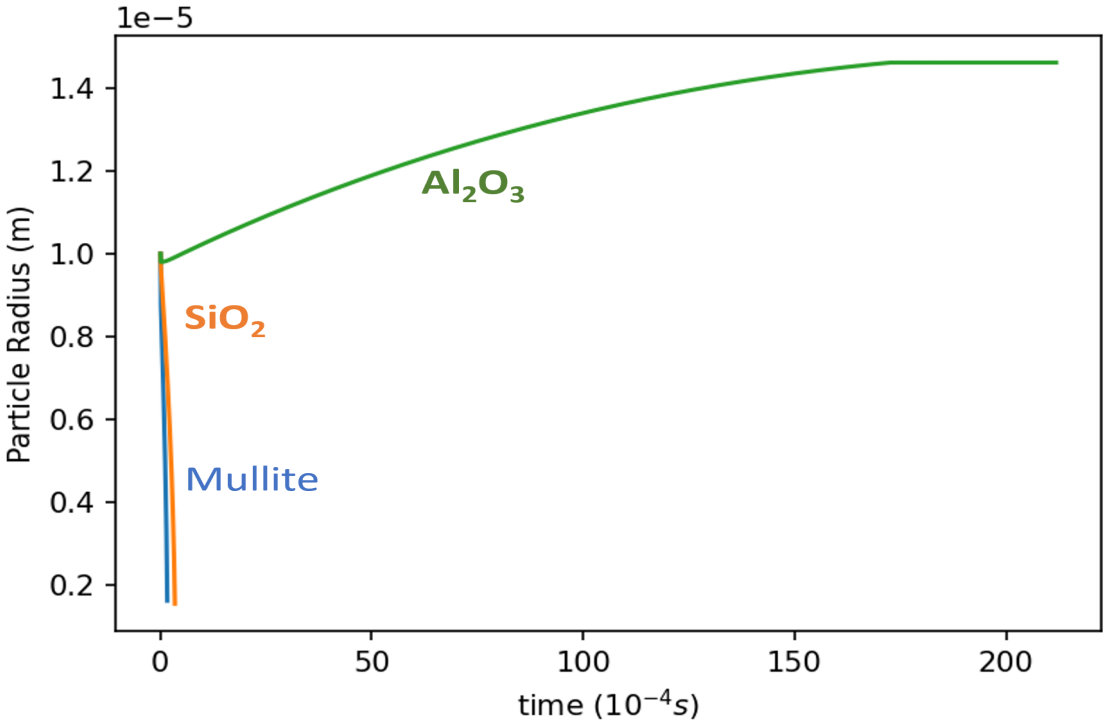

Figure 138: Multi-Phase stability of Al_2O_3, mullite and SiO_2 in TiAl melt

Figures 139 and 140 illustrate the oxygen exchange among the three oxides. As mullite and SiO_2 dissolve, they quickly release oxygen into the liquid (figure 140), which is then absorbed more slowly by Al_2O_3 (figure 139). The rapid release of oxygen from SiO_2 and mullite, due to their higher dissolution rates, contrasts with the slower diffusion of oxygen into Al_2O_3, indicating a slower growth rate for Al_2O_3.

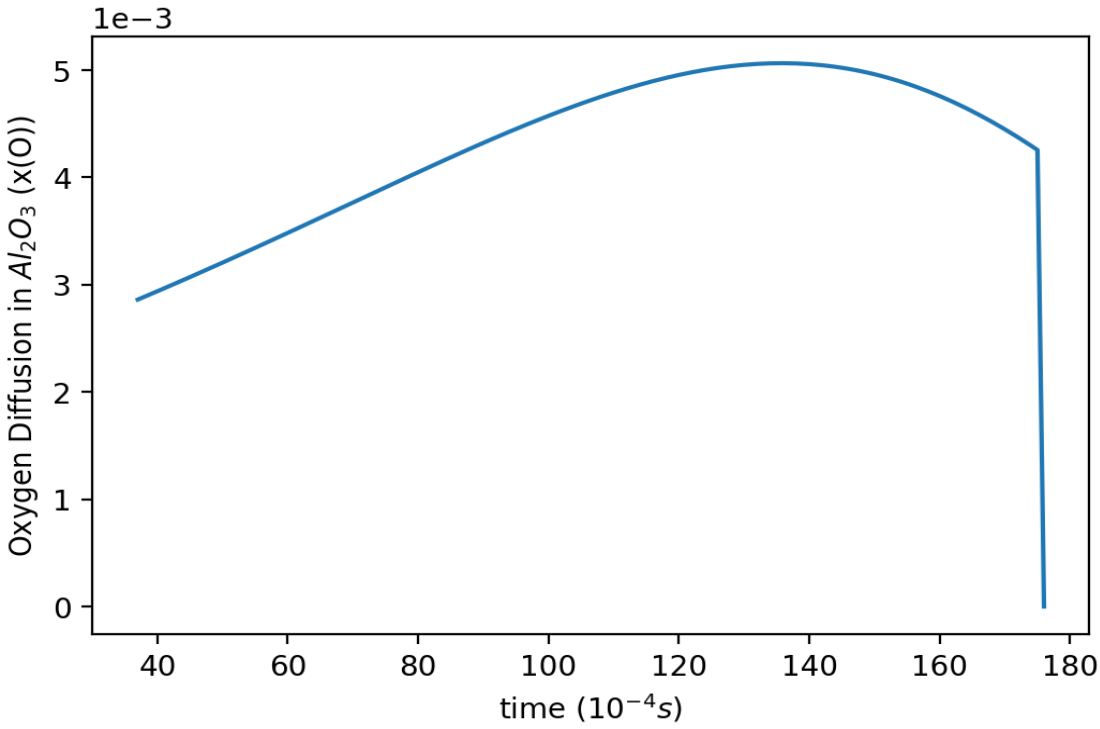

Figure 139: Oxygen diffusion into Al_2O_3 (Al_2O_3-SiO_2-mullite)

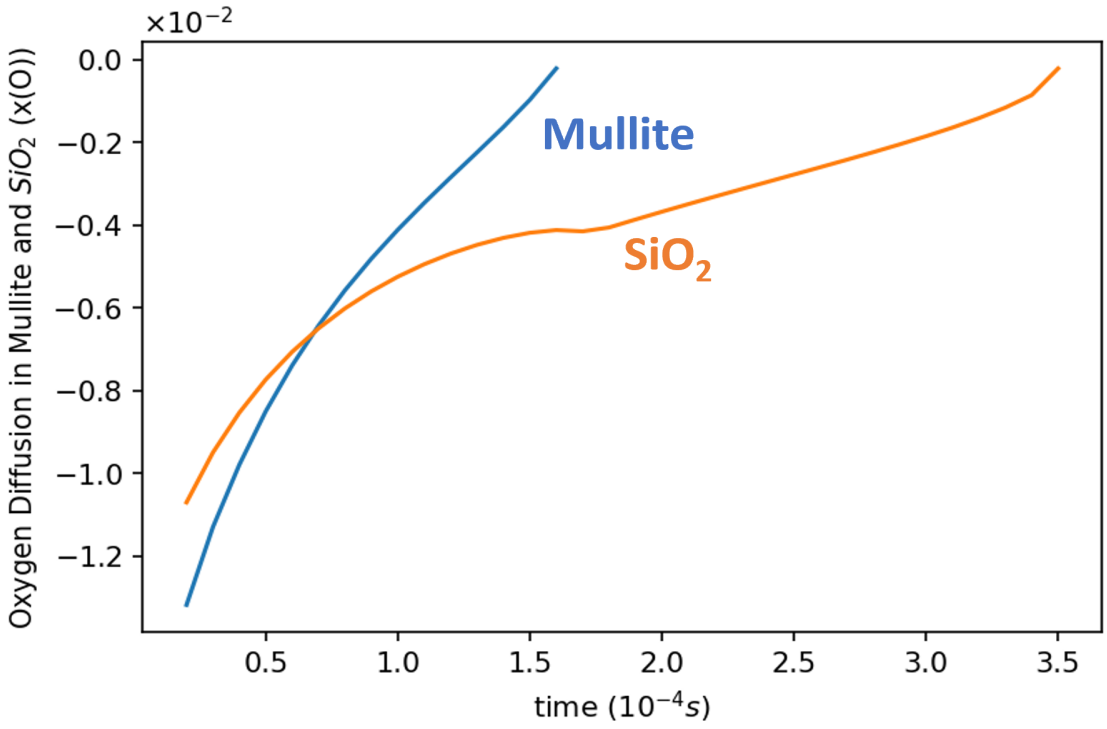

Figure 140: Oxygen dissolution from mullite and SiO_2 in the presence of Al_2O_3 particle

Figure 141 shows the effects of higher ratio of mullite on Al_2O_3 particle, in Al_2O_3-Mullite-SiO_2 system, that is a larger Mullite particle in the system. Increasing the size of mullite particle from 0.3 to 0.4 to 0.5, increases the equilibrium particle size of Al_2O_3. Al_2O_3 achieves higher stability with mullite dissolution. In contrast, increasing the fraction of SiO_2 in the liquid (figure 142) initially increases the size of Al_2O_3 particle but eventually, at 0.5 fraction of SiO_2, the Al_2O_3 particle destabilises to a smaller radius. So the right ratios of oxides are required to obtain the optimum

stability.

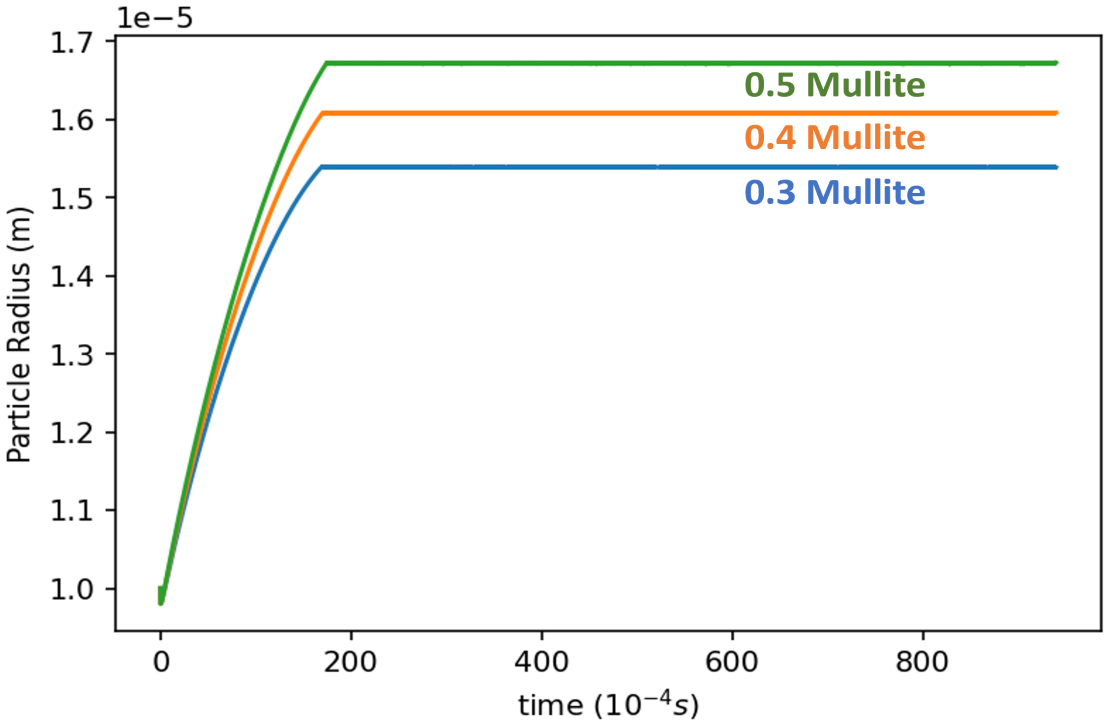

Figure 141: Effect of Al_2O_3 growth in varying mullite fraction in liquid

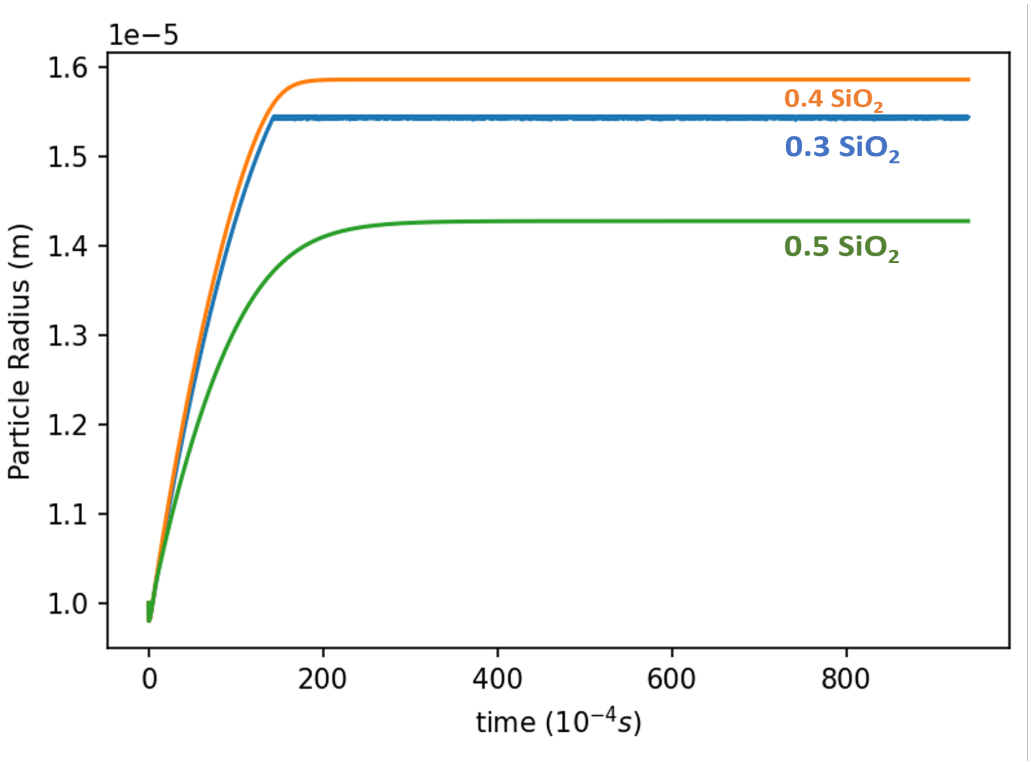

Figure 142: Effect of Al_2O_3 growth in varying SiO2 fraction in liquid

Figure 143 depicts the kinetics of a system consisting of ZrO_2, CaO, and $CaZrO_3$ particles. Similar to the previous simulations shown in figures 134 and 138, this simulation demonstrates the growth of $CaZrO_3$ resulting from the dissolution of ZrO_2 and CaO particles. As previously observed (figure 100), a single $CaZrO_3$ particle completely dissociated into the liquid without establishing equilibrium with the liquid phase. However, in this instance, the particle establishes an equilibrium state with the liquid after undergoing slight dissolution. The particle is subsequently stabilized

by the dissolving ZrO_2 and CaO particles. Nonetheless, the final particle size is smaller than the initial radius of the $CaZrO_3$ particle.

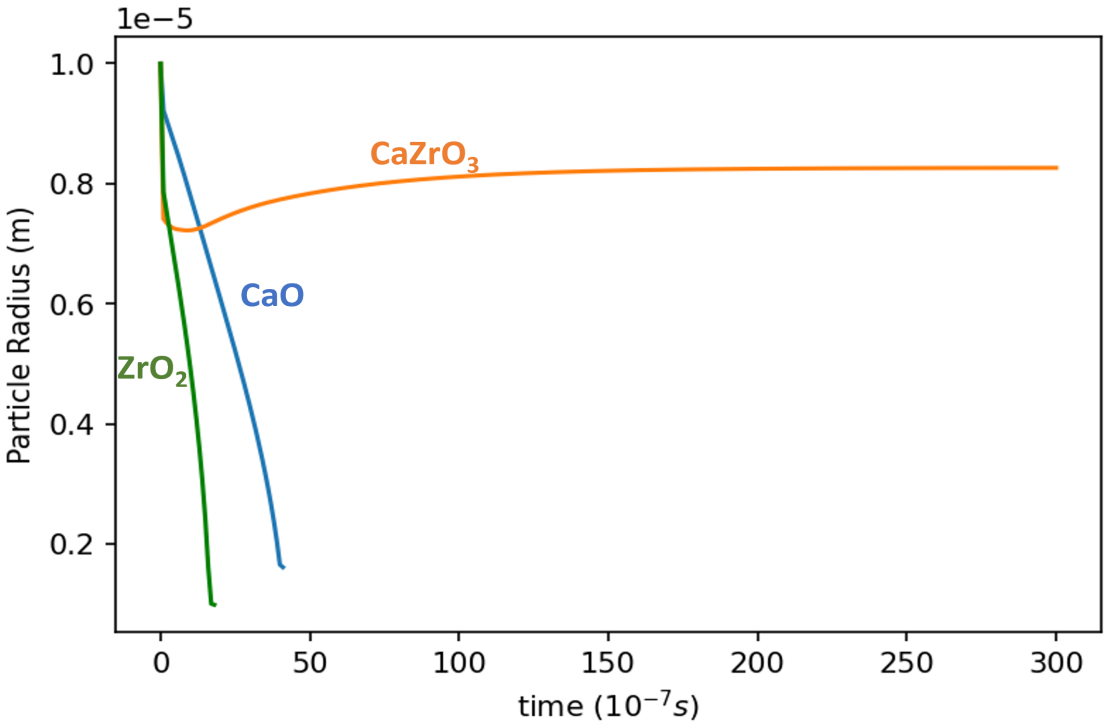

Figure 143: Multi-Phase stability of CaO-ZrO_2-$CaZrO_3$ in TiAl melt

4.6.7 Identifying Stable Oxide Combination

Table 10 presents the final equilibrium state of various reactant oxide combinations. The presence of two Al_2O_3 and Y_2O_3 particles in the liquid results in the formation of YAM and YAP. When only YAM is present in the liquid, it undergoes minimal dissolution and establishes an equilibrium state with the liquid as shown in figure

144. Conversely, when only YAP is present in the liquid, it completely dissolves, as shown in figure 145 and the resultant dissolution product is YAM. The kinetic stability, of YAP and YAM compared to some previous results, indicates that YAM is highly stable, second only to Y_2O_3. Moreover, the simultaneous presence of YAM and YAP in the liquid enhances the stability of both particles, as illustrated in figure 146. Meaning the combined stability of both oxides is much superior than when they are present as single oxides. This behaviour demonstrates that YAM and YAP mutually stabilize each other, resulting in greater stability for both phases. An analytical solution to the simulation can be found in Appendix 7.6.

Mould Oxides	Reaction Product (TCOX11)
$Al_2O_3 + Y_2O_3$	YAM + YAP + IONIC
YAP	YAM + IONIC
YAM	YAM + IONIC
YAM + YAP	YAM + YAP + IONIC

Table 10: Mould oxides and resultant reaction product for Al_2O_3 and Y_2O_3 systems

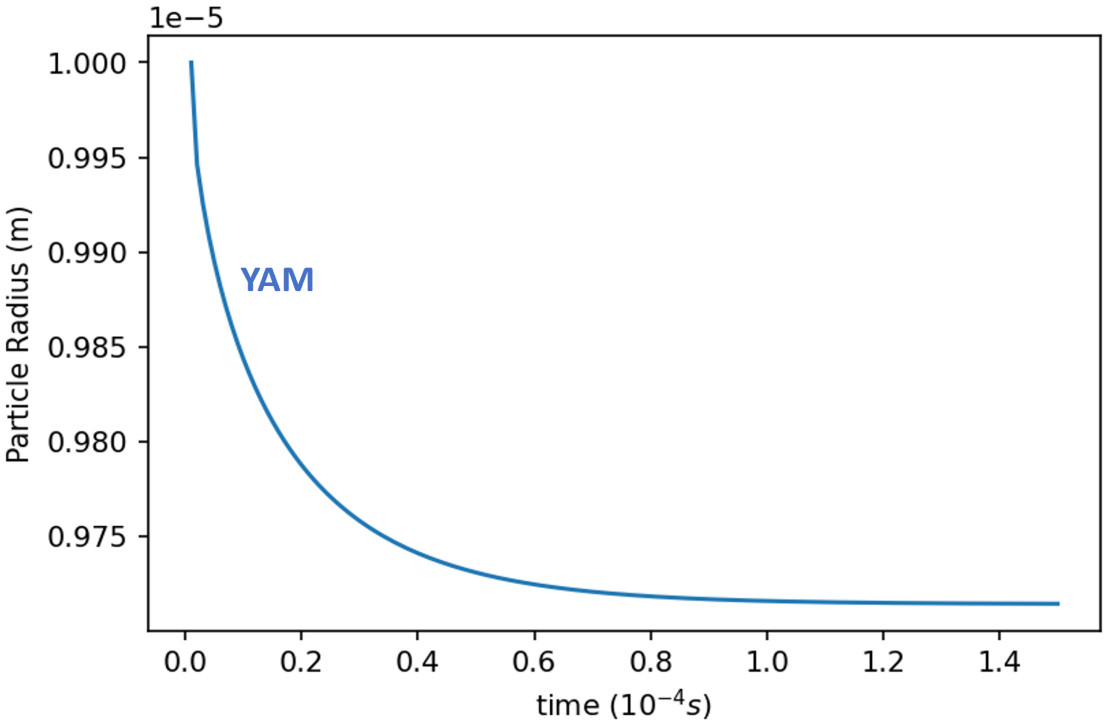

Figure 144: Dissolution kinetics of YAM in TiAl

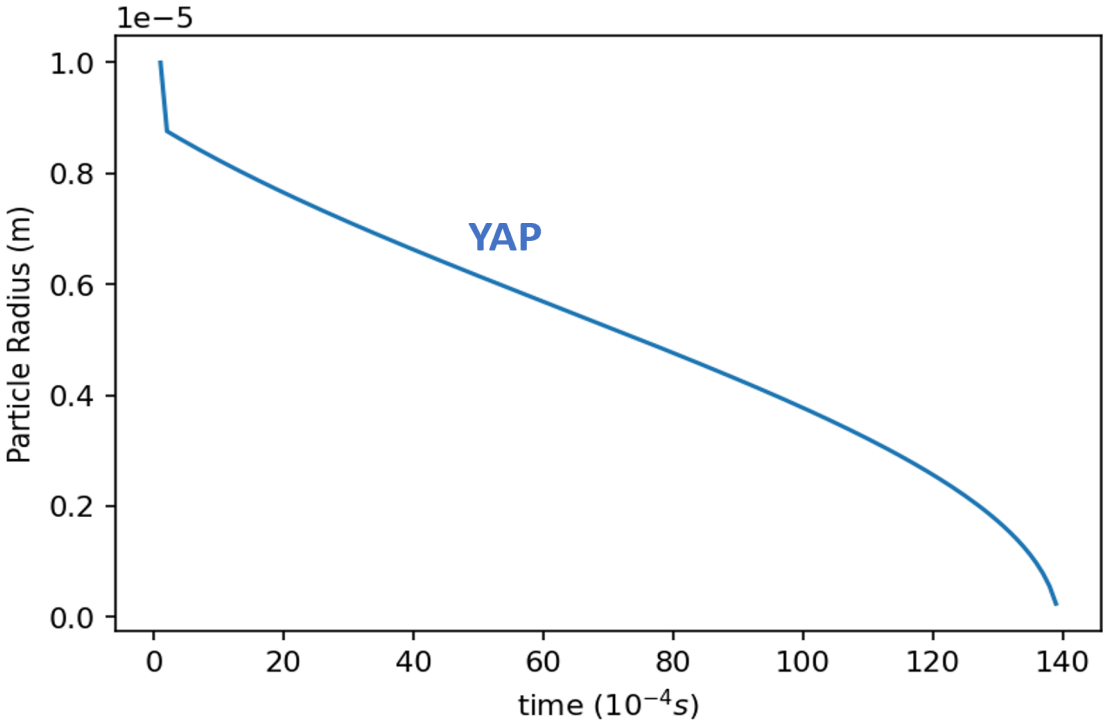

Figure 145: Dissolution kinetics of YAP in TiAl

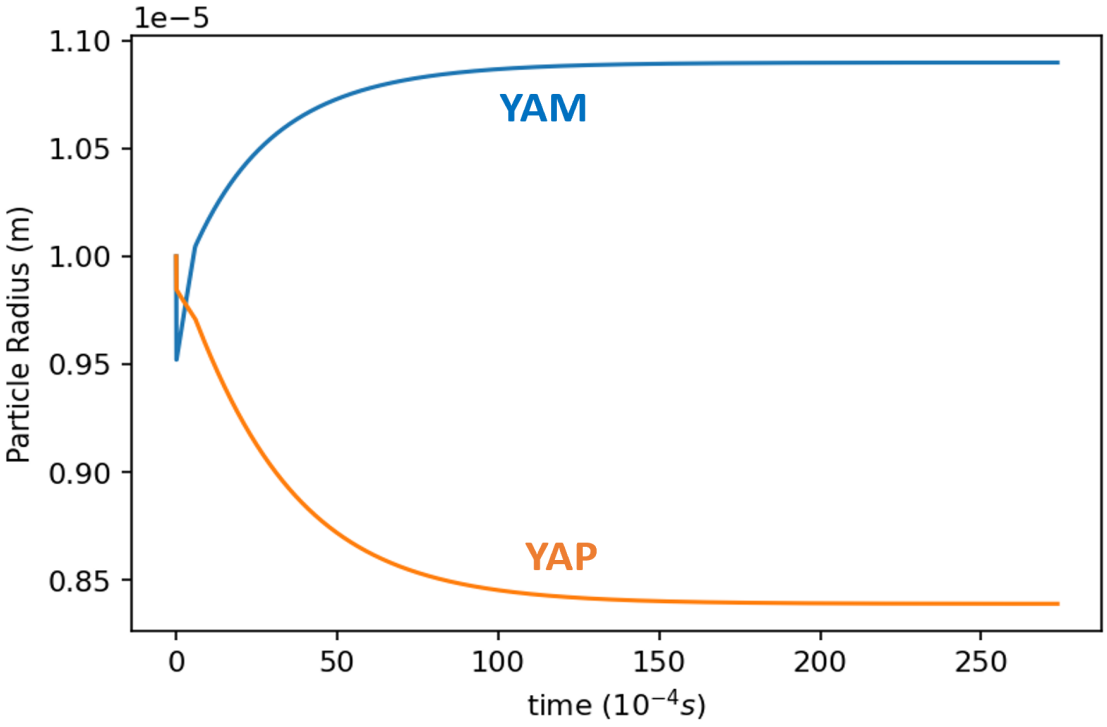

Figure 146: Multi-Phase stability of YAM-YAP system in TiAl melt

Table 11 shows the resulting products when Al_2O_3, Y_2O_3, and YAG are combined in the liquid, leading to the formation of YAG and YAP through similar reactions. As previously observed, both YAG and YAP undergo significant dissolution when present individually. However, figure 147 illustrates that, when both phases are present together, their stability is substantially improved. Although some initial dissolution occurs at the beginning of the reaction, both particles subsequently begin to grow, mutually stabilizing each other. The approach to equilibrium is very sharp

rather than a gradual approach to equilibrium. YAG also exhibits distinct growth patterns, before finally stabilizing.

Reactant Combination	Resultant Product (Stable Oxide/s)
Al_2O_3 + Y_2O_3 + YAG	YAG + YAP+ IONIC
YAG	YAG + YAP + IONIC
YAG + YAP	YAG + YAP + IONIC

Table 11: Reaction products with YAG based systems

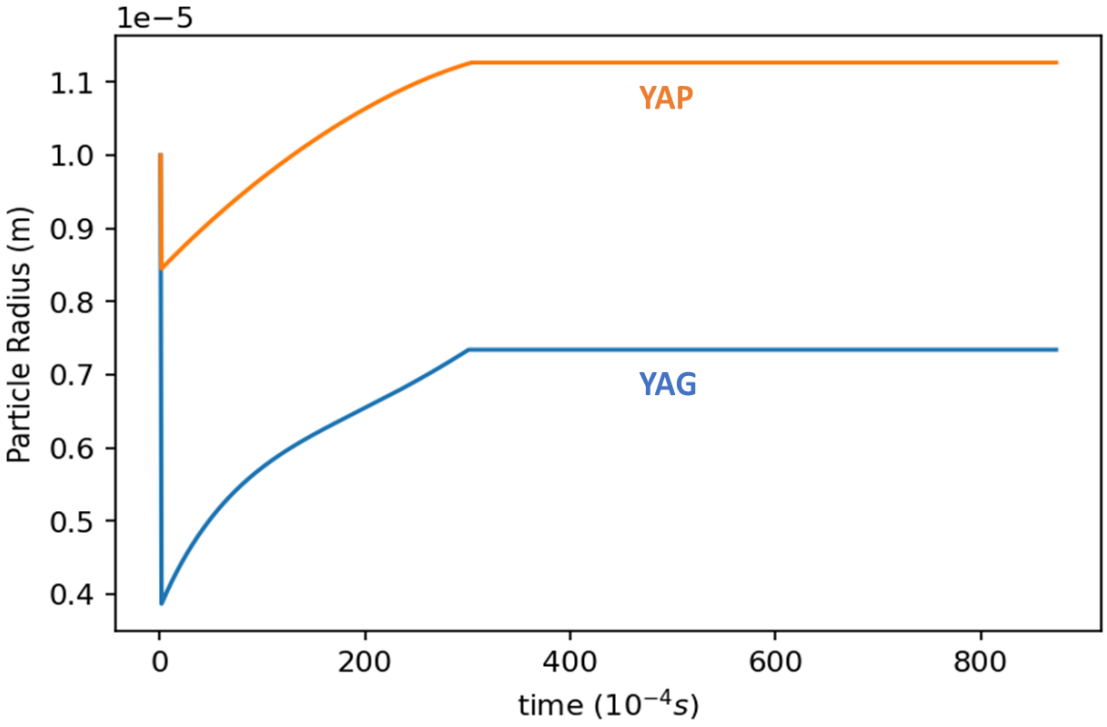

Figure 147: Multi-Phase stability of YAP-YAM system in TiAl melt

Table 12 presents the final reaction products for various reactions involving Al_2O_3. When Al_2O_3 is used alone, its dissolution yields multiple reaction products at different stages. Initially, the dissolution produces HCP (this is the alpha case), but as the reaction progresses, Al_2O_3 itself becomes the final stable product. When Al_2O_3 is combined with mullite, the resulting stable phase is Al_2O_3 and liquid. Similarly, the combination of Al_2O_3 with SiO_2 and mullite results in Al_2O_3 as the final stable phase, with no other stable phases observed.

Mould Oxides	Resultant Product (Stable Oxide/s)
Al_2O_3	HCP_A3 Intitally then Al_2O_3
Al_2O_3 + Mullite	Al_2O_3 + IONIC
Al_2O_3 + SiO2 + Mullite	Al_2O_3 + IONIC

Table 12: Mould oxides and resultant stable reaction product for Al_2O_3 based systems

Table 12 also highlights the impact of mullite on the formation of Al_2O_3 and HCP. The presence of mullite suppresses HCP formation, thereby enhancing the stability of Al_2O_3. This is illustrated in figures 148 and 149. Figure 148 shows the phase stability of Al_2O_3 and HCP without mullite as a function of oxygen composition. A value of 1 indicates phase stability, while a value of -1 indicates instability. The HCP phase becomes stable at an oxygen composition of approximately 0.04 mol fraction and remains stable up to about 0.09 mol fraction of oxygen. In contrast, Al_2O_3 becomes stable at approximately 0.12 mol fraction of oxygen. Figure 149 on the other hand, shows the stability of HCP and Al_2O_3 in the presence of mullite. In this case, the HCP phase is unstable across all oxygen compositions, while Al_2O_3 becomes stable at approximately 0.09 mol fraction of oxygen, indicating a slight improvement in Al_2O_3 stability compared to the scenario without mullite, where Al_2O_3 only became stable at 0.12 mol fraction of oxygen. The suppression of HCP by mullite facilitates

the stabilization of the Al_2O_3 phase at a lower oxygen saturation.

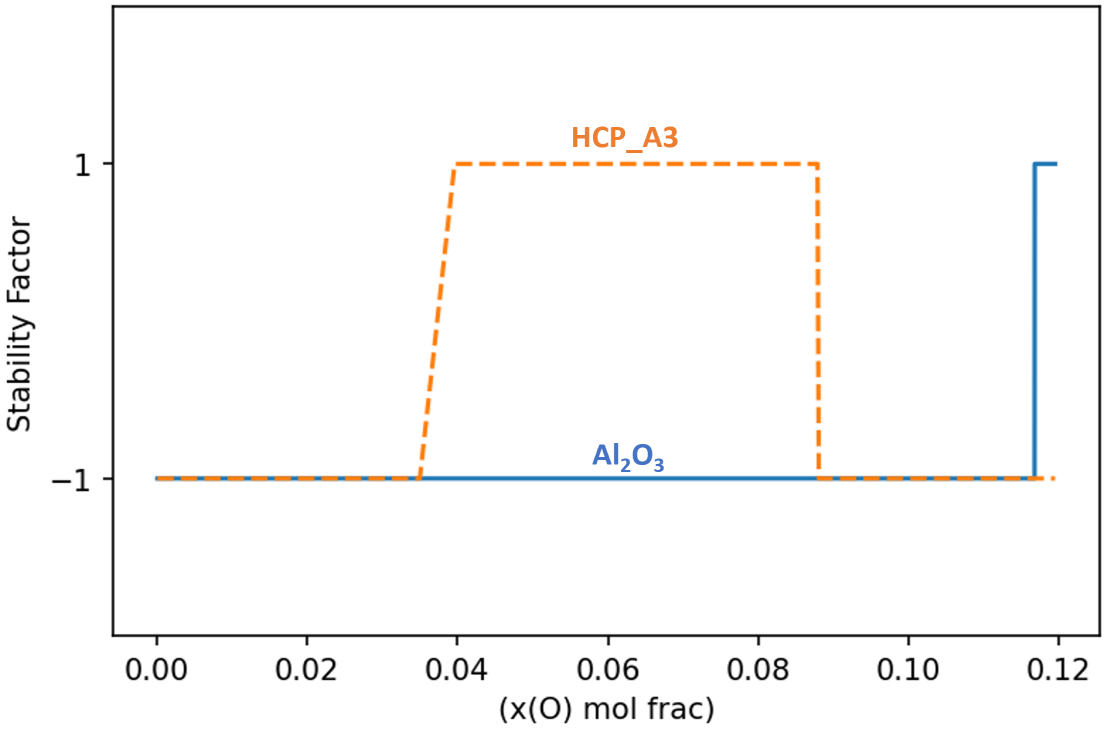

Figure 148: Stability profile of HCP and Al_2O_3 for Al_2O_3 in TiAl melt. Value of 1 indicates stable phase and -1 indicates unstable.

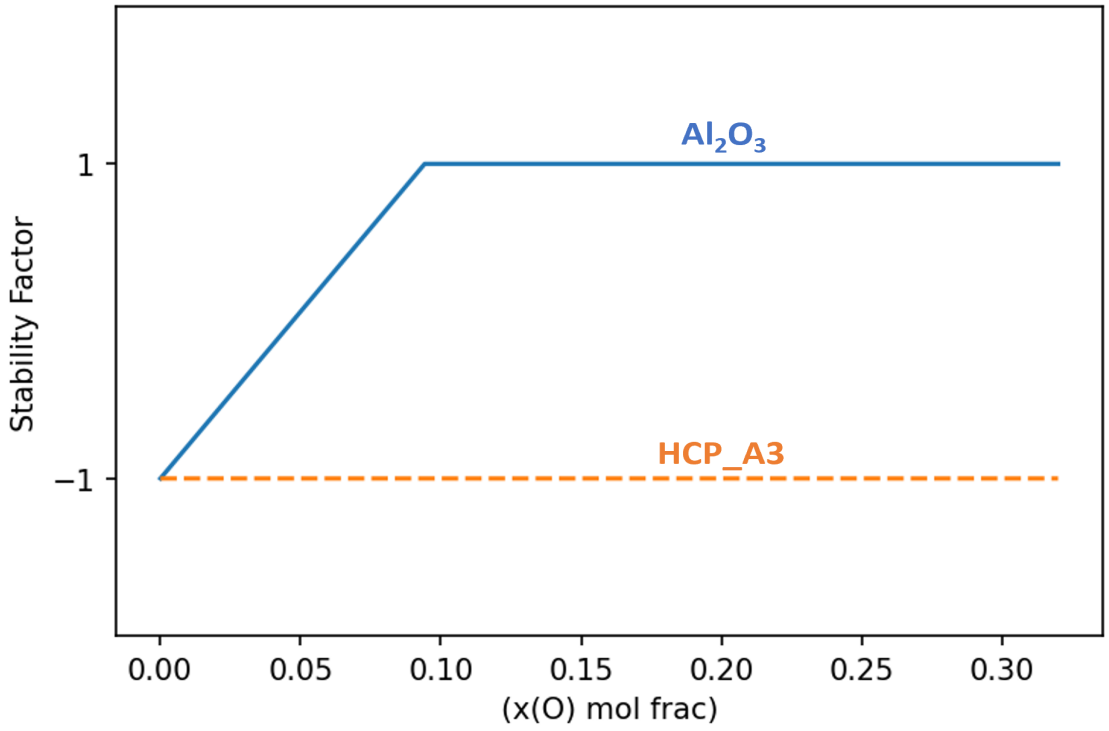

Figure 149: Stability profile of HCP and Al_2O_3 for Al_2O_3 and mullite in TiAl melt. Value of 1 indicates stable phase and -1 indicates unstable.

Table13, shows other mould oxides and their respective reaction products. For many of the single phase oxides, the most common reaction product is the HCP phase. Simulations of $CaYAlO_4$ and Mullite can be found in Appendix 165 and YAG-Al_2O_3 can be found in 166.

Oxide System	Reaction Product
ZrO_2 (Fluorite)	HCP_A3, IONIC
ZrO_2 (Fluo+Tetra)	HCP_A3 + IONIC
CaO	IONIC + CaO
$CaZrO_3$	IONIC
Mullite	IONIC + CORUNDUM
ZrO_2 Tertra	HCP_A3, IONIC
ZrO_2 Mono	HCP_A3
Y_2O_3 + CaO	$CAYAlO_4$ + Y_2O_3
CaO-$CaZrO_3$	IONIC
Y_2O_3 + YAG	YAM + YAP + HCP_A3 + IONIC
Al_2O_3 + YAG	YAG + IONIC
CaO + $CaZrO_3$ + ZrO_2	$CaZrO_3$ + IONIC
CaO-Y_2O_3-Al_2O_3	$CAYAlO_4$ + IONIC

Table 13: All other oxide systems and their reaction products

Figure 150 illustrates the kinetics of a system containing two ZrO_2 particles, each with either a fluorite or tetragonal crystal structure. The tetragonal structure completely destabilizes, while the fluorite structure stabilizes after initial dissolution,

eventually attaining a radius larger than its original size. This demonstrates a marked improvement in the stability of the fluorite structure compared to its behaviour as a single particle. Conversely, the tetragonal structure displays reduced stability in the presence of the fluorite structure compared to when it exists as a single oxide. Nevertheless, the dissolution of tetragonal structure contributes towards improving stability of the fluorite.

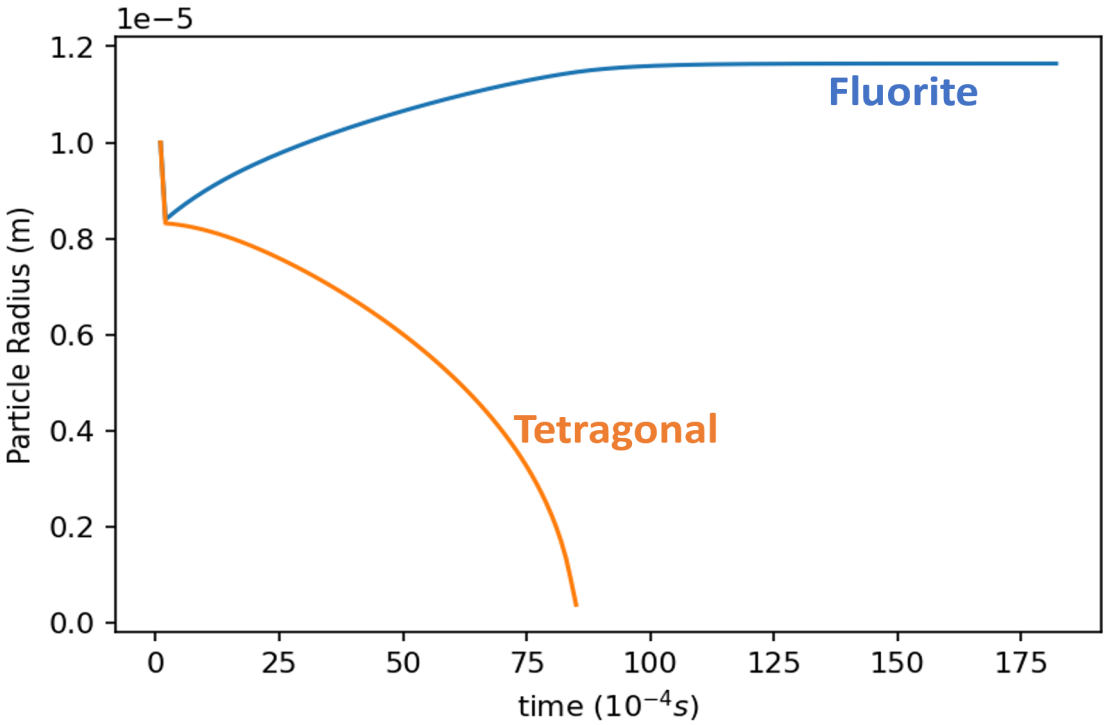

Figure 150: Stability of tetragonal and fluorite Structures of ZrO_2 in TiAl melt

4.6.8 Effect of Changing Stoichiometric Coefficients in Reactions

Figure 151 shows the effects of varying the stoichiometric ratios of Y_2O_3 and Al_2O_3 on the stability of the Y_2O_3 particle. Comparing these results to figure 108, where Y_2O_3 and Al_2O_3 are present in a 1:1 ratio, doubling the amount of Y_2O_3 appears to destabilize the Y_2O_3 particle more quickly. In contrast, doubling the Al_2O_3 ratio slightly extends the stability of Y_2O_3, though not significantly.

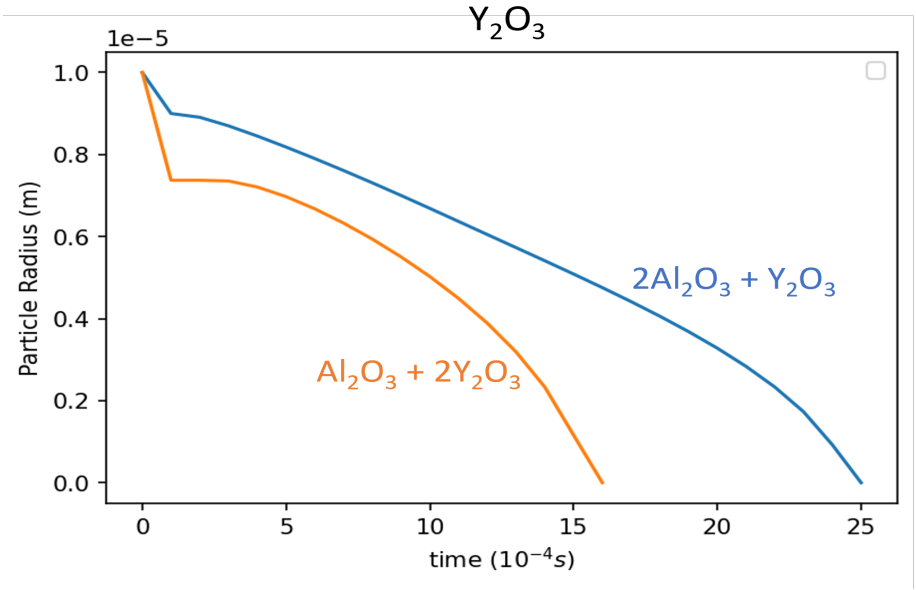

Figure 151: Effects of varying stoichiometric coefficients of Y_2O_3 and Al_2O_3 in Y_2O_3 + Al_2O_3 system

Figure 152 shows the effects of varying stoichiometric ratios on the Al_2O_3 particle. Whether the ratio of Al_2O_3 or Y_2O_3 is doubled, the dissolution of Al_2O_3 occurs at a

faster rate compared to figure 108.

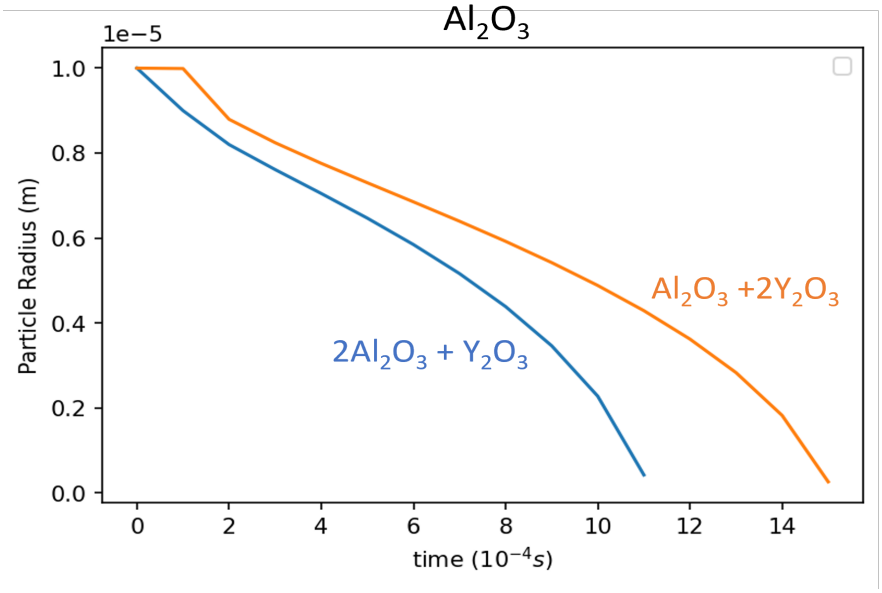

Figure 152: Effects of varying stoichiometric coefficients of Y_2O_3 and Al_2O_3 in Y_2O_3 + Al_2O_3 system

4.6.9 Calculated Equilibrium Contamination for Various Oxide Systems

Figure 153 shows the equilibrium oxygen composition for various oxide systems examined in this thesis. The results indicate that Y_2O_3 establishes equilibrium with the liquid while dissolving the least amount of oxygen, making it the most stable oxide. In contrast, the CaO-Y_2O_3-Al_2O_3 system is the least stable, saturating the liquid with the highest oxygen content. Some oxide combinations dissolve less oxygen than when present individually showing that an improved stability can be achieved.

For instance, systems like YAG-YAP, Al_2O_3-Mullite, Y_2O_3-Mullite-SiO_2, and YAM-YAP show improvements, with reduced oxygen contamination and enhanced stability compared to when these oxides are present as a single phase.

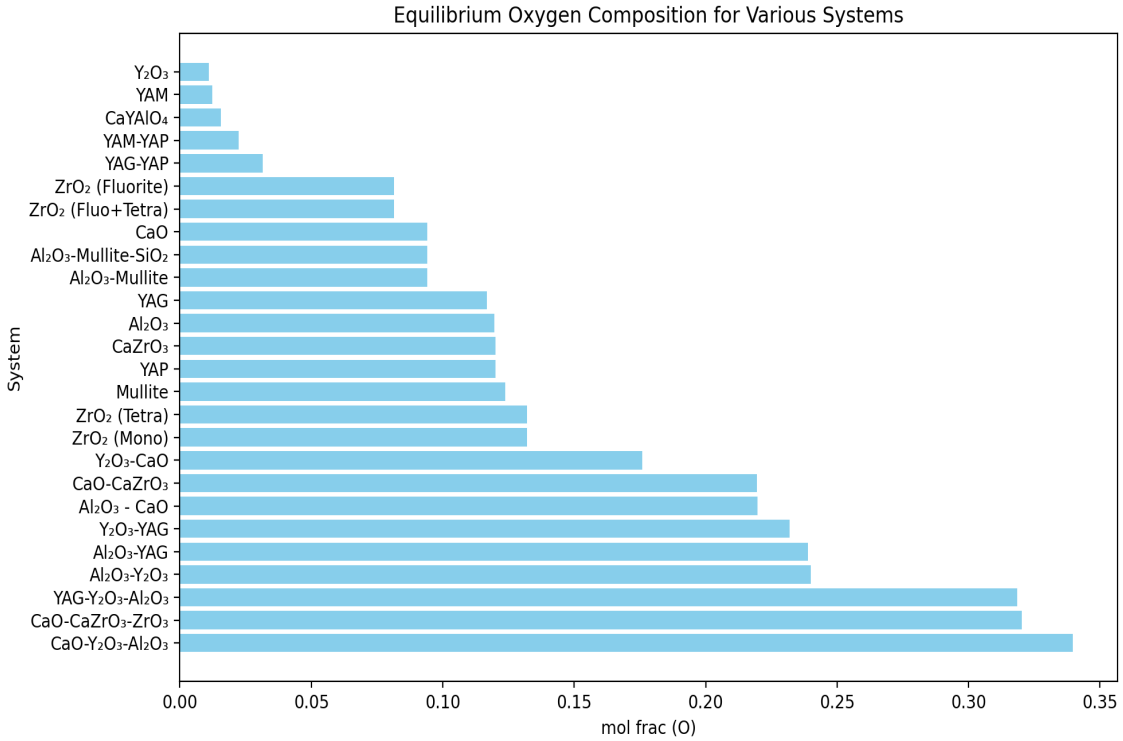

Figure 153: Equilibrium oxygen composition in various oxide systems in TiAl melt

In existing literature, Y_2O_3 is recognized as the most stable oxide for titanium casting, with CaO typically considered the second most stable. However, through the use of sequential oxide selection method used in this study, figure 153 highlights various other oxides and oxide combinations that exhibit stability levels that lie

between yttria and calcia. Among these, systems YAM, $CaYAlO_4$ and the YAM-YAP combination show promise as potential alternatives, offering intermediate stability.

4.7 Chapter 4 Discussion

4.7.1 Numerical Simulation of Ti_2O_3 and Al_2O_3 Growth in Ti-O Melt

In chapter 4, simulations of growth and dissolution of Ti_2O_3 and Al_2O_3 in Ti melt was simulated. The primary goal of this study was to establish a foundational understanding of the FGA model and to understand the types of results the model can generate.

The growth dynamics of the Ti_2O_3 particle in figure 80 provide valuable insights into the model's behaviour. The parabolic growth profile is characteristic of reactions involving reactant to product transformations, reflecting kinetic patterns commonly observed in many reactive systems[181, 182, 183, 184]. This growth trend, where the reaction rate initially peaks and then gradually slows as equilibrium is approached, is a hallmark of such transformations. Studies dating back to foundational research in reaction kinetics have consistently documented this behaviour, making it a standard observation when examining reactant to product transformations.

The initial high reaction rate predicted for Ti_2O_3 growth is attributed to the abundance of reactant (oxygen molecules) available to drive the reaction—quantified in this simulation by the driving force of supersaturation. In a supersaturated matrix, as reactants (oxygen) are consumed during the reaction, fewer molecules remain to sustain the reaction, causing a decrease in supersaturation resulting in a deceleration

of the growth rate as observed in figure 81. When no more reactants are available, supersaturation approaches zero and the reaction ceases. This explains the characteristic shape of the growth profile, with the steep initial rise followed by a gradual levelling off as equilibrium is approached. The equilibrium between the solid and liquid phases is characterized by a balance between the rate of material deposition on the particle surface and the rate of dissolution back into the liquid. The degree of supersaturation is determined by the difference in oxygen composition in the liquid and the solid, greater the difference higher the supersaturation and bigger the particle will grow. Notably, the transition from the initial state to equilibrium occurs rapidly, this is likely due to the smaller particle size and a large volume of liquid surrounding it.

The phase fraction of Ti_2O_3 and the liquid where a sigmoid growth and dissolution curve is observed (figure 83). The presence of this sigmoid curve is a direct consequence of the particle's 3-D spherical shape. As the volume of a small-radius spherical particle increases, it naturally follows a sigmoid growth pattern, confirmed by Shirzad [179]. Initially, when a small particle nucleates, growth is slow because the surface area available for material deposition is small. Once the particle reaches a critical size, the surface area increases significantly, leading to a rapid increase in growth rate. More atoms or molecules can attach to the growing surface and the

growth accelerates. This corresponds to the exponential or rapid growth phase of the sigmoid curve. As the particle continues to grow, the availability of growth material in the surrounding environment decreases, or other limiting factors (such as diffusion limitations or depletion of reactants) come into play. The growth rate slows down, leading to the plateau phase of the curve, where the growth eventually stabilizes. Results in figure 83, can also be modelled through various other methods such as TC-Prisma. However, the uniqueness of the present approach lies in its use of the reaction driving force, ΔG_r, which enables the study of phase transformations from a reaction-based perspective using a standard reaction equation. This allows growth kinetics to be governed purely by evolving chemical potential gradients, without the need for interface mobility functions. Moreover, TC-PRISMA is designed specifically for precipitation modelling and does not account for dissolution kinetics, which is the primary focus of this study.

To validate the effectiveness of the ΔG_r approach, a simulation was conducted comparing the growth of Ti_2O_3 using both the Supersaturation approach and ΔG_r approach. The results, shown in figure 84, demonstrate close agreement between the two approaches, with minor differences in reaction rates. These differences arise primarily from the distinct initial values of the driving forces. In the supersaturation approach, the driving force is derived solely from the oxygen composition in the

liquid whereas, ΔG_r approach integrates both oxygen and titanium compositions, leading to slight variations in the predicted driving forces and subsequently in the reaction rates. Despite these variations, the general behaviour of the system remains consistent between the two methods, further validating the ΔG_r approach. The identical equilibrium radius observed in both cases indicates that the ultimate size of the Ti_2O_3 particles is determined by the same set of thermodynamic conditions, regardless of the growth path taken. This suggests that while the kinetics of particle growth can vary depending on the driving force, the final equilibrium state is governed by the inherent properties of the Ti-O system, in this instance the thermodynamics are the chosen tie line. The comparison of driving forces was further extended to study a ternary system involving an Al_2O_3 particle in a Ti-Al-O melt (figure 87). The growth profile predicted in this ternary system follows a similar trend to that observed in the binary system previously simulated, with both the supersaturation and ΔG_r approaches ultimately leading to the same equilibrium particle radius. This equilibrium radius is dictated by the same thermodynamic conditions. However, minor differences in the reaction rates were observed once again, though these differences were less pronounced in the Al_2O_3 system compared to the Ti_2O_3 system. The difference arises due to solute interactions, where the ΔG_r approach takes into account the activities of both aluminium and oxygen to determine the driving force.

In contrast, the supersaturation approach focuses solely on the oxygen composition. While these variations are relatively minor in binary and simple ternary systems, it is anticipated that in more complex, higher-order systems with multiple interacting components, the differences between the two approaches could become significantly greater. The results provide an understanding of the relationship between the two approaches and confirm they share similar characteristics.

4.7.2 Dissolution of Oxides in Ti-Al melt with ΔG_r as the driving force

The dissolution profile of Al_2O_3 in the Ti-Al-O melt, depicted in figure 88, exhibits a behaviour characteristic of diffusion-controlled dissolution reactions, which have been widely reported in the literature for Ti-mould systems [19, 36, 175]. These processes typically follow a pattern where the reaction rate initially peaks and then gradually decreases as equilibrium is approached—a hallmark of dissolution kinetics. Although the experimental data do not perfectly mirror the simulation setup in this study, they can still offer valuable insights into reaction kinetics. Specifically, by tracking the oxygen concentration profile in the liquid, a distinct parabolic increase is observed, reflecting a pattern similar to the simulated results. In the early stages of dissolution, the driving forces are at their maximum, causing the reaction to occur at the highest rate. However, as time progresses, the driving force diminishes, resulting in a cor-

responding reduction in the dissolution rate. This aligns well with diffusion-limited dissolution mechanisms, where the reaction rate slows as equilibrium is approached, consistent with the gradual balancing of chemical potentials between the solid and liquid phases.

Unlike particle growth, dissolution is driven by the under-saturation of solute in the liquid phase. The degree of under-saturation dictates the magnitude of the driving force, which, in turn, depends on the difference in chemical potential between the two phases, which is well captured in the ΔG_r approach. It is also important to note that the thermodynamic results in chapter 3, shows that as Ti becomes increasingly saturated with solutes like Al and O, its reactivity decreases. This saturation leads to a significant reduction in the ΔG_r for dissolution, thereby causing the reaction to become less aggressive as more Al and O dilute the liquid titanium. This reduction in the driving force for dissolution explains the characteristic slowing of the process as the system approaches thermodynamic equilibrium. As the solute concentration rises, the chemical potential difference between the phases decreases, resulting in a diminished driving force for further dissolution.

Comparing the growth of Al_2O_3 particle in figure 86 to the dissolution in figure 88 reveals that the equilibrium radius reached by the dissolving particle is the same as that achieved by the growing particle. When comparing the behaviour of ΔG_r for

growth and dissolution, a clear contrast emerges. For particle growth, ΔG_r starts with a positive value and gradually approaches zero (figure 87), while for dissolution, the driving force begins with a negative value (figure 89) and also approaches zero. The negative driving force indicates that the dissolution of Al_2O_3 is thermodynamically favourable at the start, driven by the under-saturation of oxygen in the melt. This outcome is expected because the reactions are modelled using the same tie line, indicating that for a given alloy composition, the phase fractions of the liquid and solid remain consistent, regardless of the initial conditions. Thus, the final equilibrium state of the system is not influenced by the initial conditions, provided the alloy composition remains unchanged. This is also in alignment with the principle that dissolution is energetically favourable when the system is far from equilibrium (i.e., when the melt is under-saturated with the dissolved species) and becomes less favourable as the system nears equilibrium (i.e., when the melt becomes saturated). The parabolic nature of ΔG_r for Al_2O_3 dissolution (figure 89), as opposed to the strictly linear trend predicted by the supersaturation approach, can be attributed to the interactions between dissolving Al and O particles and the Ti-Al melt. In this case, the system deviates from ideal behaviour as Al and O saturate the melt, causing the reactivity of titanium to decrease in a parabolic rather than a linear manner. This behaviour results from non-ideal interactions between Ti, Al, and O in the liq-

uid phase, which are well accounted for in the ΔG_r approach. The model's ability to capture this non-linear behaviour of elements in the liquid phase highlights its reliability and robustness in simulating real-world chemical interactions. By accurately reflecting the complex behaviour of elements within the melt, the ΔG_r approach demonstrates a significant advantage in predicting the dissolution kinetics of oxide particles in liquid metal systems.

In the literature, this type of reaction profile is often used to determine the lifespan of a reaction or material, identify solubility limits and assess the extent of a reaction. These factors are critical for evaluating the stability of ceramic oxides, making this model highly relevant for the current study.

4.7.3 Model Testing with the ΔG_r Approach

Factors such as particle size, no. of particles in the melt, surface area to volume ratio, temperature, nucleation have been found to significantly influence reaction rates; though such findings have already been outlined in literature many times [185], [186], [27], [187] the uniqueness of this study is the use of ΔG_r to predict these outcome which has not been done previously through this model. Use of ΔG_r also allows for the compatibility of CALPHAD databases which in turn provides more realistic results. In addition, any number of alloying elements in the melt can be considered

when using ΔG_r as long as thermodynamic data is available.

As illustrated in figure 91, increasing the number of particles in the liquid significantly affects the dynamics of the reaction. When four or less particles are present, the liquid composition remains within the boundaries of the tie line, shown in the Appendix 7.1. Under these conditions, the liquid is over-saturated with elements, leading to particle growth. However, when more than four particles are present, the liquid composition moves outside the boundaries of the tie line (C_m), similar to the example in the Appendix 7.3. This shift results in under-saturation of oxygen and aluminium in the liquid, causing the reaction to favour dissolution in order to balance the chemical potential. Despite the variation in the number of particles, the final equilibrium state (phase fraction) of the system remains the same because it corresponds to the same tie line and alloy composition. In the same way, the total volume of the solid remains the same whilst the equilibrium radius of each particle changes depending on the number of particles in the system. The rate constants (figure 92) slows down as shown by the parabolic trend, because the volume of the solid is continuously increasing which causes the system to reach equilibrium quicker. Moreover, the increase in no. of particles also lead to an increase in surface area, the effects of which are difficult to estimate in this simulation because the liquid volume

changes as a result of increase in no. of particle. The effects of surface area are discussed in the following section.

When the surface area increases in a fixed volume simulation, a greater proportion of the material's surface becomes exposed relative to its volume. This increase in surface area allows for more interactions between the material and the surrounding elements, such as those present in a liquid medium, thereby enhancing the rate of reaction. However, this increase in surface area does not alter the final equilibrium state of the system for instance the solid-to-liquid equilibrium phase fraction remains constant, regardless of the number of particles. This is why larger particles reach larger equilibrium radii and smaller particles reach smaller radii, while the total volume fraction of solid at equilibrium is conserved across the system. As the number of particles increases, a linear increase in the reaction rate constant is evident, suggesting that the increase in surface area due to the higher number of particles significantly boosts the reaction rate linearly, underscoring the critical role of surface area in governing reaction kinetics. The dissolution behaviour of individual Al_2O_3 particles with different initial radii in a melt, as depicted in figure 95, demonstrates how initial particle size influences the overall dissolution kinetics and equilibrium states. Despite the variation in initial sizes, all Al_2O_3 particles ultimately reach the same equilibrium radius because it is governed by the same set of thermodynamic

conditions (tie line). However, the reaction rates differ significantly as larger particles dissolve more quickly, showing a higher initial reaction rate. This rapid initial dissolution is due to the larger surface area of the bigger particles, which provides more surface for the melt to interact with as also observed in the previous simulation. Conversely, while smaller particles have a slower dissolution rate, they reach equilibrium faster because their initial state is closer to equilibrium. In this case, the system's total volume remains constant, and the increase in particle radius is compensated by a corresponding decrease in liquid volume. This dynamic ensures that even though smaller particles dissolve more slowly, their proximity to the equilibrium state allows them to stabilize more quickly, The relationship between the reaction rate constant and the initial particle radius is not strictly linear but shows a trend that approaches parabolic behaviour. This suggests that as the initial particle size increases, the reaction rate constant increases at a decreasing rate. This non-linear relationship could be due to interaction between elements in the liquid causing it to behave in a complex manner. Numerous studies on various reactive systems have explored the effects of surface area on reaction rates and thermodynamics [186], [188] further validating these findings. These findings highlight the importance of initial particle size in dissolution dynamics and can have practical implications when considering kinetic stability of a material. Controlling particle size can be an effective

strategy to manipulate dissolution rates and achieve lower dissolution rates.

The effects of temperature shown in figure 97 reveals that as temperature increases, the liquid phase becomes more dominant, resulting in a higher proportion of liquid within the system at elevated temperatures. In contrast, the solid phase becomes increasingly unstable as the temperature rises. It is evident that as the temperature increases, the liquid boundary of the tie line shifts while the solid boundary remains unchanged. This shift in the liquid boundary alters the phase fractions of the solid and liquid phases, leading to a greater presence of the liquid phase at higher temperatures. Consequently, the oxide becomes progressively more unstable as the temperature increases. This is expected since, studies by Kostov [27], [28] have shown that at higher temperatures the ceramic mould becomes increasing unstable.

The model is also capable of accounting for the effects of nucleation in the liquid. Though nucleation is not an essential part of the current study, it is still important to point out its effects on reaction rates and thermodynamics. The effects of introducing new particles at regular intervals into a matrix, as shown in figure 98, provide a some insight into the dynamics of particle nucleation and dissolution in the melt. The overall trend observed is that the dissolution rate increases as more particles are nucleated at fixed intervals. Each time a new particle is nucleated the surface area to volume ratio increases further increasing dissolution. The surface effects become

more dominant as more particles are nucleated.

4.7.4 Non-Equilibrium, Non-Standard State Reactions

4.7.4.1 Dissolution of Oxides Under Non-Equilibrium, Non-Ideal and Low Initial Oxygen Composition The following simulations are designed to replicate the most aggressive conditions that ceramics can encounter. Among the single oxide dissolution simulations (figure 99), Y_2O_3 demonstrated the highest stability. This observation aligns with several experimental studies conducted by [19, 20], which have similarly reported higher stability of Y_2O_3 compared to other ceramic oxides. The high thermodynamic stability of Y_2O_3 can be attributed to several factors, including strong ionic bonds, high melting point and specific electronic configurations as [189], [190]. Yttrium in Y_2O_3, exists in the (+3) oxidation state, which is the most stable oxidation state for yttrium. Because yttrium is most stable in this state, Y_2O_3 is less likely to participate in chemical reactions that would alter this oxidation state. The oxide ions (O^{2-}) form strong ionic bonds with the yttrium ions (Y^{3+}), resulting in a highly stable crystal lattice structure. This strong ionic interaction makes it difficult for the Y_2O_3 compound to interact with other elements, contributing to its high lattice energy. As a result, a substantial amount of energy is required to disrupt this stable micro-structure, making Y_2O_3 highly inert. There

are likely several other contributing factors, identifying the exact reasons for this high inertness is complex and beyond the scope of this project but it is still the aim to identify more stable oxides. In contrast, Al_2O_3 exhibited the least stability among the oxides studied. Although Al_2O_3 is typically considered a highly stable oxide due to its high free energy of formation, it becomes highly unstable in contact with TiAl melt. The underlying reasons for this instability have been discussed in chapter 3, where strong intermetallic interactions between Ti and Al are suggested to contribute significantly towards the destabilization of Al_2O_3. The stability of CaO and YAG ($Y_3Al_5O_{12}$) falls between that of Y_2O_3 and Al_2O_3, indicating a moderate level of stability under these conditions.

The dissolution rates of each of the oxides show in figure 103 confirms YAG dissolution occurs at the fastest rate compared to Al_2O_3 and CaO, yet its overall thermodynamic stability is higher than that of Al_2O_3. From a casting perspective, Al_2O_3 would be a better option due to its slower dissolution rate compared to YAG. Although the decision will depend on casting time. A non-linear dissolution curve, as shown in figure 100, is more common for cases where the dissolution process does not reach equilibrium, resulting in the complete dissolution of the particle into the liquid phase. This type of dissolution has already been observed in studies by Wang and Vermolen[191, 192] and is in agreement with the current study. The distinct disso-

lution profiles can be attributed to several key factors. Initially, a significant drop in particle radius occurs due to the high ΔG_r of the reaction during the early stages of the reaction. This large ΔG_r arises because the oxygen composition in the liquid is almost zero at the start, creating a substantial chemical potential difference between the oxide and the liquid. Consequently, there is a pronounced change in particle radius at the beginning of the reaction. Following this initial stage, the dissolution process becomes more steady and exhibits a linear trend, where the dissolution is almost constant. However, as the particle size decreases and reaches a certain particle size, the dissolution rate exponentially accelerates. This acceleration is due to the effects of surface-area to volume ratio which is more pronounced when particles reach a certain size. As shown in figure 101, smaller particle has a higher surface area-to-volume ratio which leads to an accelerated dissolution rate, causing smaller particle to dissolve more rapidly. This proportional relationship between surface area and dissolution rate explains why smaller particles dissolve faster.

Figure 102 demonstrates that Y_2O_3 exhibits minimal oxygen dissolution, highlighting its remarkable resistance to degradation even under extreme conditions, thereby confirming its high inertness. Following Y_2O_3, the stability ranking progresses with CaO, YAG, Al_2O_3, $CaZrO_3$, and ZrO_2. This order aligns with the thermodynamic rankings reported in the literature and discussed in Chapter 3. However, ZrO_2 presents a

notable discrepancy; experimental and thermodynamic data often rank it as highly stable compared to oxides such as Al_2O_3 and YAG. This inconsistency underscores the need to account for the different structural phases of ZrO_2 when interpreting its stability. Figure 106 illustrates the dissolution profiles of three ZrO_2 structures. The yttria-stabilised-zirconia (fluorite structure) shows the most stability. This stabilization improves the material's stability and structural integrity. Yttrium doping introduces oxygen vacancies into the zirconia crystal lattice. Yttrium ions (Y^{3+}) replace zirconium ions (Zr^{4+}), creating oxygen vacancies to maintain charge neutrality. These vacancies lower the chemical potential of oxygen in the oxide, thus reducing the solubility barrier. This modification in the crystal structure helps explain the observed higher stability of yttria-stabilized zirconia compared to other oxides and other ZrO_2 structures like monoclinic and tetragonal. Although the simulation data are not directly comparable to experimental data, it is still valid since, it follows the oxide stability ranking. While oxygen data does not inherently provide detailed insights into the kinetics of the system, it does reflect relative stability and resistance of these oxides to dissolution.

Figure 103 illustrates the interaction of oxides under various Ti-alloy compositions, revealing that oxides are most reactive in pure titanium (Ti) and least reactive in gamma-Ti alloys. This trend occurs because higher titanium content in the liq-

uid phase results in increased reactivity of the oxides. As titanium is progressively diluted with other alloying components, its reactivity diminishes, leading to a corresponding decrease in its impact on oxide dissolution. These observations align with the experimental results presented in chapter 3, which show that a higher titanium content in the melt correlates with more intense reactions, also confirmed by Kostov [27] and Cui [28]. When titanium is diluted with other alloying elements, its reactivity is reduced, thereby decreasing its influence on the dissolution behaviour of ceramic oxides. This reduction in reactivity with lower titanium content suggests that alloying can be an effective strategy to mitigate the aggressive dissolution of oxides in high-temperature environments, providing a means to enhance the stability of ceramics in titanium-based systems.

4.7.4.2 Non-Equilibrium, Non-Standard State, Multi-Phase Reactions

Although Y_2O_3 has been found to be the most stable of the single oxides, Y_2O_3 is also the most expensive, in addition the thermal stability of Y_2O_3 is generally found to be poor as discovered from literature review. This then propelled this research to improve/identify other oxide ceramics that exhibit similar or higher stability to Y_2O_3 but with little or no yttrium. When both Y_2O_3 and Al_2O_3 are present in the liquid, the dissolution rates of both oxides are significantly accelerated, leading to the complete disappearance of the particles into the liquid phase. Al_2O_3 disappears

first because it is predominantly a lesser stable oxide compared to Y_2O_3. The reaction rate constants are significantly higher with -0.28 for Al_2O_3 and -0.20 for Y_2O_3 as depicted in figure 109. This behaviour contrasts with the dissolution profile of twin Al_2O_3 particles modelled in figure 107, where Al_2O_3 particles stabilise while, a destabilizing interaction occurs when Y_2O_3 is replaced for an Al_2O_3 particle in the liquid. The driving forces for the respective oxides, as shown in figure 110, indicate that only one oxide phase is likely to be stable at any given time, but not both simultaneously. This dip and rise relationship suggests that the stability of one oxide directly influences the instability of the other by shifting the equilibrium position of the entire reaction. In other words, the presence of Al_2O_3 can shift the equilibrium position of Y_2O_3 from a stable to an unstable state, highlighting a competitive interaction where the stabilization of one oxide phase promotes the destabilization of the other. This reciprocal behaviour suggests a competitive dynamic between the two oxides: as Al_2O_3 moves towards stabilization, Y_2O_3 becomes more unstable, and as Al_2O_3 becomes more unstable, Y_2O_3 tends towards stability. This destabilization can be evaluated through Y-Al activities in the liquid (figure 111 which shows Y and Al having opposing effects on their chemical activities. When one increases, the other decreases and vice versa. These effects are likely due to the strong negative interaction between Y and Al, as illustrated in figure 112, where Y activity

deviates significantly from ideal behaviour with increasing Al content. This deviation contributes to the observed instability of the combined oxides and the dip and rise relationship between the driving forces, as seen in figure 110. Such interactions indicate the formation of reaction products that are more stable than the respective individual oxides. This interaction highlights the complex chemical dynamics in multi-component systems, where the presence of one element can significantly alter the stability and behaviour of others. Therefore, having both Al and Y in the liquid phase is undesirable, as it promotes the rapid dissolution and destabilization of oxides potentially compromising the stability of the entire system. Little to no literature is currently available for Al_2O_3-Y_2O_3 mixed system. However, there are some studies showing Al_2O_3 coated Y_2O_3, to be somewhat stable [120].

4.7.5 Improving Stability of Y_2O_3 via Solute Compositions

4.7.5.1 Analytical Solution for the Dissolution of Al_2O_3 and Y_2O_3 in TiAl Melt The close agreement between the analytical and numerical solutions, as shown in figures 113 to 115, provides strong evidence that the numerical model is capturing the dissolution process as expected. The numerical solution's less continuous nature compared to the smoother analytical solution suggests that the numerical

model can effectively account for non-linearity within the reaction process, which can be absent in the analytical solution. This capability is demonstrated by the sharp changes in the dissolution profile observed at certain stages of the reaction, which indicate the model's sensitivity to dynamic changes in the system's behaviour. One aspect where the analytical solution becomes highly useful is in establishing relationships between reaction rate constants. Understanding the relationship between the reaction rate constants of the Al_2O_3 and Y_2O_3 system is particularly important for developing strategies to improve the stability of moulds. By analysing how these constants interact, it is possible to optimize conditions that minimize the dissolution rates of these oxides, thereby enhancing the durability and effectiveness of ceramic moulds in high-temperature environments. The results show that increasing k_1 has an opposing effect of decreasing k_2. The increased dissolution of Al_2O_3 slows down the dissolution of Y_2O_3. As a result the strategy to reduce the reactivity of Y_2O_3 is to increase the rate of dissolution of Al_2O_3. Since, Al decreases the activity of yttrium and that a decrease in chemical activity of yttrium is cause of dissolution, increasing the activity of yttrium in the liquid would allow the oxide to be more stable and react at a slower rate.

As shown in figure 116, increasing the activity of yttrium by increasing the composition of Y has several positive impact on stability of Y_2O_3. Firstly, adding excess

Y raises the reaction rate constant k_1 and lowers the reaction rate constant k_2. This slows down the reaction of Y_2O_3, eventually leading to stabilisation if Y concentration is above 0.07 (118) in the liquid. This stabilization occurs due to the increased activity of yttrium, which shifts the equilibrium toward Y_2O_3 stability. As the yttrium concentration rises, it reduces the oxygen content in the liquid, as the shift in equilibrium position toward Y_2O_3 consumes oxygen. This, in turn, stabilizes the Y_2O_3 and prevents further dissolution. Such a strategy, where excess of one component shifts the equilibrium in a desired direction, is a well-established approach in chemical reaction studies and has been thoroughly documented across various reaction systems. This method leverages Le Chatelier's principle, where the system responds to changes in concentration by shifting the equilibrium to counteract the imposed change. In the case of Y_2O_3, the addition of excess yttrium drives the equilibrium toward greater oxide stability, a technique that has been previously reported by Kobayashi [32]. Kobayashi observed that adding excess yttrium in Ti-alloys effectively reduces the oxygen activity (figure 50) in the liquid phase, thus shifting the equilibrium toward Y_2O_3 stability. This mechanism highlights the importance of controlling solute concentrations to achieve desired stability in complex systems, particularly in preventing oxide dissolution and enhancing material performance in extreme environments.

Increasing yttrium composition has a notable impact on the driving force of Y_2O_3 dissolution, as shown in figure 110. At lower yttrium concentrations, there is a clear 'dip-and-rise' effect, indicating mutual destabilization of the oxides. However, as yttrium levels increase, this effect gradually diminishes and eventually disappears at higher yttrium compositions. This suggests that adding excess yttrium can stabilize Y_2O_3 and reduce the undesirable destabilization effect. The dip-and-rise behaviour is minimized as more yttrium is added to the liquid, primarily because yttrium reduces the activity of aluminium. At higher concentrations, yttrium tends to behave more ideally in the liquid. This behaviour is depicted in the activity diagram in figure 112, where a lower yttrium mol fraction combined with a higher aluminium mol fraction shifts the yttrium activity curve away from ideal behaviour. Conversely, as the yttrium content increases and the aluminium composition decreases, the system moves closer to ideal behaviour. The dip-and-rise effect, which signifies deviations from the ideal state, is therefore minimized as additional yttrium drives the system closer to equilibrium. This shift ultimately stabilizes the Y_2O_3 particles in the melt, preventing the destabilizing interactions that occur at lower yttrium concentrations, further enhancing the stability of the oxide in high-yttrium environments.

The addition of alloying elements such as Nb and Cr has led to a reduced reaction rate, even though the oxides still completely dissolved into the liquid. This trend has

also been observed in the study by Cui [36], where a decrease in oxygen contamination was linked to the presence of Nb in the TiAl alloy melt. Cui suggested that increasing Nb content decreases the melt's reactivity to some extent, a phenomenon that is confirmed through this study. Other studies by Chen [24], Yang [25] have also discussed the oxidation resistance of Nb added alloys. The presence of Nb and Cr not only lowers the activity of Ti but also of Al, as confirmed by figure 126. The high activity of Al in the liquid was initially responsible for the dissolution of Y_2O_3 in the TiAl melt. However, the presence of Nb reduced Al activity, thereby slowing the dissolution rate of Y_2O_3. Although Nb does not completely eliminate the dip-and-rise effect, it spreads the destabilization over a longer period, meaning the destabilization effect takes longer to complete. Moreover, Nb decreases the activity of Y, which could have led to an increase in the dissolution of Y_2O_3. However, the increased oxygen activity countered this effect (figure 125), further slowing the reaction rate. Thus, a combination of these factors plays a crucial role in determining the overall stability of the oxide in the melt.

4.7.6 Improving Stability Via Oxide Combinations

When Al_2O_3 was replaced with CaO, the stability of the Y_2O_3 particle improved significantly as shown in figure 127. This enhancement can be attributed to the pos-

itive interaction between calcium and yttrium, which suggests a repulsive behaviour between these elements. In such scenarios, the likelihood of yttrium bonding with calcium is minimized, eliminating any substantial driving force for the formation of reaction products. While CaO eventually dissolved into the liquid, similar to Al_2O_3, it did so without destabilizing Y_2O_3 to the same extent. Additionally, the dissolution of CaO was considerably slower compared to that of Al_2O_3. Driving force analysis (figure 128) revealed that the dip-and-rise effect observed in the Al_2O_3-Y_2O_3 system is minimised in the CaO-Y_2O_3 system, with both phases tending toward stability. The major issue with the Y_2O_3-Al_2O_3 system was the saturation of Al through Al2O3 dissolution, which destabilised the Y_2O_3. Since, this is minimised in the CaO-Y_2O_3 system, the Y_2O_3 particle stabilises. This suggests that CaO is a more suitable option than Al_2O_3 for maintaining Y_2O_3 stability in the melt. Figure 129 illustrates why Y_2O_3 stabilizes in the presence of CaO as opposed to Al_2O_3. As CaO dissolves into the liquid, the activity of Y remains relatively high, which supports the stability of Y_2O_3. In contrast, when Al dissolves, the activity of Y decreases significantly, contributing to the destabilization of Y_2O_3 as it seeks to re-establish equilibrium. This trend is further corroborated by the activity diagram in figure 77, where Y activity is consistently higher in the presence of Ca compared to Al. However, despite these differences in activity, the simulations have not yet shown any significant improve-

ment in either stability or reaction rates when mixed oxides are used, compared to using a single oxide phase. When Al_2O_3, Y_2O_3 and CaO are present together in the liquid, all the oxides become unstable, leading to their complete dissolution (figure 130). Analysing the driving force of each of the phases (figure 131), the dip and rise relationship previously observed in figure 119 for Al_2O_3 and Y_2O_3, reappears for this system. Despite the presence of CaO, this interaction causes the oxides to destabilize each other, resulting in the dissolution of all three oxides into the liquid. However, it is notable that Y_2O_3 shows a slower reaction rate compared to the two particle system. The destabilization is again driven by negative interaction between Y and Al just like in the previous case. This not only destabilises Al_2O_3 and Y_2O_3 but also CaO to a significant extent.

When YAG (Yttrium aluminium Garnet) and Y_2O_3 are both present in the liquid, the dissolution of YAG exhibits a parabolic behaviour, which contrasts with the conventional non-linear dissolution pattern typically observed for complete dissolution. This parabolic behaviour likely occurs because YAG is near equilibrium with Y_2O_3. The close proximity to equilibrium between these two phases reduces the driving force for dissolution, leading to a more gradual and controlled parabolic dissolution curve, rather than a rapid non-linear one. This behaviour suggests that

the interaction between YAG and Y_2O_3 in the liquid is more stable than in systems where the oxides are far from equilibrium. However, despite this relative stability, the combination of YAG and Y_2O_3 in the liquid remains unstable. This instability persists even though YAG and Y_2O_3 share a common ion, (yttrium), which would typically be expected to promote stability. The fact that only a very small shift in equilibrium is required for YAG to become stable highlights the delicate balance within this system, indicating that the presence of both YAG and Y_2O_3 together does not result in a fully stable environment.

The dissolution of the ZrO_2-Y_2O_3 system yielded unexpected results. This is because Y-Zr interaction has been predicted to be positive in figure 77 much like Ca-Y interaction is positive. Yet this did not prevent both oxides from becoming unstable. This behaviour can be due to the activity of Al in the liquid as ZrO_2 and Y_2O_3 dissolves. As was observed previously high activity of Al in the liquid in presence of Y and O can significantly lower the stability of Y_2O_3. Such is the case with ZrO_2-Y_2O_3 system where Al is the prime cause of oxide dissolution. The main reason Al destabilises Y_2O_3 in presence of Y and O is the formation of more stable secondary phases or by-products during the dissolution process. These secondary phases could alter the overall stability of the system, leading to the destabilization of ZrO_2 and

Y_2O_3 despite the seemingly favourable interaction between Y and Zr. In this case, it is not just the Y-Zr interaction that is critical but also the Al in the liquid.

Having YAG, Al_2O_3 and Y_2O_3 led to the dissolution of Al_2O_3 and Y_2O_3 but stabilised YAG. The dissolution profiles also varied during the simulation. This change in dissolution rates can be attributed to the common ion effect. As Al_2O_3 and Y_2O_3 dissolve, they release aluminium and yttrium into the melt. YAG, which shares these common ions, absorbs the released aluminium and yttrium, stabilizing itself in the liquid and thereby switching the driving force to growth. This is evident in figure 135, which shows the transport of oxygen from between the oxides. At steady state, YAG absorbs oxygen, while Al_2O_3 and Y_2O_3 release oxygen into the melt. This interaction between the oxides creates a dynamic where YAG becomes increasingly stable as it takes in oxygen, Yttrium and aluminium from the dissolving Al_2O_3 and Y_2O_3 particles. It is important to note that the stabilization of YAG requires the presence of two common oxides to supply the necessary ions. This explains why, in the system containing only Y_2O_3 and YAG, the YAG did not stabilize—there was no additional supply of aluminium available to support its stabilization. Without the dissolution of Al_2O_3, which provides aluminium and oxygen, YAG lacks the necessary elements to maintain equilibrium in the melt, leading to continued instability.

In addition, the reaction rates for growth and dissolution significantly vary. Y_2O_3 and Al_2O_3 completely dissociate in the liquid within a few time-steps whereas the growth of YAG is much slower. Comparing the stability of single YAG to a mixed system, the mixed system containing Al_2O_3 and Y_2O_3 shows much higher stability of YAG compared to other combinations. This combination is much more desirable than the combinations previously observed largely due to the stabilising effect that takes place. This result is evidence that stability of an oxide can be improved by the presence of oxides that contain common ions.

In the case of the Al_2O_3-Mullite system, the dissolution of Mullite promotes the growth of Al_2O_3 (figure 136). This behaviour makes the combination highly desirable because it leads to the greatest stability for Al_2O_3. Unlike the instability seen when Al_2O_3 is present in Ti-Al melt on its own or combined with Y_2O_3, in this instance, the Al_2O_3 particle size actually increases, growing beyond its initial particle radius. This demonstrates a synergistic effect, where the dissolution of Mullite actively supports the stabilization and growth of Al_2O_3. Mullite dissolves rapidly due to its instability and the fact Al_2O_3 is striping Al and O from the liquid. As illustrated in figure 137 the diffusion of oxygen into Al_2O_3 is high initially because of the availability of Al and O in the liquid by the dissolution of mullite. Once mul-

lite is all dissociated the diffusion of oxygen into Al_2O_3 slows down. This is another clear example of the common ion effect, where the dissolution of Mullite provides the necessary ions (Al and O) for the growth and stabilization of Al_2O_3. Interestingly, in this case, it is Al_2O_3 that stabilizes, in contrast to the previous example with the spinel (YAG), where YAG was the phase that became stable. This highlights how the common ion effect can influence different phases depending on the system's composition, with stabilization shifting to the oxide that benefits most from the ion supply in the liquid phase.

When SiO_2 is introduced alongside Al_2O_3 and mullite (figure 138), a notable acceleration in the growth rate of Al_2O_3 is observed, although the thermodynamic equilibrium remains unchanged. This suggests that while the final particle radius of Al_2O_3 and the complete dissolution of mullite are dictated by the same equilibrium conditions, the presence of SiO_2 has significantly accelerated these processes. The enhanced growth rate of Al_2O_3 can be attributed to the dual sources of oxygen provided by both SiO_2 and mullite. Additionally, the faster reaction rate of mullite further increases the availability of Al and O, promoting the rapid growth of Al_2O_3. Figure 139 shows the diffusion profile of oxygen into Al_2O_3. This profile has similarities to the one observed in figure 137, as both exhibit a rapid increase in oxygen intake

followed by a decline. However, the rates of oxygen intake in these profiles differ significantly, largely due to the presence of SiO_2. SiO_2 accelerates the dissolution of mullite, making oxygen more readily available for Al_2O_3 growth. In this case, while SiO_2 did not alter the final equilibrium radius of Al_2O_3, it has certainly played a role in accelerating the dissolution of mullite and the growth of Al_2O_3. This highlights the effect of SiO_2 in altering reaction kinetics without influencing the overall thermodynamic balance. The increase in the radius of Al_2O_3 due to the rise in the phase fraction of mullite can be attributed to the enhanced availability of aluminium (Al) and oxygen (O) in the liquid. As larger mullite particles dissolve, they release more Al and O, which are then absorbed by Al_2O_3, promoting its further growth. The increased concentration of Al and O in the liquid raises their respective activities, which significantly shifts the equilibrium in favour of Al_2O_3 growth. Moreover, the increase in Al and O activity causes an expansion in the particle radius of Al_2O_3, meaning that the particle requires more time to reach equilibrium. Mullite, on the other hand, dissolves at a slower rate due to the larger particle size, which inherently takes longer to break down. This example demonstrates how the stability of Al_2O_3 can be enhanced by increasing the phase fraction of mullite, as the availability of Al and O from mullite dissolution supports the continued growth of Al_2O_3. In another case, increasing the phase fraction of SiO_2in the liquid initially promotes the growth

of Al_2O_3, but only up to a certain limit. When the phase fraction of SiO_2reaches 0.5, the Al_2O_3 particle becomes destabilized and grows to a smaller radius. This suggests that the impact of SiO_2on the stability of Al_2O_3 is constrained. The reduction in Al_2O_3 particle size can be attributed to the higher activity of silicon (Si) in the liquid, which suppresses the activities of aluminium (Al) and oxygen (O). As a result, the equilibrium radius of the Al_2O_3 particle decreases. This indicates that although SiO_2initially supports Al_2O_3 growth, its effect is limited as Si begins to dominate the system, reducing the potential for further Al_2O_3 stabilization.

ZrO_2-CaO-$CaZrO_3$ system provides another clear example of the common ion effect, where the dissolution of ZrO_2 and CaO leads to the stabilization of the $CaZrO_3$ particle. The dissolved ZrO_2 and CaO supply the necessary zirconium (Zr), oxygen (O), and calcium (Ca) ions required for the stabilization of $CaZrO_3$. It is important to note that, in this case, the $CaZrO_3$ particle does not increase its radius beyond the initial size; instead, it becomes smaller. Initially, $CaZrO_3$ experiences some dissolution before sufficient amounts of ZrO_2 and CaO have dissolved to stabilize it. By increasing the dissolution rates of CaO and ZrO_2, the $CaZrO_3$ particle can stabilize more quickly. This suggests that controlling the dissolution kinetics of the precursor oxides is crucial for the timely stabilization of $CaZrO_3$ in the system.

Sequential oxide selection method showed that the dissolution of the combined oxides Al_2O_3 and Y_2O_3 facilitates the formation of YAM, $YAlO_3$ and YAP. In this case, YAM and YAP are significantly more stable in the liquid than Al_2O_3 and Y_2O_3 combined, leading to the dissolution of the oxides to produce these more stable compounds. The dip-rise relationship shown in figure 119 is a direct result of YAM and YAP formation. The negative interaction between Y and Al, as demonstrated in the activity diagram (figure 77) and the simulation results (figures 108 and 111), clearly indicates that these elements have a strong tendency to form spinels (like YAM and YAP) rather than remaining in their individual oxide states. This drive towards spinel formation highlights the destabilizing effect that occurs when these oxides are in a reactive melt. Since, YAM, $YAlO_3$ and YAP have been identified as reaction products of Al_2O_3 and Y_2O_3, their use as mould oxides seems ideal for enhancing stability in Ti-Al melts. In the case of YAM in Ti-Al melt, it undergoes some dissolution and no other reaction products are found as a result of dissolution. However, YAP on its own, completely dissolves into the liquid, rendering it highly unstable in a Ti-Al environment. Furthermore, the reaction product as a result of dissolution has been identified to be YAM. When YAP and YAM are combined, as illustrated in figure 146, the results shift significantly in favour of stability. YAM, which experiences

some dissolution when alone, now grows past its initial particle radius. On the other hand, YAP, which fully dissolves on its own, stabilizes considerably, reducing the extent of dissolution. This is another example of the common ion effect, where both particles help stabilize each other in the liquid, enhancing overall stability. And there are no reaction products when YAP and YAM are combined. Unlike previous systems (YAG-Al_2O_3-Y_2O_3, SiO_2-Al_2O_3-Mullite, ZrO_2-CaO-$CaZrO_3$), where only one oxide stabilized at the expense of others, this case shows that both YAM and YAP positively contribute to each other's stability. Their mutual stabilization represents a promising strategy for achieving greater mould durability in reactive melt environments.

Table 11 shows that YAG and YAP are the stable oxides. YAG on its own has a drive towards formation of YAP which is the reason YAG exhibited high dissolution when present on its own. Simulation results, as shown in figure 147, confirm that YAP grows beyond its initial radius, while YAG, although initially dissolving, eventually stabilizes at a radius smaller than its initial size. The growth and dissolution profiles of YAP and YAG display highly non-linear behaviour compared to the smoother curves observed for YAM and YAP in figure 146. The improved

stability exhibited by YAG and YAP when combined, compared to their individual stability, highlights the common ion effect. Both oxides, by sharing common ions, mutually stabilize each other, resulting in an overall enhanced stability within the system. This stabilization pattern again emphasizes the importance of combining oxides that support each other's equilibrium in high-temperature Ti-Al melts. There are no further reaction products for YAP + YAG, and so the oxides have reached their maximum stability.

The high dissolution of single phase Al_2O_3 particle is the result of formation of HCP-A3 phase formation as indicated by table 12. However, when Al_2O_3 is combined with mullite, the reaction pathway changes and resulting reaction product is simply Al_2O_3 + IONIC. Once the HCP phase is suppressed the Al_2O_3 is no longer dissolves but grows even larger than its initial radius (figure 138). Mullite in this instance acts as a suppressant for HCP phase which then allows the Al_2O_3 particle to become highly stable. This effect is clearly seen in figures 148 and 149 where, the presence of mullite suppresses HCP and as a result Al_2O_3 becomes stable sooner.

Changing stoichiometric ratios of Y_2O_3-Al_2O_3 has had a significant impact on the stability of oxides. The results highlight a nuanced relationship between particle sta-

bility and stoichiometric balance, with significant implications for optimizing mixed-oxide formulations to control dissolution rates in high-temperature environments. This highlights the potential to fine-tune oxide performance by adjusting the Y_2O_3 and Al_2O_3 ratio, balancing the benefits of enhanced stability against the risk of premature dissolution.

The stability ranking illustrated in figure 153 offers significant insights into the thermodynamic stability of various oxides. While Y_2O_3 consistently ranks as the most stable oxide, literature typically identifies CaO or ZrO_2 as the next most stable. However, this study reveals that additional oxides or oxide combinations fall within the stability range between Y_2O_3 and CaO. For instance, single oxides like YAM and $CaYAlO_4$ demonstrate stability levels comparable to Y_2O_3. Yttria-Stabilized-ZrO_2 (ZrO_2 with a Fluorite structure) serves as an example of a doped oxide that exhibits higher stability than CaO. This suggests that more oxides or oxide combinations with stability within the Y_2O_3-CaO range may exist, warranting further research to identify potential candidates. Conversely, several combined systems show marked instability, ranking lower on the stability bar chart. Many of these systems lack more than one common ion, and those with multiple common ions, such as the CaO-$CaZrO_3$-ZrO_2 system, require substantial oxygen levels in the liquid to remain

stable—an impractical condition for titanium casting. But it is promising to see many of the combined oxide systems like YAM-YAP, Al_2O_3-Mullite exhibit higher stability than as individual oxides.

5 Overall Discussion

5.1 Thermodynamic Stability of Mould Oxides

In Chapter 1, several challenges in modelling metal-mould reactions were discussed, with the first being the prediction of the thermodynamic stability of oxides (ΔG_r) for selecting suitable oxide materials for casting titanium alloys. The most commonly used method in the literature for oxide selection in Ti-alloy casting is the Ellingham method. Numerous studies [19], [33], [136] have leveraged this method to predict the thermodynamic stability of various oxide systems, providing a foundational approach for oxide selection in casting processes. In this study, the Ellingham method was also employed, utilizing three different thermodynamic databases to predict the stability of oxide systems. However, several inconsistencies became evident when comparing the predictions with experimental data. For instance, there remain unresolved questions such as the formation of the alpha-case layer, the observed high levels of oxygen contamination in titanium alloys and discrepancies in the stability ranking of certain oxides observed by Saha [150]. These inconsistencies suggest that while the Ellingham method is a useful tool, it may not fully capture the complexities of metal-mould interactions during casting. The reason was primarily because of the calculations being strictly limited to standard state conditions. Similarly, Kostov

model [27] made some approximations which accounted for some non-ideal behaviour of the liquid yet the predicted ΔG_r values were significantly higher than expected and no dissolution behaviour was observed other than SiO_2.

A better understanding of metal-mould reactions was obtained when rigorous activity data from CALPHAD databases was used in the mass action law. It was also evident that a high concentration of oxygen is required in the melt for any oxide ceramics to establish an equilibrium with the liquid. Meaning there is a high chemical potential different between the oxide and the liquid metal when they are brought into contact with each other. This is illustrated in figure 154 (a). The difference in chemical potential ($\Delta\mu$) varies depending on the oxide in contact with the metal. This limit was obtainable from CALPHAD databases.

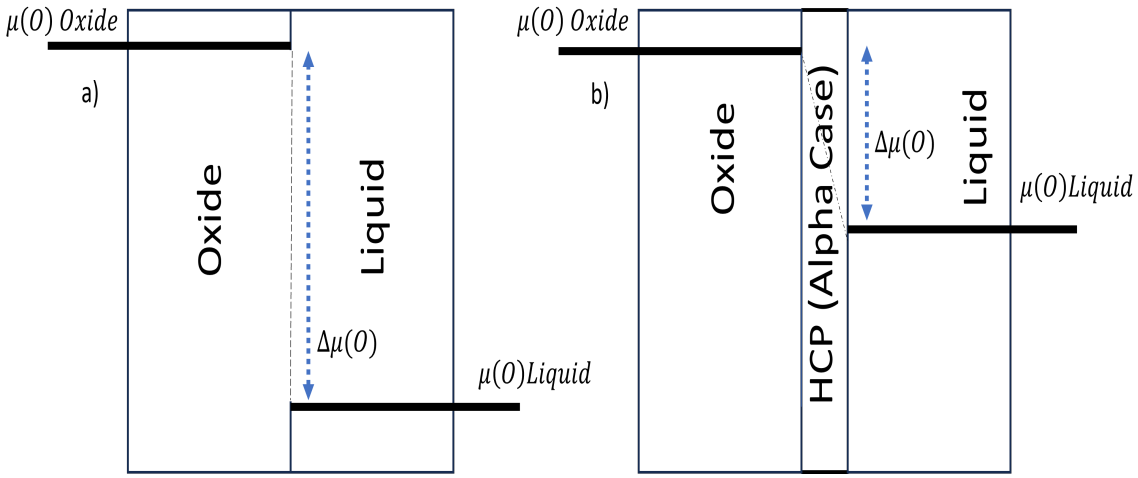

Figure 154: Illustration of dissolution mechanism during metal-mould contact

Given this scenario, it is unsurprising that oxides in contact with the TiAl melt react, as the difference in chemical potential is exceedingly high even for Y_2O_3. With regards to this, Y_2O_3 required the least amount of oxygen to establish an equilibrium with the liquid TiAl melt followed by CaO, ZrO_2 and Al_2O_3. SiO_2 was unstable even when high amount of Si and O concentrations was present in the melt (figure 66). The problem here is high solubility of oxygen in titanium, this well captured in section 2.3.5.1, by Wagner's model outlining the absence of a protective layer on

the metal side at temperatures above 1000°C, which exposes the large diffuse layer causing oxygen to diffuse freely into the liquid. Since, oxygen is an alpha stabilizer, it likely promotes the stabilization of the alpha (HCP) phase. Consequently, the alpha case begins to form at the metal-mould interface, as shown in figure 154 (b). The emergence of the HCP phase reduces the chemical potential difference between the metal and the mould forming a thick layer at the metal-mould interface.

It is critical to note that not all CALPHAD databases predict similar stability. Vast differences in stability is observed depending on the database used, in some cases the differences are too significant. One instance is ΔG_r predicted predicted for CaO (67), where TCFE7 database predicts a stable CaO oxide ($+\Delta G_r$), TCOX11 predicts an unstable CaO ($-\Delta G_r$). These difference are common when using CALPHAD databases so it is critical that appropriate databases are chosen.

5.2 Kinetics Stability of Mould Oxides

The advantage of using the ΔG_r approach lies in its ability to rigorously study the effects of elemental interactions within the melt. This method allows for a more comprehensive analysis, especially in complex systems. However, using ΔG_r requires high-quality thermodynamic data. In contrast, the supersaturation approach only

requires oxygen data, making it simpler but limited to binary interactions. While it is possible to model oxide growth in a ternary system using supersaturation, this approach does not account for the influence of alloying elements. In systems as simple as Al_2O_3 in a Ti-Al melt, it is crucial to consider the interactions between Ti, Al, and O, as these significantly impact the kinetics of particle growth. Therefore, the choice of approach depends on the amount of available data and the complexity of the system being studied.

From thermodynamic analysis it was clear that dissolution of oxides take place because of the large chemical potential difference that exists between the oxide and the melt. It was also noticed that the difference in chemical potential differ depending on the type of oxide. The basis for the kinetic study was to identify oxides that react at the slowest rate and to introduce new strategies to limit the solubility of oxygen in the liquid thereby, increasing mould stability. To study these reaction rates, a model was required and the frozen gradient approximation was chosen as the basis for studying the kinetics of metal-mould reactions. However, this approach was initially limited to binary systems and restricted to a total of two phases in the system. These limitations were addressed by substituting the driving force 'Supersaturation' with 'ΔG_r' as detailed in section 4.3.1. This substitution enables the model to account for multi-component interactions during dissolution, providing a

more realistic representation of the system. The advantage of using ΔG_r lies in its use of chemical activities, which reflect the actual thermodynamic driving forces in the liquid phase. Unlike idealized approaches, which assumes interaction between elements in the liquid are ideal, this method captures the influence of all interacting elements in the liquid phase, making it especially suitable for complex, non-ideal multicomponent systems.

From the study, several important insights was obtained regarding the stability of oxides in liquid environments. Firstly, no oxides are completely stable in the liquid phase and both ΔG_r and dissolution rates vary significantly depending on the type of oxide used. Liquids with higher titanium (Ti) content tend to show more negative ΔG_r values, faster dissolution rates and higher levels of oxygen contamination. The crystal structure of oxides also plays a crucial role, as seen with yttrium-stabilized ZrO_2, where stability depends on the crystal structure.

The interaction between multi-phase oxides in a liquid can either destabilize or stabilize depending on the combination of oxides. Therefore, choosing the correct combination is essential for optimum stability. In a system with Al_2O_3-Y_2O_3, the two oxides destabilized each other through the 'dip-rise' effect. This destabilization could

be minimized by adding excess yttrium (Y) into the liquid, which increased the dissolution rate of Al_2O_3 (k_1) while decreasing the dissolution rate of Y_2O_3 (k_2). At a certain concentration (about 0.07 mol fraction of yttrium), Y_2O_3 particles stabilized, although this required a significant amount of yttrium in the liquid phase. Another method to slow the reaction rate involved the addition of alloying elements like niobium (Nb) and chromium (Cr). This approach slowed down the reaction rates of both Al_2O_3 and Y_2O_3.

Interestingly, switching Al_2O_3 with CaO significantly improved the stability of Y_2O_3. The dip-rise effect was minimized in this system, although CaO dissolved completely while Y_2O_3 showed initial dissolution before stabilizing. However, this system was not significantly more stable than having just one oxide phase in the liquid. On the other hand, having oxides in the liquid without any common ions (other than oxygen) led to complete destabilization. Conversely, oxides sharing common metallic ions, such as YAG, Al_2O_3, and Y_2O_3, tended to stabilize each other through the common ion effect. There are two types of stabilising effect that was observed. First includes the destabilising of one or two phases which then leads to stabilising another this is illustrated in figure 155. This results in complete dissolution of one or two phases while the stabilising phase establishes an equilibrium with the liquid. The examples of such systems are Al_2O_3-Mullite, Al_2O_3-Y_2O_3-YAG and

$CaO\text{-}ZrO_3\text{-}CaZrO_3$.

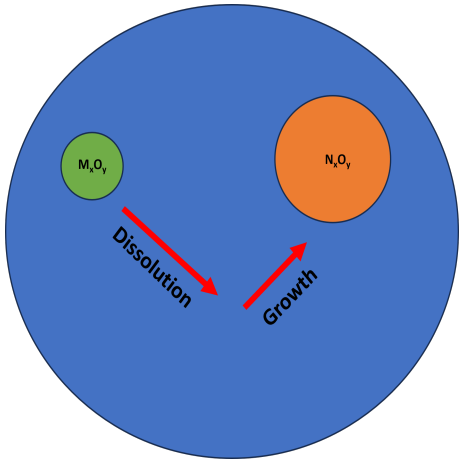

Figure 155: Stabilising effect via particle dissolution

The second, is the mutual stabilisation of two particles, where both particles stabilise each other, establishing an equilibrium with the liquid simultaneously as shown in figure 156.

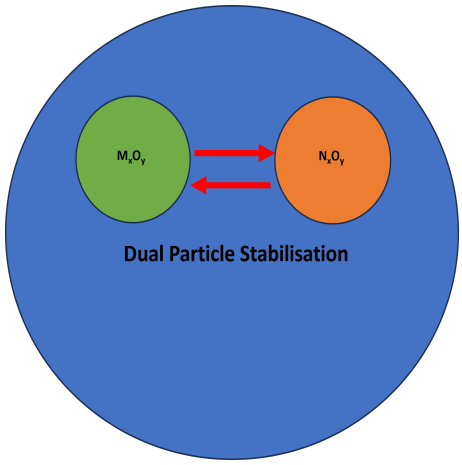

Figure 156: Stabilising effect via mutual stabilisation

Significant improvements in stability were also observed when reaction products from the systems assessed were used as the mould oxides. For instance, YAG-YAP combinations showed much higher stability when present together, compared to when they existed as single phases. In this case, both oxides stabilized, leading to lower oxygen content in the liquid, illustrating another common ion effect. Additionally, a reaction product known as the alpha case (HCP phase) was found to stabilize under certain conditions. This alpha case formation could be suppressed through multiphase systems, as seen in the Al_2O_3-Mullite combination, where the addition of Mullite prevented the formation of the HCP phase. The HCP phase appeared to be more common when single-phase mould oxides were used especially ZrO_2.

6 Conclusion and Future Work

This project modelled interactions between liquid titanium and mould oxides during Ti-alloy casting, aiming to identify more stable oxide systems. Although a universally stable oxide was not found, the study provided valuable insights into oxide behaviour using three criteria: the free energy change of reaction (ΔG_r), reaction rate constant (k), and post-reaction oxygen contamination. These factors offered strategies for improving current mould materials. The thermodynamic analysis, based on the mass action law, showed that approximation methods like the Ellingham diagram, Kostov model, and its modified form are effective for comparing relative oxide stability, even if they tend to overestimate ΔG_r. Their predictions closely matched experimental rankings, making them useful for pre-selecting oxide materials when detailed thermodynamic data is lacking.

Using CALPHAD databases with the mass action law enabled deeper understanding of Ti-mould reactions. It captured dissolution dynamics and equilibrium shifts, particularly in complex systems like Ti-Al-O, where the stability of Al_2O_3 is composition-dependent. This approach, free from ideal approximations, provided more realistic assessments. However, results highlighted the need for careful database selection, as shown by differences in CaO stability between databases. TCOX11, designed for oxides, was more reliable than TCFE7, which is Fe-focused. Both ap-

proximation models and CALPHAD data generally agreed with experimental oxide rankings, consistently identifying Y_2O_3, CaO, ZrO_2, and Al_2O_3 as promising. However, discrepancies between ZrO_2 and CaO in CALPHAD rankings caution against overreliance on database predictions, especially in reactive systems like Ti.

This study advanced the frozen gradient approximation by replacing supersaturation with ΔG_r, enabling multi-component, multi-phase analysis of dissolution reactions. This improved model revealed that even stable oxides like Y_2O_3 partially dissolve under non-equilibrium conditions, with varying dissolution rates. Exploring multi-phase particles exposed complexities in elemental interactions. Some combinations, such as Y_2O_3 + Al_2O_3, dissociated rapidly due to negative Y–Al interactions in the melt. Y_2O_3 + CaO performed better, due to positive interactions, though with limited benefits over single phases. This showed that oxides with fewer than two common ions tend to destabilize each other, emphasizing the importance of melt-phase metallic interactions. Improved stability was achieved when oxides shared multiple common ions. In the YAG–Al_2O_3–Y_2O_3 system, YAG eventually stabilized despite initial dissolution of Y_2O_3 and Al_2O_3. Similarly, $CaZrO_3$ stabilized in the CaO–$CaZrO_3$–ZrO_2 system, in contrast to the destabilization of CaO and ZrO_2 under oxygen-rich conditions. The Al_2O_3–mullite system was particularly promising: mullite dissolved, driving the growth of stable Al_2O_3 and reducing final oxygen con-

tamination. Another effective strategy was sequential oxide selection—using reaction products from oxide dissolution as new mould oxides. For instance, Al_2O_3 and Y_2O_3 dissolved to form YAM and YAP, which, when combined, stabilized each other and reduced oxygen contamination more than YAP alone. YAG + YAP also proved more stable than either on their own. These findings introduced intermediate oxides and combinations with stability between that of Y_2O_3 and CaO, such as single-phase YAM, $CaYAlO_4$, and combinations like YAM + YAP or YAG + YAP. The effect of oxide ratios also played a critical role. In the Al_2O_3–mullite–SiO_2 system, excess SiO_2 destabilized Al_2O_3, showing that optimal phase ratios are key for stability. The HCP phase, often associated with the alpha case in Ti castings, emerged as a reaction product in many single-phase systems but was suppressed in certain combinations, notably Al_2O_3 + mullite. Eliminating HCP improved oxide stability and reduced oxygen contamination in the melt.

Below points summarise the several stabilising and destabilising mechanisms were identified using the model:

- Excess metallic additions help deoxidize the melt, shifting equilibrium toward oxide stability.
- Negative interactions between metallic species in the melt can destabilize oxides via the dip and rise effect.

- Positive metallic interactions mitigate destabilising effects and enhance stability.
- Alloying elements such as Nb reduce oxygen solubility, improving oxide stability, whereas high Ti content increases reaction rates.
- Dissimilar oxides with fewer than two shared ions destabilize each other.
- Common ion effect 1: Oxides sharing at least two common ions may stabilize each other through dissolution-growth processes.
- Common ion effect 2: Oxides sharing three or more common ions may mutually stabilize one another.
- Specific oxide combinations, such as Al_2O_3 and mullite, can suppress HCP phase formation and improve stability.
- Mixing ratio: The proportion of each oxide in a mixture influences overall stability.

6.1 Mould Recommendation for TiAl Casting

Based on the simulation results presented in figure 153 Y_2O_3 emerges as the most suitable oxide for casting Ti-Al alloys. This is also in line with evidence from literature,

formation energy analysis, and the Kostov model. However, its high cost presents a significant drawback. A more economical alternative is $CaYAlO_4$, which incorporates Ca and Al to reduce the required yttrium content. In particular, $CaYAlO_4$ offers a comparable level of stability to Y_2O_3, making it a promising candidate. However, no experimental studies have yet evaluated $CaYAlO_4$ in direct contact with Ti-Al alloys and it therefore, remains a potential option for future investigation. Other candidates such as YAM and YAG-YAP mixtures also demonstrate high thermodynamic stability. However, the fabrication of highly pure YAG and YAP particles presents a notable challenge. Additionally, the Al_2O_3–Mullite composite exhibits a marked improvement in performance compared to the individual use of either Al_2O_3 or mullite. Notably, figures 148 and 149 illustrate clear suppression of alpha-case formation with this composite and lower oxygen contamination which makes it an ideal mould material. In summary, $CaYAlO_4$, YAM, YAG-YAP, and Al_2O_3–Mullite stand out as promising oxide candidates for Ti-Al alloy casting, each balancing stability, cost and manufacturability in distinct ways.

6.2 Model Conclusion

The novelty of the model lies in its ability to capture a wide range of complex phenomena despite its simplicity. It can simulate particle dissolution in multicomponent

melts, competitive growth of multi-phase particles, and the effects of composition, temperature, and diffusion on transformation rates. Importantly, it can also account for non-ideal interactions such as the 'dip and rise' effect and the common ion effect—phenomena that cannot be predicted using simpler approaches like the Kostov model or formation energy calculations but require rigorous modelling frameworks. Compared to other available models such as TC-PRISMA, Phase Field, and ab initio methods, the developed model offers several significant advantages. For example, while TC-PRISMA is well-suited for studying nucleation within solid or liquid matrices but it cannot simulate dissolution kinetics or growth driven by dissolution, processes that are critical for understanding multi-phase systems such as Al_2O_3 and mullite. Unlike TC-PRISMA, which assume stable phase nucleation and growth, this model treats phase change as a chemical reaction, allowing direct modelling of reactant–product conversion. This allows to study the effects of impurities in the melt as a result of dissolution. More advanced approaches, such as Phase Field modelling, offer higher accuracy but come with significant computational cost and time demands. Similarly, ab initio methods, though powerful, become impractical for multi-component systems due to their intensive computational requirements. The model presented in this study strikes a pragmatic balance between simplicity, accuracy, and computational efficiency. It provides a fast solution to study wide range of

multi-component systems in quick time. Therefore, it has the potential to serve as an effective preliminary screening tool for searching and identifying stable oxides, significantly narrowing the range of candidates before applying more rigorous, resource-intensive methods like Phase Field, thus reducing both time and computational cost. Although the model has not yet been fully validated through experiments, it still shows reliability. The thermodynamic and kinetic rankings reported earlier match well with experimental data, formation energy calculations and predictions from the Kostov model. This shows that results predicted from the model are at large valid.

6.3 Future Work

While this study yielded many findings, there remains substantial room for development, particularly in model refinement. Several areas could enhance accuracy and provide further insights. Below are few ideas where the model could be developed further to add few more levels of accuracy.

6.3.1 Model Development

Curvature Effects: Particle curvature significantly affects chemical potential and stability. Smaller particles, due to higher surface energy, dissolve more readily—a process contributing to coarsening. This occurs to reduce the system's overall free

energy, usually by minimizing surface or interface energy. This can be accounted for by adding a curvature term to the driving force:

$$\Delta G_r + \frac{\gamma}{2r} \tag{57}$$

where γ is interfacial energy and r is radius. The difficult part is obtaining accurate values for the interface energy and may have to rely on molecular dynamics or experimental studies for accurate values.

Realistic Diffusion: This study assumes uniform liquid composition throughout the liquid, omitting spatial diffusion. To address this limitation, spatially discretizing the liquid phase into multiple shells, as illustrated in figure 157 and modelling the diffusion of elements between each of these shells would provide a more realistic representation of elemental diffusion across the liquid phase. This approach would not only resolve the issue of spatial diffusion but also be highly effective for modelling localized nucleation, whether it occurs near the particle surface or further away in the liquid.

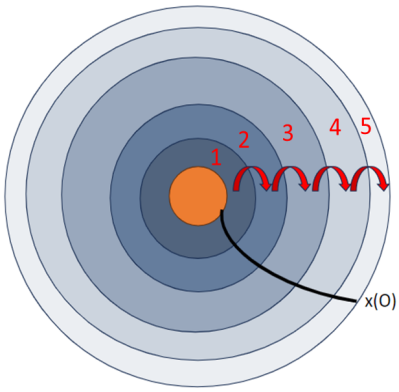

Figure 157: Illustration of spatially discretised liquid phase for modelling of elemental diffusion across the liquid

To model the diffusion of elements between inner shells (2-4), Fick's second law in spherical coordinates can be applied, as shown in the following equation [153]:

$$\frac{\partial C}{\partial t} = D\left(\frac{1}{r^2}\frac{\partial}{\partial r}\left(r^2\frac{\partial C}{\partial r}\right)\right) \tag{58}$$

with finite differences, diffusion into shells 2 is given below, similar is also true for shells 3 and 4:

$$\Delta C_2 = D \cdot dt \cdot \left(\frac{C_3 - C_2}{\Delta r_2 \Delta r_3} + \frac{2}{r_2} \cdot \frac{C_3 - C_2}{\Delta r_2 + \Delta r_3}\right) \tag{59}$$

Shell 5, can be treated as no-flux boundary condition, while shell 1 is governed by the original mass balance in equation 42. This allows to track the diffusion of elements in the liquid spatially, close to more realistic conditions.

Non-Stoichiometric Dissolution: All simulations in this model assume the oxides are perfectly stoichiometric and that dissolution is also stoichiometric. In reality, many oxides have solubility of other elements in them and may dissolve non-stoichiometrically, forming oxygen-deficient structures (e.g., M_xO_{y-a}) [150]. Incorporating this would improve accuracy and show how non-stoichiometry affects stability. Additionally, exploring different particle shapes (cubic, irregular) could clarify morphology effects on kinetics.

Nucleation: While nucleation is not the primary focus of this study, reaction products as a result of metal-mould interaction have been identified and they have the potential change oxide stability once they nucleate. Classical nucleation model in equations 60 and 61 can be incorporated into the current model to account for both heterogeneous or homogeneous nucleation.

$$\Delta G_N = \left(-\frac{4}{3}\pi r^3 \Delta G_v + 4\pi r^2 \gamma_{sl} \right) \tag{60}$$

$$\Delta G^* = \frac{16\pi\gamma_{sl}^3}{3\Delta G_v^2} \cdot S \tag{61}$$

Here, S is a factor ($0 < S \leq 1$) that lowers the energy barrier for heterogeneous nucleation. Estimating S typically relies on experimental data.

Interface Effects: The current model assumes diffusion-controlled kinetics, implying interface equilibrium. In reality, slow attachment/detachment at interfaces

may limit reaction rates. To model this, an Arrhenius-type expression can used as shown below [18]:

$$k_s = A_s \exp\left(-\frac{E_a}{RT}\right) \tag{62}$$

where, A_s is the pre-exponential factor and E_a is the activation energy. The interface rate constant k_s can be combined with the driving force:

$$\Delta G_r + k_s \tag{63}$$

Determining k_s is often challenging and requires detailed knowledge of the specific surface processes involved, such as the mechanisms of atomic attachment and detachment, the nature of the interface, and the characteristics of the materials involved.

6.3.2 Phase Interaction Studies

Particle-Particle Interaction: Solid-solid particle interactions are mediated solely through the liquid phase, excluding direct solid-to-solid interactions. While these interactions are negligible, they can still play a role in phase transformation which can affect the mould stability. This approach also neglects micro-scale forces, such as Van der Waals and electrostatic interactions, which can significantly influence particle behaviour at small scales due to high surface area-to-volume ratios. Advanced models—e.g., Mean Field Theory or Cluster Expansion—could capture solid-solid

interactions more accurately. Incorporating these approaches could enhance the current model's predictive accuracy. Additionally, the current model excludes particle overlap which can become a problem particularly in densely populated particles in the liquid, potentially triggering displacement reactions or new phase transformations.

Alpha Case Formation: Alpha-case (HCP phase) formation remains poorly understood. Building on findings where certain oxides (e.g., mullite) suppressed HCP formation, future work could test other oxide or alloy combinations to inhibit this layer. Modelling alpha-case as a particle would allow evaluation of its interactions, stability, and growth. Certain mould microstructures promote protective oxide layers, reducing oxygen ingress and reducing alpha case formation. Growth of oxide layer around the mould particle is represented in figure 158.

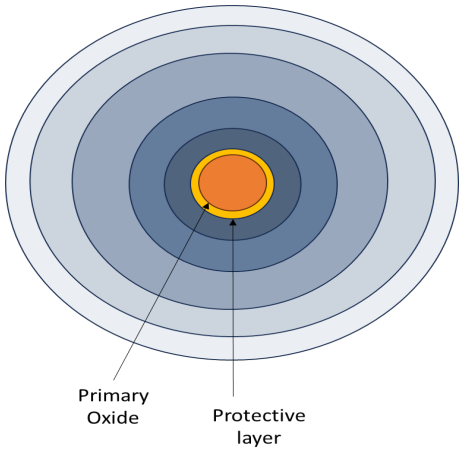

Figure 158: Illustration of protective oxide layer growth on primary mould oxide

Modelling oxide layer around mould particle involves:

- Nucleation likelihood at the interface
- Growth rate and morphology
- Effects of melt composition

Wetting angle influences oxide adhesion. Lower angles promote continuous films; higher angles result in isolated particles. Including wetting behaviour helps predict:

- Film continuity
- Adhesion strength
- Breakdown conditions

Once nucleated, growth of the oxide layer depends on oxygen diffusion, thermal stability, and possible dissolution—especially under non-equilibrium conditions.

Experimental Validation: This model requires quantitative validation. A suitable approach is to replicate conditions from Kobayashi's Y_2O_3 levitation experiment [32]. Matching particle/liquid volume and temperature enables comparison of equilibrium time, metal mass, ΔG_r, and oxygen content (Table 14).

Reaction rate validation follows Cui's method [36], comparing Arrhenius plots of rate constants vs. temperature (figure 159). Similar gradients between experiment and model indicate good agreement.

Parameter	Model	Experiment
Equilibrium O (wt%)	0.56	0.11
Equilibration Time (min)	∼10	∼8
Metal Mass at Equilibrium (g)	10.096	10.034
ΔG_r (J/mol·K)	-632584.37	-544824.79

Table 14: Comparison of model vs. experiment for Y_2O_3 dissolution in TiAl melt [32]

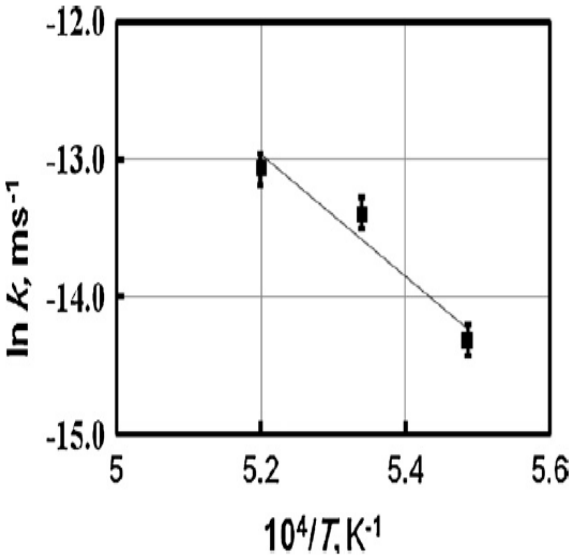

Figure 159: Rate constant vs. temperature from Cui [36]

6.3.3 Built to Become Obsolete: Final Thoughts

The developments outlined in the previous section show a clear path toward building a model that fully captures the complex interplay of thermodynamics, kinetics, diffusion, nucleation, and interfacial phenomena during metal–mould interactions. Each proposed extension brings the model closer to a comprehensive tool—capable not just of simulating, but of explaining and predicting real-world behaviour with high fidelity. However, the ultimate aim of this model is not perpetual refinement, but resolution. When it reaches a point where it can consistently and accurately answer all critical questions about oxide stability, reaction pathways and casting outcomes, the model will have fulfilled its purpose. At that point, it becomes less a tool for discovery and more a guide for decision-making—quietly stepping into the background as understanding takes its place. The end goal, paradoxically, is for the model to become obsolete—not through failure, but through complete success.

7 Appendix

7.1 Ti-Al-O Phase Diagram

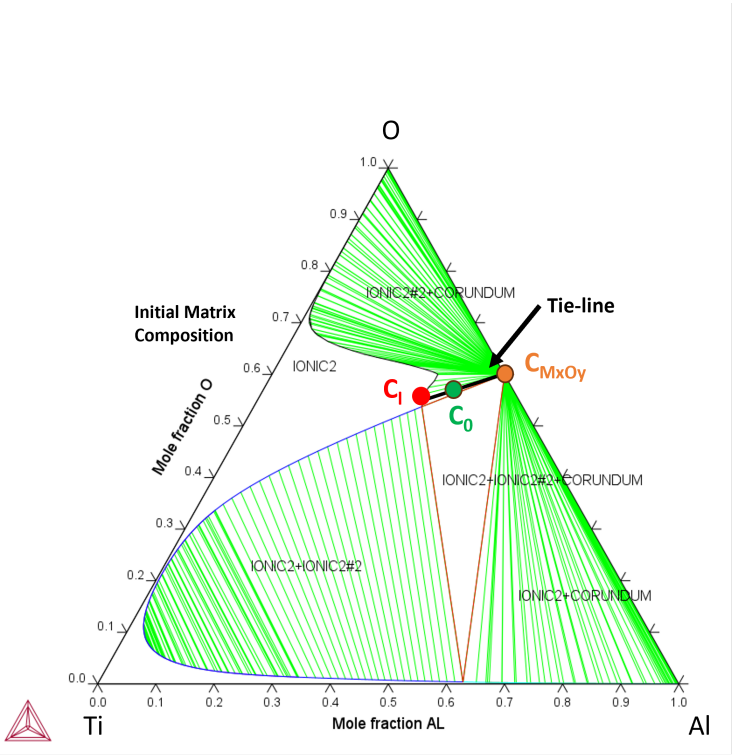

Figure 160: Ti-Al-O Phase Diagram at 2000 K (TCOX11 Database) with simulation boundaries for growth, Thermo-Calc

7.2 Model Parameters for Al_2O_3 Growth

Parameter	**Value**
System Size (m^3)	$2.09 \cdot 10^{-14}$
Initial Particle Size (m)	$0.18 \cdot 10^{-5}$
Oxygen Alloy Composition C_0 (O)	0.563
Aluminium Alloy Composition C_0 (Al)	0.33
Fixed Oxygen Composition in Particle $C_{M_xO_y}$ (O)	0.597
Fixed Aluminium Composition in Particle $C_{M_xO_y}$ (Al)	0.399
Oxygen Composition in Liquid at Equilibrium C_l (O)	0.537
Aluminium Composition in Liquid at Equilibrium C_l (Al)	0.278
Time-step (s)	$1 \cdot 10^{-4}$
Diffusion Coefficient (m^2/s)	$1 \cdot 10^{-8}$

Table 15: Model conditions for Al_2O_3 growth in Ti-Al-O liquid (2000 K)

7.3 Ti-Al-O Phase Diagram - Dissolution Boundaries

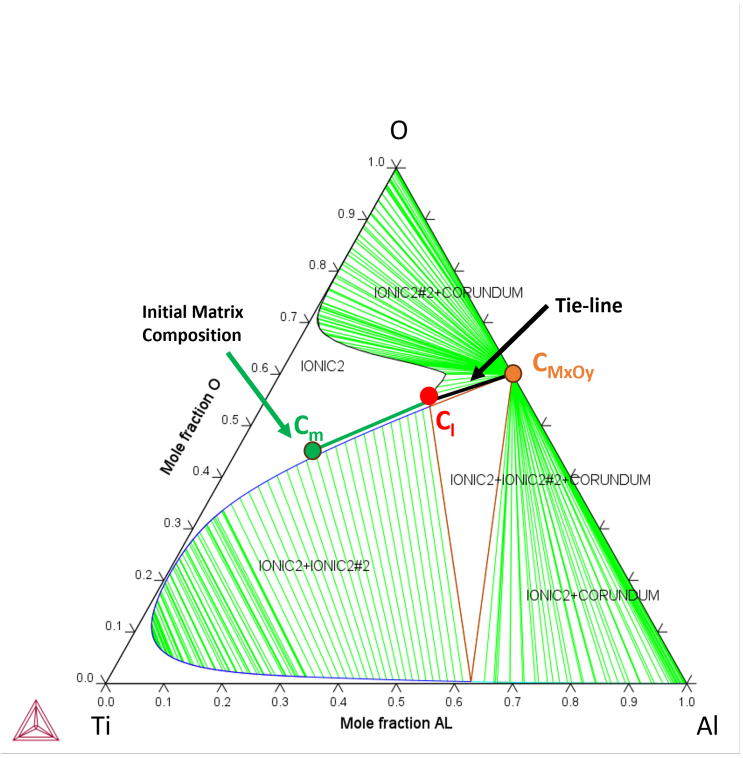

Figure 161: Ti-Al-O phase diagram at 2000 K (TCOX11 Database) with simulation boundaries for dissolution, Thermo-Calc

7.4 Model Parameters for Al_2O_3 Dissolution

Parameter	**Value**
System Size (m^3)	$2.09 \cdot 10^{-14}$
Initial Particle Size (m)	$1.60 \cdot 10^{-5}$
Oxygen Alloy Composition C_0 (O)	0.563
Aluminium Alloy Composition C_0 (Al)	0.33
Fixed Oxygen Composition in Particle $C_{M_xO_y}$ (O)	0.597
Fixed Aluminium Composition in Particle $C_{M_xO_y}$ (Al)	0.399
Oxygen Composition in Liquid at Equilibrium C_l (O)	0.537
Aluminium Composition in Liquid at Equilibrium C_l (Al)	0.278
Initial Oxygen Liquid Composition $C_{m(\mathrm{O})}$	0.443
Initial Aluminium Liquid Composition $C_{m(\mathrm{Al})}$	0.126
Time-step (s)	$1.0 \cdot 10^{-4}$
Diffusion Coefficient (m^2/s)	$1.0 \cdot 10^{-8}$

Table 16: Model conditions for Al_2O_3 dissolution in Ti-Al-O liquid (2000 K)

7.5 Model Parameters for Non-ideal Single Oxide Reactions

TiAl alloy

Parameter	**Value**
Ti Initial Composition in Liquid (mol frac)	0.5
Al Initial Composition in Liquid (mol frac)	0.4998
O Initial Composition in Liquid (mol frac)	0.0001
Initial Composition of Metallic Elements in Liquid (Zr, Y, Ca, etc.) (mol frac)	0.0001
Initial Particle Size (m)	0.00001
Total System Volume (m^3)	2.09×10^{-14}
Time Step (s)	1.00×10^{-4}
Diffusion Coefficient (m^2/s)	1.00×10^{-8}

Table 17: System parameters for single oxides in TiAl alloy, under non-ideal conditions (2000 K)

7.5.1 Model Parameters for Non-ideal Single Oxide Reactions Ti6Al4V alloy

Parameter	**Value**
Ti Initial Composition in Liquid (mol frac)	0.8999
Al Initial Composition in Liquid (mol frac)	0.06
O Initial Composition in Liquid (mol frac)	0.0001
V Initial Composition in Liquid (mol frac)	0.04
Other Metallic Elements in Liquid (Zr, Y, Ca, etc.) (mol frac)	0.0001
Initial Particle Size (m)	0.00001
Total System Volume (m^3)	2.09×10^{-14}
Time Step (s)	1.00×10^{-4}
Diffusion Coefficient (m^2/s)	1.00×10^{-8}

Table 18: System parameters for Ti-Al-V-O liquid simulation (2000 K)

7.5.2 Model Parameters for Non-ideal Single Oxide Reactions Pure Ti alloy

Parameter	**Value**
Ti Initial Composition in Liquid (mol frac)	0.9998
O Initial Composition in Liquid (mol frac)	0.0001
Other Metallic Elements in Liquid (Zr, Y, Ca, etc.) (mol frac)	0.0001
Initial Particle Size (m)	0.00001
Total System Volume (m^3)	2.09×10^{-14}
Time Step (s)	1.00×10^{-4}
Diffusion Coefficient (m^2/s)	1.00×10^{-8}

Table 19: System parameters for Ti-O Liquid Simulation (2000 K)

7.5.3 Model Parameters For Multiple Particles of the Same Type

Parameter	**Value**
Ti Initial Composition in Liquid (mol frac)	0.4999
Al Initial Composition in Liquid (mol frac)	0.5
O Initial Composition in Liquid (mol frac)	0.0001
Initial Particle Size 1 (m) (M_xO_y)	0.00001
Initial Particle Size 2 (m) (M_xO_y)	0.00001
Initial Particle Size 3 (m) (if present) (M_xO_y)	0.00001
Total System Volume (m^3)	2.09×10^{-14}
Time Step (s)	1.00×10^{-4}
Diffusion Coefficient (m^2/s)	1.00×10^{-8}

Table 20: Initial parameters for multiple M_xO_y oxide in TiAl melt

7.5.4 Model Parameters for Non-ideal Al_2O3 and Y_2O_3 in Ti-Al alloy

Parameter	**Value**
Ti Initial Composition in Liquid (mol frac)	0.4999
Al Initial Composition in Liquid (mol frac)	0.5
O Initial Composition in Liquid (mol frac)	0.0001
Initial Particle Size 1 (m) (Al_2O_3)	0.00001
Initial Particle Size 2 (m) (Y_2O_3)	0.00001
Total System Volume (m^3)	2.09×10^{-14}
Time Step (s)	1.00×10^{-4}
Diffusion Coefficient (m^2/s)	1.00×10^{-8}

Table 21: System parameters for Ti-Al-O liquid simulation with Al_2O_3 and Y_2O_3 particles (2000 K)

7.5.5 Model Parameters for Multiple Different Phases in Ti-Al alloy

Parameter	**Value**
Ti Initial Composition in Liquid (mol frac)	0.5
Al Initial Composition in Liquid (mol frac)	0.4998
O Initial Composition in Liquid (mol frac)	0.0001
Other Metallic Elements in Liquid (Ca) (mol frac)	0.0001
Initial Particle Size 1 (m)	0.00001
Initial Particle Size 2 (m)	0.00001
Initial Particle Size 3 (m) (If in the Liquid)	0.00001
Total System Volume (m^3)	2.09×10^{-14}
Time Step (s)	1.00×10^{-4}
Diffusion Coefficient (m^2/s)	1.00×10^{-8}

Table 22: System parameters for Ti-Al-O-Ca liquid simulation with three particles (if in liquid)

2000 K

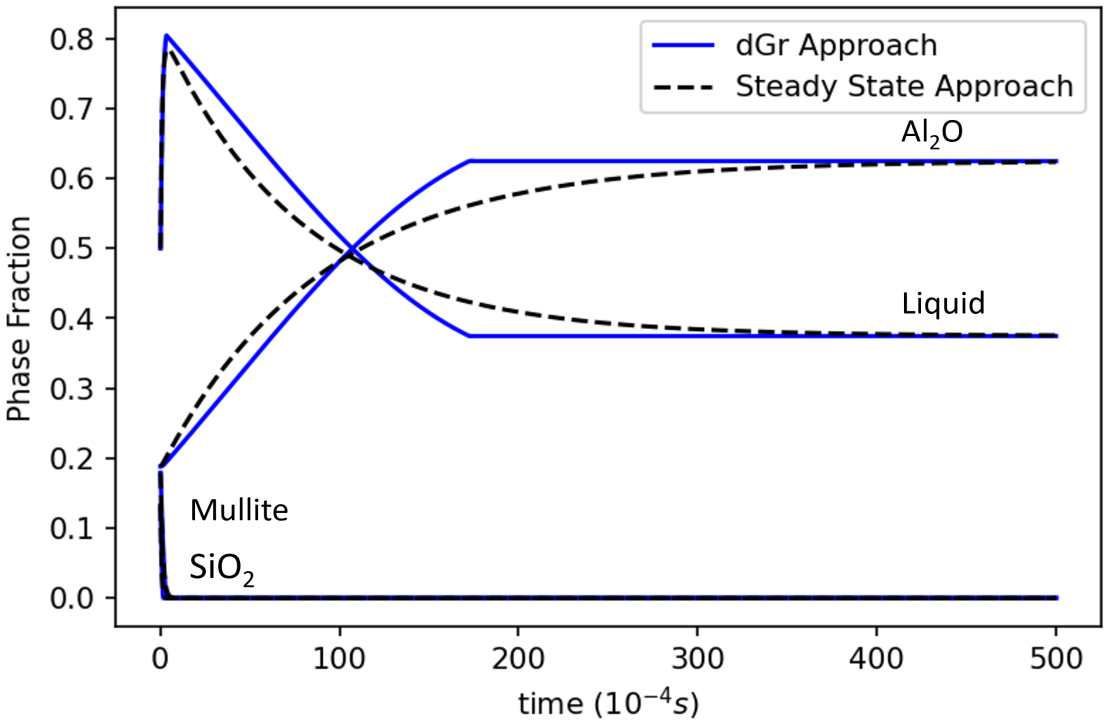

Figure 162: Analytical solution for Al_2O_3-SiO_2-Mullite system

7.5.6 Model Parameters for Multiple Different Phases in Ti-Al alloy

The sharp approach to equilibrium predicted by the ΔG_r (driving force) approach, compared to the smoother profile predicted by the steady-state approach, is characteristic of the fundamental differences between these combinations. The sharp transitions observed in the ΔG_r approach reflect a rapid rearrangement of phases as the system energetically 'settles' into its equilibrium configuration once the conditions are favourable. This suggests that, when conditions for phase transformation are met, the system can undergo a transformation with minimal gradual change, resulting in the sharp inflection point seen in the graph. In contrast, the steady-state approximation typically models the system as slowly approaching equilibrium. It tends to smooth out abrupt transitions because it only accounts for the reaction rate constant, which changes continuously and provides an approximation of the process. As a result, the steady-state model does not capture sudden phase shifts or transformations as sharply as the ΔG_r approach, which takes the entire thermodynamic landscape into account. This distinction underlines the more dynamic and sensitive nature of the ΔG_r approach in detecting phase changes.

7.6 Comparison of Numerical and Analytical Solution for YAM and YAP System

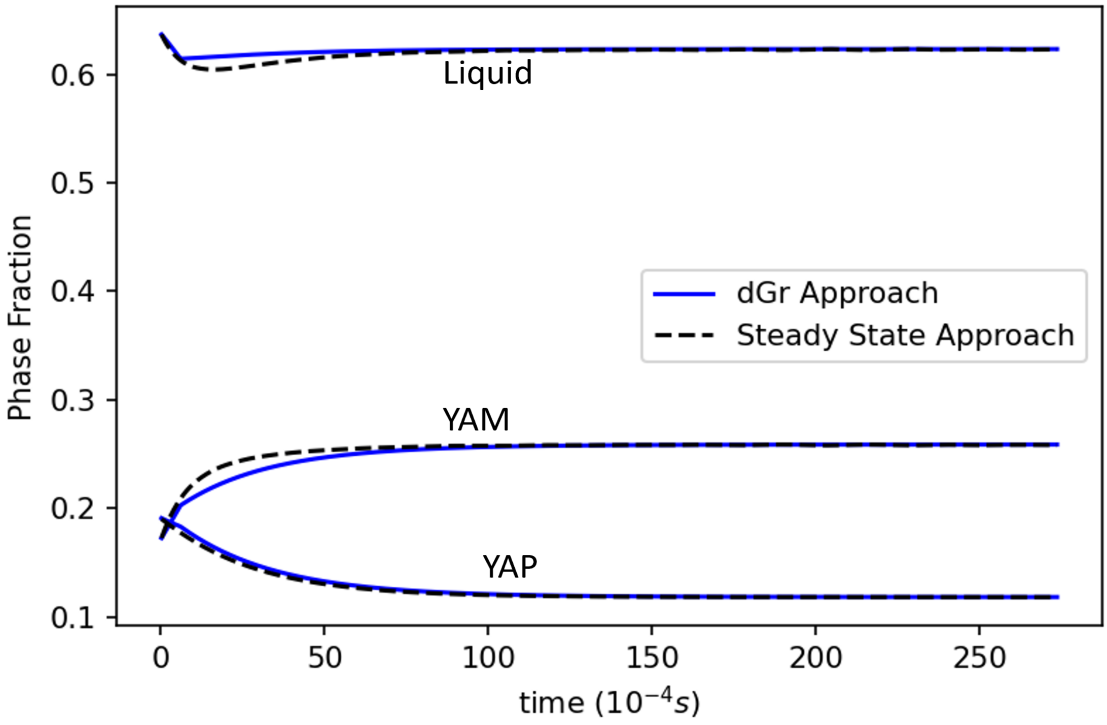

Figure 164: Comparison of analytical and numerical solution for YAM-YAP system (2000 K)

7.6.1 Other Oxide Simulations

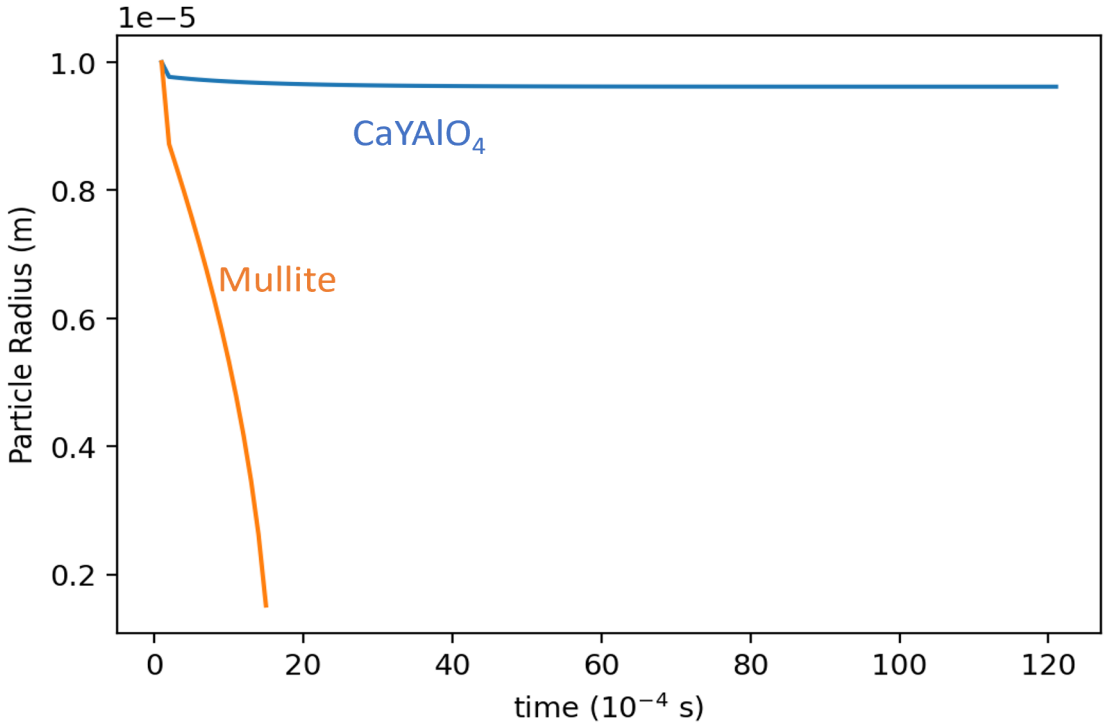

Figure 165: Single oxide simulation of mullite, $CaYAlO_4$ in TiAl melt (2000 K)

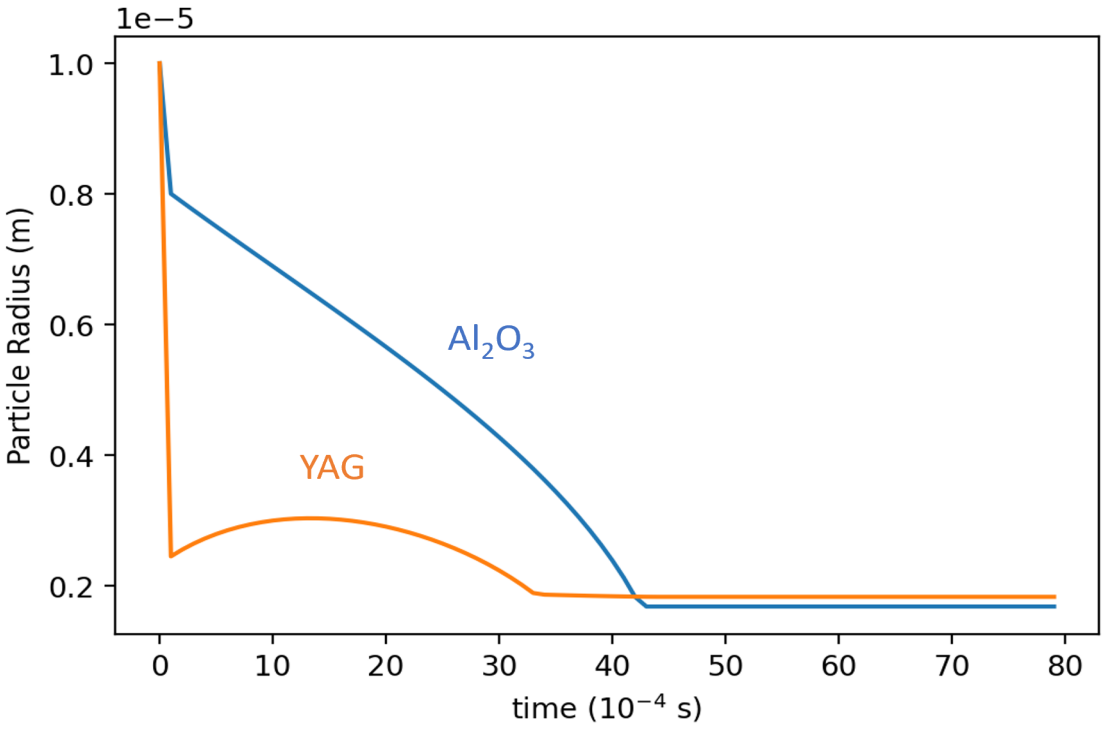

Figure 166: Combined oxide simulation of YAG and Al_2O_3 in TiAl melt

Crucible	Interaction Time/min	Interaction Layer Thickness/µm	Contamination Level: wt%
SiO_2	0.5–5	[a]	O:1.7, Si:1.7
Mullite ($3Al_2O_3 \cdot 2SiO_2$)	15–60	190–840	–
MgO	18–60	1296–3570	O:0.95–1.09
Al_2O_3	0.5–60	30–247	O:0.16–2.5
ZrO_2 (incl. stabilized)	0.5–60	120–300	O:0.55–1.29
Y_2O_3–$15ZrO_2$	3	[a]	O:0.38
CaO	0.5–60	5	O:0.10–0.71
Y_2O_3	0.5–60	8–100	O:0.06–0.33
Y_2O_3-coated MgO	18–60	10–19	O:0.016–0.21
Y_2O_3-coated Al_2O_3	10–34	[a]	O:0.04–0.13
Y_2O_3-coated ZrO_2 (incl. stabilized)	60–120	15–65	O:0.21–0.31
Y_2O_3-coated $ZrO_2 \cdot SiO_2$	1	[a]	O:0.19–0.22
$CaZrO_3$	5–20	300–350	O:0.13–0.73
$CaZrO_3$- Al_2O_3 Composite	30	150	–
$BaZrO_3$	5	870–2000	O:0.065–0.13
Ca-Doped $BaZrO_3$	2	5	O:0.09
AlN	5–25	1.1–6.4	O:0.025–0.113
BN	5–25	250->500	–
Graphite	0.3–2	[a]	C:4

Figure 163: Summary literature data collected by Fashu et al. on contamination of TiAl alloys during vacuum induction melting in different crucibles [20]

References

[1] Christoph Leyens and Manfred Peters. *Titanium and titanium alloys: fundamentals and applications*. Wiley Online Library, 2006.

[2] Chris M. Young and M. S. Bowers. Weight And Volume Scaling Of Pulsed Power For Laser Systems. In Tom R. Burkes and G. Glen McDuff, editors, *Pulse Power for Lasers II*, volume 1046, pages 24 – 27. International Society for Optics and Photonics, SPIE, 1989.

[3] Ozge Genc and Rahmi Unal. Development of gamma titanium aluminide (γ-TiAl) alloys: A review. *Journal of Alloys and Compounds*, page 167262, 2022.

[4] Mikael Perrut, Pierre Caron, Marc Thomas, and Alain Couret. High temperature materials for aerospace applications: Ni-based superalloys and γ-TiAl alloys. *Comptes Rendus Physique*, 19(8):657–671, 2018. New trends in metallic alloys / Alliages métalliques : nouvelles tendances.

[5] Sanna Fager Franzén and Joakim Karlsson. γ-titanium aluminide manufactured by electron beam melting. *Sanna Fager Franzen, Joakim Karlsson*, 2010.

[6] Fritz Appel, Ulrich Brossmann, Ulrich Christoph, Stefan Eggert, Peter Janschek, Uwe Lorenz, Johann Müllauer, Michael Oehring, and Jonathan DH

Paul. Recent progress in the development of gamma titanium aluminide alloys. *Advanced Engineering Materials*, 2(11):699–720, 2000.

[7] Dennis Lundström. *Creep behaviour of titanium aluminides and its relation to phase distributions and dislocation structures*. Chalmers University of Technology, 2001.

[8] P.R. Beeley and R.F. Smart. *Investment Casting*. CRC Press, 2023.

[9] Emergen Research. Investment casting market size, trend, demand analysis till 2032. Available at: https://www.emergenresearch.com/industry-report/investment-casting-market.

[10] Omkar Bemblage and D Benny Karunakar. A study on the blended wax patterns in investment casting process. In *Proceedings of the world Congress on Engineering*, volume 1, pages 6–8. WCE, 2011.

[11] S Jones and C Yuan. Advances in shell moulding for investment casting. *Journal of Materials Processing Technology*, 135(2):258–265, 2003. Special Issue containing paper from the conference 'Research and Development in Net shape Manufacturing'.

[12] Sarojrani Pattnaik, D. Benny Karunakar, and P.K. Jha. Developments in

investment casting process—a review. *Journal of Materials Processing Technology*, 212(11):2332–2348, 2012.

[13] Serope Kalpakjian. *Manufacturing processes for engineering materials*. Pearson Education India, 1984.

[14] Matthias Bünck, Todor Stoyanov, Jan Schievenbusch, Heiner Michels, and Alexander Gußfeld. Titanium aluminide casting technology development. *JOM*, 69:2565–2570, 2017.

[15] Don Larsen and Greg Colvin. Vacuum-die casting titanium for aerospace and commercial components. *JOM*, 51(6):26–27, 1999, Springer.

[16] Xu Cheng, Lianjing Chai, Guoqing Wu, Hong Wang, and H. Nan. Evaluation of interfacial interactions between Ti-6Al-4V and mold use Ti-added backup coat in investment casting. *Metallurgical and Materials Transactions A*, 47, 03 2016.

[17] Kwai S. Chan, Marie Koike, B. W. Johnson, and Toru H. Okabe. Modeling of alpha-case formation and its effects on the mechanical properties of titanium alloy castings. *Metallurgical and Materials Transactions A*, 39:171–180, 2008.

[18] Meijia Liu, Zhi Wang, Junyan Wu, and Qinggang Li. Ti/Al_2O_3 interfacial dif-

fusion: Kinetic equation for growth of reaction layer and formation mechanism. *Journal of Alloys and Compounds*, 652:260–265, 2015.

[19] J.P. Kuang, R.A. Harding, and J. Campbell. Investigation into refractories as crucible and mould materials for melting and casting -tial alloys. *Materials Science and Technology*, 16(9):1007–1016, 2000, Taylor Francis.

[20] Simbarashe Fashu, Mykhaylo Lototskyy, Moegamat Wafeeq Davids, Lydia Pickering, Vladimir Linkov, Sun Tai, Tang Renheng, Xiao Fangming, Pavel V. Fursikov, and Boris P. Tarasov. A review on crucibles for induction melting of titanium alloys. *Materials Design*, 186:108295, 2020.

[21] J.P. Kuang, R.A. Harding, and John Campbell. A study of refractories as crucible and mould materials for melting and casting γ-TiAl alloys. *Materials Science and Technology*, 16:1007–1016, 09 2000.

[22] Birhan Sefer. *Oxidation and Alpha–Case Phenomena in Titanium Alloys used in Aerospace Industry: Ti–6Al–2Sn–4Zr–2Mo and Ti–6Al–4V*. PhD thesis, 06-2014, Lulea University of Technology, Department of Engineering Sciences and Mathematics.

[23] Lyndsey Benson, Ian Mellor, and Martin Jackson. Direct reduction of synthetic

rutile using the ffc process to produce low-cost novel titanium alloys. *Journal of Materials Science*, 51:4250–4261, 05 2016.

[24] G. Holt X. Cheng, C. Yuan and P. A. Withey. Interactions between high Nb containing tial alloy and yttria facecoat during investment casting. *International Journal of Cast Metals Research*, 28(5):283–289, 2015.

[25] R Yang, Y.Y Cui, L.M Dong, and Q Jia. Alloy development and shell mould casting of gamma TiAl. *Journal of Materials Processing Technology*, 135(2):179–188, 2003. Special Issue containing paper from the conference 'Research and Development in Net shape Manufacturing'.

[26] Laura I. V. Holz. Yttria-stabilized zirconia with beige colour, Masters Thesis. 2017, Universidade de Aveiro (Portugal).

[27] Ana I. Kostov and Bernd Friedrich. Predicting thermodynamic stability of crucible oxides in molten titanium and titanium alloys. *Computational Materials Science*, 38:374–385, 2006.

[28] Ren-jie C, Xiao-xia Tang, Gao Ming, Hu Zhang, and Sheng-kai Gong. Thermodynamic analysis of interactions between Ti–Al alloys and oxide ceramics. *Transactions of Nonferrous Metals Society of China*, 22(4):887–894, 2012.

[29] MG Nicholas and B Drevet. *Wettability at High Temperatures. Pergamon Materials Series, Volume 3*. Elsevier Science & Technology, 1999.

[30] Raymundo Arróyave. *Thermodynamics and kinetics of ceramic/metal interfacial interactions*. PhD thesis, Massachusetts Institute of Technology, 2004.

[31] Bang sheng LI, Ai hui LIU, Hai NAN, Wei sheng BI, Jing jie GUO, and Heng zhi FU. Wettability of tial alloy melt on ceramic moulds in electromagnetic field. *Transactions of Nonferrous Metals Society of China*, 18(3):518–522, 2008.

[32] Yoshinao Kobayashi and Fumitaka Tsukihashi. Thermodynamics of yttrium and oxygen in molten Ti, Ti_3Al, and TiAl Y_2O_3. *Metallurgical and materials transactions B*, 29(5):1037–1042, 1998.

[33] JP Kuang, RA Harding, and John Campbell. Investigation into refractories as crucible and mould materials for melting and casting gamma-tial alloys. *Materials Science and Technology*, 16:1007–1016, 09 2000.

[34] Xu Cheng, Chen Yuan, Nick R. Green, and Paul A. Withey. Evaluation of the inertness of investment casting molds using both sessile drop and centrifugal casting methods. *Metallurgical and Materials Transactions A*, 44:888–898, 2013.

[35] Mariia Ilatovskaia, Galina Savinykh, and Olga Fabrichnaya. Thermodynamic description of the ti-al-o system based on experimental data. *Journal of Phase Equilibria and Diffusion*, 38:175–184, 2017.

[36] R.J. Cui, X.X. Tang, M. Gao, H. Zhang, and S.K. Gong. Microstructure and composition of cast Ti–47Al–2Cr–2Nb alloys produced by yttria crucibles. *Materials Science and Engineering: A*, 541:14–21, 2012.

[37] Celestino Veiga, J. Paulo Davim, and A. Loureiro. Properties and applications of titanium alloys: A brief review. *Reviews on Advanced Materials Science*, 32:133–148, 12 2012.

[38] Simon Winchester. The map that changed the world: a tale of rocks, ruin and redemption. 2002.

[39] G. Lütjering and J.C. Williams. *Titanium*. Engineering Materials and Processes. Springer Berlin Heidelberg, 2013.

[40] *William J. Kroll, Method for Manufacturing Titanium and Alloys Thereof, https://books.google.co.uk/books?id=R4PvjwEACAAJ.*

[41] John Emsley. *Nature's building blocks: an AZ guide to the elements*. Oxford University Press, USA, 2011.

[42] F Froes. History and extractive metallurgy. *Titanium: Physical Metallurgy, Processing, and Applications*, pages 1–27, 2015.

[43] Akshar Kota. *Study of Energy Consumption in Metal Additive Manufacturing*. PhD thesis, IIT Hyderabad, India, 2021.

[44] Pallavi Pushp, S.M. Dasharath, and C. Arati. Classification and applications of titanium and its alloys. *Materials Today: Proceedings*, 54:537–542, 2022. 5th International Conference on Advanced Research in Mechanical, Materials and Manufacturing Engineering-2021.

[45] Chaganti RVS Nagesh. Titanium extraction metallurgy developments and control of impurity elements. In *Titanium Alloys-Recent Progress in Design, Processing, Characterization, and Applications*. IntechOpen, 2022.

[46] Mohammed El Khalloufi, Olivier Drevelle, and Gervais Soucy. Titanium: An overview of resources and production methods. *Minerals*, 11(12), 2021.

[47] MJ Donachie. Titanium: A technical guide. *ASM International*, 369, 2000.

[48] Osamu Takeda and Toru H Okabe. Current status of titanium recycling and related technologies. *Jom*, 71(6):1981–1990, 2019.

[49] Chandima Subasinghe and Amila Ratnayake. General review of titanium ores

in exploitation: present status and forecast revisão geral dos minérios de titânio em exploração: estado atual e previsão. *Comunicações Geológicas*, 109:21–31, 07 2022.

[50] Saleem H. Ali, Damian Giurco, Nicholas Arndt, Edmund Nickless, Glen Brown, Alecos Demetriades, Raymond Durrheim, Miguel A. Enriquez, Judith Kinnaird, Andrew Littleboy, Lawrence D. Meinert, Roland Oberhänsli, Jennifer Salem, Richard Schodde, Gerald Schneider, Olivier Vidal, and Natalia Yakovleva. Mineral supply for sustainable development requires resource governance. *Nature*, 543(7645):367–372, 2017.

[51] Katherine Bourzac. The rare-earth crisis, mit technology review, publisher: Mit technology review, Apr 2020. Available at: (https://www.technologyreview.com/2011/04/19/195225/the-rare-earth-crisis/).

[52] Laura Wood. Research and markets: The worldwide titanium industry is expected to reach $33.5 billion by 2026, 2021. Available at: https://www.businesswire.com/news/home/20211012006021/en (Accessed on January 2022).

[53] Madhumitha Jaganmohan. Global titanium production by country 2024,

statista, Mar year of 2025, https://www.statista.com/statistics/759972/mine-production-titanium-minerals-worldwide-by-country/.

[54] Madhumitha Jaganmohan. Titanium industry worldwide, Statista, year of Sep 2024, https://www.statista.com/topics/11141/titanium-industry-worldwide/topicOverview.

[55] Pranad Seth, Jyoti S Jha, Alankar Alankar, and Sushil K Mishra. Alpha-case formation in Ti-6Al-4V in a different oxidizing environment and its effect on tensile and fatigue crack growth behavior. *Oxidation of Metals*, 97(1):77–95, 2022.

[56] David Whittaker and Francis H. (Sam) Froes. 30 - future prospects for titanium powder metallurgy markets. In Ma Qian and Francis H. (Sam) Froes, editors, *Titanium Powder Metallurgy*, pages 579–600. Butterworth-Heinemann, Boston, 2015.

[57] N. Singh, P. Hameed, R. Ummethala, G. Manivasagam, K.G. Prashanth, and J. Eckert. Selective laser manufacturing of ti-based alloys and composites: impact of process parameters, application trends, and future prospects. *Materials Today Advances*, 8:100097, 2020.

[58] Precedence Research. Titanium market size, share, and trends 2024 to 2034,

available at: https://www.precedenceresearch.com/titanium-market. *Precedence Research*, Nov 2023.

[59] Celestino Veiga, J Paulo Davim, AJR Loureiro, et al. Properties and applications of titanium alloys: a brief review. *Rev. Adv. Mater. Sci*, 32(2):133–148, 2012.

[60] Ritanjali Sethy. Glass coating effects on Ti-6Al-4V hot forging. 2017, PhD Thesis, Mondragon University, Arrasate, Spain.

[61] Helmut Clemens and Svea Mayer. Design, processing, microstructure, properties, and applications of advanced intermetallic tial alloys. *Advanced engineering materials*, 15(4):191–215, 2013.

[62] European Commission, Directorate-General for Mobility, Transport, Directorate-General for Research, and Innovation. *Flightpath 2050 – Europe's vision for aviation – Maintaining global leadership and serving society's needs*. Publications Office, 2011.

[63] Xinhua Wu. Review of alloy and process development of tial alloys. *Intermetallics*, 14(10-11):1114–1122, 2006.

[64] David Rugg, Mark Dixon, and Justin Burrows. High-temperature application of titanium alloys in gas turbines. material life cycle opportunities and threats–

an industrial perspective. *Materials at High Temperatures*, 33(4-5):536–541, 2016.

[65] Dierk Raabe, C Cem Tasan, and Elsa A Olivetti. Strategies for improving the sustainability of structural metals. *Nature*, 575(7781):64–74, 2019.

[66] Stefano Gialanella, Alessio Malandruccolo, et al. *Aerospace alloys*. Springer, 2020.

[67] Ozge Genc and Rahmi Unal. Development of gamma titanium aluminide (γ-TiAl) alloys: A review. *Journal of Alloys and Compounds*, 929:167262, 2022.

[68] Ezra L Kotzin. *Metal casting and molding processes*. American Foundrymen's Society, 1981.

[69] SO Barnett. Investment casting–the multi-process technology. *Foundry Trade J. Int.*, 11(3):33, 1988.

[70] SKY QUEST. Investment casting market size, share, growth analysis, by type(steel, aluminum, and superalloys), by application(aerospace defense, automotive, oil gas, medical), by end user(automotive, aerospace, aefense, and healthcare), by region - industry forecast 2024-2031. Available at: https://www.skyquestt.com/report/investment-casting-market.

[71] Yaozheng Liu, William R Aimutis, and MaryAnne Drake. Dairy, plant, and novel proteins: Scientific and technological aspects. *Foods*, 13(7):1010, 2024.

[72] Dirk Lehmhus. Advances in metal casting technology: A review of state of the art, challenges and trends—part i: changing markets, changing products. *Metals*, 12(11):1959, 2022.

[73] Airbus 2024. Envision future demand to connect today and tomorrow, global services forecast (gsf) — 2024-2043. Available at: https://aircraft.airbus.com/en/global-services-forecast-gsf-2024-2043.

[74] Robert G Craig, JD Eick, and Floyd Avery Peyton. Properties of natural waxes used in dentistry. *Journal of Dental Research*, 44(6):1308–1316, 1965.

[75] Sunpreet Singh and Rupinder Singh. Precision investment casting: A state of art review and future trends. *Proceedings of the Institution of Mechanical Engineers, Part B: Journal of Engineering Manufacture*, 230(12):2143–2164, 2016.

[76] David W Richerson and William E Lee. *Modern ceramic engineering: properties, processing, and use in design*. CRC press, 2018.

[77] Nikhil Yadav and DB Karunakar. Effect of process parameters on mechanical properties of the investment castings produced by using expandable

polystyrene pattern. *International journal of advances in engineering & technology*, 1(3):128, 2011.

[78] Toshimitsu Tetsui. Identifying low-cost, machinable, impact-resistant tial alloys suitable for last-stage turbine blades of jet engines. *Intermetallics*, 168:108263, 2024.

[79] Daniel P. Barbis, Robert M. Gasior, Graham P. Walker, Joseph A. Capone, and Teddi S. Schaeffer. 7 - titanium powders from the hydride–dehydride process. pages 101–116, 2015.

[80] Zhigang Zak Fang, James D Paramore, Pei Sun, KS Ravi Chandran, Ying Zhang, Yang Xia, Fei Cao, Mark Koopman, and Michael Free. Powder metallurgy of titanium–past, present, and future. *International Materials Reviews*, 63(7):407–459, 2018.

[81] Andrej Šalak, Marcela Selecká, and Herbert Danninger. *Machinability of powder metallurgy steels*. Cambridge Int Science Publishing, 2005.

[82] Qinyang Zhao, Qiaoyan Sun, Shewei Xin, Yongnan Chen, Cong Wu, Huan Wang, Jianwei Xu, Mingpan Wan, Weidong Zeng, and Yongqing Zhao. High-strength titanium alloys for aerospace engineering applications: A review on

melting-forging process. *Materials Science and Engineering: A*, 845:143260, 2022.

[83] M Jackson and K Dring. A review of advances in processing and metallurgy of titanium alloys. *Materials science and technology*, 22(8):881–887, 2006.

[84] Alec Mitchell. Melting, casting and forging problems in titanium alloys. *Materials Science and Engineering: A*, 243(1-2):257–262, 1998.

[85] Zidong Lin, Kaijie Song, and Xinghua Yu. A review on wire and arc additive manufacturing of titanium alloy. *Journal of Manufacturing Processes*, 70:24–45, 2021.

[86] Amit Bandyopadhyay, Kellen D Traxel, Melanie Lang, Michael Juhasz, Noam Eliaz, and Susmita Bose. Alloy design via additive manufacturing: Advantages, challenges, applications and perspectives. *Materials Today*, 52:207–224, 2022.

[87] RK Mishra. Development of low emission combustion technologies for modern aero gas turbine engines: An overview. *Journal of Aerospace Sciences and Technologies*, pages 65–75, 2021.

[88] Ulrike Habel, Falko Heutling, Claudia Kunze, Wilfried Smarsly, Gopal Das, and Helmut Clemens. Forged intermetallic γ-tial based alloy low pressure turbine

blade in the geared turbofan. In *Proceedings of the 13th World Conference on Titanium*, pages 1223–1227. Wiley Online Library, 2016.

[89] Ayush Sinha, Biswajit Swain, Asit Behera, Priyabrata Mallick, Saswat Kumar Samal, H. M. Vishwanatha, and Ajit Behera. A review on the processing of aero-turbine blade using 3d print techniques. *Journal of Manufacturing and Materials Processing*, 6(1), 2022.

[90] Cui Renjie, Gao Ming, Zhang Hu, and Gong Shengkai. Interactions between TiAl alloys and yttria refractory material in casting process. *Journal of Materials Processing Technology*, 210(9):1190–1196, 2010.

[91] Rajath N. Rao, Shrikantha S. Rao, and Vijeesh Vijayan. Achieving ultra-fine grains in Ti-6Al-4V alloy welds through pre-weld friction stir processing. *Results in Engineering*, 24:103019, 2024.

[92] R. Gaddam, M-L. Antti, and R. Pederson. Influence of alpha-case layer on the low cycle fatigue properties of Ti-6Al-2Sn-4Zr-2Mo alloy. *Materials Science and Engineering: A*, 599:51–56, 2014.

[93] Raghuveer Gaddam, Birhan Sefer, Robert Pederson, and Marta-Lena Antti. Study of alpha-case depth in Ti-6Al-2Sn-4Zr-2Mo and Ti-6Al-4V. In *IOP Con-*

ference Series: Materials Science and Engineering, volume 48, page 012002. IOP Publishing, 2013.

[94] GQ Wu, X Cheng, Wei Sha, XJ Cheng, JQ Zhao, and H Nan. Effect of the interaction layer on the mechanical properties of Ti-6Al-4V alloy castings. *Materials Chemistry and Physics*, 175:125–130, 2016.

[95] Xing-Yuan Miao, Chi-Jen Chen, Søren Fæster, Seyed Sina Samareh-Mousavi, and Xiao Chen. Fatigue and post-fatigue static crack characterisation of a wrinkled thick glass fibre laminate in a composite wind turbine blade. *International Journal of Fatigue*, 176:107855, 2023.

[96] Nikita Mohite, Sachin Biradar, Jyoti Shankar Jha, Sushil Mishra, and Asim Tewari. Development and removal of alpha-case layer from heat treated titanium alloys. In *Gas Turbine India Conference*, volume 58516, page V002T10A011. American Society of Mechanical Engineers, 2017.

[97] William J Boettinger, Maureen E Williams, Sam R Coriell, Ursula R Kattner, and BA Mueller. Alpha case thickness modeling in investment castings. *Metallurgical and materials transactions B*, 31:1419–1427, 2000.

[98] Zi-Kui Liu. First-principles calculations and calphad modeling of thermodynamics. *Journal of phase equilibria and diffusion*, 30:517–534, 2009.

[99] Ming Gao, Renjie Cui, Limin Ma, Huarui Zhang, Xiaoxia Tang, and Hu Zhang. Physical erosion of yttria crucibles in Ti–54Al alloy casting process. *Journal of Materials Processing Technology*, 211(12):2004–2011, 2011.

[100] Carl TF Ross, A Chilver, et al. *Strength of materials and structures*. Elsevier, 1999.

[101] L. Denardo, G. Raffaini, F. Ganazzoli, and R. Chiesa. Metal surface oxidation and surface interactions. In *Surface Modification of Biomaterials*, Woodhead Publishing Series in Biomaterials, pages 102–142. Woodhead Publishing, 2011.

[102] Entao Dong, Wei Yu, Qingwu Cai, Lei Cheng, and Jiaxin Shi. High-temperature oxidation kinetics and behavior of Ti-6Al-4V alloy. *Oxidation of Metals*, 88:719–732, 2017.

[103] Jingjie Dai, Jiyun Zhu, Chuanzhong Chen, and Fei Weng. High temperature oxidation behavior and research status of modifications on improving high temperature oxidation resistance of titanium alloys and titanium aluminides: A review. *Journal of Alloys and Compounds*, 685:784–798, 2016.

[104] Dalibor Vojtěch, Barbora Bártová, and Tomáš Kubatık. High temperature oxidation of titanium–silicon alloys. *Materials Science and Engineering: A*, 361(1-2):50–57, 2003.

[105] P Kofstad, K Hauffe, and H Kjollesdal. Investigation on the oxidation mechanism of titanium. *Acta chem. scand*, 12(2):239–266, 1958.

[106] Hasan Guleryuz and Huseyin Cimenoglu. Oxidation of Ti–6Al–4V alloy. *Journal of Alloys and Compounds*, 472(1):241–246, 2009.

[107] Maciej Bik, Mathias Galetz, Lukas Mengis, Emma White, Wojciech Wieczorek, Klaudia Łyszczarz, Krzysztof Mroczka, Jakub Marchewka, and Maciej Sitarz. Oxidation behaviour of uncoated and PDC-SiAlOC glass-coated TiAl at 750°C in dry and humid air. *Applied Surface Science*, 632:157601, 2023.

[108] S Frangini, A Mignone, and F De Riccardis. Various aspects of the air oxidation behaviour of a Ti6Al4V alloy at temperatures in the range 600-700°C. *Journal of Materials Science*, 29(3):714–720, 1994.

[109] H.L. Du, P.K. Datta, D.B. Lewis, and J.S. Burnell-Gray. Air oxidation behaviour of Ti-6Al-4V alloy between 650 and 850°C. *Corrosion Science*, 36(4):631–642, 1994.

[110] J.P. Lin, L.L. Zhao, G.Y. Li, L.Q. Zhang, X.P. Song, F. Ye, and G.L. Chen. Effect of Nb on oxidation behavior of high Nb containing TiAl alloys. *Intermetallics*, 19(2):131–136, 2011. Proceedings of the 7th International Workshop on Advanced Intermetallics and Metallic Materials (2008).

[111] Xu Cheng, Chen Yuan, Dmytro Shevchenko, and Paul Withey. The influence of mould pre-heat temperature and casting size on the interaction between a Ti-46Al-8Nb-1B alloy and the mould comprising an Al_2O_3 face coat. *Materials Chemistry and Physics*, 146(3):295–302, 2014.

[112] Chen Yuan, Xu Cheng, GS Holt, Dmytro Shevchenko, and PA Withey. Investment casting of Ti-46Al-8Nb-1B alloy using moulds with CaO-stabilized zirconia face coat at various mould pre-heat temperatures. *Ceramics International*, 41(3):4129–4139, 2015.

[113] Toshifumi Yahata, Takashi Ikeda, and Masafumi Maeda. Deoxidation of molten titanium by electron-beam remelting technique. *Metallurgical Transactions B*, 24(4):599–604, 1993.

[114] Ryosuke Suzuki and Shuichi Inoue. Calciothermic reduction of titanium oxide in molten $CaCl_2$. *Metallurgical and Materials Transactions B: Process Metallurgy and Materials Processing Science*, 34:277–285, 06 2003.

[115] Toru H. Okabe, Chenyi Zheng, and Yu-ki Taninouchi. Thermodynamic Considerations of Direct Oxygen Removal from Titanium by Utilizing the Deoxidation Capability of Rare Earth Metals. *Metallurgical and Materials Transactions B*, 49(3):1056–1066, June 2018.

[116] I.-S. Kim. Thermal shock resistance of the Al_2O_3-metal composites made by reactive infiltration of Al into oxide fiber board. *Materials Research Bulletin*, 33(7):1069–1075, 1998.

[117] Rui L Neto, Teresa P Duarte, Jorge L Alves, and Tiago G Barrigana. The influence of face coat material on reactivity and fluidity of the Ti6Al4V and TiAl alloys during investment casting. *Proceedings of the Institution of Mechanical Engineers, Part L: Journal of Materials: Design and Applications*, 231(1-2):38–48, 2017.

[118] Kai Li, Dalei Wang, Han Chen, and Lucun Guo. Normalized evaluation of thermal shock resistance for ceramic materials. *Journal of Advanced Ceramics*, 3:250–258, 2014.

[119] HR Zhang, XX Tang, L Zhou, M Gao, CG Zhou, and H Zhang. Interactions between Ni-44Ti-5Al-2Nb-Mo alloy and oxide ceramics during directional solidification process. *Journal of Materials Science*, 47:6451–6458, 2012.

[120] Huarui Zhang, Xiaoxia Tang, Chungen Zhou, Hu Zhang, and Shaowei Zhang. Comparison of directional solidification of γ-TiAl alloys in conventional Al_2O_3 and novel Y_2O_3-coated Al_2O_3 crucibles. *Journal of the European Ceramic Society*, 33(5):925–934, 2013.

[121] Federico Smeacetto, Milena Salvo, and Monica Ferraris. Protective coatings for induction casting of titanium. *Surface and Coatings Technology*, 201(24):9541–9548, 2007.

[122] F Gomes, H Puga, Joaquim Barbosa, and C Silva Ribeiro. Effect of melting pressure and superheating on chemical composition and contamination of yttria-coated ceramic crucible induction melted titanium alloys. *Journal of materials science*, 46:4922–4936, 2011.

[123] Joaquim Barbosa, C Silva Ribeiro, OMND Teodoro, and Caetano Monteiro. Evaluation of Y_2O_3 as front layer of ceramic crucibles for vacuum induction melting of TiAl based alloys. *Journal of The Minerals, Metals and Materials Society*, pages 573–584, 2005.

[124] ED Eastman, Leo Brewer, LeRoy A Bromley, Paul W Gilles, and Norman I Lofgren. Preparation and tests of refractory sulfide crucibles. *Journal of the American Ceramic Society*, 34(4):128–136, 1951.

[125] Toshimitsu Tetsui, Toshiharu Kobayashi, Takashi Mori, Tatsuya Kishimoto, and Hiroshi Harada. Evaluation of yttria applicability as a crucible for induction melting of TiAl alloy. *Materials Transactions*, 51(9):1656–1662, 2010.

[126] D Camel, B Drevet, V Brizé, F Disdier, E Cierniak, and N Eustathopoulos.

The crucible/silicon interface in directional solidification of photovoltaic silicon. *Acta Materialia*, 129:415–427, 2017.

[127] SK Kim, TK Kim, MG Kim, TW Hong, and YJ Kim. Investment casting of titanium alloys with CaO crucible and $CaZrO_3$ mould. *Lightweight Alloys for Aerospace Application*, pages 251–260, 2001.

[128] Stefan Schafföner, Christos G Aneziris, Harry Berek, Jana Hubálková, Björn Rotmann, and Bernd Friedrich. Corrosion behavior of calcium zirconate refractories in contact with titanium aluminide melts. *Journal of the European Ceramic Society*, 35(3):1097–1106, 2015.

[129] Zhao ZHANG, Kailiang ZHU, Lanjie LIU, Xionggang LU, Guangxin WU, and Chonghe LI. Preparation of $BaZrO_3$ crucible and its interfacial reaction with molten titanium alloys. *Journal of the Chinese ceramic society*, 41(9):1278–1283, 2013.

[130] RL Saha and KT Jacob. Casting of titanium and its alloys. *Defence Science Journal*, 36(2):121–141, 1986.

[131] US Department of Defence. High Performance Steel and Titanium Casting, National Materials Advisory Board (NAS-NAE). *High Performance Steel and Titanium Casting, https://apps.dtic.mil/sti/pdfs/ADA512853.pdf.*

[132] BD Begg, AJ Ruys, and CC Sorrell. Slip casting of Y_2O_3-stabilized ZrO_2. In *Science and Technology of Zirconia V*, pages 267–274. CRC Press, 2023.

[133] Guangyao Chen, Juyun Kang, Pengyue Gao, Ziwei Qin, Xionggang Lu, and Chonghe Li. Dissolution of $BaZrO_3$ refractory in titanium melt. *International Journal of Applied Ceramic Technology*, 15(6):1459–1466, 2018.

[134] B Gorr, F Mueller, H-J Christ, T Mueller, H Chen, A Kauffmann, and M Heilmaier. High temperature oxidation behavior of an equimolar refractory metal-based alloy 20Nb-20Mo-20Cr-20Ti-20Al with and without Si addition. *Journal of Alloys and Compounds*, 688:468–477, 2016.

[135] B Gorr, M Azim, H-J Christ, T Mueller, D Schliephake, and M Heilmaier. Phase equilibria, microstructure, and high temperature oxidation resistance of novel refractory high-entropy alloys. *Journal of Alloys and Compounds*, 624:270–278, 2015.

[136] Lavina Backman and Elizabeth J. Opila. Thermodynamic assessment of the group IV, V and VI oxides for the design of oxidation resistant multi-principal component materials. *Journal of the European Ceramic Society*, 39(5):1796–1802, 2019.

[137] Alan Wesley Weimer. *Carbide, nitride and boride materials synthesis and processing*. Springer Science & Business Media, 2012.

[138] DR Glasson and JA Jones. Formation and reactivity of borides, carbides and silicides. I. review and introduction. *Journal of Applied Chemistry*, 19(5):125–137, 1969.

[139] AV Kartavykh, VV Tcherdyntsev, and J Zollinger. TiAl-Nb melt interaction with pyrolytic boron nitride crucibles. *Materials Chemistry and Physics*, 119(3):347–350, 2010.

[140] E.J. Chapin, W.H. Friske, and Naval Research Laboratory (U.S.). *A Metallurgical Evaluation of Refractory Compounds for Containing Molten Titanium: Part 1: Oxides*. AD (United States. National Technical Information Service). Naval Research Laboratory, 1973.

[141] Sergio Trasatti. Physical electrochemistry of ceramic oxides. *Electrochimica acta*, 36(2):225–241, 1991.

[142] WG Fahrenholtz and GE Hilmas. Oxidation of ultra-high temperature transition metal diboride ceramics. *International Materials Reviews*, 57(1):61–72, 2012.

[143] SM McDeavitt, GW Billings, and JE Indacochea. High temperature interaction behavior at liquid metal-ceramic interfaces. *Journal of materials engineering and performance*, 11:392–401, 2002.

[144] C. Yuan, X. Cheng, G.S. Holt, D. Shevchenko, and P.A. Withey. Investment casting of Ti–46Al–8Nb–1B alloy using moulds with CaO-stabilized zirconia face coat at various mould pre-heat temperatures. *Ceramics International*, 41(3, Part A):4129–4139, 2015.

[145] Andrei B Koudriavtsev, Reginald F Jameson, and Wolfgang Linert. *The law of mass action*. Springer Science & Business Media, 2011.

[146] Tao Cheng, Hai Xiao, and William A Goddard III. Free-energy barriers and reaction mechanisms for the electrochemical reduction of CO on the Cu (100) surface, including multiple layers of explicit solvent at pH 0. *The journal of physical chemistry letters*, 6(23):4767–4773, 2015.

[147] DP Mishra. *Fundamentals of combustion*. PHI Learning Pvt. Ltd., 2007.

[148] Norman Sutin. Free energies, barriers, and reactivity patterns in oxidation-reduction reactions. *Accounts of Chemical Research*, 1(8):225–231, 1968.

[149] Noy Cohen and Sydney William Benson. Estimation of heats of formation

of organic compounds by additivity methods. *Chemical Reviews*, 93(7):2419–2438, 1993.

[150] RL Saha, TK Nandy, RDK Misra, and KT Jacob. On the evaluation of stability of rare earth oxides as face coats for investment casting of titanium. *Metallurgical Transactions B*, 21(3):559–566, 1990.

[151] PR Chidambaram, GR Edwards, and DL Olson. A thermodynamic criterion to predict wettability at metal-alumina interfaces. *Metallurgical Transactions B*, 23:215–222, 1992.

[152] Fumitaka Tsukihashi, Toshiyuki Hatta, and Eiji Tawara. Thermodynamics of calcium and oxygen in molten titanium and titanium-aluminum alloy. *Metallurgical and Materials Transactions B*, 27(6):967–972, 1996.

[153] Baron Peters. *Reaction rate theory and rare events*. Elsevier, 2017.

[154] Toshimitsu Tetsui, Toshiharu Kobayashi, Tsuyoshi Ueno, and Hiroshi Harada. Consideration of the influence of contamination from oxide crucibles on TiAl cast material, and the possibility of achieving low-purity tial precision cast turbine wheels. *Intermetallics*, 31:274–281, 2012.

[155] Juraj Lapin, Zuzana Gabalcová, and Tatiana Pelachová. Effect of Y_2O_3 cru-

cible on contamination of directionally solidified intermetallic Ti–46Al–8Nb alloy. *Intermetallics*, 19:396–403, 2011.

[156] C. Yuan, X. Cheng, and P.A. Withey. Investigation into the use of $CaZrO_3$ as a facecoat material in the investment casting of TiAl alloys. *Materials Chemistry and Physics*, 155:205–210, 2015.

[157] N. Vaché, Y. Cadoret, B. Dod, and D. Monceau. Modeling the oxidation kinetics of titanium alloys: Review, method and application to ti-64 and ti-6242s alloys. *Corrosion Science*, 178:109041, 2021.

[158] Maria Peressi, Alfonso Baldereschi, and Stefano Baroni. 2 - ab initio studies of structural and electronic properties. In Carlo Lamberti, editor, *Characterization of Semiconductor Heterostructures and Nanostructures*, pages 17–54. Elsevier, Amsterdam, 2008.

[159] Nigel Saunders and A Peter Miodownik. *CALPHAD (calculation of phase diagrams): a comprehensive guide*. Elsevier, 1998.

[160] Peter V Coveney and Shunzhou Wan. On the calculation of equilibrium thermodynamic properties from molecular dynamics. *Physical Chemistry Chemical Physics*, 18(44):30236–30240, 2016.

[161] PJ Spencer. Estimation of thermodynamic data for metallurgical applications. *Thermochimica Acta*, 314(1-2):1–21, 1998.

[162] Eberhard Engel. *Density functional theory*. Springer, 2011.

[163] Luís M.N.B.F. Santos, Ana I.M.C. Lobo Ferreira, Vojtech Štejfa, Ana S.M.C. Rodrigues, Marisa A.A. Rocha, Manuel C. Torres, Fernando M.S. Tavares, and Francisco S. Carpinteiro. Development of the knudsen effusion methodology for vapour pressure measurements of low volatile liquids and solids based on a quartz crystal microbalance. *The Journal of Chemical Thermodynamics*, 126:171–186, 2018.

[164] Günter Walter Heinrich Höhne, Wolfgang Hemminger, Hans-Jürgen Flammersheim, et al. *Differential scanning calorimetry*, volume 2. Springer, 2003.

[165] SH Jabarov, AV Trukhanov, SV Trukhanov, AI Mammadov, VA Turchenko, RZ Mehdiyeva, RE Huseynov, et al. Xrd, dta and tga investigations of the bafe12-xalxo19 (x= 0.3, 0.9 and 1.2) solid solutions. *Optoelectronics and Advanced Materials-Rapid Communications*, 9:468–470, 2015.

[166] SV Meschel and OJ Kleppa. Standard enthalpies of formation of some 3d transition metal carbides by high temperature reaction calorimetry. *Journal of alloys and compounds*, 257(1-2):227–233, 1997.

[167] György Inzelt. Crossing the bridge between thermodynamics and electrochemistry. from the potential of the cell reaction to the electrode potential. *ChemTexts*, 1:1–11, 2015.

[168] Kiran K. Yalamanchi, Yang Li, Tairan Wang, M. Monge-Palacios, and S. Mani Sarathy. Large-scale thermochemistry calculations for combustion models. *Applications in Energy and Combustion Science*, 12:100084, 2022.

[169] Tao Cheng, Hai Xiao, and William Goddard. The free energy barriers and reaction mechanisms for the electrochemical reduction of CO on the Cu(100) surface including multiple layers of explicit solvent at pH 0. *The journal of physical chemistry letters*, 6, 11 2015.

[170] Dimitra Spathara, Dmitry Sergeev, Dietmar Kobertz, Michael Müller, Duncan Putman, and Nils Warnken. Thermodynamic study of single crystal, ni-based superalloys in the + two-phase region using knudsen effusion mass spectrometry, dsc and sem. *Journal of Alloys and Compounds*, 870:159295, 2021.

[171] C. H. P. Lupis. *Chemical thermodynamics of materials / C.H.P. Lupis.* North Holland New York, 1983.

[172] Koichi Sakamoto, Katsuyuki Yoshikawa, Tatsuhiko Kusamichi, and Toshio Onoye. Changes in oxygen contents of titanium aluminides by vacuum induc-

tion, cold crucible induction and electron beam melting. *ISIJ International*, 32(5):616–624, 1992.

[173] Y Kobayashi and F Tsukihashi. Thermodynamics of oxygen in molten Ti-Al and Zr-Al alloys Al_2O_3. *High Temperature Materials and Processes*, 19(3-4):211–218, 2000.

[174] AR Miedema. Simple model for alloys. *Philips Tech. Rev*, 33(6):149–160, 1973.

[175] Joaquim Barbosa, Carlos Ribeiro, and António Monteiro. Influence of superheating on casting of $\gamma - TiAl. Intermetallics, 15 : 945 - -955, 072007$.

[176] Lorenz Ratke and Peter W. Voorhees. *Growth*, pages 65–67. Springer Berlin Heidelberg, Berlin, Heidelberg, 2002.

[177] Thermo-Calc Software TCOX Oxides/Metal Slag and Oxides Database, version 11. Available at: https://thermocalc.com/solutions/solutions-by-material/oxides/ and https://thermocalc.com/products/databases/metal-oxide-solutions/.

[178] JW Rogers Jr, KL Erickson, DN Belton, RW Springer, TN Taylor, and JG Beery. Low temperature diffusion of oxygen in titanium and titanium oxide films. *Applied surface science*, 35(1):137–152, 1988.

[179] Kiana Shirzad and Christopher Viney. A critical review on applications of the avrami equation beyond materials science. *Journal of the Royal Society Interface*, 20(203):20230242, 2023.

[180] Wayne Lin and Catherine J Murphy. A demonstration of le chatelier's principle on the nanoscale. *ACS Central Science*, 3(10):1096–1102, 2017.

[181] Paul L Houston. *Chemical kinetics and reaction dynamics*. Courier Corporation, 2006.

[182] Darl H McDaniel and Charles R Smoot. Approximations in the kinetics of consecutive reactions. *The Journal of Physical Chemistry*, 60(7):966–969, 1956.

[183] GH Nancollas and N Purdie. The kinetics of crystal growth. *Quarterly Reviews, Chemical Society*, 18(1):1–20, 1964.

[184] Stephen J Harris and Anita M Weiner. Chemical kinetics of soot particle growth. *Annual Review of Physical Chemistry*, 36(1):31–52, 1985.

[185] Julius Beretka and Trevor Brown. Effect of particle size on the kinetics of the reaction between magnesium and aluminum oxides. *Journal of the American Ceramic Society*, 66(5):383–388, 1983.

[186] Masato Machida, Koichi Eguchi, and Hiromichi Arai. Effect of additives on the

surface area of oxide supports for catalytic combustion. *Journal of catalysis*, 103(2):385–393, 1987.

[187] Guangwen Zhou. Nucleation-induced kinetic hindrance to the oxide formation during the initial oxidation of metals. *Physical Review B—Condensed Matter and Materials Physics*, 81(19):195440, 2010.

[188] Mikhaylo A Trunov, Mirko Schoenitz, Xiaoying Zhu, and Edward L Dreizin. Effect of polymorphic phase transformations in Al_2O_3 film on oxidation kinetics of aluminum powders. *Combustion and flame*, 140(4):310–318, 2005.

[189] Xian Zhang, Sen Gao, Wenhua Gui, and Qingfeng Zeng. First-principles study of structure, mechanical and optical properties of La and Sc doped Y_2O_3. *Journal of Rare Earths*, 37(8):879–885, 2019.

[190] Gerdjan Busker, Alex Chroneos, Robin W Grimes, and I-Wei Chen. Solution mechanisms for dopant oxides in yttria. *Journal of the American Ceramic Society*, 82(6):1553–1559, 1999.

[191] G. Wang, D.S. Xu, N. Ma, N. Zhou, E.J. Payton, R. Yang, M.J. Mills, and Y. Wang. Simulation study of effects of initial particle size distribution on dissolution. *Acta Materialia*, 57(2):316–325, 2009.

[192] F. Vermolen, C. Vuik, and S. Zwaag. The dissolution of a stoichiometric second phase in ternary alloys: A numerical analysis. *Materials Science and Engineering: A*, 246:93–103, 05 1998.